TECHNISCHE UNIVERSITÄT MÜNCHEN
Fakultät für Physik

Theory and Phenomenology of the out of Equilibrium Evolution of Heavy Probes in a Quark Gluon Plasma

Peter Vander Griend

Vollständiger Abdruck der von der Fakultät für Physik der Technischen Universität München zur Erlangung des akademischen Grades eines

Doktors der Naturwissenschaften (Dr. rer. nat.)

genehmigten Dissertation.

Vorsitzender: Prof. Dr. Bastian Märkisch

Prüfer der Dissertation: 1. apl. Prof. Dr. Antonio Vairo

2. Prof. Dr. Björn Garbrecht

Die Dissertation wurde am 11.08.2022 bei der Technischen Universität München eingereicht und durch die Fakultät für Physik am 13.09.2022 angenommen.

Zusammenfassung

Schwere Quarks und ihre gebundenen Zustände gehören zu den am besten zugänglichen theoretischen und experimentellen Sonden des in Schwerionenkollisionen geformten Mediums. In dieser Doktorarbeit nutzen wir den Formalismus der offenen Quantensysteme, Methoden der effektiven Feldtheorie und thermische Quantenfeldtheorie, um die mediuminterne nicht Gleichgewichtsevolution solcher Zustände zu beschreiben. Wir beginnen mit einer Einleitung in Schwerionenkollisionen, nichtrelativistische und potential-nichtrelativistische effektive Feldtheorien der starken Wechselwirkung, offene Quantensysteme und thermische Feldtheorie. Mittels dieser Methoden stellen wir eine Mastergleichung auf, die die mediuminterne Evolution schwerer Coulomb-Quarkonia beschreibt, und fernerhin analysieren wir sie in einer Vielzahl von Parameterräumen. Wir untersuchen die Bedingungen, unter denen die mediuminterne Evolution durch Langevin- und Lindbladgleichungen beschrieben wird, und dazu die ausschlaggebenden Transportkoeffizienten der beiden Fälle. Wir stellen den `QTraj` Code vor, der die Monte Carlo Methode der Quantenpfade nutzt, um die Lindbladgleichung zu lösen. Mit dem `QTraj` Code rechnen wir den Kernmodifikationskoeffizient R_{AA} und den elliptischen Fluss v_2 der $\Upsilon(1S)$, $\Upsilon(2S)$ und $\Upsilon(3S)$ Zustände aus und vergleichen sie mit experimentellen Ergebnissen der ALICE-, ATLAS- und CMS-Kollaborationen. Wir finden in allen Fällen eine zufriedenstellende Übereinstimmung zwischen unseren Ergebnissen und den experimentellen Daten.

Abstract

Heavy quarks and their bound states are among the best available theoretical and experimental probes of the medium formed in heavy ion collision experiments. In this thesis, we utilize the formalism of open quantum systems, effective field theory methods and quantum field theory at finite temperature to describe the in-medium, out of equilibrium evolution of these states. We begin with an introduction to heavy ion collisions, nonrelativistic and potential nonrelativistic effective field theories of the strong interaction, open quantum systems and quantum field theory at finite temperature. Using these methods, we present a master equation describing the in-medium evolution of heavy, Coulombic quarkonium and analyze it in a number of limits. We investigate the conditions under which the in-medium evolution is described by Langevin and Lindblad equations and the transport coefficients characterizing the evolution in both regimes. We present the `QTraj` code which utilizes the Monte Carlo quantum trajectories method to solve the Lindblad equation. Using the `QTraj` code, we calculate the nuclear modification factor R_{AA} and the elliptic flow v_2 of the $\Upsilon(1S)$, $\Upsilon(2S)$ and $\Upsilon(3S)$ states and compare against experimental measurements by the ALICE, ATLAS and CMS collaborations. We find, in general, good agreement between our results and the experimental data.

Contents

Part I

Introduction

Chapter 1

Heavy quarkonium and heavy ion collisions

In the first instants after the big bang, the universe was immensely hotter and denser than in its current state. Theoretical and experimental investigation of hot, dense media is thus a matter of great importance to trace the history of the universe back to its earliest moments. Current heavy ion collision (HIC) experiments including the ALICE, ATLAS and CMS experiments at the European Organization for Nuclear Research's (CERN) Large Hadron Collider (LHC) and the PHENIX and STAR experiments at Brookhaven National Laboratory's (BNL) Relativistic Heavy Ion Collider (RHIC) have succeeded in creating an environment of extraordinarily high temperature and density and thus provide an unparalleled window into the earliest times of the universe. The data from these experiments have spurred theorists to push forward with analyses of such hot, dense environments and to formulate and calculate observable quantities signaling the nature of the medium formed in and the dynamics which govern heavy ion collisions for comparison against these experimental data.

The dynamics of HICs are governed by the strong nuclear interaction. The strong force is confining such that at large distances and low energies the quarks and gluons which carry and mediate the color charge responsible for the strong interaction exist only as constituent particles of neutral bound states. Conversely, at high energies, the strong force becomes weaker, and the constituent particles carrying color charge can be liberated from bound states and propagate freely. Such a deconfined medium is denoted a quark gluon plasma (QGP) as the colored particles, i.e., quarks and gluons, propagate freely within it. It is conceivable that at temperatures achieved in current HIC experiments a deconfined QGP is created. From the beginning of the HIC experimental program, it has thus been a matter of great importance to identify observables signaling the formation and existence of this deconfined medium.

Among the best available probes of the medium formed in HIC experiments are heavy quarks and their bound states. Their presence from the earliest stages of and persistence through to the end of the collision allow for the probing of the medium formed during the entirety of its existence. An observable of particular interest in the theoretical and

experimental HIC program is heavy quarkonium suppression. Heavy quarkonium is a meson consisting of a heavy quark and the corresponding heavy antiquark, i.e., $c\bar{c}$ or $b\bar{b}$. As discussed above, at low energies, due to the confining nature of the strong interaction, such states cannot dissociate into constituent quarks and are, with respect to the strong interaction, stable. In a deconfined medium, decay of heavy quarkonium into a deconfined quark and antiquark is not forbidden. In a seminal work [1], Matsui and Satz proposed reduced yield of heavy quarkonium states in HIC experiments due to dissociation in the deconfined medium with respect to yield in proton-proton collisions, in which no medium is formed, as a signal of the formation of a QGP.

In Ref. [1], the proposed mechanism of the in-medium dissociation was Debye screening. In this scenario, the potential binding the quark and the antiquark is screened over length scales greater than the inverse of the Debye mass m_D^{-1} due to interactions with the medium. If the Debye mass becomes sufficiently large such that its inverse is below the radius of the state, the constituent quarks are no longer held together by the potential, and the state dissociates. Our understanding of the mechanism of heavy quarkonium suppression underwent a paradigmatic shift with the findings of Laine, et. al., of a nonzero imaginary part of the heavy quark potential [2]. This imaginary part leads to in-medium decay of the state and in the screening regime was found to be large, a result confirmed by subsequent calculations performed using nonrelativistic effective field theories of the strong interaction [3–8] and perturbative QCD resummation [9]. Furthermore, recombination effects in the charm sector have been found to play a significant role in the in-medium dynamics of charmonium such that the J/ψ does not provide as clear a signal of heavy quarkonium suppression or, therefore, of the formation of a QGP [10–13] as in the bottom sector. Due to the lower mass of the charm quark with respect to temperatures achieved in current HIC experiments, $c\bar{c}$ states are sufficiently copiously produced such that the interaction and recombination of open charm after dissociation cannot be discounted thus complicating the simple dissociation picture [14–17]. Nevertheless, heavy quarkonium suppression, specifically in the bottom sector, remains a subject of great experimental and theoretical interest as a clear signal of the formation of a deconfined QGP.

To accurately describe heavy quarkonium suppression, one needs an accurate description of in-medium heavy quarkonium dynamics which should, ideally, take into account: the quantum and non-Abelian nature of the system and the strongly coupled nature of the medium. In this thesis, we make use of a number of theoretical tools to allow us to provide such a description with the goal of calculating experimental observables, foremost among them heavy quarkonium suppression, for comparison against experimental data in order to characterize the medium formed in HICs. Our main theoretical tools in this effort are effective field theory (EFT) methods, the formalism of open quantum systems (OQS) and quantum field theory (QFT) at finite temperature and out of equilibrium.

Effective field theories are QFTs which exploit hierarchies of scale present in physical systems to provide an effective description valid in a specific energy regime up to a specific order in expansions in a small parameter. In a physical system with widely

separated energy scales, one can perform an expansion in the ratio of the small to the large scale. At the Lagrangian level, this produces an effective Lagrangian defining a resulting EFT. The effective Lagrangian contains an infinite number of operators allowed by the symmetries of the underlying theory of which only a finite number are necessary to accurately reproduce the results of the fundamental theory up to a given order in the expansion parameter. The coefficients of the effective operators are denoted Wilson coefficients and encode the information of the fundamental theory in the higher energy region. In the energy region in which the expansion is valid, observables can be calculated using the EFT and reproduce the results of the full theory up to a given order in the expansion.

In this thesis, we make extensive use of nonrelativistic EFTs which take advantage of the nonrelativistic nature of particles of large mass. Specifically, working at an energy scale μ much less than the mass M of the heavy particle, the system is nonrelativistic, and its dynamics are well described by the nonrelativistic dispersion relation $E = \frac{1}{2}Mv^2$, where $v \ll 1$ is the velocity of the particle. Nonrelativistic quantum chromodynamics (NRQCD) [18,19] is the EFT describing the dynamics of the strong interaction below the scale M. At the Lagrangian level, it consists of Pauli two component spinors separately creating and annihilating nonrelativistic heavy quarks and antiquarks and is organized as an expansion in the velocity v. In bound states consisting of a heavy quark and a heavy antiquark, there remain two dynamical scales below the scale M: the momentum transfer Mv and the binding energy Mv^2. Restricting oneself to the energy scale Mv^2, one has the EFT potential NRQCD (pNRQCD) [20–22]. At the Lagrangian level, pNRQCD describes color singlet and octet bound states interacting via electric dipole interactions and is organized as an expansion in the bound state radius and the inverse of the heavy quark mass. It is thus ideally suited to describe the lowest lying bottomonium states which are both heavy and small.

The inherent hierarchy of scales of heavy quarkonium due to the large quark mass and nonrelativistic velocities make it an ideal system to describe with EFTs. To describe heavy quarkonium suppression, one must additionally consider scales induced by the medium, namely the temperature T. Studies of heavy quarkonium in medium have made extensive use of NRQCD and pNRQCD in different temperature regimes compared to the inherent scales of the quarkonium [5–8]. Heavy quarkonium in medium is a fully quantum system coupled to a highly complex environment. The combined system possesses multiple separate energy scales, and treating it accurately is a daunting task. The formalism of open quantum systems (OQS) [23] allows for the rigorous treatment of a quantum system of interest coupled to and evolving out of equilibrium with a bath or reservoir and thus provides a natural framework in which to treat a heavy quark or heavy quarkonium state propagating in the QGP. This approach has proven especially fruitful in the past decade with a large number of groups utilizing OQS methods to investigate in-medium dynamics of heavy quarkonium [24–38]; for reviews, see Refs. [39,40]. Within the OQS formalism, the inherent energy scales of the system and the medium characterize time scales of the system, the medium and their interaction. Hierarchies among these time scales characterize different evolution paradigms; two ubiquitous regimes are the

quantum optic and quantum Brownian motion regimes. As we explain and justify in more detail in the body of this thesis, heavy quarkonium in the medium formed in current HIC experiments realizes quantum Brownian motion which allows for the use of a number of simplifying assumptions in treating the system and deriving evolution equations. In this regime, the evolution of the system and the medium factorize in such a way that an evolution equation describing the time evolution of the density matrix of the system can be derived with medium interactions described by medium correlators. We find, furthermore, that in certain regimes these correlators reduce to transport coefficients characterizing the medium and governing the interaction of the system with it.

As the QGP is at finite temperature and the heavy particle is out of equilibrium with the medium, standard QFT methods do not provide an accurate description of the combined system. We must make use of finite temperature [41–43] and out of equilibrium QFT [44, 45]. As we explain in more detail in the body of this thesis, the fundamental idea of finite temperature QFT consists in taking the operator form of the Boltzmann factor $e^{-H/T}$ of quantum statistical mechanics as an evolution operator in imaginary time. Evolution at finite temperature thus represents evolution by time $t = -i/T$. There exist two approaches to this imaginary time evolution: the imaginary and real time formalisms. In the former, the periodicity of the imaginary time propagator is used to relate it to a Fourier sum over discrete Matsubara frequencies given by $\omega_n = 2\pi nT$ for bosons and $\omega_n = (2n + 1)\pi T$ for fermions; observables can be calculated as sums over these Matsubara frequencies. In the latter, one evolves to time $t = -i/T$ along an indirect path proceeding along the real time axis to gain access to real time correlator information. In this thesis, we make use of the real time formalism.

EFT methods, the OQS formalism and QFT at finite temperature allow us to systematically take into account all relevant physical aspects of the in-medium propagation of heavy quarkonium. The results presented in this thesis represent an important contribution to the body of theoretical and experimental work investigating the in-medium evolution of heavy quarkonium in order to characterize the medium formed in current HIC experiments. In the last decade, numerous works by the experimental collaborations at the LHC and RHIC have studied and reported on bottomonium suppression; for a representative selection of such works, see Refs. [46–55]. On the theory side, groups have utilized approaches including kinetic rate equations [56] and coupled transport equations [36] to describe the in-medium evolution of heavy quarkonium to compare against these experimental data. Other theory groups have additionally investigated the in-medium properties of heavy quarkonium by studying complex 1D potentials [57], Schrödinger-Langevin [27] and Langevin equations [29] and stochastic potentials [24], while the comovers approach has additionally been utilized in the charm sector [58].

This thesis is organized into three parts: I an introduction, II a presentation of theoretical results and III a presentation of phenomenological results. In the remainder of part I, we present more quantitatively and in greater detail the theory of the strong interaction and effective field theories thereof, the formalism of open quantum systems and quantum field theory at finite temperature in chapters 2, 3 and 4, respectively. In chapters 3 and 4, we rederive the master equation governing the in-medium evolution of heavy

10

quarkonium previously derived in Refs. [28, 30]. In part II, we present novel theoretical results. The transport coefficients describing the interactions of the heavy particles with the medium are objects of key importance, and fixing their values is necessary to solve the evolution equations and extract the phenomenological results of part III. In chapter 5, we detail our current understanding of the nature of these coefficients and give state of the art results fixing their values. In chapter 6, we derive Langevin equations describing the in-medium Brownian motion of heavy quarkonium and heavy quarks. In chapter 7, we present an evolution equation derived without making use of the dilute approximation which may be of use to describe in-medium charmonium where recombination effects are significant. In part III, we present various phenomenological results describing heavy quarkonium suppression and provide comparison against current experimental data. These results were obtained by solving the master equation first derived in Refs. [28] and [30] at orders 0 and 1 in an expansion in the binding energy E of the quarkonium state over the temperature T of the medium. The resulting evolution equations were solved using the `QTraj` code presented in Ref. [59] and reviewed in appendix A. In chapter 8, we present results from Refs. [60] and [61] in which the master equation is solved at leading order in the binding energy of the quarkonium state over the temperature of the medium and in chapter 9 results from Ref. [62] in which the master equation is solved at next-to-leading order in the same expansion. We conclude in chapter 10 and collect assorted information in various appendices.

Chapter 2

Effective field theories of the strong interaction

As stated in chapter 1, in order to rigorously describe heavy quarkonium suppression in heavy ion collision experiments, we must take into account the quantum and non-Abelian nature of the system. In this chapter, we present the non-Abelian quantum field theory quantum chromodynamics (QCD) which governs the strong nuclear interaction. In sec. 2.1, we present the QCD Lagrangian and discuss the transformation properties of the quark and gluon fields it describes. We emphasize the non-Abelian nature of the theory which gives rise to a richer structure than other sectors of the Standard Model; we present the QCD beta function describing the running of the strong coupling and discuss its implications at high and low energies. Furthermore, as we aim to describe heavy quarkonium which contains a hierarchically ordered set of well separated energy scales, we introduce effective field theories of the strong interaction which naturally describe the relevant physics at each of these energy scales. In sec. 2.2, we present nonrelativistic QCD (NRQCD) [18, 19] which describes the physics of the strong interaction in heavy-heavy bound states below the scale of the heavy quark mass M. In sec. 2.3, we present potential NRQCD (pNRQCD) [21, 22] which describes heavy-heavy bound states below the scale of the momentum transfer Mv, where v is the relative velocity in the bound state. We represent this hierarchy schematically in fig. 2.1.

2.1   Quantum chromodyanmics

The strong nuclear force governs the interactions of the quarks and gluons. At low energies, they form bound states of protons and neutrons of which (along with electrons) macroscopic matter consists, whereas at high energies, e.g., in the QGP formed in HIC experiments, they propagate freely. The strong interaction is rigorously described by quantum chromodynamics (QCD) which is an SU(3) gauge theory describing the interaction of 3 colored quarks with 8 gluons which carry color charge and mediate the strong force. The QCD Lagrangian describing a quark ψ_i of mass m interacting with a gluon
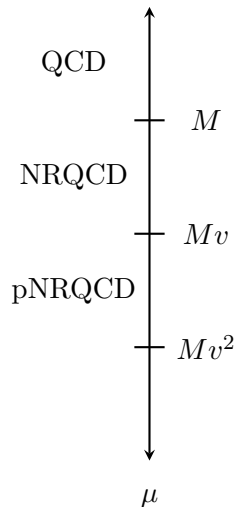
Figure 2.1: Schematic representation of the hierarchy of scales and effective field theories relevant to describe the strong sector dynamics of heavy-heavy bound states. In heavy quarkonium physics, the relative velocity v and the heavy quark mass M define three hierarchically ordered scales denoted the hard, soft and ultrasoft scales: $M \gg Mv \gg Mv^2$, respectively. Integrating out the hard scale $\mu = M$ from the fundamental theory QCD gives rise to the EFT nonrelativstic QCD (NRQCD); further integrating out the soft scale $\mu = Mv$ gives rise to the EFT potential NRQCD (pNRQCD).

field A_μ is given by

$$\mathcal{L} = \bar{\psi}_i \left(i\slashed{\partial}\delta_{ij} - g\gamma^\mu T^a_{ij}\slashed{A}^a - \delta_{ij}m \right) \psi_j - \frac{1}{4}F^a_{\mu\nu}F^{a\mu\nu}, \tag{2.1}$$

where the Feynman slash indicates contraction with a gamma matrix, i.e., $\slashed{\partial} = \gamma^\mu\partial_\mu$; $F_{\mu\nu}$ is the gluon field strength tensor; and $\bar{\psi} = \psi^\dagger\gamma_0$. The quark is a spin-$\frac{1}{2}$ particle represented by the four component spinor ψ_i; the gluon is a spin-1 vector field represented by A^a_μ. The T^a_{ij} are traceless, Hermitian 3×3 matrices and are elements of the Lie algebra $\mathfrak{su}(3)$ generating the Lie group SU(3). The lower indices $\{i, j, \cdots\}$ are fundamental and run from 1 to 3; the upper indices $\{a, \cdots\}$ are adjoint and run from 1 to 8. At a mathematical level, the presence of the gluon field serves to ensure the invariance of the QCD Lagrangian under local SU(3) gauge transformations, i.e.,

$$\psi_i(x) \to U_{ij}(x)\psi_j(x), \tag{2.2}$$

where $U_{ij}(x)$ is an element of SU(3) in the fundamental representation. The gauge field transforms under local SU(3) transformations in the adjoint representation as

$$T^a_{ij}A^a_\mu(x) \to U_{ki}(x)T^a_{ij}A^a_\mu(x)U^{-1}_{jl}(x) + U^{-1}_{ki}(x)\left(\partial_\mu U_{il}(x)\right). \tag{2.3}$$

13

We define the covariant derivative

$$(D_\mu)_{ij} = \partial_\mu \delta_{ij} + ig A_\mu^a T_{ij}^a, \qquad (2.4)$$

with gauge transformation properties

$$(D_\mu)_{ij} \rightarrow U_{ij}(x) (D_\mu)_{jk} U_{kl}^{-1}(x), \qquad (2.5)$$

such that the gauged kinetic term $\bar\psi \slashed{D} \psi$ is gauge invariant. The gluon field strength tensor $F_{\mu\nu}^a$ is given in terms of the covariant derivative as

$$(F_{\mu\nu})_{ij} = T_{ij}^a F_{\mu\nu}^a = \frac{1}{ig} [D_\mu, D_\nu]_{ij} = T_{ij}^a \left(\partial_\mu A_\nu^a - \partial_\nu A_\mu^a - g f^{abc} A_\mu^b A_\nu^c \right), \qquad (2.6)$$

where f^{abc} is a totally antisymmetric structure constant arising from the commutation relation of the generators

$$[T^a, T^b]_{ij} = i f^{abc} T_{ij}^c. \qquad (2.7)$$

Making use of the relation

$$T_{ij}^a T_{ji}^b = \frac{1}{2} \delta^{ab}, \qquad (2.8)$$

giving the trace of the product of the generators in the fundamental representation, we write the field strength term of Eq. (2.1) as a trace over the fundamental indices of the generators

$$-\frac{1}{4} F_{\mu\nu}^a F^{a\mu\nu} = -\frac{1}{2} \text{Tr} \left[F_{\mu\nu} F^{\mu\nu} \right]. \qquad (2.9)$$

The QCD Lagrangian is thus manifestly invariant under local SU(3) gauge transformations.

In contrast to the Abelian $U(1)$ gauge theory quantum electrodynamics (QED) governing the electromagnetic interaction, the non-Abelian nature of QCD, i.e., that the group generators are noncommutative $[T^a, T^b] \neq 0$, gives rise to nontrivial structure and an interacting theory also in the pure gauge sector. The gluons mediating the strong force are themselves charged under SU(3) and are, therefore, selfinteracting. The field strength tensor term of Eq. (2.1) gives rise to three- and four-point gluon vertices. The rich structure of QCD is further manifest in its behavior at high and low energies. Its beta function is given by

$$\mu^2 \frac{d\alpha_s(\mu^2)}{d\mu^2} = \beta(\alpha_s) = -\left(b_0 \alpha_s^2 + b_1 \alpha_s^3 + b_2 \alpha_s^4 + \cdots \right), \qquad (2.10)$$

where $\alpha_s = g^2/(4\pi)$ is the strong coupling constant, μ is the unphysical renormalization scale and b_n represents the $(n+1)$-loop coefficient of the beta function [63]. The $1-$loop coefficient is given by $b_0 = (11 N_c - 2 N_f)/(12\pi)$ where (in the Standard Model) $N_c = 3$ is the number of colors and $N_f \leq 6$ is the number of fermions (here quarks) contributing to the running of the coupling. We thus observe that in the Standard Model b_0 is positive and the strong coupling goes to 0 as the energy scale is increased, a phenomenon denoted

asymptotic freedom [64, 65]; it is this property which leads to deconfinement and the creation of a QGP in HIC experiments. Conversely, the coupling increases as the energy scale decreases and, in fact, diverges at a finite, positive energy scale denoted Λ_{QCD}. On the calculational level, the energy scale Λ_{QCD} and the diverging of the coupling represent the breakdown of weakly coupled perturbation theory; on a physical level, this sets the scale of confinement, i.e., at length scales $r \gtrsim \Lambda_{\mathrm{QCD}}^{-1}$ only color neutral states are observed.

2.2 Nonrelativistic quantum chromodynamics

In parts II and III of this thesis, we consider heavy quarkonium of mass M propagating in a thermal medium of temperature T. For $M \gg T$, we take the state to propagate nonrelativistically within the medium. The QCD Lagrangian given in Eq. (2.1) describes the fully Lorentz covariant, relativistic propagation of a quark. As we consider the nonrelativistic propagation of a bound state, we make use of EFT methods to describe the physics relevant at the scales at which we work.

Let us consider the propagation of a heavy quark of mass M inside a heavy-heavy bound state. We designate the momentum of the quark p, the velocity of the hadron v_h and the residual momentum of the quark k; these are related by

$$p = Mv_h + k. \tag{2.11}$$

The quark is heavy, i.e., M is much, much greater than any component of k, and nonrelativistic, i.e., its energy k_0 and momentum $|\mathbf{k}|$ scale as Mv^2 and Mv, respectively, (where v is the velocity of the heavy quark). Working in the rest frame of the hadron, i.e., $v_h = (1, \mathbf{0})$, and at leading order in k/M, we write the propagator of the heavy quark as

$$i\frac{\not{p} + M}{p^2 - M^2 + i\epsilon} \to \begin{pmatrix} \mathbb{1}_2 & 0 \\ 0 & 0 \end{pmatrix} \frac{i}{k_0 - \frac{\mathbf{k}^2}{2M} + i\epsilon}. \tag{2.12}$$

The gauge invariant Lagrangian corresponding to the propagator of Eq. (2.12) is

$$\mathcal{L} = \psi^\dagger \left\{ iD_0 + \frac{\mathbf{D}^2}{2M} \right\} \psi - \frac{1}{4} F^{a\mu\nu} F^a_{\mu\nu}, \tag{2.13}$$

where ψ is a nonrelativistic 2 component spinor which annihilates a heavy quark.

The leading order NRQCD Lagrangian of Eq. (2.13) (and further corrections) can be derived more rigorously from the QCD Lagrangian of Eq. (2.1) via a set of field redefinition of the 4 component spinor ψ. We follow the derivation of Ref. [66] in which the Lagrangian of heavy quark effective field theory (HQET) is derived. HQET is used to treat heavy-light states in which the momentum transfer is $k \sim \Lambda_{\mathrm{QCD}}$ and thus implements an expansion in Λ_{QCD}/M. In the heavy-heavy states described by NRQCD, the momentum transfer is $k \sim Mv$ such that the expansion is in the velocity v. For a

discussion of the similarities and differences between these two theories, see Ref. [67]. We decompose the heavy quark 4 component spinor ψ into the fields h_v and H_v

$$\psi(x) = e^{-iMv \cdot x}\left[h_v(x) + H_v(x)\right], \tag{2.14}$$

with the inverse relations

$$h_v(x) = e^{iMv \cdot x}\frac{1 + \not{v}}{2}\psi(x), \tag{2.15}$$

$$H_v(x) = e^{iMv \cdot x}\frac{1 - \not{v}}{2}\psi(x). \tag{2.16}$$

Anticipating $v \simeq (1, \mathbf{0})$, we recognize h_v as annihilating a quark of velocity v and H_v as creating a heavy antiquark of velocity v. The exponential factor serves to eliminate the heavy quark mass M from the numerator of the Lagrangian. Substituting Eqs. (2.15) and (2.16) into Eq. (2.1), the heavy quark portion of the QCD Lagrangian takes the form

$$\mathcal{L}_{\text{QCD}}|_{\text{HQ}} = \bar{h}_v i v \cdot D h_v - \bar{H}_v \left(iv \cdot D + 2M\right) H_v + \bar{h}_v i\not{D}_\perp H_v + \bar{H}_v i\not{D}_\perp h_v, \tag{2.17}$$

where we define the covariant derivative perpendicular to the heavy quark velocity $D^\mu_\perp = D^\mu - v^\mu v \cdot D$. We proceed to eliminate H_v using its equation of motion and write the heavy quark portion of the QCD Lagrangian as

$$\mathcal{L}_{\text{QCD}}|_{\text{HQ}} = \bar{h}_v i v \cdot D h_v + \bar{h}_v i\not{D}_\perp \frac{1}{2M + iv \cdot D} i\not{D}_\perp h_v. \tag{2.18}$$

We rewrite the second term as an expansion in $(v \cdot D)/M$ giving

$$\mathcal{L}_{\text{QCD}}|_{\text{HQ}} = \bar{h}_v i v \cdot D h_v + \frac{1}{2M}\sum_{n=0}^{\infty} \bar{h}_v i\not{D}_\perp \left(-\frac{iv \cdot D}{2M}\right)^n i\not{D}_\perp h_v. \tag{2.19}$$

This expression can be simplified using appropriate field redefinitions. Working in the rest frame of the heavy quark, i.e., $v = (1, \mathbf{0})$, we have the standard form of the NRQCD Lagrangian in the two heavy quark sector, which we denote $\mathcal{L}_\psi$; up to order $1/M^2$

$$\begin{aligned}
\mathcal{L}_\psi = \psi^\dagger \Big(iD_0 &+ \frac{c_k}{2M}\mathbf{D}^2 + \frac{c_4}{8M^3}\mathbf{D}^4 + \frac{c_f}{2M}\sigma \cdot g\mathbf{B} + \frac{c_D}{8M^2}\left(\mathbf{D} \cdot g\mathbf{E} - g\mathbf{E} \cdot \mathbf{D}\right) \\
&i\frac{c_S}{8M^2}\sigma \cdot \left(\mathbf{D} \times g\mathbf{E} - g\mathbf{E} \times \mathbf{D}\right) + \cdots \Big)\psi,
\end{aligned} \tag{2.20}$$

where ψ is again the 2 component spinor which annihilates a heavy quark, σ_i are the Pauli matrices and $E_i = F_{0i}$ and $B_i = -\frac{1}{2}\epsilon_{ijk}F^{jk}$ are the chromoelectric and chromomagnetic fields, respectively. We explicitly include the Wilson or matching coefficients c_i which encode the contributions of the full theory at the energy scale M. As the velocity used to construct the NRQCD Lagrangian is arbitrary, the Lagrangian must be invariant under reparametrizations of the form $v_\mu \to v_\mu + \epsilon_\mu/M$ where $\epsilon_\mu \sim \Lambda_{\text{QCD}}$; this reparametrization invariance places constraints on the relations among the Wilson coefficients [67,68]. The

unconstrained Wilson coefficients are fixed by matching Green's functions in the effective and fundamental theories; see Refs. [22, 67, 69].

A similar procedure can be carried out to derive the NRQCD antiquark Lagrangian. In its full generality, the NRQCD Lagrangian describes nonrelativistic heavy quarks and antiquarks interacting with light quarks and gluons at the soft scale Mv, four point interactions of heavy quarks and antiquarks and higher order gluonic interactions. Schematically, this is written as

$$\mathcal{L}_{\mathrm{NRQCD}} = \mathcal{L}_g + \mathcal{L}_l + \mathcal{L}_\psi + \mathcal{L}_\chi + \mathcal{L}_{\psi\chi}, \qquad (2.21)$$

where $\mathcal{L}_g$ represents the gluonic sector, $\mathcal{L}_l$ the leptonic sector, $\mathcal{L}_\psi$ the heavy quark sector, $\mathcal{L}_\chi$ the heavy quark sector and $\mathcal{L}_{\psi\chi}$ four-fermion operators. $\mathcal{L}_\chi$ is the charge conjugate of $\mathcal{L}_\psi$ where $\psi^c = -i\sigma^2\chi^*$ where χ is a 2 component spinor which creates a heavy antiquark. Upon integrating out the hard scale M, the resulting nonrelativistic effective field theory no longer dynamically describes pair creation and annihilation; this information is, however, retained in the imaginary parts of the Wilson coefficients entering $\mathcal{L}_{\psi\chi}$. The complete set of terms is given explicitly in Refs. [22, 69]. The resulting EFT inherits invariance under local SU(3) gauge transformations from QCD, and implements Poincaré and Lorentz invariance nonlinearly via relations among the Wilson coefficients [68, 70, 71].

NRQCD has been extensively utilized to derive a number of heavy quarkonium observables including, but not limited to, the heavy quarkonium spectrum and inclusive decay width; we direct the reader to the reviews [22, 69, 72–74] and references therein for detailed compendia. The expansion in the nonrelativistic velocity v in NRQCD provides a powerful tool to treat nonrelativistic heavy-heavy bound states; however, a number of computations are complicated by the fact that after integration out of the hard scale M, there remain two dynamical scales: the soft scale of the momentum transfer Mv and the ultrasoft scale of the binding energy Mv^2. This complication prevents assigning an unambiguous power counting to the operators appearing in the NRQCD Lagrangian in the absence of additional assumptions. A number of works of the mid to late 1990's sought to address this issue [75–78]. Brambilla, Pineda, Soto and Vairo rigorously integrated out the soft scale Mv from NRQCD giving rise to potential NRQCD (pNRQCD) [20, 21] in which the degrees of freedom are singlet and octet heavy-heavy bound states interacting via the exchange of ultrasoft gluons. The physics of the soft scale is encoded in a nonlocal potential which, furthermore, makes contact with a purely quantum mechanical formulation. The resulting EFT implements a double expansion in the bound state radius and the inverse of the heavy quark mass, possesses an unambiguous power counting and is ideally suited to describe the physics of the lowest lying bottomonium and charmonium states.

2.3 Potential nonrelativistic quantum chromodynamics

As discussed in the previous section, integrating out the hard scale M from full QCD gives rise to NRQCD, and further integrating out the soft scale Mv gives rise to pNRQCD (cf. fig. 2.1). The resulting EFT is tailor made to describe the lowest lying bottomonium

states relevant in in-medium heavy quarkonium suppression, and the operators entering its Lagrangian possess an unambiguous power counting. In this section, we present a derivation of weakly coupled pNRQCD. The weakly and strongly coupled versions of pNRQCD correspond to the hierarchy between the scale of the momentum transfer Mv and the scale of gluonic excitations denoted Λ_{QCD}. In strongly coupled pNRQCD, $Mv \simeq \Lambda_{\mathrm{QCD}}$. In this theory, all nonpotential effects are integrated out, and the quarkonium dynamics are determined entirely by a nonperturbative potential. Furthermore, the only remaining degree of freedom is the quarkonium singlet field corresponding to a hadron state below the confinement scale Λ_{QCD}. In weakly coupled pNRQCD, $Mv \gg \Lambda_{\mathrm{QCD}}$. In this case, the degrees of freedom are singlet and octet heavy quarkonium states interacting via the exchange of ultrasoft gluons. The noninteracting dynamics of the quarkonium state are governed by potentials which can be calculated in perturbation theory with nonperturbative corrections if $\Lambda_{\mathrm{QCD}} \gg Mv^2$. For a presentation of both versions of pNRQCD, see Refs. [21,22]. In this thesis, we utilize weakly coupled pNRQCD and present its derivation below.

After integrating out the soft scale from NRQCD, the resulting degrees of freedom in the pNRQCD Lagrangian are composite heavy-heavy fields; as such, we begin our construction of the pNRQCD Lagrangian by projecting the NRQCD Hamiltonian onto the quark-antiquark sector spanned by the operator

$$\mathcal{O}_\Psi = \int d^3\mathbf{x}_1\mathbf{x}_2 \Psi(\mathbf{x}_1, \mathbf{x}_2)\psi^\dagger(\mathbf{x}_1)\chi(\mathbf{x}_2)|\text{ultrasoft gluons}\rangle, \qquad (2.22)$$

where $\Psi(\mathbf{x}_1, \mathbf{x}_2)$ is a composite field consisting of a heavy quark at position $\mathbf{x}_1$ and a heavy antiquark at position $\mathbf{x}_2$ and the ket $|\text{ultrasoft gluons}\rangle$ is a Fock state containing an arbitrary number of ultrasoft gluons and no heavy quarks or antiquarks. We perform this projection and write the resulting pNRQCD Lagrangian in terms of the Ψ field as

$$\begin{aligned}
L_{\mathrm{pNRQCD}} = \int d^3\mathbf{x}_1 d^3\mathbf{x}_2 \mathrm{Tr}\bigg\{ &\Psi^\dagger(t, \mathbf{x}_1, \mathbf{x}_2)\bigg[iD_0 + \frac{\mathbf{D}_1^2 + \mathbf{D}_2^2}{2M} + \cdots \\
&+ V(\mathbf{r}, \mathbf{p}_1, \mathbf{p}_2, \mathbf{S}_1, \mathbf{S}_2)\bigg]\Psi(t, \mathbf{x}_1, \mathbf{x}_2)\bigg\} - \int d^3x \frac{1}{4}F^{a\mu\nu}(x)F^a_{\mu\nu}(x),
\end{aligned} \qquad (2.23)$$

where the covariant derivative acts on the composite field as

$$iD_0\Psi(t, \mathbf{x}_1, \mathbf{x}_2) = i\partial_0\Psi(t, \mathbf{x}_1, \mathbf{x}_2) - gA_0(t, \mathbf{x}_1)\Psi(t, \mathbf{x}_1, \mathbf{x}_2) + \Psi(t, \mathbf{x}_1, \mathbf{x}_2)gA_0(t, \mathbf{x}_2). \quad (2.24)$$

Here, $\mathbf{D}_{1,2}$ is the spatial covariant derivative acting on the quark, antiquark at position $\mathbf{x}_{1,2}$ and the ellipsis represents higher order terms in the $1/M$ expansion. Furthermore, V is the quark-antiquark potential which, in general, depends on the quark-antiquark separation r, the momentum of the heavy quark and heavy anti-quark $\mathbf{p}_{1,2}$ and the spin of the heavy quark and heavy antiquark $\mathbf{S}_{1,2}$. The potential is a Wilson coefficient obtained by matching gluon exchange diagrams in pNRQCD to NRQCD and encodes the information of the soft scale. The lowest order contribution comes from Coulomb exchange; it is spin and momentum independent and is simply the Coulomb potential.

18

To make explicit the ultrasoft nature of the gluons in the pNRQCD Lagrangian, we multipole expand the gauge fields in Eq. (2.23) (cf. Ref. [75]). To do so, it is more convenient to work in the coordinate system of the center of mass $\mathbf{R}$ and the radius $\mathbf{r}$ of the bound state

$$\mathbf{R} = \frac{\mathbf{x}_1 + \mathbf{x}_2}{2}, \quad \mathbf{r} = \mathbf{x}_1 - \mathbf{x}_2. \tag{2.25}$$

The gauge fields become

$$A_\mu(t, \mathbf{x}_{1,2}) = A_\mu(\mathbf{R}) \pm \frac{1}{2} \mathbf{r} \cdot \nabla A_\mu(t, \mathbf{R}). \tag{2.26}$$

Implementing this expansion in Eq. (2.23) makes explicit the power counting of the operators but spoils manifest gauge invariance. To restore it, rather than working with the quark-antiquark field $\Psi(t, \mathbf{x}_1, \mathbf{x}_2)$, we work with fields of definite gauge transformation properties $\mathrm{S}(t, \mathbf{r}, \mathbf{R})$ and $\mathrm{O}(t, \mathbf{r}, \mathbf{R})$ which transform under ultrasoft gauge transformations $g(t, \mathbf{R})$ as a singlet and an octet, respectively, i.e.,

$$\mathrm{S}(t, \mathbf{r}, \mathbf{R}) \to \mathrm{S}(t, \mathbf{r}, \mathbf{R}), \quad \mathrm{O}(t, \mathbf{r}, \mathbf{R}) \to g(t, \mathbf{R})\mathrm{O}(t, \mathbf{r}, \mathbf{R})g^{-1}(t, \mathbf{R}). \tag{2.27}$$

$\Psi(t, \mathbf{x}_1, \mathbf{x}_2)$ is given in terms of the singlet and octet fields as

$$\begin{aligned}
\Psi(t, \mathbf{x}_1, \mathbf{x}_2) =& \mathrm{P} \exp\left[ig \int_{\mathbf{x}_2}^{\mathbf{x}_2} d\mathbf{x} \cdot \mathbf{A}(t, \mathbf{x}) \right] \mathrm{S}(t, \mathbf{r}, \mathbf{R}) \\
&+ \mathrm{P} \exp\left[ig \int_{\mathbf{R}}^{\mathbf{x}_1} d\mathbf{x} \cdot \mathbf{A}(t, \mathbf{x}) \right] \mathrm{O}(t, \mathbf{r}, \mathbf{R}) \, \mathrm{P} \exp\left[ig \int_{\mathbf{x}_2}^{\mathbf{R}} d\mathbf{x} \cdot \mathbf{A}(t, \mathbf{x}) \right],
\end{aligned} \tag{2.28}$$

where P represents path ordering in the Wilson line. We implement the multipole expansion of Eq. (2.26) and work with the singlet and octet fields of Eq. (2.28) giving the pNRQCD Lagrangian in the form

$$\begin{aligned}
\mathcal{L}_{\mathrm{pNRQCD}} = \int d^3\mathbf{r} \, \mathrm{Tr}\Big[& \mathrm{S}^\dagger \left(i\partial_0 - h_s \right) \mathrm{S} + \mathrm{O}^\dagger \left(iD_0 - h_o \right) \mathrm{O} + \mathrm{O}^\dagger \mathbf{r} \cdot g\mathbf{E}\mathrm{S} \\
&+ \mathrm{S}^\dagger \mathbf{r} \cdot g\mathbf{E}\mathrm{O} + \frac{1}{2}\mathrm{O}^\dagger \left\{ \mathbf{r} \cdot g\mathbf{E}, \mathrm{O} \right\} \Big] - \frac{1}{4} F^{a\mu\nu} F^a_{\mu\nu},
\end{aligned} \tag{2.29}$$

where S and O are normalized in color space as

$$\mathrm{S} = \frac{\mathbb{1}_{N_c}}{\sqrt{N_c}} S, \quad \mathrm{O} = \frac{T^a}{\sqrt{T_f}} O^a, \tag{2.30}$$

where N_c is the number of colors and T_f is the trace of the fundamental representation of $\mathrm{SU}(N_c)$, which we take to be $\frac{1}{2}$ (cf. Eq. (2.8)). The covariant derivative acts on the octet field as

$$iD_0 O = i\partial_0 O - [gA_0, O]. \tag{2.31}$$

The singlet and octet fields (and the octet field with itself) interact via chromoelectric dipole vertices which correspond to transitions between singlet and octet states and

19

$$= ig\delta^{ab}\sqrt{\tfrac{T_f}{N_c}}\mathbf{r} \qquad = \tfrac{ig}{2}d^{abc}\mathbf{r} \qquad = gf^{cba}$$
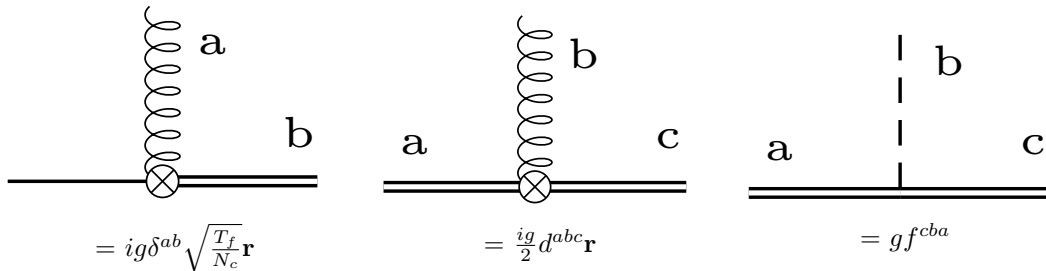
Figure 2.2: Feynman rules of the interaction vertices of pNRQCD. A single line represents a singlet state; a double line, an octet state; a curly line, a gluoelectric field; and a dashed line, a Coulombic gluon.

between octet and octet states. We present the Feynman rules corresponding to these vertices in Fig. 2.2. $h_{s,o}$ is the singlet, octet Hamiltonian consisting of a kinetic and potential term

$$h_{s,o} = \frac{p^2}{M} + V_{s,o}, \tag{2.32}$$

where p^2 is the momentum squared of the bound state. $V_{s,o}$ is the singlet, octet potential which at lowest order in the power counting is the attractive singlet, repulsive octet Coulomb potential

$$V_s = -\frac{C_f \alpha_s(1/r)}{r}, \quad V_o = \frac{\alpha_s(1/r)}{2N_c r}, \tag{2.33}$$

where $C_f = (N_c^2 - 1)/(2N_c)$ is the quadratic Casimir of the fundamental representation and N_c is the number of colors.

The Lagrangian of Eq. (2.29) possesses unambiguous power counting: derivatives with respect to the center of mass coordinate scale as the momentum transfer $\nabla_{\mathbf{r}} \sim Mv$ while derivatives with respect to time and the center of mass coordinate and ultrasoft gluons scale as the binding energy $\partial_0, \nabla_{\mathbf{R}}, g\mathbf{E}, gA_0 \sim Mv^2$. Due to the multipole expansion, the Coulombic and transverse gluons are ultrasoft and thus scale as Mv^2. The free equations of motion of the singlet and octet fields are simply Schrödinger equations with the attractive and repulsive Coulombic potentials of Eq. (2.33) thus making contact with the nonrelativistic quantum mechanical bound state formulation. Carrying out a similar exercise in the QED sector leads to the pNRQED Lagrangian (cf. Ref. [79, 80]); the equations of motion of the pNRQED bound state are the Schrödinger equation of positronium in the equal mass case and the hydrogen atom in the unequal mass case. Potential nonrelativistic theories thus make contact between the relativistic, manifestly Lorentz covariant formulations standard in quantum field theory and nonrelativistic quantum mechanical formulations which provide excellent descriptions of nonrelativistic bound states. Furthermore, they provide a natural framework in which to calculate and include relativistic corrections as necessary [80, 81].

Chapter 3

Open quantum systems

As discussed at length in chapter 1, heavy quarkonium provides among the best theoretical and experimental probes of the medium formed in heavy ion collisions. As heavy quarkonium possesses a number of widely separated and hierarchically ordered scales, it is naturally treated using effective field theory methods which exploit the inherent hierarchy of scales to provide an effective description accurate in a particular energy region up to a given order in the expansion. As discussed in chapter 2, in this thesis, we make use of pRNQCD to describe in-medium heavy quarkonium. pNRQCD provides an effective description of quarkonium taking into account the quantum and non-Abelian nature of the system. The medium, however, remains an enormously complicated object to be taken into account in order to eventually describe heavy quarkonium suppression. The formalism of open quantum systems provides a framework within which to rigorously, quantum mechanically treat a system of interest coupled to and evolving out of equilibrium with a bath or reservoir. It is thus a natural tool to utilize to treat heavy quarkonium coupled to a QGP. For a general introduction to the OQS framework, we direct the reader to Ref. [23]. Within the OQS formalism, a number of scales characterize the system, the medium and their interaction; hierarchical orderings among these scales characterize different evolution paradigms and allow for the use of various simplifying assumptions in the derivation of evolution equations.

In sec. 3.1, we introduce the physical scales of the problem and present the open quantum systems formalism. Using the hierarchy of scales of our physical system, we introduce a number of simplifying assumptions which we utilize in the derivation of our evolution equations. In sec. 3.2, we present an OQS derivation of an evolution equation in the regime of quantum Brownian motion. These OQS equations describe the quantum mechanical evolution of a probe coupled to and evolving out of equilibrium with a medium and reduce to the standard, closed quantum mechanical formulation in the limit of no coupling to the medium. From this evolution equation one can rederive, up to first order in perturbation theory, the coupled set of equations describing the in-medium evolution of Coulombic quarkonium first derived in Refs. [28, 30] We postpone a detailed derivation of the in-medium evolution equations of heavy quarkonium to chapter 4 in which we introduce the real time formalism of quantum field theory at

finite temperature to describe the thermal system with which the probe interacts. In so doing, we provide a field theoretic definition of the quantum mechanical objects defined in this chapter.

3.1 Scales of the problem

In the OQS framework, three time scales characterize the combined system: the system intrinsic time scale τ_S, the environment correlation time scale τ_E and the relaxation time scale τ_R. In a physical system, these time scales are set by the parameters present in the combined system. In this thesis, we principally concern ourselves with bottomonium propagating in the medium formed at current HIC experiments, namely lead-lead collisions at center of mass energy $\sqrt{s_{\mathrm{NN}}} = 5.02$ TeV. In this subsection, we give approximate values of the parameters entering the evolution equations. In part III of this thesis presenting phenomenological results, we fix these parameters to a higher degree of accuracy; nevertheless, the approximate values we present here suffice to establish a hierarchy and fix an evolution regime.

We take the heavy quark to be the bottom and its mass to be approximately 5 GeV. The Bohr radius of the state is given by solving its defining relation with the strong coupling set at the inverse of the Bohr radius

$$a_0 = \frac{2}{C_f \alpha_s(1/a_0) m_b},$$ (3.1)

giving $1/a_0 \sim 1.5$ GeV. We take the temperature of the medium to have a maximum of approximately 500 MeV at the initial stages of central collisions. The Coulombic binding energy of the quarkonium $|E| = 1/(Ma_0^2)$ is $|E| \sim 450$ MeV. We collect this information in table 3.1. The values of these parameters give the scale hierarchy

$$M \gg 1/a_0 \gg (\pi)T \gg E.$$ (3.2)

That the mass M of the heavy quark is the largest scale of the problem ensures that the system is nonrelativistic and enables us to make use of the nonrelativistic EFTs presented in chapter 2. The hierarchy $1/a_0 \gg (\pi)T$ ensures that the bound state is Coulombic also in medium up to thermal corrections to the potential which we assume to be small. We note that there is some ambiguity in the precise value of the thermal scale with factors of π arising naturally in momentum space; we thus take the thermal scale as proportional to T up to a factor of π. We note further that although $1/a_0 \gg \pi T$ is not rigorously fulfilled at a temperature of 500 MeV, this high temperature is only reached in the center of the most central collisions; furthermore, the medium rapidly expands and cools to temperatures at which the hierarchy is more rigorously fulfilled. A Coulombic description of the state is thus also valid in-medium in current HIC experiments. The hierarchy $(\pi)T \gg E$ enables the use of a number of simplifying assumptions discussed below and in chapter 4.

The physical scales present in the combined system specify a system intrinsic time scale τ_S, a medium intrinsic time scale τ_E and a relaxation time τ_R. τ_S characterizes

scale setting quantity	M	$1/a_0$	$(\pi)T$	E
approximate value	5 GeV	1.5 GeV	$< (\pi)0.5$ GeV	0.45 GeV

Table 3.1: Scale setting quantities in our OQS treatment of in-medium heavy quarkonium and their approximate values.

the system of interest and is related to the inverse of the spacing of the energy levels of the system. For bottomonium, this is naturally the inverse of the binding energy

$$\tau_S \sim \frac{1}{E}. \tag{3.3}$$

The intrinsic time scale of the medium τ_E represents the time scale over which it equilibrates from excitations caused by the presence of the probe; for a thermal medium, this is the inverse of the thermal scale

$$\tau_E \sim \frac{1}{(\pi)T}. \tag{3.4}$$

The relaxation time scale τ_R represents the time scale of the interaction of the system and the medium; for in-medium quarkonium, this is given by the inverse of the in-medium self energy Σ_s

$$\tau_R \sim \frac{1}{\Sigma_s} \sim \frac{1}{a_0^2((\pi)T)^3}. \tag{3.5}$$

Based on the hierarchy of scales given in Eq. (3.2) and the definitions of the OQS time scales given above, we find

$$\tau_R, \tau_S \gg \tau_E, \tag{3.6}$$

which characterizes the regime of quantum Brownian motion. In this regime, we make use of the Born and Markov approximations. The hierarchy $\tau_S \gg \tau_E$ implies that the intrinsic time scale of the probe is much longer than that of the medium. This further implies that the total density matrix describing the combined system factorizes into a tensor product of a density matrix describing the system and a density matrix describing the medium which is, furthermore, taken as constant in time, i.e.,

$$\rho(t) \propto \rho_S(t) \otimes \rho_M. \tag{3.7}$$

This is the Born approximation. Tracing over the medium degrees of freedom, we encode the medium interactions in correlators defined by

$$\langle \mathcal{O}_M \rangle = \text{Tr}[\mathcal{O}_M \rho_M], \tag{3.8}$$

where $\mathcal{O}_M$ is a medium operator, the angled brackets represent a medium correlator and the trace is over the medium degrees of freedom. The hierarchy $\tau_R \gg \tau_E$ implies that the medium reequilibrates following any fluctuations due to the presence of the system much more quickly than the time scale of the evolution of the reduced density matrix of

the system. This in turn implies that the evolution of the system at time t is sensitive only to its state at time t. This is the Markov approximation and at the calculational level ensures the resulting evolution equations are local in time.

We note that the hierarchy $\tau_R \gg \tau_S, \tau_E$ characterizes the quantum optical limit ubiquitous in the field of quantum optics. In this limit, the hierarchy $\tau_R \gg \tau_S$ enables the use of the rotating wave approximation in which rapidly oscillating terms are disregarded, and the resulting evolution equations are of Lindblad type [82, 83]. In this thesis, we work with a system realizing quantum Brownian motion.

3.2 Evolution equations from the Liouville-von Neumann equation

In this section, we derive an evolution equation describing an open quantum system undergoing quantum Brownian motion. Within the OQS framework, the combined system of the heavy particle and the medium is described by a composite Hamiltonian

$$H = H_S \otimes \mathbb{1}_M + \mathbb{1}_S \otimes H_M + H_I, \tag{3.9}$$

where H_S is the Hamiltonian of the system, H_M is the Hamiltonian of the medium, H_I is the interaction Hamiltonian and $\mathbb{1}_{M,S}$ represents an identity operator in the space of the medium and system. We take the interaction Hamiltonian to factorize into a part acting on the system and a part acting on the medium

$$H_I(t) = H_{I,S}(t) \otimes H_{I,M}(t) = H_S^\alpha(t) H_M^\alpha(t), \tag{3.10}$$

where α represents an arbitrary index (or set of indices) over which summation is understood.

The time evolution of the density matrix in the interaction picture $\rho_I(t)$ of the combined system is given by the Liouville-von Neumann equation

$$\frac{d\rho_I(t)}{dt} = -i\left[H_I(t), \rho_I(t)\right], \tag{3.11}$$

where $H_I(t)$ is the interaction Hamiltonian in the interaction picture and the density matrix is defined as the sum over the outer product of the basis states of the system weighted by their probability

$$\rho(t) = \sum_i p_i |\psi_i(t)\rangle\langle\psi_i(t)|. \tag{3.12}$$

Eq. (3.11) has solution

$$\rho_I(t) = U_I(t, t_0)\rho_I(t_0)U_I^\dagger(t, t_0), \tag{3.13}$$

where U_I is the time evolution operator in the interaction picture

$$U_I(t, t_0) = \mathrm{T}\exp\left[-i\int_{t_0}^{t} dt'\, H_I(t')\right], \tag{3.14}$$

where T indicates time ordering. We expand the exponentials of Eq. (3.13) and collect terms up to second order in H_I giving

$$
\begin{aligned}
\rho_I(t) =& \rho_I(t_0) - i \int_{t_0}^{t} dt' \left[H_I(t'), \rho_I(t_0) \right] \\
&+ \int_{t_0}^{t} dt' \int_{t_0}^{t'} dt'' \left(H_I(t')\rho_I(t_0)H_I(t'') - H_I(t')H_I(t'')\rho_I(t_0) + h.c. \right).
\end{aligned}
\tag{3.15}
$$

To arrive at an evolution equation for the density matrix of only the system, we trace Eq. (3.15) over the medium. The trace over the medium of an operator $\mathcal{O}$ on the combined system is defined as

$$
\mathrm{Tr}\left[\mathcal{O}\right] = \sum_i \left(\mathbb{1}_S \otimes \langle \psi_{M,i} | \right) \mathcal{O} \left(\mathbb{1}_S \otimes | \psi_{M,i} \rangle \right),
\tag{3.16}
$$

where $|\psi_{M,i}\rangle$ is the ith basis state of the medium. By definition, the trace over the medium degrees of freedom of the total density matrix yields the reduced density matrix of the system

$$
\mathrm{Tr}\left[\rho(t)\right] = \rho_S(t).
\tag{3.17}
$$

From the left-hand side of Eq. (3.15), we arrive at $\rho_S(t)$ in the interaction picture. Making use of the cyclicity of the trace in conjunction with the definition of the in-medium correlators given in Eq. (3.8), we find from the right-hand side of Eq. (3.15) an expression containing medium correlators. We move the system operators to the Schrödinger picture giving an equation for the density matrix of the system in the Schrödinger picture. We suppress further subscripts on the system density matrix and write the density matrix of the system in the Schrödinger picture at time t as $\rho(t)$. It is given by

$$
\begin{aligned}
\rho(t) =& e^{-ih(t-t_0)}\rho(t_0)e^{ih(t-t_0)} + \int_{t_0}^{t} dt_1 \int_{t_0}^{t_1} dt_2 \Big(\\
&- e^{-ih(t-t_1)} H_S^\alpha e^{-ih(t_1-t_2)} H_S^\beta e^{ih(t_0-t_2)} \rho(t_0) e^{ih(t-t_0)} \left\langle H_M^\alpha(t_1) H_M^\beta(t_2) \right\rangle \\
&+ e^{-ih(t-t_1)} H_S^\alpha e^{-ih(t_1-t_0)} \rho(t_0) e^{ih(t_2-t_0)} H_S^\beta e^{ih(t-t_2)} \left\langle H_M^\beta(t_2) H_M^\alpha(t_1) \right\rangle \\
&+ h.c. \Big),
\end{aligned}
\tag{3.18}
$$

where h is the system Hamiltonian. This can be written succinctly in the notation of Ref. [30] as

$$
\begin{aligned}
\rho(t) =& e^{-ih(t-t_0)}\rho(t_0)e^{ih(t-t_0)} - \int_{t_0}^{t} dt_1 \Big(e^{-ih(t-t_1)}\Sigma(t_1)e^{-ih(t_1-t_0)}\rho(t_0)e^{ih(t-t_0)} \\
&+ e^{-ih(t-t_0)}\rho(t_0)e^{ih(t_1-t_0)}\Sigma^\dagger(t_1)e^{ih(t-t_1)} - e^{-ih(t-t_1)}\Xi(\rho(t_0);t_1)e^{ih(t-t_1)} \Big),
\end{aligned}
\tag{3.19}
$$

25

where the operators Σ and Ξ contain the medium correlators and encode the interaction of the system with the medium

$$\Sigma(t) = \int_{t_0}^{t} dt_2\, H_S^\alpha e^{-ih(t-t_2)} H_S^\beta e^{ih(t-t_2)} \left\langle H_M^\alpha(t) H_M^\beta(t_2) \right\rangle, \tag{3.20}$$

$$\Xi(\rho(t_0); t) = \int_{t_0}^{t} dt_2\, H_S^\alpha e^{-ih(t-t_0)} \rho(t_0) e^{ih(t_2-t_0)} H_S^\beta e^{ih(t-t_2)} \left\langle H_M^\beta(t_2) H_M^\alpha(t) \right\rangle + h.c.. \tag{3.21}$$

Taking the derivative of Eq. (3.19), we have an equation for the time evolution of the reduced density matrix of the system. We here make use of the Markov approximation and promote $e^{-ih(t-t_0)} \rho(t_0) e^{ih(t-t_0)}$ to $\rho(t)$; we justify this assumption in more detail in the case of in-medium heavy quarkonium in chapter 4 in which we derive the evolution equations using finite temperature and out of equilibrium QFT. The time evolution of $\rho(t)$ is thus given by

$$\frac{d\rho(t)}{dt} = -i[h, \rho(t)] - \Sigma(t)\rho(t) - \rho(t)\Sigma^\dagger(t) + \Xi(\rho(t); t), \tag{3.22}$$

where

$$\Xi(\rho(t); t) = \int_{t_0}^{t} dt_2\, H_S^\alpha \rho(t) e^{-ih(t-t_2)} H_S^\beta e^{ih(t-t_2)} \left\langle H_M^\alpha(t_2) H_M^\beta(t) \right\rangle + h.c.. \tag{3.23}$$

As an *amuse-bouche*, we note that the medium correlator is peaked around times proportional to the environment correlation time scale, i.e., $t - t_2 \lesssim \tau_E$, and the eigenvalues of the system Hamiltonian h are of the order of the inverse of the system intrinsic time scale τ_S^{-1}. Observing the system over time scales longer than the environment correlation time, i.e., $t - t_2 \gg \tau_E$, in the regime of quantum Brownian motion, where $\tau_S \gg \tau_E$, we may thus set the exponentials occurring in the definitions of $\Sigma(t)$ and $\Xi(\rho(t); t)$ to 1. We suggestively define

$$\int_{t_0}^{t} dt_2 \left\langle H_M^\alpha(t) H_M^\beta(t_2) \right\rangle = \frac{\delta^{\alpha\beta}}{2} \left(\Gamma(t) + i\delta M(t) \right), \tag{3.24}$$

where $\Gamma(t)$ and $\delta M(t)$ are real scalars, such that

$$\Sigma_s(t) = H_S^\alpha H_S^\alpha \frac{1}{2} \left(\Gamma(t) + i\delta M(t) \right), \tag{3.25}$$

$$\Xi(\rho(t); t) = H_S^\alpha \rho(t) H_S^\alpha \Gamma(t), \tag{3.26}$$

and the evolution equation of Eq. (3.22) can be written as a Lindblad equation

$$\frac{d\rho(t)}{dt} = -i[H, \rho(t)] + C^\alpha(t)\rho(t)C^{\alpha\dagger}(t) - \frac{1}{2} \left\{ C^{\alpha\dagger}(t)C^{\alpha\dagger}(t), \rho(t) \right\}, \tag{3.27}$$

where

$$H = h + \mathrm{Im}\left(\Sigma(t) \right), \tag{3.28}$$

$$C^\alpha(t) = \sqrt{\Gamma(t)} H_S^\alpha. \tag{3.29}$$

In chapter 4, we use pNRQCD at finite temperature and out of equilibrium to rederive the analogous set of coupled equations describing the in-medium evolution of the singlet and octet quarkonium states first derived in Refs. [28, 30]. We, therefore, postpone a discussion on the interpretation of each of the terms of the evolution equation to chapter 4. We note, however, that the set of coupled evolution equations at order 0 in perturbation theory can be reproduced in a fully OQS setting by projecting Eq. (3.22) onto the singlet and octet sector and substituting the appropriate pNRQCD Hamiltonians into Eqs. (3.20) and (3.23).

Chapter 4

Quantum field theory at finite temperature

In order to describe the in-medium evolution of heavy quarkonium, we make use of EFT methods and the OQS formalism. The EFT pNRQCD allows us to describe the relevant physics of heavy quarkonium in-medium while explicitly accounting for the quantum and non-Abelian nature of the system; the OQS formalism allows us to rigorously and systematically take into account the interaction of the quarkonium state with the enormously complex environment formed in HIC experiments. In order to accurately describe this environment, we must take into account its thermal nature; in this chapter, we introduce finite temperature QFT and using this formalism present the set of coupled evolution equations describing the in-medium evolution of heavy quarkonium in the regime of quantum Brownian motion first derived in Refs. [28, 30]. In sec. 4.1, we present the basics of quantum field theory at finite temperature. In sec. 4.2, we use the methods of finite temperature QFT to rederive the master equation governing the in-medium, out of equilibrium evolution of Coulombic quarkonium.

4.1   QFT at finite temperature and out of equilibrium

In this section, we present a brief introduction to finite temperature QFT. For a more thorough presentation, we direct the reader to a number of review papers [84, 85] and textbooks [41–43]. As stated in chapter 1, the starting point of thermal field theory is the analogy between the quantum mechanical probability amplitude $F(q', -i\tau'; q, -i\tau)$ of a transition from state q at time $-i\tau$ to state q' at time $-i\tau'$ (where $\tau = it$ is the Euclidean time) and the partition function $Z(\beta)$ of quantum statistical mechanics (where $\beta = T^{-1}$ is the inverse temperature). The transition amplitude is given by

$$F(q', -i\tau'; q, -i\tau) = \langle q'|e^{-\hat{H}(\tau'-\tau)}|q\rangle = \int_{q(\tau)}^{q'(\tau')} \mathcal{D}q \exp\left[-\int_{\tau}^{\tau'} d\tau'' \mathcal{L}_E(\tau'')\right], \qquad (4.1)$$
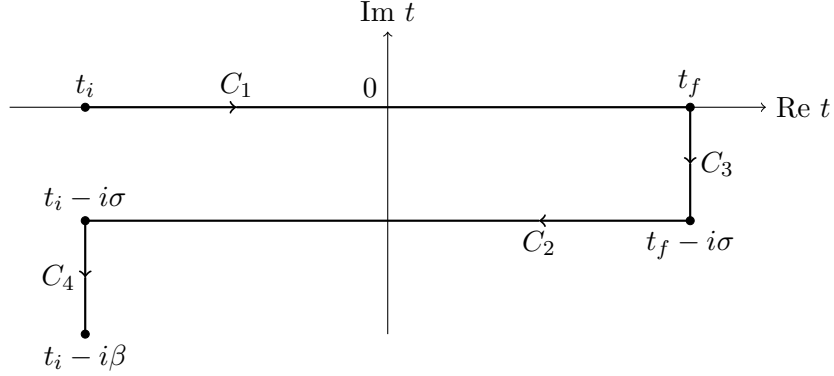
Figure 4.1: The time contours of the real time thermal field theory formalism. Taking σ as infinitesimally small gives the Schwinger-Keldysh contour. Adapted from Fig. 3.6 of Ref. [41].

where $\hat{H}$ is the Hamiltonian, $\mathcal{L}_E$ is the Euclidean Lagrangian and $\mathcal{D}q$ is the path integral measure. The partition function is given by

$$Z(\beta) = \mathrm{Tr}\left[e^{-\beta\hat{H}}\right] = \sum_n e^{-\beta E_n} = \int \mathrm{d}q \langle q|e^{-\beta\hat{H}}|q\rangle. \tag{4.2}$$

Combining Eqs. (4.1) and (4.2), we rewrite the partition function in terms of a transition amplitude from state q at time 0 to state q at time $-i\beta$

$$Z(\beta) = \int \mathrm{d}q\, F(q, -i\beta; q, 0) = \int_{q(0)}^{q(\beta)} \mathcal{D}q \exp\left[-\int_0^\beta \mathrm{d}\tau \mathcal{L}_E(\tau)\right]. \tag{4.3}$$

We thus interpret the operator form of the Boltzmann factor $e^{-H/T}$ as a time evolution operator by time $t = -i/T$. As mentioned in chapter 1, there exist an imaginary and a real time formalism to treat this evolution. In this thesis, we make use of the real time formalism; for an introduction to the imaginary time formalism, we direct the reader to the thermal field theory literature given above.

In the real time formalism, temporal evolution is taken to proceed along a contour starting from an initial time t_i and ending at a final time $t_i - i\beta$. In order to gain access to real time correlation functions, the contour follows an indirect path. Specifically, it is taken to proceed from the initial time t_i along the real axis up to time t_f, proceed parallel to the imaginary axis down to time $t_f - i\sigma$ (where $0 \leq \sigma \leq \beta$ is an arbitrary real number), proceed parallel to the real axis to $t_i - i\sigma$ and finally parallel to the imaginary axis down to the final time $t_i - i\beta$. These branches of the contour are denoted C_1, C_3, C_2 and C_4, respectively; we sketch this path in Fig. 4.1. It is standard practice in real time calculations to take $\sigma = 0$ such that C_1 and C_2 lie along the real axis. C_3 and C_4 are taken as not contributing to the evolution and are disregarded. We follow this standard

29

procedure in this thesis, although we note it remains not without controversy [86–90]. The combined path forward in time along C_1 and backwards along C_2 with $\sigma = 0$ is denoted the Schwinger-Keldysh contour [91, 92].

The Schwinger-Keldysh contour of the real time formalism leads to a doubling of the degrees of freedom as fields can live on the upper or the lower contour; we denote fields living on the upper branch with a subscript 1 and those living on the lower branch with subscript 2. Correlation functions consist of combinations of fields of type 1 and type 2 ordered along the contour. The four types of propagators are given by

$$\mathbf{D}(x) = \begin{pmatrix} D_{11}(x) & D_{12}(x) \\ D_{21}(x) & D_{22}(x) \end{pmatrix} = \begin{pmatrix} D_F(x) & D^<(x) \\ D^>(x) & D_{\tilde{F}}(x) \end{pmatrix}, \tag{4.4}$$

where, for a scalar field ϕ

$$D_F(t - t') = \langle \phi(t)\phi(t') \rangle \theta(t - t') + \langle \phi(t')\phi(t) \rangle \theta(t' - t), \tag{4.5}$$

$$D_{\tilde{F}}(t - t') = \langle \phi(t)\phi(t') \rangle \theta(t' - t) + \langle \phi(t')\phi(t) \rangle \theta(t - t'), \tag{4.6}$$

$$D^<(t - t') = \langle \phi(t')\phi(t) \rangle, \tag{4.7}$$

$$D^>(t - t') = \langle \phi(t)\phi(t') \rangle. \tag{4.8}$$

$D_F(t)$ and $D_{\tilde{F}}(t)$ are the Feynman time ordered and anti time ordered propagators, respectively, and $D^>(t)$ and $D^<(t)$ are called Wightman functions. Similar definitions apply for fermion fields with appropriate changes of sign due to the Grassmann nature of the fields and the anticommutation relations. This contour ordering can be understood as the generalization of time ordering to the nontrivial time contour used in real time thermal field theory. Time proceeds in the usual direction along the upper contour where contour ordering thus corresponds to standard time ordering; time proceeds in the opposite direction along the lower contour where contour ordering thus corresponds to anti-time ordering. The upper branch preceeds the lower branch of the contour; thus times along the lower branch are considered later than those along the upper branch. As correlation functions proceeding in the forward time direction are of interest, in a diagramatic context, an amplitude is calculated by assigning all external fields to be of type 1 and summing over all combinations of type 1 and type 2 assignments for internal vertices. Vertices, which correspond to space-time points, are taken to be of type 1 or type 2 and do not mix different branches of the contour. Type 1 vertices are equivalent to standard vertices in zero-temperature QFT while type 2 vertices enter amplitudes with an additional negative sign.

4.2   Evolution equations

In this section, we utilize the QFT at finite temperature methods presented in the previous section to rederive the evolution equations of the reduced density matrix of in-medium heavy quarkonium first derived in Refs. [28, 30]. Our theory is pNRQCD in which the Coulombic gluons are resummed via the field redefinitions

$$O(t) = \Omega(t)\tilde{O}(t)\Omega^\dagger(t), \quad E_i(t, \mathbf{0}) = \Omega(t)\tilde{E}_i(t, \mathbf{0})\Omega^\dagger(t), \tag{4.9}$$

where $\Omega(t)$ is a Wilson line extending from time $-\infty$ to time t

$$\Omega(t) = \mathrm{P}\exp\left[-ig\int_{-\infty}^{t}dt'\,A_0(t',\mathbf{0})\right]. \tag{4.10}$$

This redefinition yields a Lagrangian of the form

$$\mathcal{L}_{\mathrm{pNRQCD}} = \mathrm{Tr}\left[\mathrm{S}^\dagger\left(i\partial_0 - h_s\right)\mathrm{S} + \tilde{\mathrm{O}}^\dagger\left(i\partial_0 - h_o\right)\tilde{\mathrm{O}} + \tilde{\mathrm{O}}^\dagger\mathbf{r}\cdot g\tilde{\mathbf{E}}\mathrm{S} + \mathrm{S}^\dagger\mathbf{r}\cdot g\tilde{\mathbf{E}}\tilde{\mathrm{O}} \right. $$
$$\left. + \frac{1}{2}\tilde{\mathrm{O}}^\dagger\left\{\mathbf{r}\cdot g\tilde{\mathbf{E}},\tilde{\mathrm{O}}\right\}\right], \tag{4.11}$$

identical to the standard pNRQCD Lagrangian with the chromoelectric and octet fields replaced by their tilded counterparts and the covariant derivative replaced by a standard derivative. We use this theory to calculate the time evolution of the reduced density matrix of the quarkonium state. Our starting point is the identification of the Wightman function of the singlet state $D^<(x) = \langle S^\dagger(0)S(x)\rangle$ (and similarly for the pNRQCD octet state) with the density matrix $\rho(x_0)$, i.e., $D^<(x) = \rho(x_0)$. In making this identification, we take advantage of the ability of the real time formalism of finite temperature QFT to describe fields both in and out of equilibrium and thus provide a field theoretical definition of the quantum mechanical density matrix introduced in the previous chapter. We make use of the bosonic equal time commutation relations to write all propagators in terms of $D^<(x)$

$$D_{11}(x) = \theta(x_0)\delta^{(3)}(\mathbf{x}) + D^<(x), \tag{4.12}$$
$$D_{12}(x) = D^<(x), \tag{4.13}$$
$$D_{21}(x) = D^<(x) + \delta^{(3)}(\mathbf{x}), \tag{4.14}$$
$$D_{22}(x) = \theta(-x_0)\delta^{(3)}(\mathbf{x}) + D^<(x). \tag{4.15}$$

We calculate $\rho(t) = D_{12}(x)$, diagramatically; in the bottom sector, our task is simpler as we are in the dilute limit. Only diagrams with a single insertion of the density matrix need be considered. This implies we may approximate the correlators of Eqs. (4.12)-(4.15) as

$$D_{11}(x) \approx \theta(x_0)\delta^{(3)}(\mathbf{x}), \tag{4.16}$$
$$D_{12}(x) = D^<(x), \tag{4.17}$$
$$D_{21}(x) \approx \delta^{(3)}(\mathbf{x}), \tag{4.18}$$
$$D_{22}(x) \approx \theta(-x_0)\delta^{(3)}(\mathbf{x}). \tag{4.19}$$

Diagrams contributing to this evolution at order r^2 in the multipole expansion are shown in Fig. 4.2.
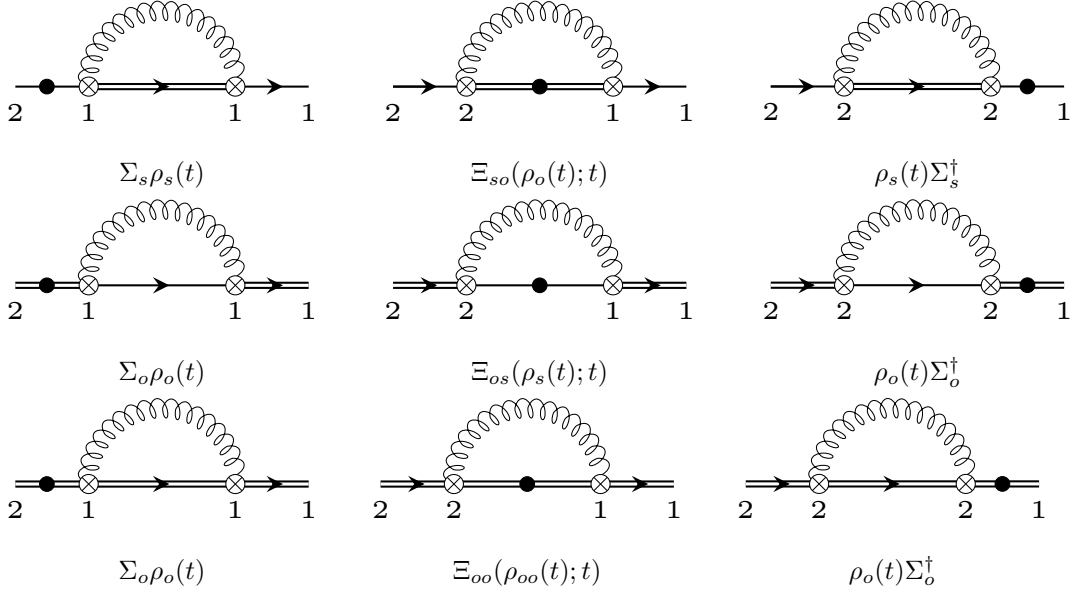
Figure 4.2: Diagrams contributing to the in-medium evolution of the singlet and octet density matrices at order r^2 in the pNRQCD multipole expansion. The labels indicate the terms of the evolution equation to which each diagram contributes. A single line represents a singlet propagator; a double line, an octet propagator; and a curly line, a gluoelectric field. A crossed circle represents a pNRQCD dipole vertex. A filled circle represents an insertion of the density matrix. The labels 1 and 2 represent the branches of the Schwinger-Keldysh contour.

The Schrödinger picture singlet and octet density matrices are given as

$$
\begin{aligned}
\rho_s(t) =& e^{-ih_s(t-t_0)}\rho_s(t_0)e^{ih_s(t-t_0)} \\
&- \int_{t_0}^t dt_1 \left[e^{-ih_s(t-t_1)}\Sigma_s(t_1)e^{-ih_s(t_1-t_0)}\rho_s(t_0)e^{ih_s(t-t_0)} \right. \\
&+ e^{-ih_s(t-t_0)}\rho_s(t_0)e^{-ih_s(t_0-t_1)}\Sigma_s^\dagger(t_1)e^{-ih_s(t_1-t)} \\
&\left. - e^{-ih_s(t-t_1)}\Xi_{so}(\rho_o(t_0);t_1)e^{ih_s(t-t_1)} \right],
\end{aligned}
$$

(4.20)

$$\rho_o(t) = e^{-ih_o(t-t_0)}\rho_o(t_0)e^{ih_o(t-t_0)}$$
$$-\int_{t_0}^t dt_1 \left[e^{-ih_o(t-t_1)}\Sigma_o(t_1)e^{-ih_o(t_1-t_0)}\rho_o(t_0)e^{ih_o(t-t_0)} \right.$$
$$+ e^{-ih_o(t-t_0)}\rho_o(t_0)e^{-ih_o(t_0-t_1)}\Sigma_o^\dagger(t_1)e^{-ih_o(t_1-t)} \tag{4.21}$$
$$- e^{-ih_o(t-t_1)}\Xi_{os}(\rho_s(t_0);t_1)e^{ih_o(t-t_1)}$$
$$\left. - e^{-ih_o(t-t_1)}\Xi_{oo}(\rho_o(t_0);t_1)e^{ih_o(t-t_1)} \right],$$

where

$$\Sigma_s(t_1) = \frac{g^2}{6N_c}\int_{t_0}^{t_1} dt_2\, r_i e^{-ih_o(t_1-t_2)} r_i e^{ih_s(t_1-t_2)} \left\langle \tilde{E}_j^a(t_1)\tilde{E}_j^a(t_2) \right\rangle, \tag{4.22}$$

$$\Xi_{so}(\rho_o(t_0);t_1) = \frac{g^2}{6N_c(N_c^2-1)}\int_{t_0}^{t_1} dt_2\, r_i e^{-ih_o(t_1-t_0)}\rho_o(t_0)e^{ih_o(t_2-t_0)} r_i e^{ih_s(t_1-t_2)}$$
$$\times \left\langle \tilde{E}_j^a(t_2)\tilde{E}_j^a(t_1) \right\rangle + h.c., \tag{4.23}$$

$$\Sigma_o(t_1) = \frac{g^2}{6N_c(N_c^2-1)}\int_{t_0}^{t_1} dt_2\, r^i \left[e^{-ih_s(t_1-t_2)} + \frac{N_c^2-4}{2}e^{-ih_o(t_1-t_2)} \right] r_i$$
$$\times e^{ih_o(t_1-t_2)} \left\langle \tilde{E}_j^a(t_1)\tilde{E}_j^a(t_2) \right\rangle, \tag{4.24}$$

$$\Xi_{os}(\rho_o(t_0);t_1) = \frac{g^2}{6N_c}\int_{t_0}^{t_1} dt_2\, r_i e^{-ih_s(t_1-t_0)}\rho_s(t_0)e^{ih_s(t_2-t_0)} r_i e^{ih_o(t_1-t_2)}$$
$$\times \left\langle \tilde{E}_j^a(t_2)\tilde{E}_j^a(t_1) \right\rangle + h.c., \tag{4.25}$$

$$\Xi_{oo}(\rho_o(t_0);t_1) = \frac{g^2(N_c^2-4)}{12N_c(N_c^2-1)}\int_{t_0}^{t_1} dt_2\, r_i e^{-ih_o(t_1-t_0)}\rho_o(t_0)e^{ih_o(t_2-t_0)} r_i e^{ih_o(t_1-t_2)}$$
$$\times \left\langle \tilde{E}_j^a(t_2)\tilde{E}_j^a(t_1) \right\rangle + h.c., \tag{4.26}$$

where we assume the plasma to be isotropic such that $r_i r_j = \frac{r^2}{3}\delta^{ij}$. Eqs. (4.20) and (4.21) for the singlet and octet reduced density matrices enable us to easily arrive at a coupled set of equations for their time evolution. We note, however, that the resulting set of coupled equations gives the time evolution of the density matrices at time t in terms of the density matrices at time t_0, i.e., they are nonlocal in time. We improve upon this by making use of the Markov approximation. We promote $e^{-ih_{s,o}(t-t_0)}\rho_{s,o}(t_0)e^{ih_{s,o}(t-t_0)}$ to $\rho_{s,o}(t)$. We note that this relation is exact at tree level and that $\rho_{s,o}(t_0)$ and $\rho_{s,o}(t)$ differ first at order r^2 in the multipole expansion such that this substitution introduces corrections to the evolution equations first at order r^4, i.e., beyond the accuracy of the presented equations.

Taking the derivative of Eqs. (4.20) and (4.21) and making use of the Markov approximation, we arrive at the following set of coupled equations for the time evolution

33

of the heavy quarkonium singlet and octet states

$$\frac{d\rho_s(t)}{dt} = -i[h_s, \rho_s(t)] - \Sigma_s(t)\rho_s(t) - \rho_s(t)\Sigma_s^\dagger(t) + \Xi_{so}(\rho_o(t); t), \tag{4.27}$$

$$\frac{d\rho_o(t)}{dt} = -i[h_o, \rho_o(t)] - \Sigma_o(t)\rho_o(t) - \rho_o(t)\Sigma_o^\dagger(t) + \Xi_{os}(\rho_s(t); t), + \Xi_{oo}(\rho_o(t); t), \tag{4.28}$$

where, after the Markov approximation, the Ξ are given by

$$\Xi_{so}(\rho_o(t); t) = \frac{g^2}{6N_c(N_c^2 - 1)} \int_{t_0}^t dt_2 \, r_i \rho_o(t) e^{-ih_o(t-t_2)} r_i e^{ih_s(t-t_2)}$$
$$\times \left\langle \tilde{E}_j^a(t_2) \tilde{E}_j^a(t) \right\rangle + h.c., \tag{4.29}$$

$$\Xi_{os}(\rho_o(t); t) = \frac{g^2}{6N_c} \int_{t_0}^t dt_2 \, r_i \rho_s(t) e^{-ih_s(t-t_2)} r_i e^{ih_o(t-t_2)} \left\langle \tilde{E}_j^a(t_2) \tilde{E}_j^a(t) \right\rangle + h.c., \tag{4.30}$$

$$\Xi_{oo}(\rho_o(t); t) = \frac{g^2(N_c^2 - 4)}{12N_c(N_c^2 - 1)} \int_{t_0}^t dt_2 \, r_i \rho_o(t) e^{-ih_o(t-t_2)} r_i e^{ih_o(t-t_2)}$$
$$\times \left\langle \tilde{E}_j^a(t_2) \tilde{E}_j^a(t) \right\rangle + h.c.. \tag{4.31}$$

In Eqs. (4.27) and (4.28), the commutator terms represent the vacuum evolution of the singlet and octet states. Interactions with the medium are encoded in the Σ and Ξ operators. At the level of both the diagrams of Fig. 4.2 and the above equations, the Σ terms are to be understood as a contribution to the in-medium density of the singlet and octet states proportional to the density of those states; furthermore, the negative sign leads to their naive interpretation as a width. $\Xi_{so}(\rho_o(t); t)$ and $\Xi_{os}(\rho_s(t); t)$ represent contributions to the in-medium density of the singlet and octet states due to the octet and singlet states, respectively. Due to the octet-octet transitions in pNRQCD, the octet density matrix also receives (naively) positive contributions to its trace due to transitions from other octet states; Ξ_{oo} represents these contributions. Σ_o, furthermore, also naively encodes the octet to octet width.

We can further improve upon our set of equations by exploiting the fact that time scales on the order of magnitude of the freeze out time are of interest such that the time from initialization of the plasma at t_0 up to t is the largest time scale of the problem. As the thermal correlators decay rapidly at times $t \gtrsim 1/T$, the time scale $t - t_0$ can be taken to be infinite. This combined with the time translation invariance of the thermal correlators allows us to perform a change of variables and write finally

$$\frac{d\rho_s(t)}{dt} = -i[h_s, \rho_s(t)] - \Sigma_s \rho_s(t) - \rho_s(t)\Sigma_s^\dagger + \Xi_{so}(\rho_o(t)), \tag{4.32}$$

$$\frac{d\rho_o(t)}{dt} = -i[h_o, \rho_o(t)] - \Sigma_o \rho_o(t) - \rho_o(t)\Sigma_o^\dagger + \Xi_{os}(\rho_s(t)), + \Xi_{oo}(\rho_o(t)), \tag{4.33}$$

where

$$\Sigma_s = \frac{g^2}{6N_c} \int_0^\infty \mathrm{d}s\, r_i e^{-ih_o s} r_i e^{ih_s s} \left\langle \tilde{E}_j^a(s)\tilde{E}_j^a(0) \right\rangle, \tag{4.34}$$

$$\Xi_{so}(\rho_o(t)) = \frac{g^2}{6N_c(N_c^2-1)} \int_0^\infty \mathrm{d}s\, \rho_o(t_0) e^{-ih_o s} r_i e^{ih_s s} \left\langle \tilde{E}_j^a(0)\tilde{E}_j^a(s) \right\rangle + h.c., \tag{4.35}$$

$$\Sigma_o = \frac{g^2}{6N_c(N_c^2-1)} \int_0^\infty \mathrm{d}s\, r^i \left[e^{-ih_s s} + \frac{N_c^2-4}{2} e^{-ih_o s} \right] r_i e^{ih_o s}$$
$$\times \left\langle \tilde{E}_j^a(s)\tilde{E}_j^a(0) \right\rangle + h.c., \tag{4.36}$$

$$\Xi_{os}(\rho_o(t)) = \frac{g^2}{6N_c} \int_0^\infty \mathrm{d}s\, r_i \rho_s(t_0) e^{-ih_s s} r_i e^{ih_o s} \left\langle \tilde{E}_j^a(0)\tilde{E}_j^a(s) \right\rangle + h.c., \tag{4.37}$$

$$\Xi_{oo}(\rho_o(t)) = \frac{g^2(N_c^2-4)}{12N_c(N_c^2-1)} \int_{t_0}^{t_1} \mathrm{d}s\, r_i \rho_o(t_0) e^{-ih_o s} r_i e^{ih_o s} \left\langle \tilde{E}_j^a(0)\tilde{E}_j^a(s) \right\rangle + h.c.. \tag{4.38}$$

Eqs. (4.32)-(4.38) describe the in-medium evolution of heavy quarkonium realizing the hierarchy of scales $M \gg 1/a_0 \gg (\pi)T \gg E$. Exploiting the hierarchy $(\pi)T \gg E$ we make a final simplification. As stated above, the gluoelectric correlators decay rapidly at times $t \gtrsim 1/T$; as the eigenvalues of the quarkonium Hamiltonian $h_{s,o}$ in the exponential factors scale as the binding energy E, in the limit $T \gg E$, these exponential factors can be set to 1. In this limit, the Σ and Ξ operators characterizing the interaction of the quarkonium state with the medium simplify considerably and can, in fact, be written in terms of the transport coefficients κ and γ

$$\kappa = \frac{g^2}{6N_c} \int_0^\infty \mathrm{d}s \left\langle \left\{ \tilde{E}_i^a(s,\vec{0}), \tilde{E}_i^a(0,\vec{0}) \right\} \right\rangle, \tag{4.39}$$

$$\gamma = -i\frac{g^2}{6N_c} \int_0^\infty \mathrm{d}s \left\langle \left[\tilde{E}_i^a(s,\vec{0}), \tilde{E}_i^a(0,\vec{0}) \right] \right\rangle., \tag{4.40}$$

where κ is the heavy quarkonium momentum diffusion coefficient and γ is its dispersive counterpart. In this limit, the Σ and Ξ operators take the form

$$\Sigma_s = \frac{r^2}{2}(\kappa + i\gamma), \tag{4.41}$$

$$\Xi_{so}(\rho_o(t)) = \frac{1}{N_c^2-1} r_i \rho_o(t) r_i \kappa, \tag{4.42}$$

$$\Sigma_o = \frac{N_c^2-2}{2(N_c^2-1)} \frac{r^2}{2}(\kappa + i\gamma), \tag{4.43}$$

$$\Xi_{os}(\rho_s(t)) = r_i \rho_s(t) r_i \kappa, \tag{4.44}$$

$$\Xi_{oo}(\rho_o(t)) = \frac{N_c^2-4}{2(N_c^2-1)} r_i \rho_o(t) r_i \kappa. \tag{4.45}$$

These equations describe the in-medium evolution of heavy Coulombic quarkonium in the strict $(\pi)T \gg E$ limit. We note the derivation makes no assumption on the coupling

strength of the medium and is thus valid also for strong coupling. In this limit, the evolution equations can be written in Lindblad form [82, 83] and solved making use of the extensive computational and algorithmic tools available to do so. In chapter 8, we present results from Refs. [60, 61] in which these evolution equations are solved in the strict $(\pi)T \gg E$ limit and in chapter 9 results from Ref. [62] in which the evolution equations are solved including the first corrections in E/T.

Part II

Theoretical Results: Langevin Equations, Transport Coefficients and Nonlinear Evolution Equations

Chapter 5

Transport coefficients

In chapters 3 and 4, we utilize pNRQCD and OQS methods to derive a master equation governing the out of equilibrium, in-medium evolution of heavy quarkonium in a strongly coupled QGP. In the limit that the binding energy E of the quarkonium state is much less than the temperature T of the plasma, the medium interactions are completely encoded in the transport coefficients κ and γ

$$\kappa = \frac{g^2}{6N_c} \int_0^\infty dt \left\langle \left\{ \tilde{E}^{a,i}(t, \mathbf{0}), \tilde{E}^{a,i}(0, \mathbf{0}) \right\} \right\rangle, \tag{5.1}$$

$$\gamma = -i\frac{g^2}{6N_c} \int_0^\infty dt \left\langle \left[\tilde{E}^{a,i}(t, \mathbf{0}), \tilde{E}^{a,i}(0, \mathbf{0}) \right] \right\rangle, \tag{5.2}$$

where the tilde represents a dressing of the electric fields with Wilson lines

$$\tilde{E}_i^a(t, \mathbf{0}) = \Omega^\dagger(t) E_i^a(t, \mathbf{0}) \Omega(t), \tag{5.3}$$

where $\Omega(t)$ is a Wilson line in the fundamental representation

$$\Omega(t) = \mathrm{P} \exp\left[-ig \int_{-\infty}^t \mathrm{d}t' A_0^a(t', \mathbf{0}) T^a \right]. \tag{5.4}$$

κ is the momentum diffusion coefficient describing the in-medium diffusion of the heavy probe, and γ is its dispersive counterpart. In this chapter, we discuss in greater detail the role, origin and interpretation of these transport coefficients; we proceed by introducing Langevin dynamics which describes the in-medium diffusion of a heavy particle characterized by the momentum diffusion coefficient κ

Due to the hierarchy of scales $M \gg T$ realized by heavy quarks and heavy quarkonium in HIC experiments, Brownian motion provides a natural paradigm to model the in-medium evolution of these heavy states. Brownian motion describes a particle undergoing a random walk due to uncorrelated interactions with its environment. Such a process is described by a Langevin equation governing the momentum evolution of the heavy particle

$$\frac{\mathrm{d}p_i}{\mathrm{d}t} = -\eta_D p_i + \xi_i(t), \quad \langle \xi_i(t)\xi_j(t') \rangle = \kappa \delta_{ij} \delta(t - t'), \tag{5.5}$$

where p_i is the momentum of the heavy particle, η_D is the drag coefficient and ξ_i represents random changes to the momentum of the particle due to uncorrelated interactions with its environment. The momentum diffusion coefficient κ is defined as the force-force correlator arising from these interactions with the medium. The drag and momentum diffusion coefficients are related by the Einstein relation

$$\eta_D = \frac{\kappa}{2MT}. \tag{5.6}$$

A large number of works have utilized such a framework to model the propagation of heavy quarks in the QGP [93–102]; formulating field theoretic definitions of κ and fixing its value have thus been active topics in the literature. Taking the trace and integrating over the definition of κ, it is clear that 3κ gives the expectation value of the squared momentum transfer per time due to the random interactions with the medium. In Ref. [103], Moore and Teaney calculate this momentum transfer due to in-medium scatterings of the heavy quark and thus derive an expression for κ. In Ref. [104], Casalderrey-Solana and Teaney derive an expression for the heavy quark momentum diffusion coefficient κ as a dressed electric-electric correlator by integrating out the heavy quarks from the in-medium force-force correlator along the Schwinger-Keldysh contour. The resulting expression has been used to calculate κ in Minkowski field theory [105, 106] and derive Euclidean expressions [107, 108] from which κ can be calculated directly on the lattice [109–111].

The remainder of this chapter is structured as follows. In sec. 5.1, we discuss operator ordering and group representation issues related to the Wilson lines dressing the electric fields in Eqs. (5.1) and (5.2). In sec. 5.2, we discuss the fixing of values of κ and γ. We present state of the art extractions including direct quenched lattice measurements, indirect extractions from quenched lattice measurements and indirect estimates from phenomenological models and experimental measurements. Our discussion and results follow Ref. [33] with new extractions based on data first available following publication of Ref. [33].

5.1 Adjoint and fundamental transport coefficients

In this section, we discuss in greater detail the operator ordering of the fields appearing in the definitions of κ and γ. Equivalently to the commutator-anticommutator definitions given in Eqs. (5.1) and (5.2), κ and γ can be written as the real and imaginary parts of a time ordered chromoelectric correlator

$$\kappa = \frac{g^2}{6N_c} \mathrm{Re} \int_{-\infty}^{\infty} dt \left\langle \mathrm{T} \tilde{E}_i^a(t, \mathbf{0}) \tilde{E}_i^a(0, \mathbf{0}) \right\rangle, \tag{5.7}$$

$$\gamma = \frac{g^2}{6N_c} \mathrm{Im} \int_{-\infty}^{\infty} dt \left\langle \mathrm{T} \tilde{E}_i^a(t, \mathbf{0}) \tilde{E}_i^a(0, \mathbf{0}) \right\rangle, \tag{5.8}$$

where T represents time ordering. In Ref. [112], working in the γ sector, Eller, Ghiglieri and Moore identify two distinct objects

$$\gamma_{\text{adj}} = \frac{g^2}{6N_c}\text{Im}\int_{-\infty}^{\infty} dt \left\langle \text{T} E_i^a(t,\mathbf{0})U^{ab}(t,0)E_i^b(0,\mathbf{0}) \right\rangle, \tag{5.9}$$

$$\gamma_{\text{fund}} = \frac{g^2}{3N_c}\text{Im}\int_{-\infty}^{\infty} dt \left\langle \text{Tr}\left[\text{P}U(-\infty,t)E_i^a(t,\mathbf{0})U(t,0)E_i^a(0,\mathbf{0})U(t,-\infty)\right]\right\rangle, \tag{5.10}$$

where T and P represent time and path ordering, respectively, and the trace is over the color matrices. The path ordering implies time ordering of the electric fields but not of the Wilson lines. $U(t_1,t_2)$ is a Wilson line in the fundamental representation

$$U(t_1,t_2) = \text{P}\exp\left[-ig\int_{t_2}^{t_1} dt' A_0^a(t')T^a\right], \tag{5.11}$$

and $U^{ab}(t_1,t_2)$ is a Wilson line in the adjoint representation

$$U^{ab}(t_1,t_2) = \text{P}\exp\left[-ig\int_{t_2}^{t_1} dt' A_0^c(t')\left(-if^{abc}\right)\right]. \tag{5.12}$$

The authors of Ref. [112] interpret the adjoint and fundamental transport coefficients as describing the in-medium evolution of heavy quarkonium and heavy quarks, respectively.

To examine the difference between these two objects, we define the electric correlators

$$G_{\text{adj}}(t) = \frac{g^2}{6N_c}\left\langle \text{T} E_i^a(t,\mathbf{0})U^{ab}(t,0)E_i^b(0,\mathbf{0}) \right\rangle, \tag{5.13}$$

$$G_{\text{fund}}(t) = \frac{g^2}{3N_c}\left\langle \text{Tr}\left[\text{P}U(-\infty,t)E_i^a(t,\mathbf{0})U(t,0)E_i^a(0,\mathbf{0})U(t,-\infty)\right]\right\rangle, \tag{5.14}$$

such that their Fourier transforms at 0 frequency give the adjoint and fundamental transport coefficients, i.e.,

$$\int_{-\infty}^{\infty} dt\, G_{\text{adj,fund}}(t) = (\kappa + i\gamma)_{\text{adj,fund}}. \tag{5.15}$$

The adjoint correlator was calculated up to next-to-leading order in Ref. [113]. To help clarify the structure of the adjoint and fundamental correlators, we examine the diagrams contributing to the in-medium diffusion and dispersion of heavy quarks and heavy quarkonium. We begin by defining, analogously to the force ansatz of Ref. [104], i.e.,

$$\mathcal{F} = \int d^3x\, \psi^\dagger(t,\mathbf{x})\mathbf{E}(t,\mathbf{x})\psi(t,\mathbf{x}), \tag{5.16}$$

where $\mathcal{F}$ is the force on an in-medium heavy quark represented by the NRQCD heavy quark field ψ, an addition to the NRQCD Lagrangian of the form

$$\delta\mathcal{L}_{\text{int}} = \psi^\dagger(t,\mathbf{x})\mathbf{x}\cdot\mathbf{E}(t,\mathbf{0})\psi(t,\mathbf{x}). \tag{5.17}$$

40
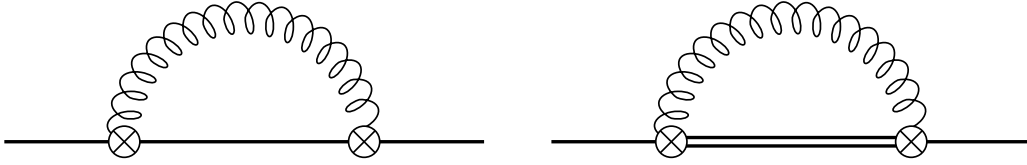
Figure 5.1: Diagrams of order g^2 in which the heavy quark (left) and heavy quarkonium (right) coefficients arise. In the left diagram, the single line represents a quark. In the right diagram, the single line represents a singlet quarkonium state, and the double line an octet quarkonium state. In both diagrams, crossed vertices represent electric field insertions, and the curly lines represent the chromoelectric field.

The above term adds an electric vertex to the NRQCD Lagrangian analogous to the dipole vertices of pNRQCD. With $\delta\mathcal{L}_{\text{int}}$ added to the leading order NRQCD Lagrangian, we consider the insertion of two electric vertices in both NRQCD and pNRQCD to elucidate the structure of κ and γ.

At order g^2 in perturbation theory, the only contribution to κ and γ, in both the modified version of NRQCD containing the vertex specified in Eq. (5.17) and in pNRQCD, comes from the diagrams displayed in Fig. 5.1; this contribution is the electric-electric correlator $\langle E_i^a(t,\mathbf{0})E_i^a(0,\mathbf{0})\rangle$. At order g^4 in perturbation theory, κ and γ receive contributions from the diagrams shown in Fig. 1 of Ref. [108] and reproduced in Fig. 1 of Ref. [112]. These contributions represent combinations of the non-Abelian terms of the electric field, higher order gluonic interactions including corrections to the gluonic propagator and coupling to Coulombic gluons from the temporal covariant derivative D_0. We display a selection of such diagrams in Fig. 5.2; both diagrams correspond to diagram j in the nomenclature of Refs. [108, 112]. They represent the insertion of an A_0 field and a 3-gluon vertex in addition to the two electric insertions. In the modified NRQCD sector, this class of contribution includes three diagrams corresponding to insertion of the A_0 field between or outside the electric fields; in the left panel of Fig. 5.2, we display only one of the latter diagrams. In the pNRQCD sector, the structure is simplified with respect to the heavy quark case as only the octet state couples to Coulombic gluons; the A_0 insertion thus only occurs between the electric field insertions. This contribution to the transport coefficients, corresponding to diagram j of Refs. [108, 112], is shown in the right panel of Fig. 5.2. Calculations of fundamental κ in Refs. [105, 106] and adjoint κ in Ref. [3] show they agree up to order $g^5 T^3$. The authors of Ref. [112] calculated adjoint and fundamental γ and found a nonzero difference at order g^4 stemming from the class of diagrams shown in Fig. 5.2.

Intuitively, we understand these differences as originating from the gauge transformation properties of the state used to probe the medium. In pNRQCD, upon interaction with the chromoelectric field, the singlet state transitions to an octet state which transforms in the adjoint representation. As only the octet state couples to Coulombic gluons, the quarkonium state interacts with the A_0 field only between the electric field insertions, i.e., at times between 0 and t. The structure of $G_{\text{adj}}(t)$ reflects this. A single
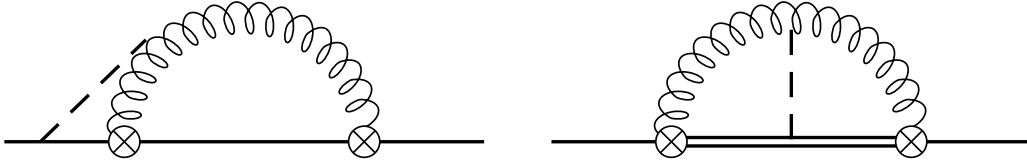
Figure 5.2: Diagrams of order g^4 in which the heavy quark (left) and heavy quarkonium (right) coefficients arise. Conventions are the same as in Fig. 5.1 with the dashed line additionally representing a Coulombic gluon.

heavy quark propagating in the medium transforms in the fundamental representation and couples to Coulombic gluons; it can, therefore, interact with a Coulombic gluon from the medium at any time. The structure of $G_{\text{fund}}(t)$ reflects this.

We note that as of the writing of this thesis, it remains a matter of active research precisely how the adjoint and fundamental transport coefficients arise from a first principles treatment of heavy probes of the QGP. We note that the adjoint versions of κ and γ arise naturally in a pNRQCD and OQS treatment of the in-medium evolution of heavy quarkonium; in this context, $G_{\text{adj}}(t)$ is the lowest order contribution to the quarkonium in-medium self energy in the pNRQCD finite temperature multipole expansion. However, in the heavy quark sector, the electric vertex of Eq. (5.17) remains an ad hoc addition to the NRQCD Lagrangian, and the origin of the path ordering prescription of $G_{\text{fund}}(t)$ less apparent than the time ordering prescription of $G_{\text{adj}}(t)$. We note that time ordering the dressed electric field $\tilde{E}_i^a(t)$ gives rise to an adjoint Wilson line, i.e.,

$$\text{T}\left(U_{ij}(-\infty, t)E_i^a(t)T_{jk}^a U_{kl}(t, \infty)\right) = E_i^a(t)U^{ab}(t, -\infty)T_{il}^b, \tag{5.18}$$

and similarly for anti time ordering

$$\tilde{\text{T}}\left(U_{ij}(-\infty, t)E_i^a(t)T_{jk}^a U_{kl}(t, \infty)\right) = T_{il}^b U^{ba}(-\infty, t)E_i^a(t). \tag{5.19}$$

This, together with the group property of the Wilson lines under time ordering

$$\text{T}\left(U_{ij}(t_1, t_2)U_{jk}(t_2, t_3)\right) = \text{T}\left(U_{ik}(t_1, t_3)\right), \tag{5.20}$$

implies that replacing the path ordering prescription in $G_{\text{fund}}(t)$ with a time ordering prescription yields $G_{\text{adj}}(t)$. This observation may be of use in the ongoing investigations into the nature of the adjoint and fundamental transport coefficients. Furthermore, we endeavor to place the NRQCD dipole vertex $\delta\mathcal{L}_{\text{int}}$ of Eq. (5.17) on a more solid theoretical basis in sec. 6.2 in which we perform a first principles treatment of a single heavy quark in-medium and investigate the circumstances under which its momentum evolution is described by a Langevin equation.

5.2 Fixing κ and γ

As shown in chapters 3 and 4, Refs. [28, 30] derived the in-medium evolution equations of heavy Coulombic quarkonium. In a strongly coupled medium of temperature $T \gg E$,

interactions with the medium are encoded in the transport coefficients κ and γ which we here identify with their adjoint versions in the sense of the previous section. In this limit, the in-medium heavy quarkonium self energy Σ_s (cf. Eq. (4.41)) is expressed in terms of κ and γ as

$$\Sigma_s = \frac{r^2}{2} \left(\kappa + i\gamma \right). \tag{5.21}$$

The projection of Eq. (5.21) onto eigenstates of the vacuum Hamiltonian gives κ and γ in terms of the in-medium width, mass shift and expectation value of the radius of the vacuum eigenstate. Using the $1S$ state, one finds

$$\Gamma(1S) = 3a_0^2 \kappa, \tag{5.22}$$

$$\delta M(1S) = \frac{3}{2} a_0^2 \gamma, \tag{5.23}$$

where $\Gamma(1S)$ and $\delta M(1S)$ are the in-medium width and mass shift, respectively, of the $1S$ state and a_0 is the Bohr radius. Via these relations, κ and γ are accessible from unquenched lattice measurements of $\Gamma(1S)$ and $\delta M(1S)$. In Ref. [33], Eqs. (5.22) and (5.23) were used to indirectly estimate κ and γ from unquenched lattice measurements of $\Gamma(1S)$ and $\delta M(1S)$ in the charm and bottom sectors. In Fig. 5.3, we plot these extractions and additional estimates using lattice data from measurements taken after publication of Ref. [33]. In the κ sector, we additionally include comparisons to extractions from direct, quenched lattice measurements, experimental measurements of the D-meson azimuthal anisotropy coefficient v_2, phenomenological models and perturbation theory calculations. In the γ sector, we include comparison to perturbation theory calculations.

To make use of Eqs. (5.22) and (5.23), we calculate the Bohr radius by solving its defining relation

$$a_0 = \frac{2}{C_f \alpha_s(1/a_0) M}, \tag{5.24}$$

with the 1-loop, 3-flavor running of the strong coupling and $\Lambda_{\text{QCD}} = 332$ MeV. Using the pole masses of $M = 1.67$ GeV and $M = 4.78$ GeV of the charm and bottom quarks, respectively, we have a Bohr radius of $a_0 = 1.19$ GeV^{-1} in the charm sector and $a_0 = 0.67$ GeV^{-1} in the bottom sector. In the left panel of Fig. 5.3, we display indirect estimates of κ obtained by inserting the measured in-medium widths of the $\Upsilon(1S)$ from Refs. [114–116] into Eq. (5.22). As these extractions utilize various values of the heavy quark mass, we normalize to the bottom and charm pole masses by rescaling the measured widths by $(m_b/(4.78 \text{ GeV}))^2$ and $(m_c/(1.67 \text{ GeV}))^2$ where $m_{b,c}$ represents the mass in GeV of the bottom, charm quark used in the respective lattice simulation. We note that although the transport coefficients are in principle independent of the heavy quark mass there be may a residual dependence due to truncations in the pNRQCD expansions underlying Eq. (5.21). We use the rescaled lower bound [117] of 22.3 MeV $\lesssim$ $\Gamma(\Upsilon(1S))$ measured in Ref. [114] at $T = 407$ MeV to place a lower bound on κ of $0.24 \lesssim \kappa/T^3$. We use the rescaled upper bound bound of $\Gamma(\Upsilon(1S)) \lesssim 481$ MeV measured in Ref. [115] at $T = 440$ MeV to place an upper bound on κ of $\kappa/T^3 \lesssim 4.2$. This range is
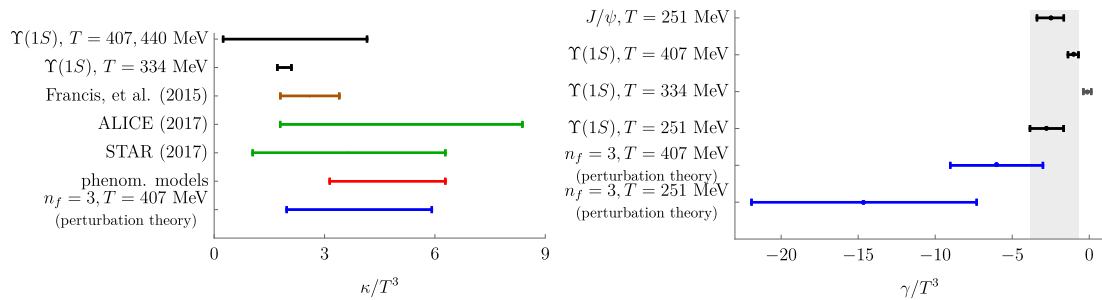
Figure 5.3: Estimates of the transport coefficients κ and γ. See the text for detailed explanations of the extractions and references. Adapted from Ref. [33].

displayed in the top row of Fig. 5.3. In the second row of Fig. 5.3, we display the estimate of κ extracted using the rescaled measurement of $\Gamma(\Upsilon(1S)) = (98 \pm 6)$ MeV measured in Ref. [116] at $T = 334$ MeV giving $\kappa/T^3 = 1.95 \pm 0.11$. In the γ sector, we perform a similar analysis using measurements of the in-medium mass shift of the $\Upsilon(1S)$ and J/ψ; as in the κ sector, we normalize the lattice measurements to the pole masses of the bottom and charm quark by rescaling the measured mass shifts by $(m_b/(4.78 \text{ GeV}))^2$ and $(m_c/(1.67 \text{ GeV}))^2$ where $m_{b,c}$ represents the mass in GeV of the bottom, charm quark used in the respective lattice simulation. We utilize the measurements of Ref. [114] of the in-medium mass shifts of the $\Upsilon(1S)$ at $T = 251$ MeV, the $\Upsilon(1S)$ at $T = 407$ MeV and the J/ψ at $T = 251$ MeV giving rescaled mass shifts of $\delta M = (-30 \pm 12)$ MeV, $\delta M = (-48 \pm 16)$ MeV and $\delta M = (-85 \pm 29)$ MeV, respectively. We also utilize the measurement of Ref. [116] of the in-medium mass shift of the $\Upsilon(1S)$ at $T = 334$ MeV giving a rescaled mass shift of $\delta M = (-3.21 \pm 6.42)$ MeV. The corresponding bounds on γ/T^3 are displayed as the black bars in Fig. 5.3. The gray band represents the range of the extractions from the measurements of Ref. [114].

In Fig. 5.3, we additionally include estimates of the transport coefficients κ and γ from other sources. The third row in the left panel (brown bar), gives the range $1.8 \lesssim \kappa/T^3 \lesssim 3.4$ obtained from the direct lattice measurement of Ref. [109] of the Euclidean correlator, corresponding to fundamental κ, defined in Ref. [107] in a quenched SU(3) lattice simulation at $T \approx 470$ MeV. The fourth and fifth rows present estimates of κ from measurements of the D meson azimuthal anisotropy coefficient v_2 by the ALICE [118] and STAR [119] collaborations. The ALICE collaboration compare their measurement of v_2 against a number of transport models [98, 99, 101, 120–126] and find that those describing the data have a heavy quark spatial diffusion coefficient D in the range $2\pi T D \approx 1.5 - 7$. The STAR collaboration compare their measurement of v_2 against the transport models of Refs. [95, 96, 101, 102, 127–134] and extract $2\pi T D$ in the range $2 - 12$. κ is estimated using the relation $\kappa/T^3 = 2/(DT)$ giving $1.8 \lesssim \kappa/T^3 \lesssim 8.4$ from the ALICE data and $1.0 \lesssim \kappa/T^3 \lesssim 6.3$ from the STAR data. The sixth row (blue bar) presents κ as extracted in Ref. [135] from the fitting of experimental observables, namely the nuclear modification factor R_{AA} and the elliptic flow v_2, in phenomenological

44

models to experimental data. The seventh row (blue bar) displays the results of the NLO perturbative calculation of Ref. [106]. This NLO result corresponds to Eq. (2.5) of Ref. [106] with the constant C set to $21/(8\pi)$ as discussed in the text. Evaluating this expression with the 1-loop, 3-flavor running of the strong coupling, $\Lambda_{\mathrm{QCD}} = 332$ MeV and the scale set at $\mu = \pi \times 407$ MeV yields a central value of $\kappa/T^3 = 3.94$; the bands represent 50% uncertainty. In the γ sector, in the right panel of Fig. 5.3, we show the leading order pertrubative expression for the thermal correction to the quarkonium mass calculated in Ref. [3]

$$\gamma = -3\zeta(3)C_f \frac{\alpha_s(\mu_T)}{\pi} T m_D^2 + \frac{4}{3}\zeta(3)N_c C_f \alpha_s^2(\mu_T)T^3, \qquad (5.25)$$

where ζ is the Riemann zeta function, $\mu_T = \pi T$, $m_D^2 = 4\pi\alpha_s(\mu_T)T^2(N_c + N_f/2)/3$ and $N_f = 3$ is the number of massless flavors. This relation (with the 1-loop, 3-flavor running of α_s with $\Lambda_{\mathrm{QCD}} = 332$ MeV) gives $\gamma/T^3 = -14.6$ and $\gamma = -6.0$ at $T = 251$ MeV and $T = 407$ MeV, respectively; these estimates are shown as the blue bars with 50% uncertainty.

Further lattice extractions of κ since the publication of Ref. [33] include the quenched SU(3) measurement of Ref. [110] in which the Euclidean discretization of κ given in Ref. [107] was measured over the temperature range $1.1 < T/T_c < 10^4$. We display the findings of Ref. [110] in the temperature range $1.1 < T/T_c < 7$ in Fig. 5.4. Additionally, the quenched SU(3) lattice measurement of Ref. [136] gives $2.31 \leq \kappa/T^3 \leq 3.70$ at $T \approx 1.5\,T_c$; the quenched SU(3) measurement of Ref. [111] gives a range of $1.70 \leq \kappa/T^3 \leq 3.12$ at $T = 1.5\,T_c$; and the quenched SU(3) measurement of Ref. [137] gives a range of $1.5 \leq \kappa/T^3 \leq 2.8$ at $T = 1.5\,T_c$. We note that the Euclidean correlators measured on the lattice correspond to fundamental κ. Refs. [111,136] utilize the gradient flow algorithm [138, 139] for noise reduction which may eventually enable unquenched lattice measurements of κ. Additionally, in Ref. [140], Bouttefeux and Laine identify higher order mass suppressed magnetic contributions to κ and propose a Euclidean discretization of the magnetic-magnetic correlator which was measured on the lattice in Refs. [111, 141].

In the $T \gg E$ limit, the in-medium evolution of heavy quarkonium in a strongly coupled QGP takes the form of a Lindblad equation. The interaction of the quarkonium with the medium is completely governed by the two transport coefficients κ and γ. Fixing their values is thus necessary to solve these equations and calculate observable quantities for comparison against experiment. As discussed above, κ in this context must be taken as the heavy quarkonium momentum diffusion coefficient and γ as its heavy quarkonium dispersive counterpart; both are related to the electric-electric correlator $G_{\mathrm{adj}}(t)$ defined in Eq. (5.13). In part III of this thesis, we present phenomenological results obtained by solving the Lindblad equation and take our dominant systematic uncertainty to be that inherited from from determinations of κ and γ. We quantify this uncertainty by performing simulations with values of γ/T^3 over the range of the gray band of Fig. 5.3 and with κ/T^3 as parametrized by the upper, central and lower curves of Fig. 5.4. In the γ sector, the explicit calculation of γ_{fund} and γ_{adj} performed in Ref. [112] shows a
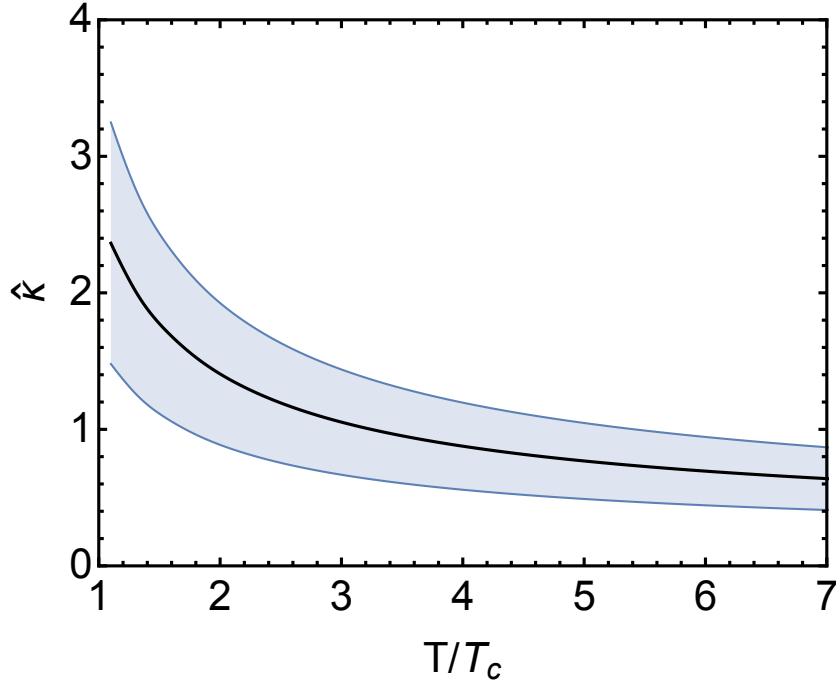
Figure 5.4: A pure SU(3) lattice measurement of the dimensionless quantity $\hat{\kappa} = \kappa/T^3$. In Ref. [110], a measurement was performed over the temperature range $1.1 < T/T_{\rm c} < 10^4$. The band represents statistical uncertainties and systematic uncertainties estimated by varying the scale of evaluation of the strong coupling by a factor of 2. Taken from Ref. [60].

nonzero difference between the quantities at order g^4. In the κ sector, $\kappa_{\rm fund}$ and $\kappa_{\rm adj}$ are equal up to order $g^5 T^3$; it remains unclear if this equality continues to higher orders. We note that the indirect lattice extractions of the heavy quarkonium momentum diffusion coefficient from lattice measurements of the heavy quarkonium thermal width overlap with the direct lattice measurements of the heavy quark momentum diffusion coefficient. We return to this point in more detail in our discussion of our theoretical uncertainties in chapter 9.

Chapter 6

Langevin dynamics of in-medium heavy particles

As discussed in chapter 5, the paradigm of Brownian motion described by Langevin equations has been used extensively in the literature to model the in-medium evolution of heavy quarks and heavy quarkonium. Due to the hierarchy of scales $M \gg T$ realized by heavy quarks and their bound states in current HIC experiments, the heavy probe is taken to undergo a random walk in the medium due to uncorrelated interactions with thermal medium particles. Such evolution is described by a Langevin equation

$$\frac{\mathrm{d}p_i}{\mathrm{d}t} = -\eta_D p_i + \xi_i(t), \quad \langle \xi_i(t)\xi_j(t') \rangle = \kappa \delta_{ij}\delta(t - t'), \tag{6.1}$$

where p_i is the momentum of the heavy particle, η_D is the drag coefficient, ξ_i encodes the changes to p_i due to interactions with the medium and κ is the momentum diffusion coefficient. In the heavy quark sector, κ has been an object of great interest in the literature [103–108, 110, 111]. In the seminal work of Ref. [104], Casalderrey-Solana and Teaney derive a field theoretic expression for κ describing the in-medium diffusion of heavy quarks in terms of a correlator of chromoelectric fields dressed with fundamental Wilson lines. As discussed in sec. 5.1, in the intervening years, interest has arisen in the heavy quarkonium momentum diffusion coefficient which takes the form of a correlator of chromoelectric fields connected by an adjoint Wilson line [112, 142]. In this chapter, we perform a first principles treatment of heavy quarkonium and heavy quarks in-medium and investigate the circumstances under which their dynamics are described by Langevin equations characterized by κ. In sec. 6.1, we work in the heavy quarkonium sector and in sec. 6.2 the single heavy quark sector.

6.1 Heavy quarkonium

In chapter 4 of this thesis, we derive the evolution equations of in-medium Coulombic quarkonium. In the strict $(\pi)T \gg E$ limit, the interactions with the medium are characterized by κ and its dispersive counterpart γ. Our procedure in this section follows

that of Blaizot and Escobedo who perform a similar calculation and analysis to that presented here using NRQCD, rather than pNRQCD, to describe the heavy quark-antiquark state [29]. The general procedure involves the inclusion of subleading terms in the E/T expansion which lead to diffusive dynamics. Working with the evolution equations at linear order in E/T, we extract the evolution equation for the steady state solution in a particular temperature regime. Wigner transforming this evolution equation leads to an equation for the time evolution of the Wigner quasi-probability distribution, the Wigner transform of the density matrix; this equation takes the form of a Fokker-Planck equation. We proceed to write the Langevin equations describing the momentum evolution of the heavy quarkonium state which correspond to the Fokker-Planck. In subsec. 6.1.1, we analyze the evolution equations in a lower temperature limit and show that they do not take the form of a Fokker-Planck equation with corresponding Langevin equation. In subsec. 6.1.2, we compare in greater detail our pNRQCD results to those of Blaizot and Escobedo from Ref. [29].

We begin with the set of coupled evolution equations given in Eqs. (4.32)-(4.38) and relax the strict $E \ll T$ limit. Specifically, we expand the exponentials of the form $e^{\pm i h_{s,o} s}$ and retain terms up to linear order (cf. the discussion under Eq. (4.38)). In this limit, electric correlators with additional factors of the temporal variable arise; we make use of the relation

$$i \frac{g^2}{6 N_c} \int_0^\infty \mathrm{d}t\, t \Big\langle \tilde{E}_i^a(t, \mathbf{0}) \tilde{E}_i^a(0, \mathbf{0}) \Big\rangle = \frac{\kappa}{4T}, \qquad (6.2)$$

which we present here but the derivation of which we postpone to subsec. 9.1.1. Working with the evolution equations expanded to order E/T and the electric correlators expressed in terms of κ and γ, we perform a Wigner transform to arrive at an evolution equation for the Wigner quasi-probability distribution in the form of a Fokker-Planck equation with corresponding Langevin equations. The Wigner quasi-probability distribution is defined as

$$\tilde{\rho}(t, \mathbf{r}_+, \mathbf{p}) = \int d^3 r_- e^{-i \mathbf{p} \cdot \mathbf{r}_-} \left\langle \mathbf{r}_+ + \tfrac{\mathbf{r}_-}{2} \right| \rho(t) \left| \mathbf{r}_+ - \tfrac{\mathbf{r}_-}{2} \right\rangle, \qquad (6.3)$$

where the bras and kets represent eigenstates of the radius of the quarkonium. We define the coordinates $\mathbf{r}_+$ and $\mathbf{r}_-$

$$\mathbf{r}_+ = \frac{\mathbf{r} + \mathbf{r}'}{2}, \quad \mathbf{r}_- = \mathbf{r} - \mathbf{r}', \qquad (6.4)$$

such that

$$\mathbf{r} = \mathbf{r}_+ + \frac{\mathbf{r}_-}{2}, \quad \mathbf{r}' = \mathbf{r}_+ - \frac{\mathbf{r}_-}{2}. \qquad (6.5)$$

We interpret $\mathbf{r}$ and $\mathbf{r}'$ as the radius of the quarkonium before and after interaction with the medium and $\mathbf{r}_+$ and $\mathbf{r}_-$ as the average and change of radius during the interaction, respectively. The projection onto $\langle \mathbf{r}|$ and $|\mathbf{r}'\rangle$ thus represents a projection onto the off-diagonal elements of the density matrix. Under this projection, the terms of the

evolution equations take the form

$$i\langle\mathbf{r}|[\rho_{s,o}(t),h_{s,o}]|\mathbf{r}'\rangle = \left[\frac{2i}{M}\nabla_+\nabla_- - i\mathbf{r}_-\cdot\nabla V_{s,o}\right]\rho_{s,o}^{\mathbf{rr}'}(t), \tag{6.6}$$

$$\langle\mathbf{r}|\left(\Sigma_s\rho_s(t)+\rho_s(t)\Sigma_s^\dagger\right)|\mathbf{r}'\rangle = \left\{\kappa\,\mathcal{A}_+^{LO}\left(1+\frac{\Delta V_{so}}{2T}\right)+i\gamma\,\mathbf{r}_+\cdot\mathbf{r}_-\right.$$
$$\left.+\frac{\kappa}{2MT}\mathcal{A}_+^{NLO}\right\}\rho_s^{\mathbf{rr}'}(t), \tag{6.7}$$

$$\langle\mathbf{r}|\left(\Sigma_o\rho_o(t)+\rho_o(t)\Sigma_o^\dagger\right)|\mathbf{r}'\rangle = \left\{\kappa\,\mathcal{A}_+^{LO}\left(\frac{N_c^2-2}{2}-\frac{\Delta V_{so}}{2T}\right)+i\gamma\,\mathbf{r}_+\cdot\mathbf{r}_-\right.$$
$$\left.+\frac{\kappa}{2MT}\mathcal{A}_+^{NLO}\frac{N_c^2-2}{2}\right\}\frac{\rho_o^{\mathbf{rr}'}(t)}{N_c^2-1}, \tag{6.8}$$

$$\langle\mathbf{r}|\Xi_{so}(\rho_o(t))|\mathbf{r}'\rangle = \left\{\kappa\,\mathcal{A}_-^{LO}\left(1-\frac{\Delta V_{so}}{2T}\right)+\frac{\kappa}{2MT}\mathcal{A}_-^{NLO}\right\}\frac{\rho_o^{\mathbf{rr}'}(t)}{N_c^2-1}, \tag{6.9}$$

$$\langle\mathbf{r}|\Xi_{os}(\rho_s(t))|\mathbf{r}'\rangle = \left\{\kappa\,\mathcal{A}_-^{LO}\left(1+\frac{\Delta V_{so}}{2T}\right)+\frac{\kappa}{2MT}\mathcal{A}_-^{NLO}\right\}\rho_s^{\mathbf{rr}'}(t), \tag{6.10}$$

$$\langle\mathbf{r}|\Xi_{oo}(\rho_o(t))|\mathbf{r}'\rangle = \left\{\kappa\,\mathcal{A}_-^{LO}+\frac{\kappa}{2MT}\mathcal{A}_-^{NLO}\right\}\frac{N_c^2-4}{2\left(N_c^2-1\right)}\rho_o^{\mathbf{rr}'}(t), \tag{6.11}$$

where

$$\mathcal{A}_\pm^{LO} = \left(\mathbf{r}_+^2\pm\frac{\mathbf{r}_-^2}{4}\right), \quad \mathcal{A}_\pm^{NLO} = \mathbf{r}_+\cdot\nabla_+\pm\mathbf{r}_-\cdot\nabla_-, \tag{6.12}$$

$\rho_{s,o}^{\mathbf{rr}'}(t) = \langle\mathbf{r}|\rho_{s,o}(t)|\mathbf{r}'\rangle$ and $\Delta V_{so} = V_s - V_o$. All potentials in the above equations are expanded in $\mathbf{r}_-$ and evaluated at $|\mathbf{r}_+|$. In the following, we discuss the power counting of the terms appearing in the above equations thus justifying the expansion in $\mathbf{r}_-$.

Our underlying EFT description of the system allows us to assign a power counting to the terms appearing in the above evolution equations. The state is Coulombic constraining its radius to be of order $1/\sqrt{EM}$. Therefore, r^+ and ∇_+ scale as:

$$r^+ \sim \frac{1}{\sqrt{EM}}, \quad \nabla_+ \sim \sqrt{EM}. \tag{6.13}$$

The singlet and octet potentials and, therefore, their difference scale as the binding energy:

$$V_{s,o},\,\Delta V_{so} \sim E. \tag{6.14}$$

Derivatives acting on the potential scale as the heavy-quark momentum; in terms of the binding energy and the heavy quark mass, this gives

$$\nabla V_{s,o} \sim p\,E = \sqrt{EM}\,E. \tag{6.15}$$

κ and γ are thermal quantities of dimension mass to the third; we, therefore, take them to scale as the thermal scale to the third

$$\kappa,\,\gamma \sim ((\pi)T)^3 \tag{6.16}$$

49

quantity	r^+	r^-	∇_+	∇_-	$V_{s,o}(r^+),\ \Delta V(r^+)$	$\nabla V_{s,o}(r^+)$	$\kappa,\ \gamma$
scaling	$\frac{1}{\sqrt{EM}}$	$\frac{1}{\sqrt{\pi TM}}$	$\sqrt{EM}$	$\sqrt{\pi TM}$	E	$\sqrt{EME}$	$(\pi T)^3$

Table 6.1: Scaling of quantities appearing in the evolution equations with respect to the relevant scales in our effective field theory framework.

Consistent with the Langevin picture, we assume the interactions of the quarkonium with the medium to drive the state to thermalization such that its energy is of order πT and its momentum of order $\sqrt{\pi TM}$

$$r^- \sim \frac{1}{\sqrt{\pi TM}}, \quad \nabla_- \sim \sqrt{\pi TM}. \tag{6.17}$$

The information of Eqs. (6.13)–(6.17) is collected in Tab. 6.1.

We assume the state to be Coulombic such that the hierarchy

$$\frac{1}{a_0} \gg \pi T, \Lambda_{\text{QCD}}, \tag{6.18}$$

is realized. The Bohr radius a_0 is given by solving its defining relation

$$a_0 = \frac{2}{MC_f \alpha_s(1/a_0)}, \tag{6.19}$$

with the strong coupling evaluated at the inverse of the Bohr radius. We use the 1-loop, 3-flavor running of the strong coupling with the 3-flavor $\overline{\text{MS}}$ value of $\Lambda_{\text{QCD}} = 332$ MeV [143]. In the bottom sector, we use the pole mass of $M_b = 4.78$ GeV [143] giving $1/a_0 \approx 1.5$ GeV for the $\Upsilon(1S)$. The hierarchy of scales of Eq. (6.18) thus constrains $T \lesssim 473$ MeV. Using these values of the heavy quark mass and the Bohr radius, we compute a Coulombic binding energy of the $\Upsilon(1S)$ as

$$|E| = \frac{1}{Ma_0^2} = 461 \text{ MeV}. \tag{6.20}$$

Following the same procedure in the charm sector using the pole mass of $M_c = 1.67$ GeV [143], we find an inverse Bohr radius of $1/a_0 = 0.839$ GeV and a binding of energy of $|E| = 421$ MeV for the J/ψ. We collect this information in 6.2.

The hierarchy of scales

$$M \gg \pi T \gg E, \tag{6.21}$$

provides two small dimensionless quantities in which we can expand, namely $E/(\pi T)$ and $(\pi T)/M$. In order to proceed, we must establish a hierarchy between these quantities. In the following analysis, we take $E/(\pi T) \sim (\pi T)/M$ which is true to an excellent degree of accuracy for bottomonium in the early stages of central collisions; at temperatures $T \approx 475$ MeV, this statement is nearly exact. In Fig. 6.1, we plot the quantities $E/(\pi T)$ and $(\pi T)/M$ and in the bottom and charm sectors with Bjorken temperature evolution

$$T = T_0 \left(\frac{t_0}{t}\right)^{v_s^2}, \tag{6.22}$$

quantity	M	$1/a_0$	πT	$|E|$
bottomonium	4.80 GeV	1.49 GeV	(π)0.473 GeV	0.461 GeV
charmonium	1.67 GeV	0.839 GeV	(π)0.267 GeV	0.421 GeV

Table 6.2: Values of the relevant effective field theoretical quantities for bottomonium and charmonium. πT is the temperature less than which the Coulombic assumption for the in-medium bound state is valid (c.f. Eq. (6.18)). Furthermore, from the definition of the Coulombic binding energy E given in Eq. (6.20), we note that this is also the temperature at which $E/(\pi T) = (\pi T)/M$.
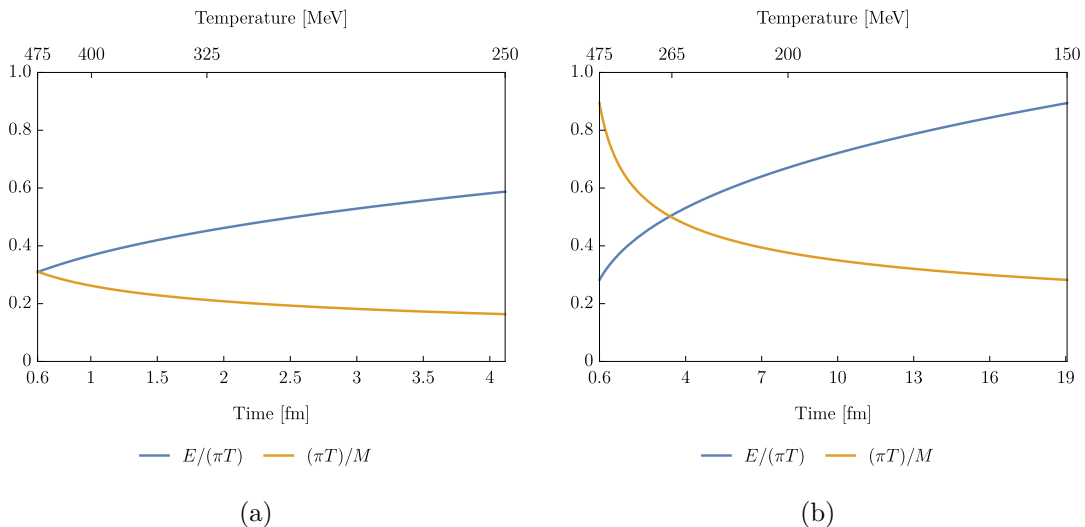

Figure 6.1: Evolution of the effective field theory hierarchies in the bottom (a) and charm (b) sectors using Bjorken evolution: Eq. (6.22) with $T_0 = 475$ MeV, $t_0 = 0.6$ fm and $v_s^2 = 1/3$.

where $T_0 = 475$ MeV is the initial temperature of the medium, $t_0 = 0.6$ fm is the initial time and $v_s^2 = 1/3$ is the square of the velocity of sound in the medium. In the bottom sector, we observe $E/(\pi T) = (\pi T)/M$ to be nearly exactly 1 at time $t = 0.6$ fm. We denote the square root of the resulting small number ϵ, i.e., $\epsilon \sim \sqrt{E/(\pi T)} \sim \sqrt{(\pi T)/M}$. This hierarchy is of interest in analyzing the projected evolution equations to derive a Langevin equation, as we show below; we note, however, that this temperature regime is precisely the region in which $\pi T \sim 1/a_0$ and the multipole expansion may break down.

With this power counting, the dominant terms of the evolution equations are proportional to $r_+^2 \kappa$ and are of order πT. In matrix form, the coupled set of evolution equations reduces to

$$\frac{d}{dt}\begin{pmatrix} \rho_s^{\mathbf{rr'}} \\ \rho_o^{\mathbf{rr'}} \end{pmatrix} = \left\{ \begin{pmatrix} -r_+^2\kappa & \frac{1}{N_c^2-1}r_+^2\kappa \\ r_+^2\kappa & -\frac{1}{N_c^2-1}r_+^2\kappa \end{pmatrix} + \mathcal{O}(\pi T\epsilon) \right\} \begin{pmatrix} \rho_s^{\mathbf{rr'}} \\ \rho_o^{\mathbf{rr'}} \end{pmatrix}. \tag{6.23}$$

The above equations describe a quarkonium state transitioning between singlet and

octet color configurations with decay widths $\Gamma_{s\to o} = r_+^2 \kappa$ and $\Gamma_{o\to s} = r_+^2 \kappa/(N_c^2 - 1)$. We examine the steady state solution of this evolution equation via diagonalization of the evolution matrix. Its eigenvalues are

$$\{\lambda_0, \lambda_8\} = \left\{0, -r_+^2 \kappa \frac{N_c^2}{N_c^2 - 1}\right\}, \tag{6.24}$$

where the negative eigenvalue λ_8 describes the evolution of a state decaying with width $\Gamma = r_+^2 \kappa N_c^2/(N_c^2 - 1)$ and the 0 eigenvalue λ_0 describes the evolution of the steady state solution. We diagonalize the evolution equations and work in this new diagonal basis which we denote ρ_0 and ρ_8 given in terms of ρ_s and ρ_o as

$$\rho_0 = \frac{\rho_s + \rho_o}{N_c^2}, \quad \rho_8 = \frac{(N_c^2 - 1)\rho_s - \rho_o}{N_c^2}. \tag{6.25}$$

Projecting ρ_0 onto singlet and octet states, one observes that the steady state solution is equally likely to be in a color singlet or any specific octet color configuration.

Following the procedure of Blaizot and Escobedo, we proceed by including corrections in ϵ. The evolution equations now take the form

$$\frac{d}{dt}\begin{pmatrix} \rho_0^{\mathbf{rr}'} \\ \rho_8^{\mathbf{rr}'} \end{pmatrix} = \left\{ \begin{pmatrix} \ell_{00}^{(1)} + \ell_{00}^{(2)} & \ell_{08}^{(1)} + \ell_{08}^{(2)} \\ \ell_{80}^{(1)} + \ell_{80}^{(2)} & \lambda_8 + \ell_{88}^{(1)} + \ell_{88}^{(2)} \end{pmatrix} + \mathcal{O}(\pi T \epsilon^3) \right\} \begin{pmatrix} \rho_0^{\mathbf{rr}'} \\ \rho_8^{\mathbf{rr}'} \end{pmatrix}, \tag{6.26}$$

where the superscripts in parenthesis represent the degree of suppression in ϵ with respect to λ_8 and the subscripts represent the quadrant of the matrix. These terms are given explicitly by

$$\ell_{00}^{(1)} = \frac{2i}{M}\nabla_+ \cdot \nabla_- - \frac{i}{2}\mathbf{r}_+ \cdot \mathbf{r}_- \gamma, \tag{6.27}$$

$$\ell_{00}^{(2)} = -\kappa \left(\frac{\mathbf{r}_- \cdot \nabla_-}{2MT} + \frac{\mathbf{r}_-^2}{4} \right), \tag{6.28}$$

$$\ell_{08}^{(1)} = -\frac{1}{N_c^2 - 1}\frac{i}{2}\mathbf{r}_+ \cdot \mathbf{r}_- \gamma, \tag{6.29}$$

$$\ell_{80}^{(1)} = -\frac{i}{2}\mathbf{r}_+ \cdot \mathbf{r}_- \gamma, \tag{6.30}$$

$$\ell_{88}^{(0)} = -\frac{N_c^2}{N_c^2 - 1}\mathbf{r}_+^2 \kappa. \tag{6.31}$$

We diagonalize Eq. (6.26) and denote its eigenvalues, which reduce to $\lambda_{0,8}$ in the $\epsilon \to 0$ limit, $\lambda'_{0,8}$; λ'_0 is given by

$$\lambda'_0 = \ell_{00}^{(1)} + \ell_{00}^{(2)} - \frac{\ell_{08}^{(1)} \ell_{80}^{(1)}}{\ell_{88}^{(0)}} + \mathcal{O}\left(\pi T \epsilon^3\right). \tag{6.32}$$

We complete the Wigner transform by Fourier transforming the evolution equation specified by λ'_0

$$\frac{d}{dt}\rho_0'^{\mathbf{rr}'}(t) = \lambda'_0\, \rho_0'^{\mathbf{rr}'}(t). \tag{6.33}$$

52

where $\rho_0'^{\mathbf{rr}'}(t)$ is the state evolved by λ_0'. This gives the Fokker-Planck equation

$$\left(\frac{\partial}{\partial t} + \mathbf{v} \cdot \nabla_+\right)\tilde{\rho}_0(t) = \left[\frac{\kappa}{4}\nabla_{\mathbf{p}}^2 + \frac{M}{2}\eta\nabla_{\mathbf{p}}\cdot\mathbf{v} + \frac{\gamma}{2}\mathbf{r}_+\cdot\nabla_{\mathbf{p}} + \left(\frac{\gamma}{\sqrt{\kappa}}\frac{\mathbf{r}_+\cdot\nabla_{\mathbf{p}}}{2N_c|\mathbf{r}_+|}\right)^2\right]\tilde{\rho}_0(t),$$

(6.34)

where $\tilde{\rho}_0(t)$ is the Wigner quasi-probability distribution and the Fourier transform of $\rho_0'^{\mathbf{rr}'}(t)$, $\mathbf{v} = 2\mathbf{p}/M$ is the velocity and the drag coefficient η is related to the momentum diffusion coefficient κ via the Einstein relation

$$\eta = \frac{\kappa}{2MT}.$$

(6.35)

Eq. (6.34) describes the evolution of the Wigner quasi-probability distribtuion; the corresponding Langevin equation for the momentum evolution is given by

$$\frac{\mathrm{d}r_i^+}{\mathrm{d}t} = \frac{2p_i}{M}, \quad \frac{M}{2}\frac{\mathrm{d}^2 r_i^+}{\mathrm{d}t^2} = -F_i(\mathbf{r}^+) - \eta_{ij}p_j + \xi_i(t,\mathbf{r}^+) + \theta_i(t,\mathbf{r}^+).$$

(6.36)

where

$$F_i(\mathbf{r}^+) = -\gamma\frac{r_i^+}{2},$$

(6.37)

$$\langle\theta_i(t,\mathbf{r}^+)\theta_j(t',\mathbf{r}^+)\rangle = \delta(t-t')\frac{r_i^+ r_j^+ \gamma^2}{4N_c^2\kappa\, r_+^2},$$

(6.38)

$$\langle\xi_i(t,\mathbf{r}^+)\xi_j(t',\mathbf{r}^+)\rangle = \delta(t-t')\delta_{ij}\,\kappa,$$

(6.39)

$$\eta_{ij}(\mathbf{r}^+) = \frac{\kappa}{2MT}\delta_{ij}.$$

(6.40)

We observe a similar form to the Langevin equation presented in the introduction to this chapter with a number of additional terms. As in the standard case, the momentum evolution contains a drag term proportional to the drag coefficient η_{ij} and a random force term ξ_i related to the uncorrelated interactions with the medium. The force-force correlator of Eq. (6.39) defines the momentum diffusion coefficient κ which is related to the drag coefficient η by the Einstein relation of Eq. (6.40). The Langevin equation of Eq. (6.36) contains the additional force terms θ_i and F_i not present in the standard Langevin equation. θ_i represents a second random force due to the fluctuating of the force between the quark and the antiquark originating from the difference in sign of the singlet and octet potential. F_i represents an additional force proportional to the transport coefficient γ. As discussed in chapter 5, γ is a correction to the quark-antiquark potential due to the in-medium mass shift of the heavy quarkonium state. The exact origin and interpretation of this term are under active investigation at the time of the writing of this thesis.

6.1.1 The regime $E/(\pi T) > (\pi T)/M$

The above analysis assumes a temperature T of the medium such that $E/(\pi T) \sim (\pi T)/M$ is realized. This is true to an excellent degree of accuracy in the bottomonium sector in the early stages of central lead-lead collisions (cf. Figs (6.1) and (B.1)).

However, the medium rapidly expands and cools such that $E/(\pi T) > (\pi T)/M$. In Refs. [60, 61], the Lindblad equation derived in the strict $E \ll (\pi)T$ limit was solved terminating the medium evolution at $T_f = 250$ MeV in order to not evolve the evolution equations outside their range of validity. At this temperature, $E/(\pi T) = 0.587$ and $(\pi T)/M = 0.164$, and the power counting is more accurately $(E/(\pi T))^3 \sim (\pi T)/M$ rather than $(E/(\pi T)) \sim (\pi T)/M$. In this section, we analyze the projected evolution equations specified in Eqs. (6.6)-(6.11) with this power counting. We denote the small quantity $\epsilon' \sim \sqrt{E/(\pi T)}$.

In this regime, the kinetic and potential terms

$$\frac{2i}{M}\nabla_+\nabla_- \sim \sqrt{E(\pi T)}, \; ir_-\nabla V_{s,o}(r_+) \sim \sqrt{E(\pi T)}\epsilon'^2, \tag{6.41}$$

dominate rather than medium interaction terms as in Eq. (6.23). Relative to these contributions, the leading order medium evolution is suppressed by an additional factor of ϵ'

$$r_+^2\kappa \sim \sqrt{E(\pi T)}\epsilon'^3. \tag{6.42}$$

The evolution equations take the form

$$\frac{d}{dt}\begin{pmatrix}\rho_s\\\rho_o\end{pmatrix} = \left\{\begin{pmatrix}h'_s - r_+^2\kappa & \frac{1}{N_c^2-1}r_+^2\kappa\\r_+^2\kappa & h_o - \frac{1}{N_c^2-1}r_+^2\kappa\end{pmatrix} + \mathcal{O}\left(\sqrt{E(\pi T)}\epsilon'^4\right)\right\}\begin{pmatrix}\rho_s\\\rho_o\end{pmatrix}, \tag{6.43}$$

where $h'_{s,o} = (2i/M)\nabla_+\cdot\nabla_- - i\mathbf{r}_-\cdot\nabla V_{s,o}(r_+)$.

The eigenvalues of the evolution matrix are

$$\{\lambda_s, \lambda_o\} = \left\{h'_s - r_+^2\kappa, \; h'_o - \frac{1}{N_c^2-1}r_+^2\kappa\right\} + \mathcal{O}\left(\sqrt{E(\pi T)}\epsilon'^4\right). \tag{6.44}$$

In contrast to the higher temperature case $E/(\pi T) \sim (\pi T)/M$, in the lower temperature regime considered in this subsection, the vacuum dynamics of the quarkonium dominate, and medium interactions represent subleading corrections. The eigenstates of this evolution are to leading order the singlet and octet states of vacuum pNRQCD, and the system is no longer driven to the steady state solution ρ_0 as in the higher temperature regime. Furthermore, in this scale hierarchy, which we note is consistent with the multipole expansion and is fulfilled for the majority of the evolution time in a heavy ion collision (cf. the left panel of Fig. 6.1), we do not find the evolution equations to be related to a Fokker-Plank equation with corresponding Langevin equation.

6.1.2 NRQCD in the quark-antiquark sector

A similar calculation is carried out in Ref. [29] using an NRQCD rather than pNRQCD description of the heavy-heavy bound state. We present here a derivation of the NRQCD Lagrangian describing a heavy quark and a heavy antiquark which gives rise to their Langevin equation.

The evolution equations in Ref. [29] can be derived by projecting NRQCD onto the subspace of a heavy quark and a heavy antiquark in the Coulomb gauge at order g in the coupling and order Mv^2 in the expansion in the heavy quark velocity

$$L_{NRQCD}^{Q\bar{Q}} = \int d^3\mathbf{x}_1 d^3\mathbf{x}_2 \text{Tr}\left[\Psi^\dagger(t,\mathbf{x}_1,\mathbf{x}_2)\left(iD_0 + \frac{\nabla_{\mathbf{x}_1}^2 + \nabla_{\mathbf{x}_2}^2}{2m} \right)\Psi(t,\mathbf{x}_1,\mathbf{x}_2) \right], \quad (6.45)$$

where $\Psi(t,\mathbf{x}_1,\mathbf{x}_2)$ is a composite field describing a heavy quark at $\mathbf{x}_1$ and a heavy antiquark at $\mathbf{x}_2$ and the covariant derivative acts as

$$iD_0\Psi(t,\mathbf{x}_1,\mathbf{x}_2) = i\partial_0\Psi(t,\mathbf{x}_1,\mathbf{x}_2) - gA_0(t,\mathbf{x}_1)\Psi(t,\mathbf{x}_1,\mathbf{x}_2) + \Psi(t,\mathbf{x}_1,\mathbf{x}_2)gA_0(t,\mathbf{x}_2). \quad (6.46)$$

Ψ can be uniquely decomposed into singlet and octet fields S and O as

$$\begin{aligned} \Psi(t,\mathbf{x}_1,\mathbf{x}_2) =& \text{P} \exp\left[ig\int_{\mathbf{x}_2}^{\mathbf{x}_2} d\mathbf{x}\cdot\mathbf{A}(t,\mathbf{x}) \right] \text{S}(t,\mathbf{r},\mathbf{R}) \\ &+ \text{P} \exp\left[ig\int_{\mathbf{R}}^{\mathbf{x}_1} d\mathbf{x}\cdot\mathbf{A}(t,\mathbf{x}) \right] \text{O}(t,\mathbf{r},\mathbf{R})\, \text{P} \exp\left[ig\int_{\mathbf{x}_2}^{\mathbf{R}} d\mathbf{x}\cdot\mathbf{A}(t,\mathbf{x}) \right], \end{aligned} \quad (6.47)$$

where $\mathbf{R} = (\mathbf{x}_1 + \mathbf{x}_2)/2$ is the center of mass coordinate, $\mathbf{r} = \mathbf{x}_1 - \mathbf{x}_1$ is the heavy quarkonium radius and the octet field transforms under gauge transformations as $\text{O}(t,\mathbf{x}_1,\mathbf{x}_2) \to g(t,\mathbf{R})\text{O}(t,\mathbf{x}_1,\mathbf{x}_2)g^{-1}(t,\mathbf{R})$. Inserting Eq. (6.47) at order 0 in the coupling, i.e., $\Psi(t,\mathbf{x}_1,\mathbf{x}_2) = \text{S}(t,\mathbf{x}_1,\mathbf{x}_2) + \text{O}(t,\mathbf{x}_1,\mathbf{x}_2)$, into Eq. (6.45), we write the NRQCD Lagrangian density as

$$\begin{aligned} L_{NRQCD}^{Q\bar{Q}} =& \int d^3\mathbf{x}_1 d^3\mathbf{x}_2 \text{Tr}\Bigg[\text{S}^\dagger\left(i\partial_0 + \frac{\nabla_{\mathbf{x}_1}^2 + \nabla_{\mathbf{x}_2}^2}{2m} \right)\text{S} \\ &+ \text{O}^\dagger\left(iD_0 + \frac{\nabla_{\mathbf{x}_1}^2 + \nabla_{\mathbf{x}_2}^2}{2m} \right)\text{O} - \text{S}^\dagger g\Big(A_0(t,\mathbf{x}_1)\text{O} - \text{O}A_0(t,\mathbf{x}_2) \Big) \\ &- \text{O}^\dagger g\Big(A_0(\mathbf{x}_1) - A_0(\mathbf{x}_2) \Big)\text{S} \Bigg], \end{aligned} \quad (6.48)$$

where the singlet and octet fields are functions of the time t and the heavy quark and antiquark positions $\mathbf{x}_1$ and $\mathbf{x}_2$ and the covariant derivative acts on the octet field as

$$iD_0\, \text{O}(t,\mathbf{x}_1,\mathbf{x}_2) = i\partial_0 \text{O}(t,\mathbf{x}_1,\mathbf{x}_2) - gA_0(t,\mathbf{x}_1)\text{O}(t,\mathbf{x}_1,\mathbf{x}_2) + \text{O}(t,\mathbf{x}_1,\mathbf{x}_2)A_0(t,\mathbf{x}_2). \quad (6.49)$$

Eq. (6.48) represents NRQCD in the Coulomb gauge in the heavy quark-antiquark sector in terms of the singlet and octet fields up to order g in the coupling and order Mv^2 in the velocity expansion.

Performing the analysis carried out above with the Lagrangian of Eq. (6.48) rather than that of resummed pNRQCD gives rise to the Fokker-Planck equation

$$\begin{aligned} \frac{d\tilde{\rho}_0(t)}{dt} =& \Bigg(-\frac{2\mathbf{p}\cdot\nabla_\mathbf{r}}{M} + \frac{C_f}{4}\nabla_\mathbf{p}\cdot\mathcal{H}(0)\cdot\nabla_\mathbf{p} + \frac{C_f\,(\mathbf{F}(\mathbf{r})\cdot\nabla_\mathbf{p})^2}{2N_c^2\Gamma(\mathbf{r})} \\ &+ \frac{C_f}{2MT}\nabla_\mathbf{p}\cdot\mathcal{H}(0)\cdot\mathbf{p} \Bigg)\tilde{\rho}_0(t), \end{aligned} \quad (6.50)$$

with corresponding Langevin equation

$$\frac{M}{2}\ddot{r}_i = -\frac{\eta_{ij}}{2T}v_j + \xi_i(t) + \Theta_i(t,\mathbf{r}),$$ (6.51)

where $v_i = 2p_i/M$ is the velocity and

$$\langle \xi_i(t)\xi_j(t')\rangle = \delta(t-t')\eta_{ij},$$ (6.52)

$$\eta_{ij} = \frac{C_f}{2}\mathcal{H}_{ij}(0),$$ (6.53)

$$\langle \Theta_i(t,\mathbf{r})\Theta_j(t',\mathbf{r})\rangle = \delta(t-t')\frac{C_f F_i(\mathbf{r})F_j(\mathbf{r})}{N_c^2\Gamma(\mathbf{r})},$$ (6.54)

where in the notation of Ref. [29] $\mathbf{r}$ is equivalent to our $\mathbf{r}_+$. The integral of the correlator of the Coulombic gluons is decomposed into real and imaginary parts

$$\int_0^\infty dt \, \langle A_0(t,\mathbf{x})A_0(0,\mathbf{x}')\rangle = \frac{i}{2}V(\mathbf{x}-\mathbf{x}') - \frac{1}{2}W(\mathbf{x}-\mathbf{x}').$$ (6.55)

Furthermore, the small $\mathbf{r}_- = \mathbf{r} - \mathbf{r}'$ expansion is implemented using the notation

$$\mathcal{H}_{ij}(\mathbf{r}_-) = \frac{\partial^2 W(\mathbf{r}_-)}{\partial r_i^- \partial r_j^-},$$ (6.56)

$$\Gamma(\mathbf{r}) = W(\mathbf{r}) - W(\mathbf{0}),$$ (6.57)

$$\mathbf{F}(\mathbf{r}) = \nabla V(\mathbf{r}).$$ (6.58)

We observe a number of features in common between the pNRQCD Langevin equation given in Eq. (6.36) and that of Blaizot and Escobedo, namely the presence of the fluctuating force Θ_i due to singlet-octet transitions which change the sign of the quark-antiquark potential and hence the direction of the force between the pair. We note the absence of the additional force proportional to γ present in the pNRQCD case. Placing this correspondence on a more quantitative footing is a subject of active research at the time of the writing of this thesis.

6.2 Single heavy quark

In this section, we apply a similar analysis to that of the previous section in the case of a single heavy quark. Our objective is the derivation of a Langevin equation describing the in-medium diffusion of a single heavy quark characterized by the heavy quark momentum diffusion coefficient κ in its electric-electric correlator form. In Ref. [29], Blaizot and Escobedo carry out a similar analysis using NRQCD; they derive a Langevin equation with the force-force correlator related to the correlator of Coulombic gluons (cf. Eqs (6.52), (6.53), (6.55) and 6.56)).

6.2.1 Ultrasoft NRQCD

We aim to describe a heavy quark of mass M in a thermal medium of temperature T where $M \gg T$. As the quark is heavy, we treat its interaction with the medium using non-relativistic QCD (NRQCD). Our starting point is the NRQCD Lagrangian:

$$\mathcal{L}_{\text{NRQCD}} = \psi^\dagger \left(iD_0 + \frac{\mathbf{D}^2}{2M} \right) \psi, \tag{6.59}$$

where $iD_0 = i\partial_0 - gA_0$ and $i\mathbf{D} = i\nabla + g\mathbf{A}$; we note that all fields are functions of the spatial coordinate $\mathbf{x}$ and temporal coordinate t unless explicitly noted otherwise. The Lagrangian of Eq. (6.59) is gauge invariant and contains the lowest order terms in the velocity expansion: $i\partial_0$ and $\nabla^2/(2M)$, both of order Mv^2. In heavy-heavy bound states described by pNRQCD, the system naturally possesses a momentum scale associated with the center of mass $\nabla_{\mathbf{R}} \sim Mv^2$ and with the radius $\nabla_{\mathbf{r}} \sim Mv$. As the system is nonrelativistic, v and hence the radius $\mathbf{r}$ are small, and pNRQCD implements an expansion $\mathbf{r}$ at the Lagrangian level. Furthermore, the ultrasoft gauge fields of wavelength $\sim 1/Mv^2$ do not resolve the radius of the quarkonium $\sim 1/Mv$.

In the case of a single heavy quark in medium, such a scale hierarchy is lacking without additional assumptions. In order to perform a similar set of manipulations as in the case of pNRQCD, we assume the quark to be propagating with a velocity v distinct from the thermal velocity $v_T \sim \sqrt{T/M}$. In order to assign a specific power counting to the gauge fields in the NRQCD Lagrangian and isolate contributions from thermal gluons at the scale $T \sim Mv_T^2$, we introduce the coordinate $|\mathbf{r}| \sim 1/(Mv_T) \sim 1/\sqrt{MT}$. We decompose the coordinate $\mathbf{x}$ as $\mathbf{x} = \mathbf{R} + \mathbf{r}$ and interpret $\mathbf{R}$ as the initial position of the quark; in this context, $\mathbf{r}$ represents displacement due to thermal fluctuations on the order of $|\mathbf{r}| \sim 1/Mv_T$ not resolved by thermal gluons of momentum transfer Mv_T^2. We multipole expand the gauge field to isolate contributions from thermal gluons at the scale $T \sim Mv_T^2$

$$\mathcal{L}_{\text{NRQCD}} = \psi^\dagger \bigg(i\partial_0 - gA_0(t, \mathbf{R}) - g\mathbf{r}\nabla A_0(t, \mathbf{R}) \tag{6.60}$$

$$+ \frac{1}{2M} \left[\nabla^2 - ig\nabla\mathbf{A}(t, \mathbf{R}) - 2g\mathbf{A}(t, \mathbf{R})\nabla + g^2\mathbf{A}^2(t, \mathbf{R}) \right] + \cdots \bigg) \psi, \tag{6.61}$$

where the ellipsis indicates higher order terms. The terms in the above Lagrangian now have a definite power counting: ∂_0 acting on ψ scales as Mv^2, ∇ acting on ψ scales as Mv, and gA_μ and ∂_0 and ∇ acting on A_μ scale as Mv_T^2. Taking $v > v_T^2$ and retaining terms up to order Mv^2 and Mv_T^3, we have

$$\mathcal{L}_{\text{NRQCD}} = \psi^\dagger \left(i\partial_0 - gA_0(t, \mathbf{R}) - g\mathbf{r}\nabla A_0(t, \mathbf{R}) + \frac{\nabla^2}{2M} + \cdots \right) \psi. \tag{6.62}$$

The multipole expansion provides an unambiguous power counting but spoils the man-

ifest gauge invariance of Eq. (6.59); this can be restored via the field redefinition

$$\psi(t, \mathbf{x}) \to \mathrm{P} \exp \left[ig \int_{\mathbf{R}}^{\mathbf{x}} \mathrm{d}\mathbf{x}' \cdot \mathbf{A}(t, \mathbf{x}') \right] \psi(t, \mathbf{x}), \tag{6.63}$$

where P indicates path ordering of the exponential. We note that under gauge transformations the redefined $\psi(t, \mathbf{x})$ on the right-hand side of Eq. (6.63) transforms at $\mathbf{R}$, i.e., $\psi(t, \mathbf{x}) \to g(t, \mathbf{R})\psi(t, \mathbf{x})$. Implementing the multipole expansion on the Wilson line, Eq. (6.63) becomes

$$\psi(t, \mathbf{x}) = [1 + ig\mathbf{r}\mathbf{A}(t, \mathbf{R}) + \cdots]\psi(t, \mathbf{x}). \tag{6.64}$$

The first nontrivial term in the expansion is of order v_T, and the ellipsis represents terms of order v_T^2 and higher. We note that as part of the field redefinition we endow ψ with the color structure $\psi \sim \psi^i/\sqrt{N_c}$. We implement the field redefinition of Eq. (6.64) on the Lagrangian of Eq. (6.62) and retain terms up to order Mv^2 and Mv_T^3. We have

$$\mathcal{L}_{\mathrm{NRQCD}} = \psi^\dagger \left\{ i\partial_0 - gA_0 - g\mathbf{r}\partial_0\mathbf{A} - g\mathbf{r}\nabla A_0 - ig^2\mathbf{r}\left[A_0, \mathbf{A}\right] + \frac{\nabla^2}{2M} + \cdots \right\} \psi. \tag{6.65}$$

We note that this can be rewritten in terms of the chromoelectric field as

$$\mathcal{L}_{\mathrm{NRQCD}} = \psi^\dagger \left\{ i\partial_0 - gA_0 + \mathbf{r} \cdot g\mathbf{E} + \frac{\nabla^2}{2M} + \cdots \right\} \psi. \tag{6.66}$$

where ψ is a function of the temporal coordinate t and position $\mathbf{x}$ and undergoes gauge transformations at $\mathbf{R}$, i.e., $\psi(t, \mathbf{x}) \to g(t, \mathbf{R})\psi(t, \mathbf{x})$ and A_0 and $\mathbf{E}$ are evaluated at time t and position $\mathbf{R}$. Eq. (6.66) describes a heavy quark propagating with non-relativistic velocity $v \ll 1$ inside and out of equilibrium with a medium of temperature T; as the quark and the medium are out of equilibrium, we take $v \lesssim v_T \sim \sqrt{T/M}$. The quark is at position $\mathbf{x}$ which we decompose as $\mathbf{x} = \mathbf{R} + \mathbf{r}$ where $|\mathbf{r}| \sim 1/Mv_T$. We interpret $\mathbf{R}$ as the initial position of the quark and $\mathbf{r}$ as the change to this position due to kicks from the medium which are not resolved by the thermal gluons. Eq. (6.66) contains all terms contributing to the evolution up to order Mv^2 and Mv_T^3.

We proceed one step further and resum the Coulombic gluons via the field redefinition

$$\psi(t, \mathbf{x}) \to \exp \left[-ig \int_{-\infty}^{t} \mathrm{d}t' A_0(t', \mathbf{R}) \right] \psi(t, \mathbf{x}), \tag{6.67}$$

arriving at a Lagrangian we designate $\mathcal{L}_{\mathrm{NRQCD}}^{\mathrm{us}}$ which serves as the starting point of our further calculations

$$\mathcal{L}_{\mathrm{NRQCD}}^{\mathrm{us}} = \psi^\dagger \left\{ i\partial_0 + \mathbf{r} \cdot g\tilde{\mathbf{E}}(t, \mathbf{R}) + \frac{\nabla^2}{2M} \right\} \psi, \tag{6.68}$$

where

$$\tilde{E}_i(t, \mathbf{0}) = \Omega^\dagger(t) E_i(t, \mathbf{0}) \Omega(t), \tag{6.69}$$

and

$$\Omega(t) = \mathrm{P} \exp \left[-ig \int_{-\infty}^{t} dt' A_0(t', \mathbf{0}) \right]. \tag{6.70}$$

58

6.2.2 Evolution equations

In this subsection, we carry out an analogous OQS and EFT derivation to those presented in chapters 3 and 4. We derive a similar evolution equation for a single in-medium heavy quark using the Lagrangian of Eq. (6.68) and derive a Fokker-Planck equation with corresponding Langevin equations. Analogously to Eqs. (4.32)-(4.38) describing heavy quarkonium, in the heavy quark case, we have the evolution equation

$$\frac{\mathrm{d}\rho(t)}{\mathrm{d}t} = -i\,[h, \rho(t)] - \Sigma\rho(t) - \rho(t)\Sigma^\dagger + \Xi(\rho(t)), \tag{6.71}$$

where $\rho(t)$ is the heavy quark density matrix, $h = \mathbf{p}^2/(2M)$ is the heavy quark Hamiltonian and

$$\Sigma = \frac{g^2}{6N_c} \int_0^\infty \mathrm{d}s\, e^{-ihs} x^i e^{ihs} \langle \tilde{E}^{a,j}(s, \mathbf{0}) \tilde{E}^{a,j}(0, \mathbf{0}) \rangle, \tag{6.72}$$

$$\Xi(\rho(t)) = \frac{g^2}{6N_c} \int_0^\infty \mathrm{d}s\, e^{-ihs} x^i e^{ihs} \rho(t) x^i \langle \tilde{E}^{a,j}(s, \mathbf{0}) \tilde{E}^{a,j}(0, \mathbf{0}) \rangle + h.c.. \tag{6.73}$$

Our procedure is the same as in the heavy quarkonium sector: namely, we begin by expanding the exponentials in Eqs. (6.72) and (6.73) to linear order making use of Eq. (6.2) to express the higher order correlators in terms terms of κ. In light of the discussion of sec. 5.1, we note that κ and γ are here to be interpreted as their fundamental versions. We proceed by Wigner transforming the resulting evolution equation to arrive at an evolution equation for the Wigner quasi-probability distribution function with corresponding Langevin equation.

Projecting Eq. (6.71) expanded to order E/T onto eigenstates of the position of the heavy quark $\langle \mathbf{x}|$ and $|\mathbf{x}'\rangle$, we have

$$i\langle \mathbf{x}|\,[h, \rho(t)]\,|\mathbf{x}'\rangle = \frac{i}{2M}\left(\nabla^2 - \nabla'^2\right)\rho_{\mathbf{xx}'}(t), \tag{6.74}$$

$$\langle \mathbf{x}|\left(\Sigma\rho(t) + \rho(t)\Sigma^\dagger\right)|\mathbf{x}\rangle = \left[\frac{\kappa}{2}(\mathbf{x}^2 + \mathbf{x}'^2) + \frac{i\gamma}{2}(\mathbf{x}^2 - \mathbf{x}'^2)\right.$$
$$\left. + \frac{\kappa}{4MT}\left(\mathbf{x}\cdot\nabla + \mathbf{x}'\cdot\nabla'\right)\right]\rho_{\mathbf{xx}'}(t), \tag{6.75}$$

$$\langle \mathbf{x}|\Xi(\rho(t); t)|\mathbf{x}'\rangle = \left[\kappa\,\mathbf{x}\cdot\mathbf{x}' + \frac{\kappa}{4MT}\left(\mathbf{x}\cdot\nabla' + \mathbf{x}'\cdot\nabla\right)\right]\rho_{\mathbf{xx}'}(t), \tag{6.76}$$

where $\rho_{\mathbf{xx}'}(t) = \langle \mathbf{x}|\rho(t)|\mathbf{x}'\rangle$. We complete the Wigner transform by Fourier transforming the coordinate $\mathbf{x}_-$ where

$$\mathbf{x}_+ = \frac{\mathbf{x} + \mathbf{x}'}{2}, \quad \mathbf{x}_- = \mathbf{x} - \mathbf{x}'. \tag{6.77}$$

We denote the Fourier transform of the projected density matrix $\tilde{\rho}(t)$, i.e.,

$$\tilde{\rho}(t) = \int d^3r_-\, e^{-i\mathbf{p}\cdot\mathbf{x}_-} \left\langle \mathbf{x}_+ + \tfrac{\mathbf{x}_-}{2}\right| \rho(t) \left|\mathbf{x}_+ - \tfrac{\mathbf{x}_-}{2}\right\rangle. \tag{6.78}$$

The equation of motion of $\tilde{\rho}(t)$ takes the form of a Fokker-Planck equation

$$\left(\frac{\partial}{\partial t} + \mathbf{v} \cdot \nabla_+\right) \tilde{\rho}(t) = \left[\frac{\kappa}{2}\nabla_{\mathbf{p}}^2 + M\eta\nabla_{\mathbf{p}}\mathbf{v} + \gamma\,\mathbf{x}_+ \cdot \nabla_{\mathbf{p}}\right] \tilde{\rho}(t), \qquad (6.79)$$

where $\mathbf{p}$ is the momentum of the heavy quark, $\mathbf{v} = \mathbf{p}/M$ is its velocity and $\eta = \kappa/(2MT)$ is the heavy quark drag coefficient. The Fokker-Planck equation of Eq. (6.79) has corresponding Langevin equation

$$\frac{\mathrm{d}p_i}{\mathrm{d}t} = -F_i - \eta\,p_i + \xi_i(t), \qquad (6.80)$$

where

$$F_i = -\gamma\,x_i^+, \quad \langle\xi_i(t)\xi_j(t')\rangle = \kappa\,\delta_{ij}\delta(t - t'), \quad \eta = \frac{\kappa}{2MT}. \qquad (6.81)$$

The last equality of Eq. (6.81) is the Einstein relation between the drag and momentum diffusion coefficients. We here observe a number of similarities to the general Langevin equation presented in the introduction to this chapter. As in the heavy quarkonium case, we observe an additional random force proportional to γ. We note that such a term was not observed in Blaizot's and Escobedo's derivation of a Langevin equation using standard NRQCD. As a correction to the heavy quark potential, γ arises naturally in the heavy quarkonium case; its role in the single heavy quark Langevin equation is less clear and a matter of active research.

Chapter 7

Nonlinear evolution equations

In part I of this thesis, we present the pNRQCD master equation governing the in-medium evolution of heavy quarkonium. This set of coupled equations is linear in the density matrix and describes the dilute limit, i.e., the limit in which the number of heavy quarks in the medium is low. In this chapter, we examine the evolution equations beyond this limit by including terms nonlinear in the density matrix.

For simplicitly, we work initially in the Abelian sector with the singlet field $S(x)$; the analysis can be generalized to the nonabelian case with the inclusion of the octet field $O(x)$. We begin by defining the Wightman correlators

$$D^>(x) = \langle S(x)S^\dagger(0)\rangle, \tag{7.1}$$

$$D^<(x) = \langle S^\dagger(0)S(x)\rangle. \tag{7.2}$$

Within the real time formalism of finite temperature quantum field theory, time evolution proceeds along a nontrivial contour from an initial time t_i to final time $t_i - i\beta$ (cf. chapter 4 and Fig. 4.1). We utilize the standard Schwinger-Keldysh assignment of $\sigma = 0$ such that contours C_1 and C_2 lie along the real axis and disregard contours C_3 and C_4. The real time propagator is given by the four combinations of type-1 and type-2 fields living on the upper and lower branches of the contour, respectively,

$$\mathbf{D}(x) = \begin{pmatrix} D_{11}(x) & D_{12}(x) \\ D_{21}(x) & D_{22}(x) \end{pmatrix} = \begin{pmatrix} D_F(x) & D^<(x) \\ D^>(x) & D_{\tilde{F}}(x) \end{pmatrix}, \tag{7.3}$$

where $D_F(x)$ and $D_{\tilde{F}}(x)$ are the time ordered and anti time ordered propagators

$$D_F(x) = \theta(x_0)D^>(x) + \theta(-x_0)D^<(x), \tag{7.4}$$

$$D_{\tilde{F}}(x) = \theta(-x_0)D^>(x) + \theta(x_0)D^<(x). \tag{7.5}$$

We identify the propagator $D^<(x)$ with the density matrix $\rho(x_0)$. We make use of

the bosonic equal time commutation relations to write all propagators in terms of $D^<(x)$

$$D_{11}(x) = \theta(x_0)\delta^{(3)}(\mathbf{x}) + D^<(x), \tag{7.6}$$

$$D_{12}(x) = D^<(x), \tag{7.7}$$

$$D_{21}(x) = D^<(x) + \delta^{(3)}(\mathbf{x}), \tag{7.8}$$

$$D_{22}(x) = \theta(-x_0)\delta^{(3)}(\mathbf{x}) + D^<(x), \tag{7.9}$$

where the first term on the right-hand side of the above equations represents the dilute limit (cf. Eq. (4.12)-(4.15)). We proceed to calculate the density matrix in perturbation theory. For $rT \ll 1$, we write the following expression for $D_{12}(x)$ up to and including order $(rT)^2$ in the finite temperature multipole expansion

$$
\begin{aligned}
\rho(t) =& e^{-ih(t-t_0)}\rho(t_0)e^{ih(t-t_0)} + \frac{g^2}{6N_c}\Bigg\{ \\
& \int_X D_{11}(r-r_1)(-i\mathbf{x}_1)D_{11}(r_1-r_2)(-i\mathbf{x}_2)D_{12}(r_2-r_1)D_{11}^E(t_1-t_2,\mathbf{0}) \\
& + \int_X D_{12}(r-r_1)(i\mathbf{x}_1)D_{21}(r_1-r_2)(-i\mathbf{x}_2)D_{12}(r_2-r_1)D_{21}^E(t_1-t_2,\mathbf{0}) \tag{7.10} \\
& + \int_X D_{11}(r-r_1)(-i\mathbf{x}_1)D_{12}(r_1-r_2)(i\mathbf{x}_2)D_{22}(r_2-r_1)D_{12}^E(t_1-t_2,\mathbf{0}) \\
& + \int_X D_{12}(r-r_1)(i\mathbf{x}_1)D_{22}(r_1-r_2)(i\mathbf{x}_2)D_{22}(r_2-r_1)D_{22}^E(t_1-t_2,\mathbf{0})\Bigg\},
\end{aligned}
$$

where $r = (t,\mathbf{x})$, $r_1 = (t_1,\mathbf{x}_1)$, $r_2 = (t_2,\mathbf{x}_2)$, $\int_X = \int d^4r_1 \int d^4r_2$ and $D_E(t-t',\mathbf{0})$ is the chromoelectric correlator

$$D_E^>(t-s,\mathbf{0}) = \langle E^{a,i}(t,\mathbf{0})E^{a,i}(s,\mathbf{0})\rangle. \tag{7.11}$$

The nontrivial terms in the multipole expansion of Eq. (7.10) can be represented diagramatically as in Fig. (7.1).
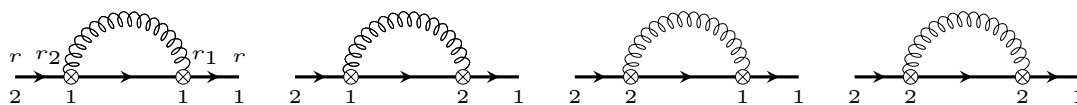

Figure 7.1: Diagrams contributing to the evolution of $\rho(t)$ at order $(rT)^2$ in the finite temperature multipole expansion. For ease of interpretation, we display the four coordinates of the vertices only on the left-most diagram; an identical assignment is implicit in the other diagrams.

We proceed line by line through the terms of Eq. (7.10) and substitute the definitions of the propagators given in Eqs. (7.6)-(7.9). The term on the second line of Eq. (7.10)

corresponding to the left-most diagram in Fig. 7.1 gives

$$
\begin{aligned}
&\int_X D_{11}(r-r_1)(-i\mathbf{x}_1)D_{11}(r_1-r_2)(-i\mathbf{x}_2)D_{12}(r_2-r_1)D_{11}^E(t_1-t_2,\mathbf{0}) \\
&= -\int_{t_0}^t dt_1 \int_{t_0}^{t_1} dt_2\, e^{-ih(t-t_1)}\mathbf{r}e^{-ih(t_1-t_2)}\mathbf{r}e^{-ih(t_2-t_0)}\rho(t_0)e^{ih(t-t_0)}D_{11}^E(t_1-t_2,\mathbf{0}) \\
&\quad -\int_{t_0}^t dt_1 \int_{t_0}^{\infty} dt_2 \int d^3x\, e^{-ih(t-t_1)}\mathbf{r}e^{-ih(t_1-t_0)}\rho(t_0)e^{ih(t_2-t_0)}\mathbf{x} \\
&\qquad \times e^{-ih(t_2-t_0)}\rho(t_0)e^{ih(t-t_0)}D_{11}^E(t_1-t_2,\mathbf{0}) \\
&\quad -\int_{t_0}^\infty dt_1 \int_{t_0}^{t_1} dt_2 \int d^3x\, e^{-ih(t-t_0)}\rho(t_0)e^{ih(t_1-t_0)}\mathbf{x}e^{-ih(t_1-t_2)}\mathbf{x} \\
&\qquad \times e^{-ih(t_2-t_0)}\rho(t_0)e^{ih(t-t_0)}D_{11}^E(t_1-t_2,\mathbf{0}) \\
&\quad -\int_{t_0}^\infty dt_1 \int_{t_0}^{\infty} dt_2 \int d^3x_1 \int d^3x_2\, e^{-ih(t-t_0)}\rho(t_0)e^{ih(t_1-t_0)}\mathbf{x}_1 \\
&\qquad \times e^{ih(t_1-t_0)}\rho(t_0)e^{ih(t_2-t_0)}\mathbf{x}_2 e^{-ih(t_2-t_0)}\rho(t_0)e^{ih(t-t_0)}D_{11}^E(t_1-t_2,\mathbf{0}).
\end{aligned}
\tag{7.12}
$$

The term on the third line of Eq. (7.10) corresponding to the second diagram from the left in Fig. 7.1 gives

$$
\begin{aligned}
&\int_X D_{12}(r-r_1)(i\mathbf{x}_1)D_{21}(r_1-r_2)(-i\mathbf{x}_2)D_{12}(r_2-r)D_{21}^E(t_1-t_2,\mathbf{0}) \\
&= \int_{t_0}^\infty dt_1 \int_{t_0}^{\infty} dt_2 \int d^3x\, e^{-ih(t-t_0)}\rho(t_0)e^{ih(t_1-t_0)}\mathbf{x}e^{-ih(t_1-t_2)}\mathbf{x} \\
&\qquad \times e^{-ih(t_2-t_0)}\rho(t_0)e^{i(t-t_0)}D_{11}^E(t_1-t_2,\mathbf{0}) \\
&\quad +\int_{t_0}^\infty dt_1 \int_{t_0}^{\infty} dt_2 \int d^3x_1 \int d^3x_1\, e^{-ih(t-t_0)}\rho(t_0)e^{ih(t_1-t_0)}\mathbf{x}_1 \\
&\qquad \times e^{-ih(t_1-t_0)}\rho(t_0)e^{ih(t_2-t_0)}\mathbf{x}_2 e^{-ih(t_2-t_0)}\rho(t_0)e^{ih(t-t_0)}D_{11}^E(t_1-t_2,\mathbf{0}).
\end{aligned}
\tag{7.13}
$$

The term on the fourth line of Eq. (7.10) corresponding to the second diagram from the

right in Fig. 7.1 gives

$$
\int_X D_{11}(r - r_1)(-i\mathbf{x}_1)D_{12}(r_1 - r_2)(i\mathbf{x}_2)D_{22}(r_2 - r)D_{12}^E(t_1 - t_2, \mathbf{0})
$$

$$
= \int_{t_0}^{t} dt_1 \int_{t_0}^{t} dt_2 \, e^{-ih(t-t_1)}\mathbf{r}e^{-ih(t_1-t_0)}\rho(t_0)e^{ih(t_2-t_0)}\mathbf{r}e^{-ih(t_2-t)}D_{12}^E(t_1 - t_2, \mathbf{0})
$$

$$
+ \int_{t_0}^{t} dt_1 \int_{t_0}^{\infty} dt_2 \int d^3x \, e^{-ih(t-t_1)}\mathbf{r}e^{-ih(t_1-t_0)}\rho(t_0)e^{ih(t_2-t_0)}\mathbf{x}
$$

$$
\times e^{-ih(t_2-t_0)}\rho(t_0)e^{ih(t-t_0)}D_{12}^E(t_1 - t_2, \mathbf{0}) \tag{7.14}
$$

$$
+ \int_{t_0}^{\infty} dt_1 \int_{t_0}^{t} dt_2 \int d^3x \, e^{-ih(t-t_0)}\rho(t_0)e^{ih(t_1-t_0)}\mathbf{x}e^{-ih(t_1-t_0)}\rho(t_0)
$$

$$
\times e^{ih(t_2-t_0)}\mathbf{r}e^{-ih(t_2-t)}D_{12}^E(t_1 - t_2, \mathbf{0})
$$

$$
+ \int_{t_0}^{\infty} dt_1 \int_{t_0}^{\infty} dt_2 \int d^3x_1 \int d^3x_2 \, e^{-ih(t-t_0)}\rho(t_0)e^{ih(t_1-t_0)}\mathbf{x}_1
$$

$$
\times e^{-ih(t_1-t_0)}\rho(t_0)e^{ih(t_2-t_0)}\mathbf{x}_2 e^{-ih(t_2-t_0)}\rho(t_0)e^{ih(t-t_0)}D_{22}^E(t_1 - t_2, \mathbf{0}).
$$

Finally, the term on the fifth line of Eq. (7.10) corresponding to the right-most diagram in Fig. 7.1 gives

$$
\int_X D_{12}(r - r_1)(i\mathbf{x}_1)D_{22}(r_1 - r_2)(i\mathbf{x}_2)D_{22}(r_2 - r)D_{22}^E(t_1 - t_2, \mathbf{0})
$$

$$
= - \int_{t_0}^{t_2} dt_1 \int_{t_0}^{t} dt_2 \, e^{-ih(t-t_0)}\rho(t_0)e^{ih(t_1-t_0)}\mathbf{r}e^{-ih(t_1-t_2)}\mathbf{r}e^{-ih(t_2-t)}D_{22}^E(t_1 - t_2, \mathbf{0})
$$

$$
- \int_{t_0}^{t_2} dt_1 \int_{t_0}^{\infty} dt_2 \int d^3x \, e^{-ih(t-t_0)}\rho(t_0)e^{ih(t_1-t_0)}\mathbf{x}e^{ih(t_2-t_0)}\mathbf{x}
$$

$$
\times e^{-ih(t_2-t_0)}\rho(t_0)e^{ih(t-t_0)}D_{22}^E(t_1 - t_2, \mathbf{0}) \tag{7.15}
$$

$$
- \int_{t_0}^{\infty} dt_1 \int_{t_0}^{t} dt_2 \int d^3x \, e^{-ih(t-t_0)}\rho(t_0)e^{ih(t_1-t_0)}\mathbf{x}e^{-ih(t_1-t_0)}\rho(t_0)
$$

$$
\times e^{ih(t_2-t_0)}\mathbf{r}e^{-ih(t_2-t)}D_{22}^E(t_1 - t_2, \mathbf{0})
$$

$$
- \int_{t_0}^{\infty} dt_1 \int_{t_0}^{\infty} dt_2 \int d^3x_1 \int d^3x_2 \, e^{-ih(t-t_0)}\rho(t_0)e^{ih(t_1-t_0)}\mathbf{x}_1
$$

$$
\times e^{-ih(t_1-t_0)}\rho(t_0)e^{ih(t_2-t_0)}\mathbf{x}_2 e^{-ih(t_2-t_0)}\rho(t_0)e^{ih(t-t_0)}D_{22}^E(t_1 - t_2, \mathbf{0}).
$$

We note that the first terms on the right-hand sides of Eqs. (7.12), (7.14) and (7.15) correspond to the dilute limit and are related to the medium interaction operators Σ, Ξ and $\Sigma^\dagger$ given in sec. 3.2. We note that terms not containing t as an upper integral bound do not contribute to $d\rho(t)/dt$ thus substantially reducing the number of terms to consider and the seeming complexity of the above set of equations. The general structure of the evolution equation at leading order in the density matrix is thus preserved, and the nonlinear terms in $\rho(t)$ of Eqs. (7.12), (7.14) and (7.15) represent corrections to terms

in the evolution equation of the form $\Sigma\rho(t)$, $\rho(t)\Sigma^\dagger$ and $\Xi(\rho(t);t)$. Thorough analysis of these new terms in the various phenomenological limits analyzed already in the dilute limit is a matter of active research; it is our hope that in these limits these terms can be written intuitively as corrections to the medium evolution operators with the eventual goal of computational implementation and solution of these equations.

Part III

Phenomenological Results: Heavy Quarkonium Suppression

Chapter 8

Heavy quarkonium suppression at leading order in binding energy over temperature

In this chapter, we solve the evolution equations presented in chapters 3 and 4 and derived originally in Refs. [28, 30]. We work in the strict $E \ll T$ limit in which the evolution equations take the form of a Lindblad equation. We utilize the `QTraj` code [59] to solve the Lindblad equation and extract the nuclear modification factor R_{AA} and the elliptic flow v_2 for comparison against experimental data from the ALICE, ATLAS and CMS collaborations. In sec. 8.1, we discuss in detail the Lindblad equation describing the in-medium evolution of Coulombic quarkonium. In sec. 8.2, we introduce the quantum trajectories algorithm used to solve the Lindblad equation, the `QTraj` code implementing this algorithm and the code and simulation parameters utilized. For a more detailed presentation of the `QTraj` code, we direct the reader to appendix A and Ref. [59]. In sec. 8.3, we discuss our results and compare against experimental data. The results presented in this chapter are taken from Ref. [61] and represent state of the art results at order 0 in the E/T expansion. A number of tests of the general framework and the `QTraj` code were carried out in Ref. [60]; the results of these tests and phenomenological results are presented in appendix B. We note that due to improvements to the `QTraj` implemented between the publication of Refs. [60] and [61], the phenomenological results presented in this chapter supersede those presented in appendix B.

8.1   Heavy quarkonium evolution in the regime $T \gg E$

As presented in the introduction to this thesis, heavy quarkonium suppression in HIC experiments serves as an observable of particular experimental and theoretical interest as a signal the formation of a deconfined quark gluon plasma. In Refs. [28, 30], Brambilla, Escobedo, Soto and Vairo utilized the OQS formalism and the EFT pNRQCD to derive a Lindblad equation governing the in-medium evolution of Coulombic quarkonium in

the limit $E \ll T$. Specifically, they resummed the Coulombic gluons of Eq. (2.29) via the field redefinitions

$$O(t) = \Omega(t)\tilde{O}(t)\Omega^\dagger(t), \quad E_i(t,\vec{0}) = \Omega(t)\tilde{E}_i(t,\vec{0})\Omega^\dagger(t), \tag{8.1}$$

where $\Omega(t)$ is a Wilson line in the fundamental representation extending from time $-\infty$ to time t

$$\Omega(t) = \mathrm{P}\exp\left[-ig\int_{-\infty}^{t} dt' A_0(t')\right]. \tag{8.2}$$

After this field redefinition, the pNRQCD Lagrangian takes the form

$$\mathcal{L}_{\mathrm{pNRQCD}} = \mathrm{Tr}\bigg[\mathrm{S}^\dagger\left(i\partial_0 - h_s\right)\mathrm{S} + \tilde{\mathrm{O}}^\dagger\left(i\partial_0 - h_o\right)\tilde{\mathrm{O}} + \tilde{\mathrm{O}}^\dagger\mathbf{r}\cdot g\tilde{\mathbf{E}}\mathrm{S} + \mathrm{S}^\dagger\mathbf{r}\cdot g\tilde{\mathbf{E}}\tilde{\mathrm{O}}$$
$$+ \frac{1}{2}\tilde{\mathrm{O}}^\dagger\left\{\mathbf{r}\cdot g\tilde{\mathbf{E}}, \tilde{\mathrm{O}}\right\}\bigg], \tag{8.3}$$

where $h_{s,o}$ are the pNRQCD singlet and octet Hamiltonians. Using the above Lagrangian and the OQS formalism, the authors of Refs. [28, 30] derived a set of coupled evolution equations governing the in-medium, out of equilibrium evolution of heavy Coulombic quarkonium

$$\frac{\mathrm{d}\rho_s(t)}{\mathrm{d}t} = -i\left[h_s, \rho_s(t)\right] - \Sigma_s\rho_s(t) - \rho_s(t)\Sigma_s^\dagger + \Xi_{so}(\rho_o(t)), \tag{8.4}$$

$$\frac{\mathrm{d}\rho_o(t)}{\mathrm{d}t} = -i\left[h_o, \rho_o(t)\right] - \Sigma_o\rho_o(t) - \rho_o(t)\Sigma_o^\dagger + \Xi_{os}(\rho_s(t)) + \Xi_{oo}(\rho_o(t)), \tag{8.5}$$

where $\rho_{s,o}(t)$ is the density matrix of the quarkonium in the singlet, octet state and medium interactions are encoded in the Σ and Ξ operators given explicitly as

$$\Sigma_s = r^i A_i^{so\dagger}, \tag{8.6}$$

$$\Sigma_o = \frac{1}{N_c^2 - 1}r^i A_i^{os\dagger} + \frac{N_c^2 - 4}{2(N_c^2 - 1)}r^i A_i^{oo\dagger}, \tag{8.7}$$

$$\Xi_{so}(\rho_o(t)) = \frac{1}{N_c^2 - 1}\left(A_i^{os\dagger}\rho_o(t)r^i + r^i\rho_o(t)A_i^{os}\right), \tag{8.8}$$

$$\Xi_{os}(\rho_s(t)) = A_i^{so\dagger}\rho_s(t)r^i + r^i\rho_s(t)A_i^{so}, \tag{8.9}$$

$$\Xi_{oo}(\rho_o(t)) = \frac{N_c^2 - 4}{2(N_c^2 - 1)}\left(A_i^{oo\dagger}\rho_o(t)r^i + r^i\rho_o(t)A_i^{oo}\right), \tag{8.10}$$

where A_i^{uv} is the medium correlator

$$A_i^{uv} = \frac{g^2}{6N_c}\int_0^\infty \mathrm{d}s\, e^{-ih_u s}r^i e^{ih_v s}\langle\tilde{E}^{a,j}(0,\mathbf{0})\tilde{E}^{a,j}(s,\mathbf{0})\rangle, \tag{8.11}$$

where

$$h_s = \frac{\vec{p}^2}{M} - \frac{C_f\alpha_s(1/a_0)}{r}, \quad h_o = \frac{\vec{p}^2}{M} + \frac{\alpha_s(1/a_0)}{2N_c r}, \tag{8.12}$$

68

i.e., the strong coupling is evaluated at the scale of the inverse Bohr radius. The coupled evolution equations can be rewritten as the master equation

$$\frac{d\rho(t)}{dt} = -i\left[H, \rho(t)\right] + \sum_{nm} h_{nm}\left(L_i^n \rho(t) L_i^{m\dagger} - \frac{1}{2}\left\{L_i^{m\dagger} L_i^n, \rho(t)\right\}\right), \tag{8.13}$$

where

$$\rho(t) = \begin{pmatrix} \rho_s(t) & 0 \\ 0 & \rho_o(t) \end{pmatrix}, \quad H = \begin{pmatrix} h_s + \mathrm{Im}(\Sigma_s) & 0 \\ 0 & h_o + \mathrm{Im}(\Sigma_o) \end{pmatrix}, \tag{8.14}$$

$$L_i^0 = \begin{pmatrix} 0 & 0 \\ 0 & 1 \end{pmatrix} r^i, \quad L_i^1 = \begin{pmatrix} 0 & 0 \\ 0 & \frac{N_c^2-4}{2(N_c^2-1)} A_i^{oo\dagger} \end{pmatrix}, \tag{8.15}$$

$$L_i^2 = \begin{pmatrix} 0 & \frac{1}{\sqrt{N_c^2-1}} \\ 1 & 0 \end{pmatrix} r^i, \quad L_i^3 = \begin{pmatrix} 0 & \frac{1}{\sqrt{N_c^2-1}} A_i^{os\dagger} \\ A_i^{so\dagger} & 0 \end{pmatrix}, \tag{8.16}$$

$$h_{nm} = \begin{pmatrix} 0 & 1 & 0 & 0 \\ 1 & 0 & 0 & 0 \\ 0 & 0 & 0 & 1 \\ 0 & 0 & 1 & 0 \end{pmatrix}. \tag{8.17}$$

Eq. (8.13) is manifestly trace preserving, but the set of coupled evolution equations is not positive definite due to the negative eigenvalues of the matrix h_{nm}. Therefore, they cannot, in general, be written in Lindblad form and are thus more difficult to solve. However, taking into account the physics of the problem, we find there exists a phenomenological region in which Eq. (8.13) does in fact take the form of a Lindblad equation.

We observe that the medium correlator defining A_i^{uv} in Eq. (8.11) decays rapidly for times $s \gtrsim 1/T$; furthermore, the eigenvalues of $h_{s,o}$ are of order E. In the temperature regime $E \ll T$, the exponentials in Eq. (8.11) can be set to 1, and A_i^{uv} can be expressed in terms of the transport coefficients κ and γ

$$\kappa = \frac{g^2}{6N_c} \int_0^\infty dt \left\langle \left\{ \tilde{E}^{a,i}(t,\mathbf{0}), \tilde{E}^{a,i}(0,\mathbf{0}) \right\} \right\rangle, \tag{8.18}$$

$$\gamma = -i\frac{g^2}{6N_c} \int_0^\infty dt \left\langle \left[\tilde{E}^{a,i}(t,\mathbf{0}), \tilde{E}^{a,i}(0,\mathbf{0}) \right] \right\rangle, \tag{8.19}$$

as

$$A_i^{uv} = \frac{r_i}{2}\left(\kappa - i\gamma\right). \tag{8.20}$$

We here interpret the transport coefficients as the heavy quarkonium, i.e., adjoint, versions in the sense discussed in sec. 5.1. In this case, the L_n vectors of the master equation are not linearly independent and, via a rotation prior to diagonalization of h_{nm}, can be made orthogonal to the eigenvectors associated to the negative eigenvalues of h_{nm}. We

discuss this procedure in greater detail in sec. 9.1.2. In this case, the master equation can be written in Lindblad form

$$\frac{d\rho(t)}{dt} = -i[H, \rho(t)] + \sum_n \left(C_i^n \rho(t) C_i^{n\dagger} - \frac{1}{2} \left\{ C_i^{n\dagger} C_i^{n\dagger}, \rho(t) \right\} \right), \qquad (8.21)$$

where C_i^n are the collapse operators

$$C_i^0 = \sqrt{\frac{\kappa}{N_c^2 - 1}} r^i \begin{pmatrix} 0 & 1 \\ \sqrt{N_c^2 - 1} & 0 \end{pmatrix}, \qquad (8.22)$$

$$C_i^1 = \sqrt{\frac{(N_c^2 - 4)\kappa}{2(N_c^2 - 1)}} r^i \begin{pmatrix} 0 & 0 \\ 0 & 1 \end{pmatrix}. \qquad (8.23)$$

The above 6 collapse operators can be reduced to 2 by utilizing the spherical symmetry of the problem to reduce the full 3 dimensional evolution to the 1 dimensional evolution of a particle in a spherically symmetric potential. We project the Lindblad equation onto spherical harmonics and sum over the magnetic quantum number m. We define

$$\rho^{lm} = \int d\Omega(\theta, \phi) d\Omega(\theta', \phi') \, Y_{lm}(\theta, \phi) \, \rho \, Y_{lm}^*(\theta', \phi'), \qquad (8.24)$$

and, due to the spherical symmetry, encode all information in the object

$$\rho^l = \sum_m \rho^{lm}. \qquad (8.25)$$

We perform this projection on the Lindblad equation and write

$$\frac{d\rho(t)}{dt} = -i[H, \rho(t)] + \sum_n \left(C_n \rho(t) C_n^\dagger - \frac{1}{2} \left\{ C_n^\dagger C_n, \rho(t) \right\} \right), \qquad (8.26)$$

where

$$C_0 = \sqrt{\frac{\kappa}{N_c^2 - 1}} r \begin{pmatrix} 0 & 1 \\ \sqrt{N_c^2 - 1} & 0 \end{pmatrix}, \qquad (8.27)$$

$$C_1 = \sqrt{\frac{(N_c^2 - 4)\kappa}{2(N_c^2 - 1)}} r \begin{pmatrix} 0 & 0 \\ 0 & 1 \end{pmatrix}. \qquad (8.28)$$

This Lindblad equation was solved in Refs. [28,30] using the open source QuTiP 2 Python package [144, 145]. Eq. (8.26) governs the in-medium evolution of heavy Coulombic quarkonium. The hermitian Hamiltonian consists of the vacuum pNRQCD Hamiltonian and the in-medium mass shift. The collapse operators encode interactions with the medium.

The relevant quantum numbers of our system are color and angular momentum. The color transitions are manifest in the 2×2 matrix structure of the collapse operators which implement singlet-octet and octet-octet transitions. In angular momentum space,

the collapse operators implement transitions between states of angular momentum l and $l \pm 1$. The anticommutator term of Eq. (8.26) preserves the quantum numbers of the state and decrease its trace; this corresponds to the decay width of the state into a state of different angular momentum and color. The term $C_n \rho(t) C_n^\dagger$ changes the quantum numbers of the state, i.e., it implements the decays described by the width term, and ensures the overall evolution is trace preserving. Refs. [60, 61], utilize the `QTraj` code implementing the quantum trajectories algorithm to solve this Lindblad equation; we present the algorithm in the following section and the `QTraj` code in appendix A.

8.2   Computation methods

In this section, we present the computational methods utilized to solve the Lindblad equation introduced in the previous section. In subsec. 8.2.1, we present the quantum trajectories algorithm as implemented in the `QTraj` code to solve the Lindblad equation. In subsec. 8.2.2, we describe the implementation of the time evolution of the state. In subsec. 8.2.3, we describe the implementation of the hydrodynamic medium evolution. In subsec. 8.2.4, we present our implementation of a feed down procedure to place `QTraj` output in a form enabling comparison against experimental data. In subsec. 8.2.5, we discuss the fixing of the parameters entering the Lindblad equation. In subsec. 8.2.6, we discuss the lattice parameters used in the `QTraj` simulations.

8.2.1   Quantum trajectories algorithm

In spite of the simplifications with respect to the master equation given in Eq. (8.13), the Lindblad equation given in Eq. (8.26) remains difficult to solve directly. Refs. [60,61] make use of a Monte Carlo method called the quantum trajectories algorithm to solve the Lindblad equation via simulation; for a general introduction to this method, we direct the reader to Ref. [146].

The quantum trajectories algorithm involves separating the evolution specified by the quantum number preserving terms of the Lindblad equation from those which alter the quantum numbers of the state. To this end, we collect the quantum number preserving terms of the Lindblad equation into a non-Hermitian effective Hamiltonian

$$H_{\text{eff}} = H - \frac{i}{2}\Gamma, \tag{8.29}$$

where

$$\Gamma = \sum_n C_n^\dagger C_n. \tag{8.30}$$

Evolution with the non-Hermitian effective Hamiltonian reduces the norm of the state $|\psi\rangle$ (equivalently the trace of the density matrix ρ). We evolve the state $|\psi(t)\rangle$ forward an infinitesimal time step δt with H_{eff}

$$|\psi(t + \delta t)\rangle \approx (1 - iH_{\text{eff}}\delta t)|\psi(t)\rangle. \tag{8.31}$$

71

Its norm is given by

$$\langle\psi(t+\delta t)|\psi(t+\delta t)\rangle \approx 1 - i\langle\psi(t)|(H_{\text{eff}} - H_{\text{eff}}^\dagger)|\psi(t)\rangle\delta t \qquad (8.32)$$

$$= 1 - \delta p, \qquad (8.33)$$

where

$$\delta p = \sum_n \langle\psi(t)|C_n^\dagger C_n|\psi(t)\rangle\delta t = \sum_n \delta p_n. \qquad (8.34)$$

The decrease in norm δp is related to the probability that the state has interacted with the environment and a change of quantum numbers has occurred.

We consider evolving the state forward with H_{eff}, preserving the quantum numbers of the state, with probability $1 - \delta p$ and changing the quantum numbers of the state by acting on it with the collapse operator C_n with probability δp. This normalized evolution is given by

$$|\tilde\psi(t+\delta t)\rangle = \begin{cases} \frac{|\psi(t+\delta t)\rangle}{\sqrt{1-\delta p}} & \text{with probability } 1 - \delta p, \\[2ex] \frac{C_n|\psi(t)\rangle}{\sqrt{\delta p_n/\delta t}} & \text{with probability } \delta p. \end{cases} \qquad (8.35)$$

We take the outer product of each line of Eq. (8.35) with itself and have the following equation for the density matrix at time $t + \delta t$

$$\rho(t+\delta t) = (1-\delta p)\frac{|\psi(t+\delta t)\rangle}{\sqrt{1-\delta p}}\frac{\langle\psi(t+\delta t)|}{\sqrt{1-\delta p}} + \delta p\sum_n \frac{\delta p_n}{\delta p}\frac{C_n|\psi(t)\rangle}{\sqrt{\delta p_n/\delta t}}\frac{\langle\psi(t)|C_n^\dagger}{\sqrt{\delta p_n/\delta t}} \qquad (8.36)$$

$$= \rho(t) - i[H_{\text{eff}}\rho(t) - \rho(t)H_{\text{eff}}^\dagger]\delta t + \sum_n C_n\rho(t)C_n^\dagger\delta t. \qquad (8.37)$$

In the limit $\delta t \to 0$, this reduces to the Lindblad equation.

We note that the above evolution is implemented on the wave function $\psi(t)$ rather than the density matrix $\rho(t)$. This vastly reduces the required memory compared to solving the Lindblad equation directly. Simulating the density matrix on n lattice sites involves an $(n \times n)$-dimensional matrix as opposed to an n-dimensional vector in the case of the wave function. Furthermore, implementing the quantum number preserving and quantum number changing modes of evolution separately allows for a further reduction in the memory requirement. In Refs. [28, 30] in which the Lindblad equation was solved directly, the angular momentum structure of the evolution equations was implemented as a tensor product with the color and position space structure, i.e., $\rho \propto \rho_c \otimes \rho_l \otimes \rho(r)$, where ρ_c is the color space density matrix, ρ_l is the angular momentum space density matrix and $\rho(r)$ is the position space density matrix. This matrix implementation of the angular momentum structure becomes prohibitively computationally expensive as states of higher angular momentum are considered: to simulate the density matrix on n spatial lattice sites with a cutoff at state $l - 1$ in angular momentum requires initializing a matrix of dimension $(n * 2 * l) \times (n * 2 * l)$. Refs. [28, 30] implemented a cutoff at $l = 1$ in angular momentum. In the quantum trajectories algorithm, the state $|\psi(t)\rangle$ possesses

definite quantum numbers and is represented by an n-dimensional vector; Refs. [60, 61] solve the Lindblad equation with no cutoff in angular momentum.

In the `QTraj` code used in Refs [60, 61], the general procedure outlined above is implemented according to the following algorithm:

1. Initialize the wave function $|\psi(t_0)\rangle$ at time t_0 where $\rho(t_0) = |\psi(t_0)\rangle\langle\psi(t_0)|$ where $\rho(t_0)$ is the initial state of the system.

2. Generate a random number $0 < p_1 < 1$ and evolve the wave function forward in time with H_{eff} until its norm squared is less than or equal to p_1, i.e.,

$$|| e^{-i \int_{t_0}^{t} dt' H_{\text{eff}}(t')} |\psi(t_0)\rangle ||^2 \leq p_1 . \tag{8.38}$$

Denote the first time step fulfilling Eq. (8.38) the jump time t_j and proceed to step 3 if $t_j < t_f$ where t_f is the simulation run time; otherwise, end the simulation at time t_f.

3. At time t_j, perform a quantum jump. Generate an additional random number $0 < p_2 < 1$ to determine which collapse operator C_n to apply to the wave function. The probability p_n of acting with collapse operator C_n is determined from its partial width, i.e.,

$$p_n = \frac{\Gamma_n}{\Gamma} = \frac{\langle\psi(t_j)|C_n^\dagger C_n|\psi(t_j)\rangle}{\sum_m \langle\psi(t_j)|C_m^\dagger C_m|\psi(t_j)\rangle} \tag{8.39}$$

4. Continue from step 2.

Each realization of the above algorithm is a *quantum trajectory*, and the average of N trajectories tends toward the solution of the Lindblad equation as $N \to \infty$. We note that each quantum trajectory is fully independent and the algorithm thus embarrassingly parallelizable, i.e., many trajectories can be run simultaneously enabling faster convergence to the solution of the Lindblad equation. We estimate the number of trajectories necessary to converge to the solution of the in-medium heavy quarkonium Lindblad equation in Figs. A.2c and A.2d.

We note that the specific procedure for calculating the jump time in the above algorithm differs from the standard procedure in which Eq. (8.38) is evaluated with a new p_1 generated at each time step; it is denoted the *waiting time approach* (see sec. IIID of Ref. [146]) and reduces the number of random numbers to be generated compared to the standard algorithm. Furthermore, in step 3 we specify the generation of a single additional random number to determine which collapse operator to act on the wave function. If the color quantum number of the state is octet, the `QTraj` code generates separate random numbers for the color and angular momentum transitions. The transition probabilities for a state of angular momentum l are $p_\uparrow = \frac{l+1}{2l+1}$ and $p_\downarrow = \frac{l}{2l+1}$ and for an octet state $p_{o \to s} = \frac{2}{N_c^2 - 2}$ and $p_{o \to o} = \frac{N_c^2 - 4}{N_c^2 - 2}$. As the singlet to octet transition probability is 1, i.e., $p_{s \to o} = 1$, no random number is generated for the color transition if the state is in the singlet color configuration.

8.2.2 Deterministic evolution of the wave function

In step 2 of the quantum trajectories algorithm, we evolve the wave function deterministically using the non-Hermitian effective Hamiltonian H_{eff}. We carry out this evolution using a split-step pseudospectral method [147–149]. This method consists in evolving the reduced radial wavefunction $u(r,t) = rR(r,t)$, where $R(r,t)$ is the radial wave function defined by $\psi(r,\theta,\phi) = R(r)Y_{lm}(\theta,\phi)$, forward in discrete time steps. The evolution one step Δt forward in time is given by

$$u(r, t + \Delta t) = \exp\left[-iH_{l,c}\Delta t\right] u(r,t), \tag{8.40}$$

where $H_{l,c}$ is the heavy quarkonium Hamiltonian projected onto the angular momentum l and color c of $u(r,t)$. To implement this evolution, we split the Hamiltonian into its kinetic and potential pieces

$$H_{l,c} = V_{l,c} + T, \tag{8.41}$$

where $V_{l,c}$ is the heavy quarkonium potential including the medium induced width and mass shift and $T = \vec{p}^2/M$ is the kinetic term. We approximate the time evolution operator of Eq. (8.40) as

$$\exp\left[-iH_{l,c}\Delta t\right] = \exp\left[-iV_{l,c}\Delta t/2\right]\exp\left[-iT\Delta t\right]\exp\left[-iV_{l,c}\Delta t/2\right] + \mathcal{O}((\Delta t)^2), \tag{8.42}$$

with higher order corrections computable via the Baker-Campbell-Hausdorff formula. A temporal step is implemented according to the following algorithm:

1. Update the wave function in configuration space: $u_1 = \exp\left[-iV_{l,c}\Delta t/2\right] u(t)$.

2. Separately Fourier sine transform the real and imaginary parts of u_1: $\tilde{u}_1 = \mathbb{F}_s\left[\text{Re}\,u_1\right] + \mathbb{F}_s\left[\text{Im}\,u_1\right]$.

3. Update the wave function in momentum space: $\tilde{u}_2 = \exp\left[-iT\Delta t\right]\tilde{u}_1$.

4. Separately inverse Fourier sine transform the real and imaginary parts of $\tilde{u}_2$: $u_2 = \mathbb{F}_s^{-1}\left[\text{Re}\,\tilde{u}_2\right] + \mathbb{F}_s^{-1}\left[\text{Im}\,\tilde{u}_2\right]$.

5. Update the wave function in configuration space: $u_3 = \exp\left[-iV_{l,c}\Delta t/2\right] u_2$.

The discrete Fourier sine transformation in the update procedure ensures $u(r) = 0$ at the extremal points $r = 0$ and $r = L$. Performing step 3 in momentum space implements an all points derivative more accurate than, for example, a three point derivative. Furthermore, the Fourier transforms can be computed using the CUDA Fast Fourier Transform (CUFFT) library [150] allowing for highly efficient computations on massively parallel graphics processing units (GPU). In Ref. [60], the `QTraj` code was calibrated against the results of Refs. [28, 30] which solved the Lindblad equation using a code implementing a three point derivative. The `QTraj` code thus contains an option implementing the three point finite difference derivative in momentum space as $T_{\text{discrete}} = 2[1 - \cos p\Delta r]/(m\Delta r)^2$; see table A.1 in appendix A and Ref. [59].

8.2.3 Hydrodynamic medium evolution

The `QTraj` code implements the hydrodynamic evolution of the medium via coupling to a realistic 3+1D dissipative relativistic hydrodynamics code which uses an equation of state fit to lattice QCD measurements. In Refs. [60–62], physical trajectories through the plasma were Monte Carlo sampled from the hydrodynamics code. A physical trajectory is specified by its production point in the transverse plane, initial transverse momentum p_T and azimuthal angle ϕ; these quantities are sampled from a nuclear binary collision overlap profile $N_{AA}^{\text{bin}}(x, y, b)$, an E_T^{-4} spectrum and uniformly in $[0, 2\pi)$, respectively. In Ref. [60], due to computational constraints, these trajectories were sampled and averaged in each centrality bin to produce an average physical trajectory through the plasma for that centrality bin; we display the temperature evolution of these average trajectories in Fig. B.1. The `QTraj` code was run using the average physical trajectory in each centrality bin and the results presented as a function of the number of participating nucleons N_{part}. In Ref. [61], increased computational resources allowed for the running of quantum trajectories along the distinct physical trajectories allowing for the extraction of differential observables, specifically the elliptic flow v_2, and the presentation of observables as functions of p_T. In Ref. [61], we sampled 7–9×10^5 physical trajectories and ran approximately 50–100 quantum trajectories along each physical trajectory.

8.2.4 Feed down

The raw output of the quantum trajectories algorithm yields a survival probability, i.e., the probability that a quarkonium state traverses the medium without dissociating. In order to compare to experimental results, however, we must account for the fact that in experiments states decay after traversing the medium but prior to detection. To place our results in a form comparable against experimental data, we implement a feed down procedure on the survival probabilities. Specifically, the nuclear modification factor R_{AA} for a given centrality class c, transverse momentum p_T and azimuthal angle ϕ is given by

$$R_{AA}^i(c, p_T, \phi) = \frac{(F \cdot S(c, p_T, \phi) \cdot \vec{\sigma}_{\text{direct}})^i}{\vec{\sigma}_{\text{exp}}^i}, \tag{8.43}$$

where $\vec{\sigma}_{\text{direct}}^i$ is a vector containing the direct cross sections of the considered states, $S(c, p_T, \phi)$ is a vector containing the survival probabilities of the considered states computed from the `QTraj` code and F is the feed down matrix related to the decay widths of the considered states. We consider the $\{\Upsilon(1S),\ \Upsilon(2S),\ \chi_{b0}(1P),\ \chi_{b1}(1P),$ $\chi_{b2}(1P),\ \Upsilon(3S),\ \chi_{b0}(2P),\ \chi_{b1}(2P),\ \chi_{b2}(2P)\}$ states and use experimental cross sections of $\vec{\sigma}_{\text{exp}} = \{57.6,\ 19,\ 3.72,\ 13.69,\ 16.1,\ 6.8,\ 3.27,\ 12.0,\ 14.15\}$ nb.

The $\Upsilon(1S)$, $\Upsilon(2S)$ and $\Upsilon(3S)$ cross sections are taken from measurements of the CMS collaboration at $\sqrt{s_{\text{NN}}} = 5.02$ TeV in the rapidity range $|y| \leq 2.4$ [48]. From the left panel of Fig. 3 of Ref. [48], we average over the rapidity giving differential cross sections weighted by the dimuon branching fractions of 1.44 nb, 0.37 nb and 0.15 nb, respectively; dividing by the dimuon branching fractions of approximately 2.5%, 1.9%

and 2.2%, respectively, gives

$$\langle d\sigma[\Upsilon(1S), \Upsilon(2S), \Upsilon(3S)]/dy\rangle_y = \{57.6, 19, 6.8\} \text{ nb}. \tag{8.44}$$

The χ_b cross sections are computed from $\sqrt{s} = 7$ and 8 TeV measurements of the LHCb collaboration [151]. Tables 5 and 6 of Ref. [151] present measurements at $\sqrt{s} = 7$ and 8 TeV, respectively, of the quantity

$$\mathcal{R}^{\chi_b(mP)}_{\Upsilon(nS)} = \frac{\sigma\left(pp \to \chi_{b1}(mP)X\right)}{\sigma\left(pp \to \Upsilon(nS)X\right)} Br_1 + \frac{\sigma\left(pp \to \chi_{b2}(mP)X\right)}{\sigma\left(pp \to \Upsilon(nS)X\right)} Br_2, \tag{8.45}$$

where $Br_{1,2}$ represents the branching ratio of $\chi_{b1,2}(mP)$ to $\Upsilon(nS)\gamma$. We use the lowest p_T measurements and extrapolate to $\sqrt{s} = 5$ TeV. For both $n = 1$ and $n = 2$, we take $\sigma[\chi_{b2}(nP)]/\sigma[\chi_{b1}(nP)] = 1.176$ [152] (which we note is consistent with available experimental data [153]); this assumption and the $\Upsilon(1S)$ cross section allow us to calculate the cross sections of the $\chi_{b1}(1P)$, $\chi_{b2}(1P)$, $\chi_{b1}(2P)$ and $\chi_{b2}(1P)$ from Eq. (8.45). Consistent with theoretical expectations, we take the $\chi_{b0}(nP)$ cross sections to be 1/4 of the average of the $\chi_{b1}(nP)$ and $\chi_{b2}(nP)$ cross sections [152]. This gives

$$\langle d\sigma[\chi_{b0}(1P), \chi_{b1}(1P), \chi_{b2}(1P)]/dy\rangle_y = \{3.72, 13.69, 16.1\} \text{ nb}, \tag{8.46}$$

$$\langle d\sigma[\chi_{b0}(2P), \chi_{b1}(2P), \chi_{b2}(2P)]/dy\rangle_y = \{3.27, 12.0, 14.15\} \text{ nb}. \tag{8.47}$$

The feed down matrix F is given by

$$F = \begin{pmatrix} 1 & 0.2645 & 0.0194 & 0.352 & 0.18 & 0.0657 & 0.0038 & 0.1153 & 0.077 \\ 0 & 1 & 0 & 0 & 0 & 0.106 & 0.0138 & 0.181 & 0.089 \\ 0 & 0 & 1 & 0 & 0 & 0 & 0 & 0 & 0 \\ 0 & 0 & 0 & 1 & 0 & 0 & 0 & 0.0091 & 0 \\ 0 & 0 & 0 & 0 & 1 & 0 & 0 & 0 & 0.0051 \\ 0 & 0 & 0 & 0 & 0 & 1 & 0 & 0 & 0 \\ 0 & 0 & 0 & 0 & 0 & 0 & 1 & 0 & 0 \\ 0 & 0 & 0 & 0 & 0 & 0 & 0 & 1 & 0 \\ 0 & 0 & 0 & 0 & 0 & 0 & 0 & 0 & 1 \end{pmatrix}, \tag{8.48}$$

where

$$F_{ij} = \begin{cases} Br(\sigma^j \to \sigma^i), & \text{for } i < j, \\ 1, & \text{for } i = j, \\ 0, & \text{for } i > j, \end{cases} \tag{8.49}$$

where $Br(\sigma^j \to \sigma^i)$ represents the branching ratio of state σ_j to σ_i as taken from the Particle Data Group [154]. The direct cross sections are related to the experimental cross sections by the relation $\vec{\sigma}^i_{\text{exp}} = F\vec{\sigma}^i_{\text{direct}}$.

8.2.5 Evolution parameters

Before running the `QTraj` code, we must establish the values of the quantities appearing in the Lindblad equation. The state of the art results at order 0 in the E/T expansion

presented in this chapter take the heavy quark mass M as the mass of the bottom quark computed as half the mass of the $\Upsilon(1S)$ state, i.e., $M = m_b = m_{\Upsilon(1S)}/2 = 4.73$ GeV, where $m_{\Upsilon(1S)}$ is taken from the PDG [154]. The coupling is calculated by solving the defining relation of the Bohr radius with the strong coupling α_s evaluated at the inverse of the Bohr radius a_0^{-1}

$$a_0 = \frac{2}{C_F \alpha_s(1/a_0) m_b}. \tag{8.50}$$

We use the 1-loop running

$$\alpha_s(\mu) = \frac{4\pi}{\beta_0 \ln \frac{\mu^2}{\Lambda_{\text{QCD}}^2}}, \tag{8.51}$$

where Λ_{QCD} is 3-flavor, $\overline{MS}$ value of $\Lambda_{\overline{MS}}^{N_f=3} = 332$ MeV [154] and

$$\beta_0 = 11 - \frac{2}{3} N_f, \tag{8.52}$$

where $N_f = 3$ is the number of flavors. This gives

$$a_0 = 0.678 \text{ GeV}^{-1} \tag{8.53}$$

and

$$\alpha_s(1/a_0) = 0.468. \tag{8.54}$$

With the value of the strong coupling fixed, the only free parameters in the Lindblad equation are the transport coefficients κ and γ. Fundamental κ has been measured directly on the lattice in quenched simulations [110]. The measurement covers the temperature range $1.1 \lesssim T/T_c \lesssim 10^4$, with $T_c = 155$ MeV, and uses pure gauge SU(3) lattice data. In Fig. 5.4, we plot the dimensionless quantity $\hat{\kappa}(T)$ as given by the "fit" curve of Fig. 13 of Ref. [110]. We estimate our systematic uncertainty due to κ by performing QTraj simulations using $\hat{\kappa}(T) = \{\hat{\kappa}_L(T), \hat{\kappa}_C(T), \hat{\kappa}_U(T)\}$ corresponding to the lower, central and upper curves, respectively, of Fig. 5.4. As discussed in chapter 5, κ and γ are related to the real and imaginary parts of the in-medium heavy quarkonium self energy Σ_s and, therefore, to the in-medium width Γ and mass shift δM of the quarkonium state. As no direct lattice measurements of γ have been performed at the time of the writing of this thesis, we estimate our systematic uncertainty due to γ by varying $\hat{\gamma}(T) = \gamma/T^3$ over the values $\hat{\gamma}(T) = \{-3.5, -1.75, 0\}$ corresponding approximately to the range of the indirect lattice extractions given in the right panel of Fig. 5.3. Our general procedure is to run a total of 5 simulations: 3 at fixed $\hat{\gamma} = -1.75$ with $\hat{\kappa}_L(T)$, $\hat{\kappa}_C(T)$ and $\hat{\kappa}_U(T)$ and 2 at fixed $\hat{\kappa}_C(T)$ with $\hat{\gamma} = -3.5$ and 0; for each extracted observable, we present 2 plots: $\hat{\kappa}$ variation on the left and $\hat{\gamma}$ variation on the right. We note that the lattice measurement of Ref. [110] corresponds to the heavy quark momentum diffusion coefficient. As noted in chapter 5, the exact nature of the difference between the heavy quark and heavy quarkonium momentum diffusion coefficients remains an active area of research. We note that the bounds placed on the heavy quark momentum diffusion coefficient by the direct lattice measurement of Ref. [110] fall within the bounds placed on the heavy

quarkonium momentum diffusion coefficient by lattice measurements of $\Gamma(\Upsilon(1S))$ (see Fig. 5.3). In the following chapter in which we solve the Lindblad equation at order 1 in the E/T expansion, we provide an additional estimate of our uncertainty due to κ by performing simulations with fixed $\hat{\kappa} = 0.24$ and 4.2; we find the resulting uncertainty due to κ to increase but remain less than the uncertainty due to γ.

8.2.6 Lattice parameters

In this subsection, we discuss the lattice parameters used in the `QTraj` simulations. In order to fix our initial state $|\psi(t_0)\rangle$, we consider the physics of quarkonium formation; we note that the spatial extent of the region in which the quarkonium forms scales as the inverse of the heavy quark mass M^{-1}. As M is the largest scale of the combined system and specifically due to the relation $M \gg T$, the quarkonium formation is point like with respect to the medium. A Dirac delta function of the radius $\delta^{(3)}(\vec{r})$ is thus the natural initial state. Unfortunately, there exists no unambiguous and stable discretization of the delta function. Refs. [28, 30] made use of the discretization given in Eq. (4.12) of Ref. [155]

$$r\delta^{(3)}(\mathbf{r}) \to \left(\frac{2}{\pi a_s}\right)^2 \frac{n}{4n^2 - 1}(-1)^{n+1},\qquad(8.55)$$

where a_s is the spatial lattice spacing and n is the nth lattice site such that $r = na_s$. This discretization was found, however, to lead to numerical instabilities with the `QTraj` code. We, therefore, utilize a Gaussian initial condition

$$\psi_l(t_0) \propto r^l e^{-r^2/(ca_0)^2},\qquad(8.56)$$

where ψ_l has angular momentum l and c is a dimensionless parameter setting the width of the Gaussian. The narrower the Gaussian, the more faithful the representation of the delta function; this must, however, be counterbalanced with increasing numerical instability and computational cost for narrower initial states. A width of $c = 0.2$ provides a reasonable faithfulness to the delta function while remaining computationally tractable; in Fig. A.1d, we show the convergence of the survival probabilities of the $\Upsilon(1S)$, $\Upsilon(2S)$ and $\Upsilon(3S)$ as $c = \Delta/a_0$ is decreased. Furthermore, comparison with the discretized delta function of Ref. [155] in Fig. 8.1 shows sub percent level relative difference of the survival probability of the $\Upsilon(1S)$ using Bjorken temperature evolution as in Refs. [28, 30].

Production runs take place on a discretized lattice with `NUM` = 4096 spatial sites and radial volume `L` = 80 GeV^{-1} corresponding to a lattice spacing of $a \approx 0.0195$ GeV^{-1}. The wavefunction is evolved using discrete time steps of size `dt` = 0.001 GeV^{-1}. The wavefunction is initialized at time $t = 0$ fm and evolved in the vacuum until interaction with the medium is initialized at time $t = 0.6$ fm. In order to ensure that the hierarchy of scales, specifically $T \gg E$, in which the evolution equations are derived is valid at all times during the simulation, we terminate medium evolution when the local temperature falls below $T_f = 250$ MeV. At temperatures $T > T_f$, the evolution is accurate up to and including terms of order $(rT)^2$ in the EFT power counting while terms of order $(rT)^2(E/T)$ and higher in the E/T expansion are neglected. Evolving in the vacuum in
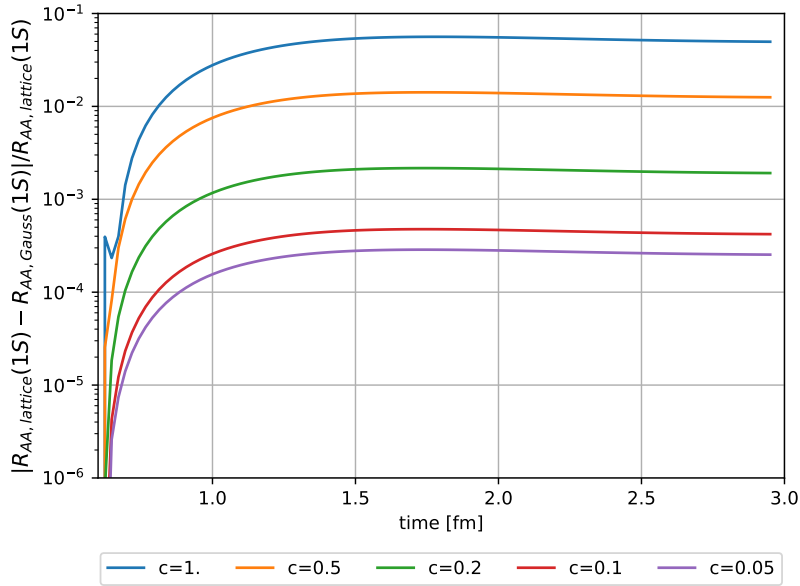
Figure 8.1: The relative difference of the survival probabilities (here called R_{AA}) of the $\Upsilon(1S)$ state computed as in Refs. [28,30] with the lattice regularized delta function initial condition of Eq. (8.55) from Ref. [155] and the Gaussian initial condition of Eq. (8.56). We observe the production level width of $c = 0.2$ to provide sub-percent level accuracy in this observable. Taken from Ref. [60].

the temperature regime $T < T_f$ is accurate neglecting contributions of order $(rT)^2$ in the evolution. As the precise value of $T_f = 250$ MeV is arbitrary, we display in Fig. B.12 the effect on the $\Upsilon(1S)$, $\Upsilon(2S)$ and $\Upsilon(3S)$ survival probabilities of a $\pm 10\%$ variation in T_f. The simulations use trajectory averaged medium evolution and H_{eff} evolution of the quarkonium state; for the $\Upsilon(1S)$, the resulting uncertainty is comparable the uncertainty due to κ and less than that due to γ.

8.3 Results

In this section, we present state of the art results solving the Lindblad equation governing the in-medium evolution of heavy Coulombic quarkonium at order 0 in the E/T expansion. These results were obtained using the `QTraj` code and distinct physical trajectories. All results displayed in this section are taken from Ref. [61].

8.3.1 Nuclear modification factor R_{AA}

We present results for the nuclear modification factor R_{AA} of the $\Upsilon(1S)$, $\Upsilon(2S)$ and $\Upsilon(3S)$ as functions of the number of participating nucleons N_{part} and the transverse
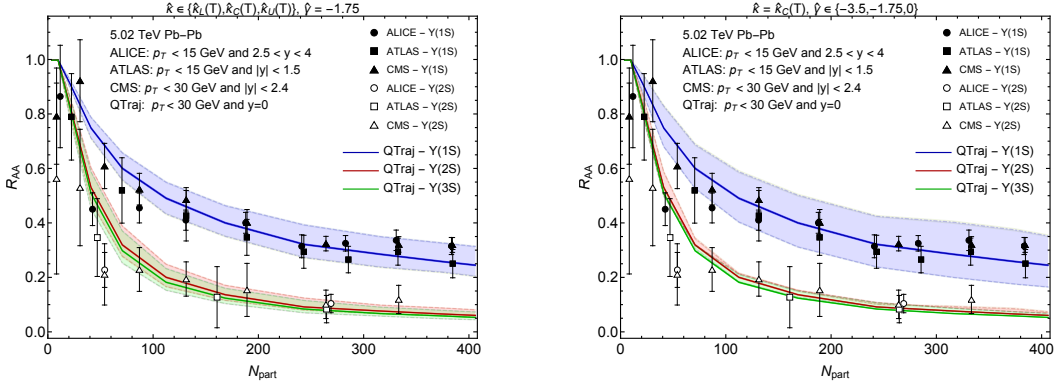
Figure 8.2: The nuclear modification factor R_{AA} of the $\Upsilon(1S)$, $\Upsilon(2S)$ and $\Upsilon(3S)$ plotted against N_{part}. The left panel displays variation with respect to $\hat{\kappa}$, and the right panel variation with respect to $\hat{\gamma}$. The dashed and dot-dashed lines show results for the lower and upper values, respectively, of $\hat{\kappa}(T)$ and $\hat{\gamma}$ while the central curves show results for $\hat{\kappa}_C(T)$ and $\hat{\gamma} = -1.75$. Our theory results are compared against experimental measurements from the ALICE [46], ATLAS [47] and CMS [48] collaborations. Taken from Ref. [61].

momentum p_T. We, furthermore, present results for the double ratios $R_{AA}[\Upsilon(2S)]$ to $R_{AA}[\Upsilon(1S)]$ and $R_{AA}[\Upsilon(3S)]$ to $R_{AA}[\Upsilon(1S)]$ as functions of both N_{part} and p_T. We compare our `QTraj` extractions to experimental measurements of the ALICE [46], AT-LAS [47] and CMS [48,49] collaborations; in all cases, we observe good agreement with the experimental data. In all figures, results displayed in the left panel correspond to simulations conducted with $\hat{\gamma}$ fixed varying $\hat{\kappa}(T)$ and on the right to $\hat{\kappa}(T)$ fixed varying $\hat{\gamma}$.

In Fig. 8.2, we display the nuclear modification factor R_{AA} of the $\Upsilon(1S)$, $\Upsilon(2S)$ and $\Upsilon(3S)$ as functions of the number of participating nucleons N_{part}. We compare our `QTraj` results to measurements of the ALICE [46], ATLAS [47] and CMS [48] collaborations. We observe good agreement with the experimental data across the range of centrality. In the most peripheral collisions, we observe moderate discrepancy with the `QTraj` results lying somewhat above the experimental measurements. We attribute this to the high value of $T_f = 250$ MeV at which the hydrodynamic evolution is terminated. In the most peripheral collisions, the initial temperature of the medium is low such that little to no hydrodynamic evolution takes place (cf. Fig. B.1). This leads to artificially higher yield in the `QTraj` results at lower N_{part} compared to the experimental data. In the following chapter, we present results in which higher order corrections in the E/T expansion are included enabling T_f to be taken to 190 MeV improving the results in peripheral collisions. We observe uncertainty due to γ to be greater than that due to κ. In Figs. 8.3 and 8.4, we plot the double ratios of $R_{AA}[\Upsilon(2S)]$ and $R_{AA}[\Upsilon(3S)]$ to $R_{AA}[\Upsilon(1S)]$, respectively, as functions of N_{part} and compare against experimental measurements of the ALICE [46], ATLAS [47] and CMS [49] collaborations. As in the
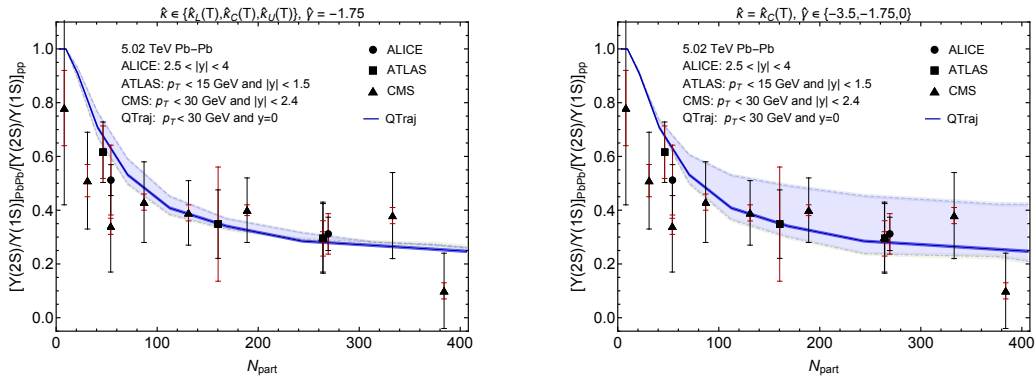
Figure 8.3: The double ratio of the nuclear modification factor $R_{AA}[\Upsilon(2S)]$ to $R_{AA}[\Upsilon(1S)]$ plotted against N_{part}. The theoretical uncertainties are represented as in Fig. 8.2. Our theory results are compared against experimental measurements from the ALICE [46], ATLAS [47] and CMS [49] collaborations. The statistical and systematic uncertainty of the experimental results are represented by black and red bands, respectively. Taken from Ref. [61].

case of the single ratios, we observe good agreement between our `QTraj` results and the experimental measurements across the range of centrality with moderate discrepancy at low N_{part}. Furthermore, we observe a much smaller uncertainty due to κ than due to γ.

In Fig. 8.5, we display `QTraj` results for $R_{AA}[\Upsilon(1S)]$, $R_{AA}[\Upsilon(2S)]$ and $R_{AA}[\Upsilon(3S)]$ as functions of transverse momentum p_T; these results are compared against experimental measurements of the ALICE [46], ATLAS [47] and CMS [48] collaborations. Such differential results were first available in Ref. [61] due to the sampling of distinct physical trajectories implemented in the `QTraj` code between the publication of Refs. [60] and [61]. As in the case of the nuclear modification factor as a function of centrality, we observe good agreement with the experimental data and in this case, furthermore, across the whole range of p_T. In Fig. 8.6, we display `QTraj` results for the double ratio of $R_{AA}[\Upsilon(2S)]$ to $R_{AA}[\Upsilon(1S)]$ as a function of p_T; these results are compared against experimental measurements of the ATLAS [47] and CMS [49] collaborations. As in the case of the double ratio as a function of N_{part}, we observe a low uncertainty due to κ variation and a considerably larger uncertainty due to γ. We observe that in a number of points, the `QTraj` bounds due to κ variation do not overlap with the experimental uncertainty bounds. We note that the experimental uncertainties are significantly larger than the `QTraj` uncertainties due to κ and look forward to further experimental data and reduced experimental uncertainties. For all data points, the `QTraj` uncertainties due to γ overlap with the experimental uncertainties.

81
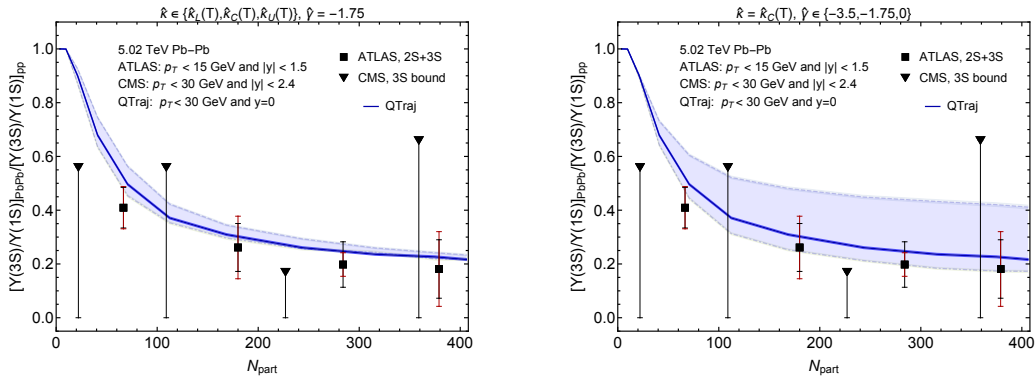
Figure 8.4: The double ratio of the nuclear modification factor $R_{AA}[\Upsilon(3S)]$ to $R_{AA}[\Upsilon(1S)]$ plotted against N_{part}. Our theory results are compared against experimental measurements from the ATLAS [47] and CMS [49] collaborations. Theoretical and experimental uncertainties are represented as in Fig. 8.3. Taken from Ref. [61].

8.3.2 Elliptic flow v_2

In addition to presenting R_{AA} results as a function of p_T, the sampling of distinct physical trajectories allows for the calculation of differential observables including the elliptic flow v_2 which quantifies an azimuthal anisotropy in the observed particle yield [156]. In this subsection, we present results from the QTraj code giving $v_2[\Upsilon(1S)]$ as a function of both centrality and transverse momentum p_T and the elliptic flow of the excited states $v_2[\Upsilon(2S)]$ and $v_2[\Upsilon(3S)]$ as a function of centrality. In Fig. 8.7, we plot $v_2[\Upsilon(1S)]$ as a function of centrality and compare against experimental measurements of the CMS [50] collaboration. We observe the central values of the QTraj results to fall within the experimental uncertainty bounds. Furthermore, the central QTraj result for the $10-90\%$ centrality bin coincides nearly exactly with the central value of the experimental measurement. In Fig. 8.8, we plot $v_2[\Upsilon(1S)]$ against transverse momentum and compare against experimental measurements of the ALICE [51] and CMS [50] collaborations. We again observe good agreement between the QTraj results and the experimental measurements. In Fig. 8.9, we plot $v_2[\Upsilon(2S)]$ and $v_2[\Upsilon(3S)]$ against centrality. We compare against an experimental measurement of the CMS [50] collaboration. We note that the central value of the QTraj results in the $10-90\%$ centrality region falls within the uncertainty of the experimental measurement; we note the uncertainties of the experimental measurement are many times greater than those of the QTraj result.

For all v_2 results presented in this subsection, we observe the central values of the QTraj results to sit within the error bars of the experimental results. We additionally observe our QTraj predictions to be significantly more precise than those currently available from the experimental data. We thus look forward to future experimental measurements and decreased uncertainties.
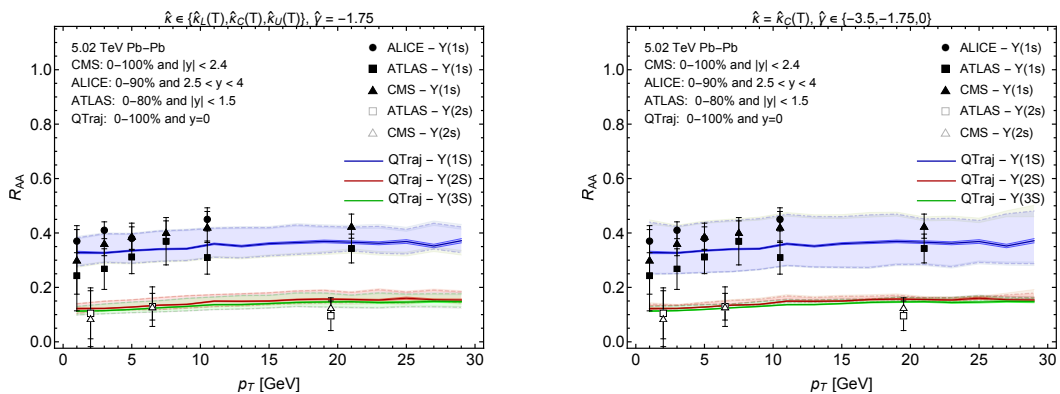
Figure 8.5: The nuclear modification factor R_{AA} of the $\Upsilon(1S)$, $\Upsilon(2S)$ and $\Upsilon(3S)$ plotted against p_T. The theoretical uncertainties are represented as in Fig. 8.2. Our theory results are compared against experimental measurements from the ALICE [46], ATLAS [47] and CMS [48] collaborations. Taken from Ref. [61].

8.3.3 Effect of quantum jumps

In this subsection, we compare `QTraj` results obtained implementing the full quantum trajectories algorithm with quantum jumps and results obtained evolving only with H_{eff} without implementing quantum jumps. In Fig. 8.10, we display results for the nuclear modification factor R_{AA} of the $\Upsilon(2S)$ as a function of p_T; in Fig. 8.11, the double ratio $R_{AA}[\Upsilon(2S)]$ to $R_{AA}[\Upsilon(1S)]$ as a function of p_T and in Fig. 8.12, the elliptic flow v_2 of the $\Upsilon(1S)$ as a function of centrality. We compare these results against experimental measurements of the ATLAS [47] and CMS [48–50] collaborations.

In Fig. 8.10, for all values of κ and γ, we observe the effect of the quantum jumps to be small in absolute terms and significantly smaller than the current uncertainties in the experimental results. We, however, observe variation in the magnitude of the effect depending on the precise values of κ and γ. The combination $\hat{\kappa}_U(T)$ and $\hat{\gamma} = -1.75$ leads to a small but visible difference between the results with and without quantum jumps similar in size to the statistical uncertainty due to averaging over quantum jumps. The combination $\hat{\kappa}_C(T)$ and $\hat{\gamma} = 0$ leads to a difference between the results obtained with and without jumps larger than the statistical uncertainty due to averaging over quantum jumps. In all other cases, the results with and without jumps largely overlap. In Fig. 8.11, we plot the double ratio $R_{AA}[\Upsilon(2S)]/R_{AA}[\Upsilon(1S)]$ as a function of p_T. As in all double ratios, we observe the uncertainty due to κ to be much less than that due to γ. Furthermore, under κ variation, the effect of the jumps is small while under γ variation, we observe a visible effect. In Fig. 8.12, we plot the elliptic flow v_2 of the $\Upsilon(1S)$ as a function of centrality and observe a visible effect of the quantum jumps. The elliptic flow may thus represent an observable in the computation of which quantum jumps play a role.
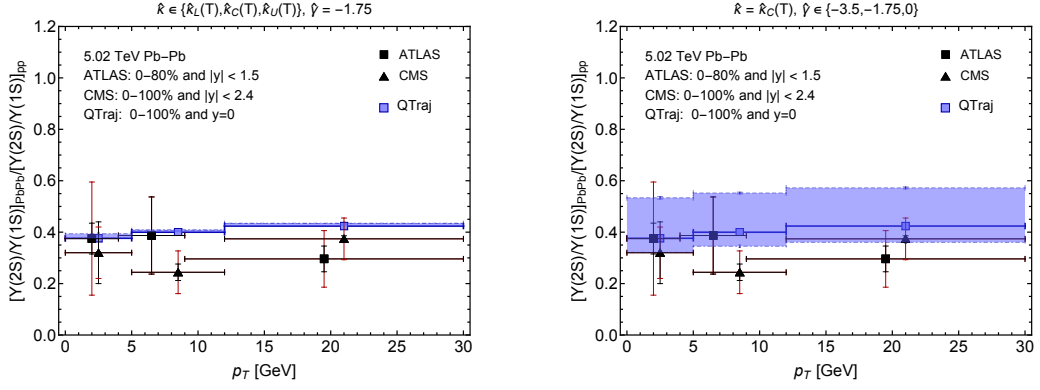
Figure 8.6: The double ratio of the nuclear modification factor $R_{AA}[\Upsilon(2S)]$ to $R_{AA}[\Upsilon(1S)]$ plotted against p_T. Our theory results are compared against experimental measurements from the ATLAS [47] and CMS [49] collaborations. Theoretical and experimental uncertainties are represented as in Fig. 8.3. Taken from Ref. [61].
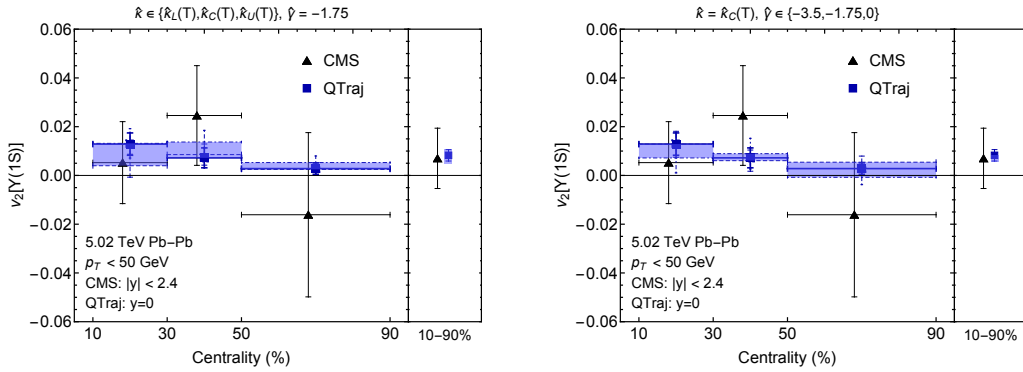

Figure 8.7: The elliptic flow v_2 of the $\Upsilon(1S)$ plotted against centrality. Our theory results are compared against experimental measurements of the CMS [50] collaboration. Uncertainties are represented as in Fig. 8.2. Taken from Ref. [61].
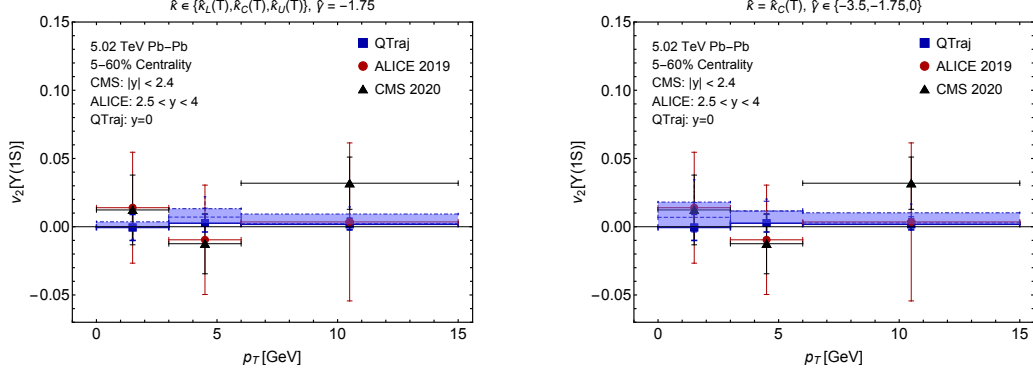
Figure 8.8: The elliptic flow v_2 of the $\Upsilon(1S)$ plotted against p_T. Our theory results are compared against experimental measurements of the ALICE [51] and CMS [50] collaborations. Uncertainties are represented as in Fig. 8.3. Taken from Ref. [61].
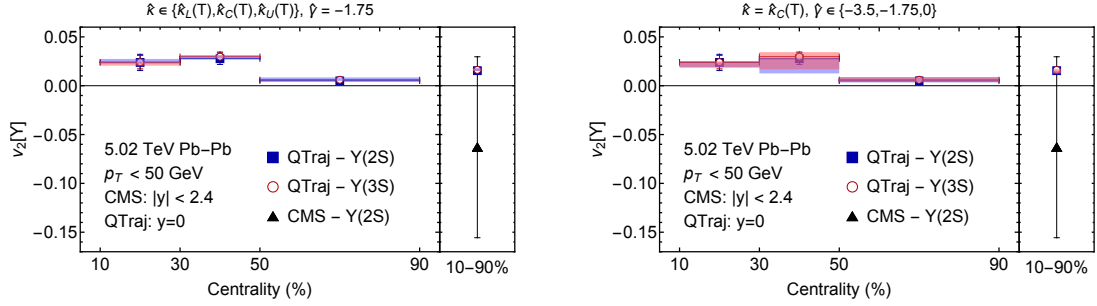
Figure 8.9: The elliptic flow v_2 of the $\Upsilon(2S)$ and $\Upsilon(3S)$ plotted against against centrality. Our theory results are compared against experimental measurements of the CMS [50] collaboration. Uncertainties are represented as in Fig. 8.2. Taken from Ref. [61]

85
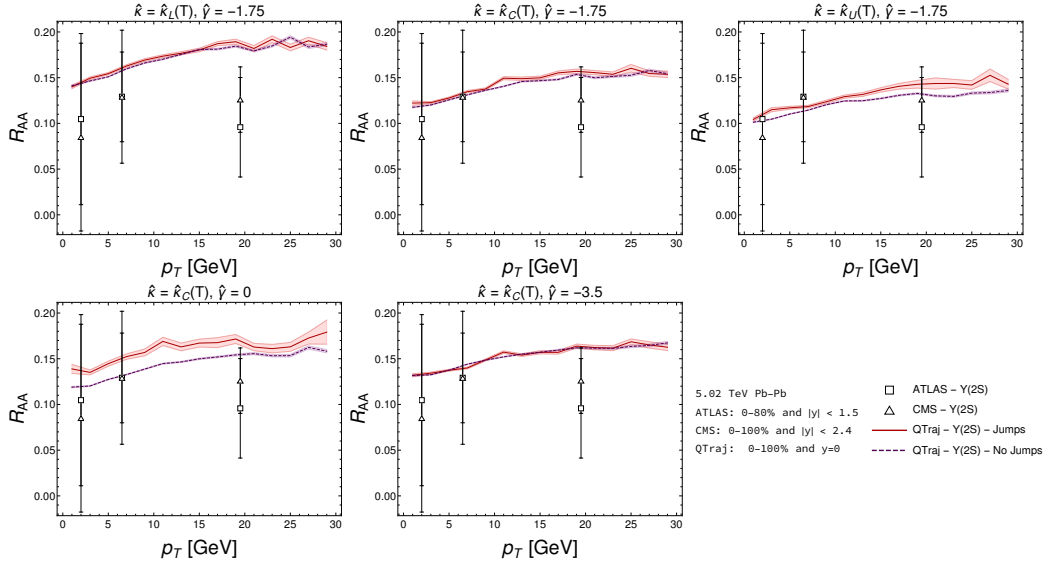
Figure 8.10: The nuclear modification factor R_{AA} of the $\Upsilon(2S)$ plotted against p_T. Each panel compares results obtained implementing only H_{eff} evolution (dotted lines) to full `QTraj` results obtained implementing quantum jumps (solid lines). The top row presents simulations performed with $\hat{\gamma} = 0$ and varying $\hat{\kappa}(T)$, and the bottom row simulations performed with $\hat{\kappa}_C(T)$ and varying $\hat{\gamma}$. Our theory results are compared against experimental measurements of the ATLAS [47] and CMS [48] collaborations. Taken from Ref. [61].
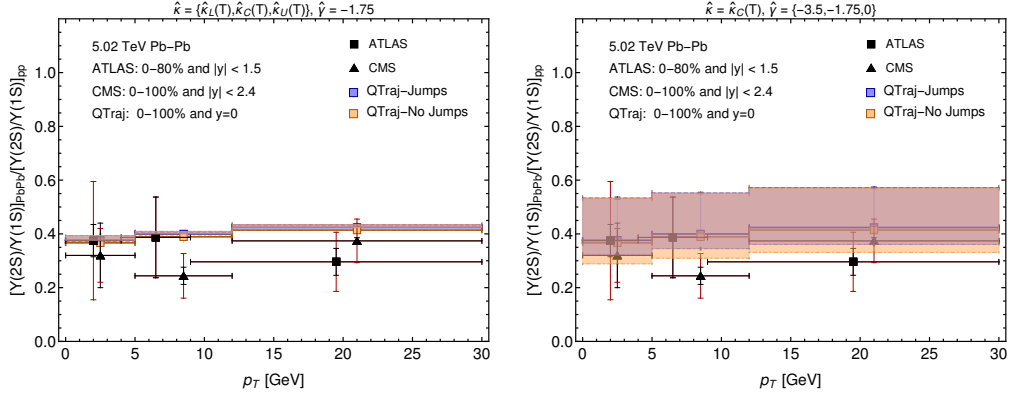
Figure 8.11: The double ratio of the nuclear modification factor $R_{AA}[\Upsilon(2S)]$ to $R_{AA}[\Upsilon(1S)]$ plotted against p_T. We compare the results obtained implementing only H_{eff} evolution (orange) to full `QTraj` results obtained implementing quantum jumps (blue). Uncertainties are represented as in Fig. 8.2. Our theory results are compared against experimental measurements of the the ATLAS [47] and CMS [49] collaborations. Taken from Ref. [61].
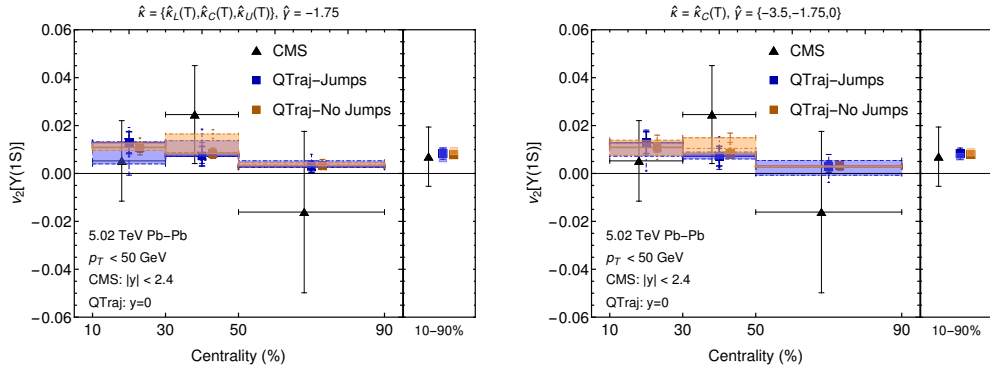
Figure 8.12: The elliptic flow v_2 of the $\Upsilon(1S)$ plotted against centrality. We compare the results obtained implementing only H_{eff} evolution (orange) to full `QTraj` results obtained implementing quantum jumps (blue). Uncertainties are represented as in Fig. 8.10. Our theory results are compared against experimental measurements of the the CMS collaboration [50]. Taken from Ref. [61].

Chapter 9

Heavy quarkonium suppression at next-to-leading order in binding energy over temperature

In this chapter, we extend the analysis of the previous chapter by including terms of order E/T in our in-medium, heavy quarkonium evolution equations. We again consider the master equation derived in Refs. [28, 30] and presented in chapters 3 and 4. The inclusion of these higher order terms allows for the extension of hydrodynamic evolution down to temperatures of $T_f = 190$ MeV much closer to the pseudocritical temperature of the QGP phase transition of $T_{pc} \simeq 158$ MeV [157,158] than the previous lower bound of $T_f = 250$ MeV. In sec. 9.1, we derive the master equation at order 1 in the E/T expansion and discuss the conditions under which the evolution equations can be written as a Lindblad equation. In sec. 9.2, we discuss the implementation of the quantum trajectories algorithm in the `QTraj` code beyond order 0 in the E/T expansion. In sec. 9.3, we present phenomenological results and compare against experimental data.

9.1 Heavy quarkonium evolution at order E/T

As discussed in the preceding chapters of this thesis, the medium correlator

$$A_i^{uv} = \frac{g^2}{6N_c} \int_0^\infty \mathrm{d}t \, e^{-ih_u t} r_i e^{ih_v t} \langle \tilde{E}_j^a(0,\vec{0})\tilde{E}_j^a(t,\vec{0})\rangle, \tag{9.1}$$

completely specifies the interaction of in-medium heavy Coulombic quarkonium with the QGP. Furthermore, in the strict $E \ll T$ limit, the exponentials can be set to unity, and the medium interaction is characterized completely by $A_i^{uv}|_{LO} = \frac{r_i}{2}(\kappa - i\gamma)$ where κ is the heavy quarkonium momentum diffusion coefficient and γ its dispersive counterpart. This case was examined in detail in Refs. [28,30] and further in Refs. [60,61], the results of which are presented in appendix B and chapter 8, respectively. The strict $E \ll T$ limit places a high lower bound on the temperature range over which our analysis is valid

compared to the pseudocritical transition temperature of the QGP. In this section, we extend the range of validity of our evolution equation to lower temperatures by including terms of order 1 in the E/T expansion. Expanding the exponentials of A_i^{uv} to linear order, we find the E/T contributions are given by

$$A_i^{uv}|_{NLO} = \frac{g^2}{6N_c} \int_0^\infty \mathrm{d}t\, t \langle \tilde{E}_j^a(0,\vec{0}) \tilde{E}_j^a(t,\vec{0}) \rangle \left(-\frac{2p_i}{M} + i\Delta V_{uv} r_i \right), \qquad (9.2)$$

where ΔV_{uv} is the difference between the u and v (singlet and octet) potentials.

In the following subsections, we examine the implications of these terms on the pN-RQCD master equation. In subsec. 9.1.1, we derive a relation allowing us to rewrite the terms of order 1 in the E/T expansion in terms of κ and the temperature T. In subsec. 9.1.2, we write the master equation at order 1 in the E/T expansion and determine the conditions under which the evolution equations can still be written in Lindblad form. In subsec. 9.1.3, we expand our NLO Lindblad equation in spherical harmonics and thereby utilize the spherical symmetry of the problem to reduce the number of collapse operators by a factor of 3. This procedure is analogous to that carried out at leading order below Eq. (8.23).

9.1.1 NLO correlator identity

In this section, we derive a relation between the electric-electric correlator at order E/T

$$A_i^{uv}|_{NLO} \sim \frac{g^2}{6N_c} \int_0^\infty \mathrm{d}t\, t \langle \tilde{E}_j^a(0,\vec{0}) \tilde{E}_j^a(t,\vec{0}) \rangle, \qquad (9.3)$$

and the heavy quarkonium momentum diffusion coefficient κ and the temperature T. We begin by defining the finite temperature correlators

$$D^>(t,t') = \left\langle \tilde{E}_i^a(t,\vec{0}) \tilde{E}_i^a(t',\vec{0}) \right\rangle = \frac{1}{Z(T)} \mathrm{Tr}\left(\tilde{E}_i^a(t,\vec{0}) \tilde{E}_i^a(t',\vec{0}) e^{-H/T} \right), \qquad (9.4)$$

$$D^<(t,t') = \left\langle \tilde{E}_i^a(t',\vec{0}) \tilde{E}_i^a(t,\vec{0}) \right\rangle = \frac{1}{Z(T)} \mathrm{Tr}\left(\tilde{E}_i^a(t',\vec{0}) \tilde{E}_i^a(t,\vec{0}) e^{-H/T} \right), \qquad (9.5)$$

where H is the Hamiltonian and $Z(T)$ is the partition function defined by

$$Z(T) = \mathrm{Tr}\left(e^{-H/T} \right). \qquad (9.6)$$

We approximate [29, 159] the NLO chromoelectric correlator as

$$i \int_0^\infty \mathrm{d}t\, t \left\langle \tilde{E}_i^a(t,\vec{0}) \tilde{E}_i^a(0,\vec{0}) \right\rangle \simeq \frac{1}{2} \left. \frac{\mathrm{d}D^>(\omega)}{\mathrm{d}\omega} \right|_{\omega=0}, \qquad (9.7)$$

where $D^>(\omega)$ is the Fourier transform of the electric correlator with respect to the time t, i.e.,

$$\int_{-\infty}^\infty \mathrm{d}t\, e^{i\omega t} \left\langle \tilde{E}_i^a(t,\vec{0}) \tilde{E}_i^a(0,\vec{0}) \right\rangle = D^>(\omega). \qquad (9.8)$$

The approximation of Eq. (9.7) corresponds to an expansion of the correlator around its instantaneous limit.

The thermal field theory interpretation of $e^{-H/T}$ as the time evolution operator in imaginary time, i.e., $e^{-H/T}E_i^a(t, \vec{0})e^{H/T} = E_i^a(t + i/T, \vec{0})$, implies the Kubo–Martin–Schwinger relation

$$D^>(t, t') = D^<(t + i/T, t'), \tag{9.9}$$

and, furthermore, $D^>(t, t') = D^>(t - t')$ and $D^<(t, t') = D^<(t - t')$. Setting $t' = 0$, we derive an expression for the right-hand side of Eq. (9.7) in terms of $D(\omega)$

$$D^>(t) = D^<(-t) = D^<(t + i/T) \tag{9.10}$$

$$\Rightarrow \int_{-\infty}^{\infty} \mathrm{d}t\, e^{i\omega t} D^>(t) = \int_{-\infty}^{\infty} \mathrm{d}t\, e^{i\omega t} D^<(-t) = \int_{-\infty}^{\infty} \mathrm{d}t\, e^{i\omega t} D^<(t + i/T) \tag{9.11}$$

$$\Rightarrow D^>(\omega) = D^<(-\omega) = e^{\omega/T} D^<(\omega) \tag{9.12}$$

$$\Rightarrow \left.\frac{\mathrm{d}D^>(\omega)}{\mathrm{d}\omega}\right|_{\omega=0} = \left.-\frac{\mathrm{d}D^<(\omega)}{\mathrm{d}\omega}\right|_{\omega=0} = \frac{1}{T}D^<(\omega = 0) + \left.\frac{\mathrm{d}D^<(\omega)}{\mathrm{d}\omega}\right|_{\omega=0} \tag{9.13}$$

$$\Rightarrow \left.\frac{\mathrm{d}D^>(\omega)}{\mathrm{d}\omega}\right|_{\omega=0} = \left.-\frac{\mathrm{d}D^<(\omega)}{\mathrm{d}\omega}\right|_{\omega=0} = \frac{1}{2T}D^<(\omega = 0). \tag{9.14}$$

We insert the last equality into Eq. (9.7) giving

$$i\int_0^\infty \mathrm{d}t\, t\left\langle \tilde{E}_i^a(t, \vec{0})\tilde{E}_i^a(0, \vec{0})\right\rangle = \frac{1}{4T}D^<(\omega = 0). \tag{9.15}$$

Inserting the above equality into the anticommutator definition of κ given in, e.g., Eq. (8.18), we derive an expression for κ in terms of $D^<(\omega = 0)$

$$\kappa = \frac{g^2}{6N_c}\int_0^{+\infty} \mathrm{d}t\left\langle \left\{\tilde{E}_i^a(t, \vec{0}), \tilde{E}_i^a(0, \vec{0})\right\}\right\rangle = \frac{g^2}{6N_c}\int_0^{+\infty} \mathrm{d}t\,\left(D^>(t) + D^<(t)\right) \tag{9.16}$$

$$= \frac{g^2}{6N_c}\int_{-\infty}^0 \mathrm{d}t\, D^<(t) + \frac{g^2}{6N_c}\int_0^{+\infty} \mathrm{d}t\, D^<(t) = \frac{g^2}{6N_c}\int_{-\infty}^\infty \mathrm{d}t\, D^<(t) \tag{9.17}$$

$$= \frac{g^2}{6N_c}D^<(\omega = 0). \tag{9.18}$$

Combining Eqs. (9.15) and (9.18), we have an expression for the NLO chromoelectric correlator in terms of the transport coefficient κ and the temperature T

$$i\frac{g^2}{6N_c}\int_0^\infty \mathrm{d}t\, t\left\langle \tilde{E}_i^a(t, \vec{0})\tilde{E}_i^a(0, \vec{0})\right\rangle = \frac{\kappa}{4T}. \tag{9.19}$$

9.1.2 NLO master equation

In this subsection, we write the master equation up to and including terms of order E/T making use of the relation of Eq. (9.19). Up to order E/T, the medium correlator A_i^{uv} is given by

$$A_i^{uv} = \frac{r_i}{2}(\kappa - i\gamma) + \kappa\left(-\frac{ip_i}{2MT} + \frac{\Delta V_{uv}}{4T}r_i\right) + \cdots, \tag{9.20}$$

where the ellipsis represents terms of order $(E/T)^2$ and higher. The master equation is given to all orders in E/T by

$$\frac{d\rho(t)}{dt} = -i\,[H, \rho(t)] + \sum_{nm} h_{nm}\left(L_i^n \rho(t) L_i^{m\dagger} - \frac{1}{2}\left\{L_i^{m\dagger} L_i^n, \rho(t)\right\}\right), \tag{9.21}$$

where

$$\rho(t) = \begin{pmatrix} \rho_s(t) & 0 \\ 0 & \rho_o(t) \end{pmatrix}, \quad H = \begin{pmatrix} h_s + \mathrm{Im}(\Sigma_s) & 0 \\ 0 & h_o + \mathrm{Im}(\Sigma_o) \end{pmatrix}, \tag{9.22}$$

$$L_i^0 = \begin{pmatrix} 0 & 0 \\ 0 & 1 \end{pmatrix} r^i, \quad L_i^1 = \begin{pmatrix} 0 & 0 \\ 0 & \frac{N_c^2-4}{2(N_c^2-1)} A_i^{oo\dagger} \end{pmatrix}, \tag{9.23}$$

$$L_i^2 = \begin{pmatrix} 0 & 1 \\ 1 & 0 \end{pmatrix} r^i, \quad L_i^3 = \begin{pmatrix} 0 & \frac{1}{N_c^2-1} A_i^{os\dagger} \\ A_i^{so\dagger} & 0 \end{pmatrix}, \tag{9.24}$$

$$h = \begin{pmatrix} 0 & 1 & 0 & 0 \\ 1 & 0 & 0 & 0 \\ 0 & 0 & 0 & 1 \\ 0 & 0 & 1 & 0 \end{pmatrix}. \tag{9.25}$$

At order 1 in the E/T expansion, the medium interaction operators L_i^1 and L_i^3 take the form

$$L_i^1 = \frac{N_c^2-4}{2(N_c^2-1)} \begin{pmatrix} 0 & 0 \\ 0 & 1 \end{pmatrix} \left[\frac{r_i}{2}(\kappa + i\gamma) + \kappa\frac{ip_i}{2MT}\right], \tag{9.26}$$

$$\begin{aligned} L_i^3 &= \begin{pmatrix} 0 & \frac{1}{N_c^2-1} \\ 0 & 0 \end{pmatrix} \left[\frac{r_i}{2}(\kappa + i\gamma) + \kappa\left(\frac{ip_i}{2MT} + \frac{\Delta V_{os}}{4T}r_i\right)\right] \\ &\quad + \begin{pmatrix} 0 & 0 \\ 1 & 0 \end{pmatrix} \left[\frac{r_i}{2}(\kappa + i\gamma) + \kappa\left(\frac{ip_i}{2MT} + \frac{\Delta V_{so}}{4T}r_i\right)\right], \end{aligned} \tag{9.27}$$

and the corrections to the potential are given by

$$\mathrm{Im}\,(\Sigma_s) = \frac{r^2}{2}\gamma + \frac{\kappa}{4MT}\{r_i, p_i\}, \tag{9.28}$$

$$\mathrm{Im}\,(\Sigma_o) = \frac{N_c^2-2}{2(N_c^2-1)}\left(\frac{r^2}{2}\gamma + \frac{\kappa}{4MT}\{r_i, p_i\}\right). \tag{9.29}$$

The above set of coupled equations describes the in-medium evolution of heavy Coulombic quarkonium at order 1 in the E/T expansion. We note that the above equations cannot in general be written in Lindblad form due to the negative eigenvalues of the matrix h_{nm}. Furthermore, in contrast to the case at leading order discussed in chapter 8, as L_1 and L_3 are linearly independent of L_0 and L_2, no rotation of the vector L_n enables us to write the above master equation in Lindblad form. In the remainder of this subsection, we present an approximation which allows us to write a Lindblad

equation containing terms up to order $(E/T)^2$ equivalent to the above master equation up to order E/T.

In the master equation, there are three distinct vector spaces corresponding to color, spatial direction and transition operator. The color vector space is unlabeled and corresponds to the entries of the transition operator matrices, i.e., $(L_i^n)_{ab}$ where a and b label the entries of the matrix operator L_i^n and take the values 0 and 1. The spatial direction is labeled by the index i and takes the values 1, 2 and 3. The transition operator is labeled by the index m or n and takes the values 0 to 3. As the matrix h_{nm} is block diagonal, i.e., only combinations of $n, m = 0$ and 1 and separately 2 and 3 are nonzero, we consider only a single block and note that the procedure is generalizable to the full vector space. For simplicity, we take

$$h_{nm} = \begin{pmatrix} 0 & 1 \\ 1 & 0 \end{pmatrix}, \quad L_n = \begin{pmatrix} L_0 \\ L_1 \end{pmatrix}. \tag{9.30}$$

Our aim is to find collapse operators C_n which enable us to write a Lindblad equation

$$\frac{d\rho(t)}{dt} = -i \left[H, \rho(t) \right] + \sum_{n=0}^{1} \left(C_n \rho(t) C_n^\dagger - \frac{1}{2} \left\{ C_n^\dagger C_n, \rho(t) \right\} \right), \tag{9.31}$$

equivalent to the master equation. Based on the structure of the scalar product in the transition operator space, i.e.,

$$L_n^\dagger \cdot L_n = h_{nm} L_m^\dagger L_n = L_0^\dagger L_1 + L_1^\dagger L_0, \tag{9.32}$$

this is equivalent to solving the equation

$$C^\dagger C = L_0^\dagger L_1 + L_1^\dagger L_0, \tag{9.33}$$

for C.

We consider first the case realized at order 0 in the E/T expansion in which L_0 and L_1 are linearly dependent, i.e., $L_1 = (a + bi)L_0$, where a and b are real scalars. Inserting this into Eq. (9.33), we have

$$C^\dagger C = 2a L_0^\dagger L_0, \tag{9.34}$$

with solution

$$C = \sqrt{2a} L_0. \tag{9.35}$$

From a linear algebra perspective, this result can be derived equivalently via a rotation of the basis state L_n which leaves the matrix h_{nm} unchanged

$$\begin{pmatrix} L_0^\dagger & (a - ib)L_0^\dagger \end{pmatrix} \begin{pmatrix} 0 & 1 \\ 1 & 0 \end{pmatrix} \begin{pmatrix} L_0 \\ (a + ib)L_0 \end{pmatrix} = a \begin{pmatrix} L_0^\dagger & L_0^\dagger \end{pmatrix} \begin{pmatrix} 0 & 1 \\ 1 & 0 \end{pmatrix} \begin{pmatrix} L_0 \\ L_0 \end{pmatrix}. \tag{9.36}$$

Diagonalization leads to the relation

$$a \begin{pmatrix} L_0^\dagger & L_0^\dagger \end{pmatrix} \begin{pmatrix} 0 & 1 \\ 1 & 0 \end{pmatrix} \begin{pmatrix} L_0 \\ L_0 \end{pmatrix} = \begin{pmatrix} 0 & \sqrt{2a}L_0^\dagger \end{pmatrix} \begin{pmatrix} -1 & 0 \\ 0 & 1 \end{pmatrix} \begin{pmatrix} 0 \\ \sqrt{2a}L_0 \end{pmatrix}, \tag{9.37}$$

92

and the clear assignment $C = \sqrt{2a}L_0$.

We examine this procedure in the case L_0 and L_1 are neither linearly dependent nor orthogonal

$$L_1 = (a + ib)L_0 + \epsilon L_1^{(1)}. \tag{9.38}$$

ϵ is here a complex scalar and $L_1^{(1)}$ is nonzero and linearly independent of L_0, i.e., there exists no scalar c for which $L_0 = cL_1^{(1)}$. We follow the diagonalization procedure implemented in the case L_0 and L_1 are linearly dependent. Rotating the basis vector L_n as in Eq. (9.36), we have

$$\left(L_0^\dagger \quad \left[aL_0^\dagger + \epsilon^* L_1^{(1)\dagger} \right] \right) \begin{pmatrix} 0 & 1 \\ 1 & 0 \end{pmatrix} \begin{pmatrix} L_0 \\ \left[aL_0 + \epsilon L_1^{(1)} \right] \end{pmatrix} = \tag{9.39}$$

$$\frac{1}{a} \left(aL_0^\dagger \quad \left[aL_0^\dagger + \epsilon^* L_1^{(1)\dagger} \right] \right) \begin{pmatrix} 0 & 1 \\ 1 & 0 \end{pmatrix} \begin{pmatrix} aL_0 \\ \left[aL_0 + \epsilon L_1^{(1)} \right] \end{pmatrix}. \tag{9.40}$$

We diagonalize the matrix h_{nm} as in Eqs. (9.37) leading to the relation

$$\frac{1}{a} \left(aL_0^\dagger \quad \left[aL_0^\dagger + \epsilon^* L_1^{(1)\dagger} \right] \right) \begin{pmatrix} 0 & 1 \\ 1 & 0 \end{pmatrix} \begin{pmatrix} aL_0 \\ \left[aL_0 + \epsilon L_1^{(1)} \right] \end{pmatrix} = \tag{9.41}$$

$$\left(\frac{\epsilon^*}{\sqrt{2a}}L_0^\dagger \quad \left[\sqrt{2a}L_0^\dagger + \frac{\epsilon^*}{\sqrt{2a}}L_1^{(1)\dagger} \right] \right) \begin{pmatrix} -1 & 0 \\ 0 & 1 \end{pmatrix} \begin{pmatrix} \frac{\epsilon}{\sqrt{2a}}L_0 \\ \left[\sqrt{2a}L_0 + \frac{\epsilon}{\sqrt{2a}}L_1^{(1)} \right] \end{pmatrix}. \tag{9.42}$$

We note that the above equation is not of Lindblad form, and a term enters the master equation with an overall negative sign relative to the sign convention of the Lindblad equation. In this case, as the L_0 and L_1 are not linearly dependent, there exists no rotation into a vector orthogonal to the eigenvector of the negative eigenvalue of h_{nm}. However, taking Eq. (9.38) as an expansion in small ϵ, i.e., $|\epsilon| \ll 1$, we may remove the term of order ϵ^2 from the master equation, and the resulting evolution equation is accurate up to order ϵ and can be written in Lindblad form. In this case, the collapse operator is given by

$$C = \sqrt{2a}L_0 + \frac{\epsilon}{\sqrt{2a}}L_1^{(1)}. \tag{9.43}$$

This corresponds to completing the square in ϵ. Inserting Eq. (9.38) into Eq. (9.33), we have the equation

$$C^\dagger C = 2aL_0^\dagger L_0 + \epsilon L_0^\dagger L_1^{(1)} + \epsilon^* L_1^{(1)\dagger} L_0, \tag{9.44}$$

which we solve at order ϵ by completing the square, i.e.,

$$C^\dagger C = 2aL_0^\dagger L_0 + \epsilon L_0^\dagger L_1^{(1)} + \epsilon^* L_1^{(1)\dagger} L_0 + \frac{|\epsilon|^2}{2a}L_1^{(1)\dagger} L_1^{(1)}, \tag{9.45}$$

with the solution given in Eq. (9.43).

93

Following the above procedure, we rewrite the master equation of Eqs. (9.21)-(9.25) at order 1 in the E/T expansion as the Lindblad equation

$$\frac{d\rho(t)}{dt} = -i\,[H, \rho(t)] + \sum_n \left(C_i^n \rho(t) C_i^{n\dagger} - \frac{1}{2} \left\{ C_i^{n\dagger} C_i^n, \rho(t) \right\} \right), \tag{9.46}$$

with Hamiltonian

$$H = \begin{pmatrix} h_s + \mathrm{Im}(\Sigma_s) & 0 \\ 0 & h_o + \mathrm{Im}(\Sigma_o) \end{pmatrix}, \tag{9.47}$$

where

$$\mathrm{Im}\,(\Sigma_s) = \frac{r^2}{2}\gamma + \frac{\kappa}{4MT}\{r_i, p_i\}, \quad \mathrm{Im}\,(\Sigma_o) = \frac{N_c^2 - 2}{2(N_c^2 - 1)} \left(\frac{r^2}{2}\gamma + \frac{\kappa}{4MT}\{r_i, p_i\} \right), \tag{9.48}$$

and collapse operators

$$\begin{aligned} C_i^0 &= \sqrt{\frac{\kappa}{N_c^2 - 1}} \begin{pmatrix} 0 & 1 \\ 0 & 0 \end{pmatrix} \left(r_i + \frac{ip_i}{2MT} + \frac{\Delta V_{os}}{4T} r_i \right) \\ &\quad + \sqrt{\kappa} \begin{pmatrix} 0 & 0 \\ 1 & 0 \end{pmatrix} \left(r_i + \frac{ip_i}{2MT} + \frac{\Delta V_{so}}{4T} r_i \right), \end{aligned} \tag{9.49}$$

$$C_i^1 = \sqrt{\frac{\kappa(N_c^2 - 4)}{2(N_c^2 - 1)}} \begin{pmatrix} 0 & 0 \\ 0 & 1 \end{pmatrix} \left(r_i + \frac{ip_i}{2MT} \right). \tag{9.50}$$

The terms of C_i^n proportional to r_i are of order $(E/T)^0$ while those proportional to p_i and ΔV_{uv} are of order E/T. The Lindblad equation thus contains terms up to and including order $(E/T)^2$; the terms up to and including order E/T are the master equation with L_i^1 and L_i^3 as given in Eqs. (9.26) and (9.27). The Lindblad equation specified by the collapse operators of Eqs. (9.49) and (9.50) is thus accurate up to and including terms of order E/T. We have thus brought the master equation at order E/T into Lindblad form at the price of introducing spurious terms at order $(E/T)^2$. We note that the above Lindblad equation is equivalent to that presented in sec. 4.2 of Ref. [39].

9.1.3 Angular momentum projection

In this subsection, we utilize the spherical symmetry of the quarkonium system to reduce the 6 collapse operators given in Eqs. (9.49) and (9.50) to 2. Our procedure follows that detailed below Eq. (8.23), i.e., we derive the form of the Lindblad equation for a state ρ^l of definite angular momentum by projecting onto spherical harmonics

$$\rho^{lm} = \int d\Omega(\theta, \phi) d\Omega(\theta', \phi')\, Y_{lm}(\theta, \phi)\, \rho\, Y_{lm}^*(\theta', \phi'), \tag{9.51}$$

and summing over the magnetic quantum number m

$$\rho^l = \sum_m \rho^{lm}. \tag{9.52}$$

The projection of the NLO collapse operators is complicated with respect to the LO case by the presence of the momentum operator p_i. We present a detailed derivation of the projection procedure in appendix C and quote the results below.

The precise form of the collapse operators and Hamiltonian acting on the density matrix depend on the color and angular momentum quantum numbers of the state. The density matrix can be decomposed as the tensor product of a color, angular momentum and radial component

$$\rho = \rho_c \otimes \rho_l \otimes \rho(r), \tag{9.53}$$

respectively. The entries of the density matrix take the form

$$\rho = \begin{pmatrix} \rho_s^0 & 0 & \dots & 0 & 0 & \cdots \\ 0 & \rho_s^1 & \dots & 0 & 0 & \dots \\ \vdots & \vdots & \ddots & \vdots & \vdots & \\ 0 & 0 & \dots & \rho_o^0 & 0 & \dots \\ 0 & 0 & \dots & 0 & \rho_o^1 & \dots \\ \vdots & \vdots & & \vdots & \vdots & \ddots \end{pmatrix}, \tag{9.54}$$

where ρ_u^l represents the radial density matrix with color u and angular momentum l. The above matrix is diagonal and of infinite dimension. The free Hamiltonian is an analogous diagonal, infinite dimensional matrix the elements of which are given by

$$h_{s,o}^l = -\frac{1}{M}\left(\frac{\partial^2}{\partial r^2} + \frac{2}{r}\frac{\partial}{\partial r}\right) + V_{s,o} + \frac{l(l+1)}{Mr^2}. \tag{9.55}$$

As shown in appendix C, the collapse operators take the form

$$C_0 = \sqrt{\frac{\kappa}{N_c^2 - 1}}\begin{pmatrix} 0 & 1 \\ 0 & 0 \end{pmatrix} \otimes \left(O^-\sqrt{\frac{l}{2l+1}}C_{o\to s}^\downarrow + O^+\sqrt{\frac{l+1}{2l+1}}C_{o\to s}^\uparrow\right) \tag{9.56}$$

$$+ \sqrt{\kappa}\begin{pmatrix} 0 & 0 \\ 1 & 0 \end{pmatrix} \otimes \left(O^-\sqrt{\frac{l}{2l+1}}C_{s\to o}^\downarrow + O^+\sqrt{\frac{l+1}{2l+1}}C_{s\to o}^\uparrow\right), \tag{9.57}$$

$$C_1 = \sqrt{\frac{\kappa(N_c^2 - 4)}{2(N_c^2 - 1)}}\begin{pmatrix} 0 & 0 \\ 0 & 1 \end{pmatrix} \otimes \left(O^-\sqrt{\frac{l}{2l+1}}C_{o\to o}^\downarrow + O^+\sqrt{\frac{l+1}{2l+1}}C_{o\to o}^\uparrow\right), \tag{9.58}$$

where the 2×2 matrices represent color transitions and $O^\pm$ are infinite dimensional matrices implementing the angular momentum transitions the elements of which are given by $O_{l'l}^\pm = \delta_{l',l\pm1}$. The operators acting on the spatial wave function take the form

$$C_{u\to v}^\uparrow = r\left(1 + \frac{\Delta V_{uv}}{4T}\right) + \frac{1}{2MT}\left(\frac{\partial}{\partial r} - \frac{l}{r}\right), \tag{9.59}$$

$$C_{u\to v}^\downarrow = r\left(1 + \frac{\Delta V_{uv}}{4T}\right) + \frac{1}{2MT}\left(\frac{\partial}{\partial r} + \frac{l+1}{r}\right). \tag{9.60}$$

As at order 0 in E/T, the isotropy of the physical system allows us to reduce the number of collapse opeartors from 6 to 2 and bring the Lindblad equation into a form amenable to solution using the `QTraj` code.

We proceed to compute the branching fractions in the color and angular momentum sectors. We first define the decay width Γ as the trace of the anticommutator term of the Lindblad equation

$$\Gamma\left[\rho_u^l(r)\right] \equiv \sum_{n=0}^{n=1} \mathrm{Tr}\left[C_n^\dagger C_n \rho_u^l(r)\right], \tag{9.61}$$

where the left-hand side of the equation is a functional of the state $\rho_u^l(r)$ and returns its decay width Γ. We define branching ratios Br in the angular momentum sector and widths Γ in the color sector

$$Br_\uparrow = \frac{l+1}{2l+1}, \tag{9.62}$$

$$Br_\downarrow = \frac{l}{2l+1}, \tag{9.63}$$

$$\Gamma_{s\to o} = \kappa\left\{r^2\left(1 + \frac{\Delta V_{so}}{4T}\right)^2 - \frac{3}{2MT} - \frac{\Delta V_{so}}{4MT^2} + \frac{\mathcal{D}^2}{4M^2T^2}\right\}, \tag{9.64}$$

$$\Gamma_{o\to s} = \frac{\kappa}{N_c^2-1}\left\{r^2\left(1 + \frac{\Delta V_{os}}{4T}\right)^2 - \frac{3}{2MT} - \frac{\Delta V_{os}}{4MT^2} + \frac{\mathcal{D}^2}{4M^2T^2}\right\}, \tag{9.65}$$

$$\Gamma_{o\to o} = \frac{\kappa(N_c^2-4)}{2(N_c^2-1)}\left\{r^2 - \frac{3}{2MT} + \frac{\mathcal{D}^2}{4M^2T^2}\right\}, \tag{9.66}$$

where

$$\mathcal{D}^2 = -\left(\frac{\partial^2}{\partial r^2} + \frac{2}{r}\frac{\partial}{\partial r}\right) + \frac{l(l+1)}{r^2}. \tag{9.67}$$

The branching ratios and width operators are defined such that the partial decay width $\Gamma_{u\to v}^{\uparrow,\downarrow}$ of the state $\rho_u^l(r)$ is calculated as

$$\Gamma_{u\to v}^{\uparrow,\downarrow}\left[\rho_u^l(r)\right] = \mathrm{Tr}_r\left[Br_{\uparrow,\downarrow}\Gamma_{u\to v}\rho(r)\right], \tag{9.68}$$

where the left-hand side of the equation represents a functional of the state $\rho_u^l(r)$ which returns the partial width to a state of angular momentum $l \pm 1$ and color v and on the right-hand side Tr_r represents a trace over the radial coordinate. We note that in contrast to the LO Lindblad equation, in the NLO case, the octet to octet and octet to singlet branching fractions can no longer be extracted trivially from the color factors in the collapse operators; they must be computed in dependence on the wave function at the time of the jump using the width operators $\Gamma_{o\to s}$ and $\Gamma_{o\to o}$ defined above.

9.2 The `QTraj` code at NLO in E/T

In this section, we discuss the implementation of the quantum trajectories algorithm in the `QTraj` code used to solve the NLO Lindblad equation. The `QTraj` code utilizes

the reduced wave function $u(r,t) = rR(r,t)$ where $R(r,t)$ is the radial wave function defined by $\psi(r,\theta,\phi) = R(r)Y_{lm}(\theta,\phi)$. The jump and width operators given in the previous section act on the radial wave function $R(r,t)$. We denote operators acting on the reduced radial wave function $u(r,t)$ as being in the reduced spherical basis and mark them with an overbar. In the reduced spherical basis, the collapse operators of Eqs. (9.59) and (9.60) take the form

$$\overline{C}^{\uparrow}_{s\to o} = r - \frac{N_c\alpha_{\mathrm{s}}}{8T} + \frac{1}{2MT}\left(\frac{\partial}{\partial r} - \frac{l+1}{r}\right), \tag{9.69}$$

$$\overline{C}^{\downarrow}_{s\to o} = r - \frac{N_c\alpha_{\mathrm{s}}}{8T} + \frac{1}{2MT}\left(\frac{\partial}{\partial r} + \frac{l}{r}\right), \tag{9.70}$$

$$\overline{C}^{\uparrow}_{o\to s} = r + \frac{N_c\alpha_{\mathrm{s}}}{8T} + \frac{1}{2MT}\left(\frac{\partial}{\partial r} - \frac{l+1}{r}\right), \tag{9.71}$$

$$\overline{C}^{\downarrow}_{o\to s} = r + \frac{N_c\alpha_{\mathrm{s}}}{8T} + \frac{1}{2MT}\left(\frac{\partial}{\partial r} + \frac{l}{r}\right), \tag{9.72}$$

$$\overline{C}^{\uparrow}_{o\to o} = r + \frac{1}{2MT}\left(\frac{\partial}{\partial r} - \frac{l+1}{r}\right), \tag{9.73}$$

$$\overline{C}^{\downarrow}_{o\to o} = r + \frac{1}{2MT}\left(\frac{\partial}{\partial r} + \frac{l}{r}\right), \tag{9.74}$$

where we write ΔV_{uv} explicitly. The color width operators in the reduced spherical basis weighted by the angular momentum branching fractions are given by

$$\overline{\Gamma}^{\uparrow}_{o\to s} = \frac{\hat{\kappa}T^3}{N_c^2-1}\frac{l+1}{2l+1}\left[\left(r+\frac{N_c\alpha_{\mathrm{s}}}{8T}\right)^2 - \frac{3}{2MT} + \frac{\overline{\mathcal{D}}^2}{(2MT)^2} - \frac{1}{2MT}\left(\frac{N_c\alpha_{\mathrm{s}}}{4T}\right)\frac{1}{r}\right], \tag{9.75}$$

$$\overline{\Gamma}^{\downarrow}_{o\to s} = \frac{l}{l+1}\overline{\Gamma}^{\uparrow}_{o\to s}, \tag{9.76}$$

$$\overline{\Gamma}^{\uparrow}_{o\to o} = \hat{\kappa}T^3\frac{N_c^2-4}{2(N_c^2-1)}\frac{l+1}{2l+1}\left[r^2 - \frac{3}{2MT} + \frac{\overline{\mathcal{D}}^2}{(2MT)^2}\right], \tag{9.77}$$

$$\overline{\Gamma}^{\downarrow}_{o\to o} = \frac{l}{l+1}\overline{\Gamma}^{\uparrow}_{o\to o}, \tag{9.78}$$

where $\overline{\Gamma}^{\uparrow,\downarrow}_{u\to v} = Br_{\uparrow,\downarrow}\overline{\Gamma}_{u\to v}$, $\hat{\kappa} = \kappa/T^3$ and

$$\overline{\mathcal{D}}^2 = -\frac{\partial^2}{\partial r^2} + \frac{l(l+1)}{r^2}. \tag{9.79}$$

At NLO in E/T, the quantum trajectories algorithm is implemented according to the following algorithm:

1. Initialize the wave function $|\psi(t_0)\rangle$ at time t_0 where $\rho(t_0) = |\psi(t_0)\rangle\langle\psi(t_0)|$ where t_0 is the initial time of the evolution.

97

2. Generate a random number $0 < p_1 < 1$ and evolve the wave function forward in time with H_{eff} until its norm squared is less than or equal to p_1, i.e.,

$$|| e^{-i \int_{t_0}^{t} dt' H_{\text{eff}}(t')} |\psi(t_0)\rangle ||^2 \leq p_1 \, . \tag{9.80}$$

Denote the first time step fulfilling Eq. (9.80) the jump time t_j and proceed to step 3 if $t_j < t_f$ where t_f is the simulation run time; otherwise, end the simulation at time t_f.

3. At time t_j, perform a quantum jump.
   If the color quantum number is singlet ($c = 0$):

   (a) Change the color quantum number to octet ($c \to 1$).
   (b) Generate an additional random number $0 < p_2 < 1$, and if $p_2 < l/(2l+1)$, take $l \to l-1$; otherwise, take $l \to l+1$.

   Else, i.e., if the color quantum number is octet ($c = 1$):

   (a) Compute the 4 branching fractions $Br_{o \to s,o}^{\uparrow,\downarrow}$.
   (b) Generate an additional random number $0 < p_2 < 1$, and if $p_2 < Br_{o \to s}^{\downarrow} + Br_{o \to o}^{\downarrow} = l/(2l+1)$, take $l \to l-1$; otherwise, take $l \to l+1$.
   (c) Generate an additional random number $0 < p_3 < 1$, and if $p_3 < Br_{o \to s}^{\downarrow} + Br_{o \to s}^{\uparrow}$, set the color quantum number to singlet ($c \to 0$); otherwise, remain in the octet configuration ($c = 1$).

4. Continue from step 2.

A realization of the above algorithm is a *quantum trajectory*; the average of N quantum trajectories converges to the solution of the NLO Lindblad equation in the limit $N \to \infty$.

At NLO, the effective Hamiltonian contains a term proportional to the anticommutator $\{r_i, p_i\}$ (cf. Eqs.(9.47) and (9.48)). This term complicates the use of the Suzuki-Trotter split-step pseudospectral method used at LO to evolve the wave function deterministically between quantum jumps. To implement the NLO evolution, we use instead the Crank-Nicolson method which approximates the time evolution operator as

$$\exp\left[-iH_{l,c}\Delta t\right] \simeq \frac{1 - i\Delta t H_{l,c}/2}{1 + i\Delta t H_{l,c}/2}, \tag{9.81}$$

where $H_{l,c}$ is the heavy quarkonium effective Hamiltonian projected onto the angular momentum l and color c of the quarkonium state and contains the in-medium corrections to the potential. In the reduced spherical basis, this allows us to write

$$\left(1 + i\Delta t \overline{H}_{l,c}/2\right) u(t + \Delta t) = \left(1 - i\Delta t \overline{H}_{l,c}/2\right) u(t). \tag{9.82}$$

The temporal update is performed by computing the right-hand side of the equation and subsequently solving for $u(t + \Delta t)$. The NLO `QTraj` code uses the open-source Armadillo [160] package's optimized sparse matrix solver `spsolve` to solve for $u(t+\Delta t)$.

9.3 Results

In this section, we present the results of our `QTraj` simulation solving the NLO Lindblad equation derived in the previous two sections. Due to the increased computational costs associated with NLO evolution, the NLO `QTraj` code implements a number of changes with respect to the LO version to decrease the computational cost of the simulations. Specifically, the results presented in this section utilize a lattice of spatial extent $L = 40$ GeV^{-1} with `NUM` $= 2048$ spatial sites; both the spatial extent of the lattice and number of lattice sites are halved with respect to values used to solve the LO Lindblad equation in chapter 8 giving an identical lattice spacing of $a \approx 0.0195$ GeV^{-1}. As in the LO case, the initial state is the Gaussian given in Eq. (8.56) with width $c = 0.2$. The heavy quark mass M, strong coupling α_s and Bohr radius a_0 are as in the LO case detailed in subsec. 8.2.5.

The remainder of this section is structured as follows. In subsec. 9.3.1, we examine the phenomenological impact of the NLO evolution terms with the aim of fixing a lower temperature bound T_f for the coupling to the medium. In subsec. 9.3.2, we quantify the effect of the NLO terms on the singlet to octet width. In subsec. 9.3.3, we quantify the effect of the NLO evolution on the survival probability of the $\Upsilon(1S)$ state. In subsec. 9.3.4, we analyze the effect of quantum jumps on the NLO Lindblad equation. In subsec. 9.3.5, we present our main phenomenological results: the nuclear modification factor R_{AA} of the $\Upsilon(1S)$, $\Upsilon(2S)$ and $\Upsilon(3S)$ as functions of N_{part}. In subsec. 9.3.6, we present results obtained initializing the coupling of the quarkonium evolution to the hydrodynamic evolution at $\tau_{\text{med}} = 0.25$ fm rather than $\tau_{\text{med}} = 0.6$ fm. In subsec. 9.3.7, we estimate our uncertainty due to the use of the fundamental rather the adjoint κ by running simulations with constant $\hat{\kappa} = 0.24$ and 4.2 corresponding to the indirect bounds placed on the heavy quarkonium momentum diffusion coefficient by lattice measurements of $\Gamma[\Upsilon(1S)]$ (cf. Fig. 5.3).

9.3.1 Phenomenological impact of NLO terms

The NLO Lindblad equation presented in this chapter allows for the coupling of the quarkonium and the medium at temperatures lower than $T_f = 250$ MeV used in Refs. [60, 61]. In Fig. 9.1, we display the relative difference of the survival probabilities of the $\Upsilon(1S)$ state calculated using the LO and NLO Lindblad equations; both simulations utilize Bjorken medium evolution and an initial temperature of $T_0 = 425$ MeV at time $t_0 = 0.6$ fm with H_{eff} evolution without quantum jumps and $\hat{\kappa}(T) = \hat{\kappa}_C(T)$ and $\hat{\gamma} = -1.75$. Furthermore, the LO deterministic evolution between quantum jumps is implemented using the Crank-Nicolson method. We observe the relative difference to reach $\sim 50\%$ at $T \approx 190$ MeV. We interpret the 50% relative difference as signaling, from a phenomenological perspective, the breakdown of the expansion in E/T. In the phenomenological results presented in the following subsections, we thus utilize a lower bound of $T_f = 190$ MeV for the NLO evolution.
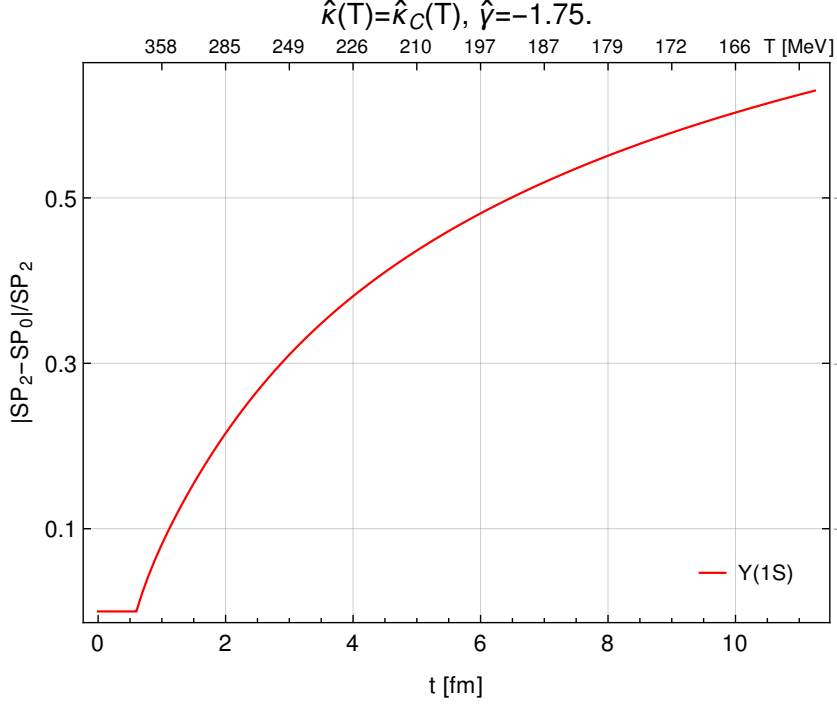
Figure 9.1: The relative difference of the survival probabilities of the $\Upsilon(1S)$ computed using the LO and NLO Lindblad equations. The evolution is performed using only the effective Hamiltonian H_{eff} without quantum jumps; the medium evolution is Bjorken with $T_0 = 425$ MeV and $t_0 = 0.6$ fm.

9.3.2 Widths

In this subsection, we analyze the effect of the inclusion of terms of order E/T and $(E/T)^2$ on the in-medium singlet to octet widths of the $\Upsilon(1S)$, $\Upsilon(2S)$ and $\Upsilon(3S)$. We project the singlet to octet width $\Gamma_{s\to o}$ of Eq. (9.64) onto the $1S$, $2S$ and $3S$ states and organize the result in powers of E/T where $E = 1/Ma_0^2 = $ is the magnitude of the Coulombic binding energy

$$\langle 1S|\Gamma_{s\to o}|1S\rangle = 3a_0^2\kappa \left\{ 1 - \frac{2N_c^2 - 1}{2(N_c^2 - 1)}\frac{E}{T} + \frac{(2N_c^2 - 1)^2}{12(N_c^2 - 1)^2}\left(\frac{E}{T}\right)^2 \right\}, \tag{9.83}$$

$$\langle 2S|\Gamma_{s\to o}|2S\rangle = 42a_0^2\kappa \left\{ 1 - \frac{5N_c^2 - 1}{28(N_c^2 - 1)}\frac{E}{T} + \frac{7N_c^4 - 4N_c^2 + 1}{672(N_c^2 - 1)^2}\left(\frac{E}{T}\right)^2 \right\}, \tag{9.84}$$

$$\langle 3S|\Gamma_{s\to o}|3S\rangle = 207a_0^2\kappa \left\{ 1 - \frac{10N_c^2 - 1}{138(N_c^2 - 1)}\frac{E}{T} + \frac{12N_c^4 - 4N_c^2 + 1}{7452(N_c^2 - 1)^2}\left(\frac{E}{T}\right)^2 \right\}. \tag{9.85}$$

The dimensionful quantity outside the curly braces represents the width at order 0 in the E/T expansion with respect to which the contributions inside the curly braces are

100
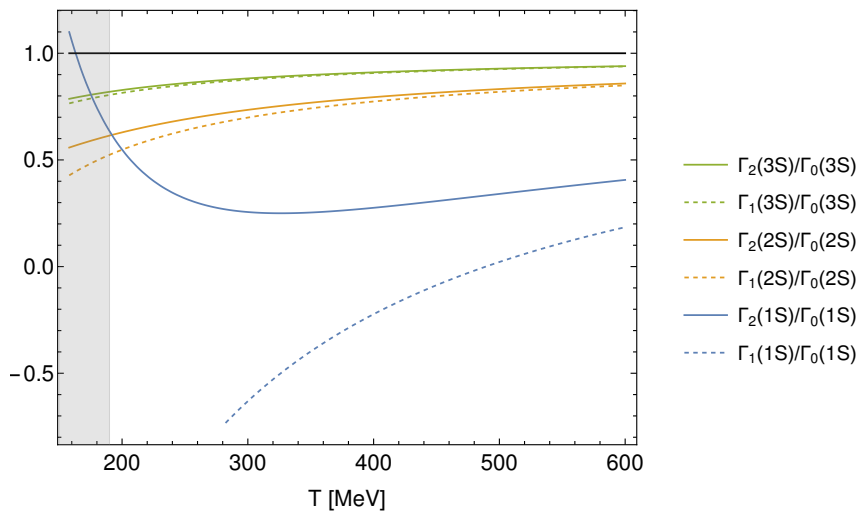
Figure 9.2: Comparison of the singlet to octet widths of the $1S$, $2S$ and $3S$ states with terms of order $(E/T)^0$, $(E/T)^1$ and $(E/T)^2$. $\Gamma_m(nS)$ represents $\langle nS|\Gamma_{s\rightarrow o}|nS\rangle$ including terms up to order $(E/T)^m$. The gray shaded area represents temperatures below $T_f = 190$ MeV below which coupling to the hydrodynamic medium evolution is not implemented in the phenomenological results presented in this chapter. The black line at 1 represents the limit of perfect convergence of the E/T expansion. Taken from Ref. [62].

normalized. We plot these contributions over the temperature range $T = 158$ MeV to $T = 600$ MeV in Fig. 9.2. We include a solid black line at 1 which indicates perfect convergence of the E/T expansion. As anticipated due to the lower magnitude of their Coulombic binding energies, the normalized widths of the states of higher principal quantum number n show better convergence than those of states of lower n. Furthermore, for all states considered, the expansion shows better convergence properties upon inclusion of higher order terms as indicated by the solid curves lying above the dotted curves of the same color. The expansion also converges as temperature is increased. The gray shaded area in the left of the plot corresponds to temperatures $T < T_f = 190$ MeV not included in the NLO phenomenological studies carried out in Ref. [62] and presented in this chapter.

9.3.3   Survival probabilities

To analyze the effect of the NLO terms, in Fig. 9.3, we display the results of simulations with H_{eff} evolution without quantum jumps carried out at LO and NLO in the E/T expansion using trajectory averaged temperature evolution in each centrality class. The left column displays variation of $\hat{\kappa}(T)$, and the right column of $\hat{\gamma}$. In the top row, we display the survival probabilities of the $\Upsilon(1S)$ state obtained using LO and NLO H_{eff} evolution both evolved to $T_f = 190$ MeV. We note that $T = 190$ MeV is well outside the
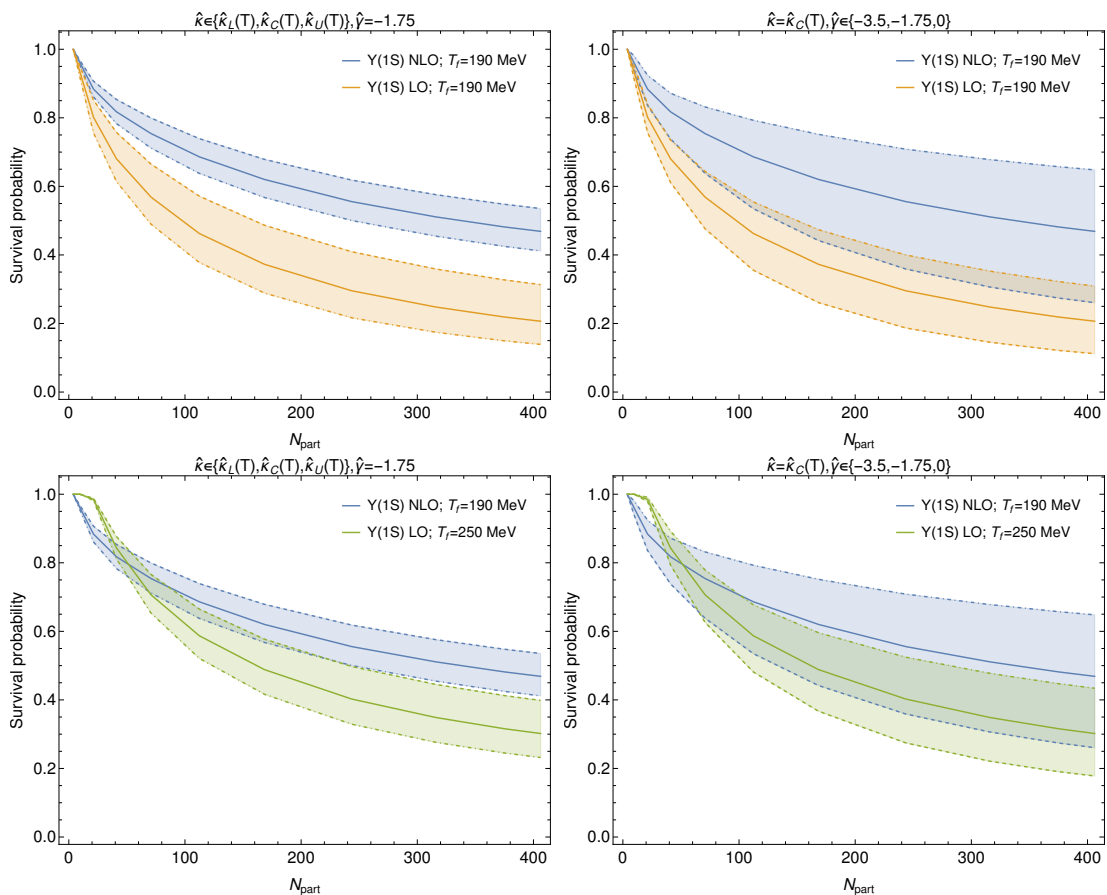
Figure 9.3: Survival probabilities of the $1S$ state as a function of centrality. All simulations are performed using H_{eff} evolution without quantum jumps and trajectory averaged temperature evolution. The upper row compares NLO results to LO results both with $T_f = 190$. The lower row compares NLO results with $T_f = 190$ MeV to LO results with $T_f = 250$ MeV. The bands in the right column display $\hat{\kappa}(T)$ variation and in the left column $\hat{\gamma}$ variation. The lower, central and upper parametrizations of $\hat{\kappa}(T)$ and values of $\hat{\gamma}$ are represented by dashed, solid and dot-dashed curves, respectively. Taken from Ref. [62].

range of validity of the LO Lindblad equation; we include these plots to illustrate the effect of the NLO terms, namely to increase the yield across the range of N_{part}. In the second row of Fig. 9.3, we display the survival probability of the $\Upsilon(1S)$ obtained using LO H_{eff} evolution down to $T_f = 250$ MeV, as used in Refs. [60, 61], against NLO H_{eff} results obtained evolving to $T_f = 190$ MeV as in Ref. [62]. In more central collisions, we observe less suppression in the NLO results consistent with the comparisons at equal T_f. In the most peripheral collisions, we observe increased suppression in the NLO compared to the LO results and a smoother approach of the NLO curves to 1 at $N_{\text{part}} = 0$ compared

102
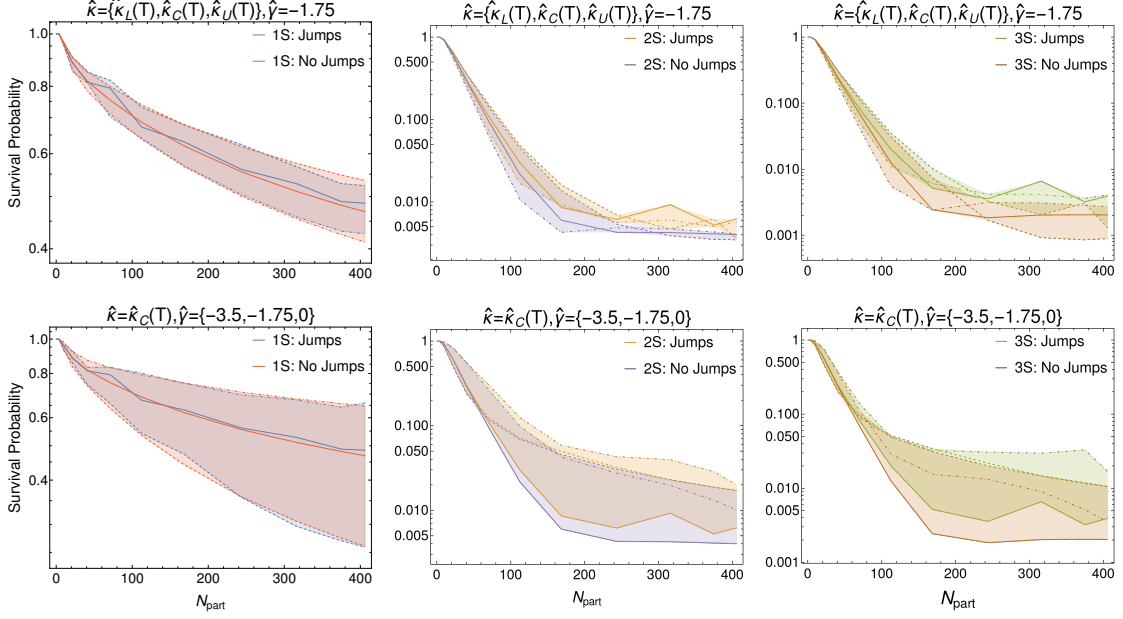
Figure 9.4: Survival probabilities of the $\Upsilon(1S)$, $\Upsilon(2S)$ and $\Upsilon(3S)$ states. In each panel, results with and without quantum jumps are compared. The top row displays $\hat{\kappa}(T)$ variation and the bottom row $\hat{\gamma}$ variation; this variation is represented as in Fig. 9.3. Taken from Ref. [62].

to the cusp in the LO results. In the most peripheral collisions, the initial temperature of the medium is sufficiently close to $T_f = 250$ MeV (cf. Fig. B.1 and table B.1) such that very little or no medium evolution takes place resulting in little to no suppression. Inclusion of the NLO terms in the evolution equation allows us to lower T_f to 190 MeV and thus more accurately treat peripheral collisions.

9.3.4 Effect of quantum jumps

In this subsection, we discuss the effect of quantum jumps at NLO. Fig. 9.4 shows the nuclear modification factor R_{AA} of the $\Upsilon(1S)$, $\Upsilon(2S)$ and $\Upsilon(3S)$ computed at NLO with and without the effect of quantum jumps using trajectory averaged temperature evolution. For the results including quantum jumps, the statistical uncertainties associated with averaging over the quantum jumps are subleading compared to the theoretical uncertainty due to κ and γ, and only the latter uncertainties are displayed. In all combinations of $\hat{\kappa}(T)$ and $\hat{\gamma}$, we observe the jumps to increase the yield of the state considered. We note that the magnitude of the difference is small, and the relative difference greater for the excited states than the ground state. With the present theoretical uncertainties due to κ and γ, the uncertainty introduced evolving with only H_{eff} neglecting the effect of quantum jumps is thus subleading.
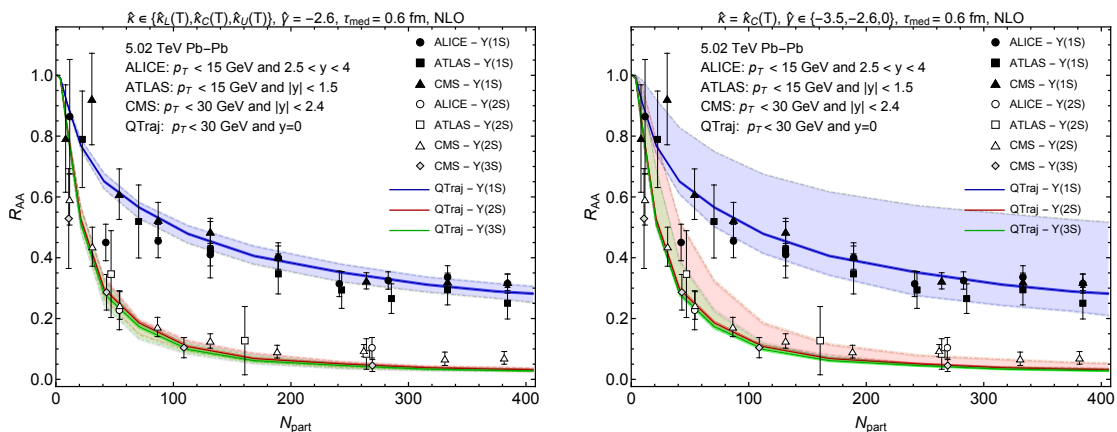
Figure 9.5: The nuclear modification factor R_{AA} of the $\Upsilon(1S)$, $\Upsilon(2S)$ and $\Upsilon(3S)$ plotted against N_{part}. The left panel displays variation with respect to $\hat{\kappa}$, and the right panel variation with respect to $\hat{\gamma}$. The dashed and dot-dashed lines show results for the lower and upper values, respectively, of $\hat{\kappa}(T)$ and $\hat{\gamma}$ while the central curves show results for $\hat{\kappa}_C(T)$ and $\hat{\gamma} = -2.6$. Our theory results are compared against experimental measurements from the ALICE [46], ATLAS [47] and CMS [48, 52] collaborations. Taken from Ref. [62].

9.3.5 Nuclear modification factor R_{AA}

In this section, we present the main results of this chapter: the nuclear modification factor R_{AA} of the $\Upsilon(1S)$, $\Upsilon(2S)$ and $\Upsilon(3S)$ as functions of N_{part} and p_T. The results were obtained sampling over $80\,000$ physical trajectories for each combination of $\hat{\kappa}(T)$ and $\hat{\gamma}$. Due to the increased computational cost of sampling quantum trajectories along each physical trajectory, only H_{eff} evolution without quantum jumps is implemented. Feed down is accounted for as in the LO case described in subsec. 8.2.4.

In Fig. 9.5, we display R_{AA} as a function of N_{part} and compare against experimental measurements of the ALICE [46], ATLAS [47] and CMS [48, 52] collaborations. In Fig. 9.6, we display R_{AA} as a function of p_T and compare against experimental measurements of the ALICE [46], ATLAS [47] and CMS [48, 52] collaborations. In both figures, we display κ variation in the left panel and γ variation in the right panel. We note that in these figures, we make use of a best fit value of $\hat{\gamma} = -2.6$ such that the best fit value of $\hat{\gamma}$ and $\hat{\kappa}_C(T)$ runs through the experimental data. Our systematic uncertainties with respect to κ are thus estimated by performing 3 simulations at $\hat{\gamma} = -2.6$ with $\hat{\kappa}_U(T)$, $\hat{\kappa}_C(T)$ and $\hat{\kappa}_L(T)$; uncertainties due to γ are estimated by running two additional simulations with $\hat{\kappa}_C(T)$ and with $\hat{\gamma} = -3.5$ and $\hat{\gamma} = 0$. We observe greater systematic uncertainty due to κ than γ. With the best fit value of $\hat{\gamma}$, we observe agreement between our `QTraj` $R_{AA}[\Upsilon(1S)]$ results and the experimental measurements. The central `QTraj` $R_{AA}[\Upsilon(2S)]$ and $R_{AA}[\Upsilon(3S)]$ results show moderate discrepancy with the experimental data which the γ variation lessens.

104
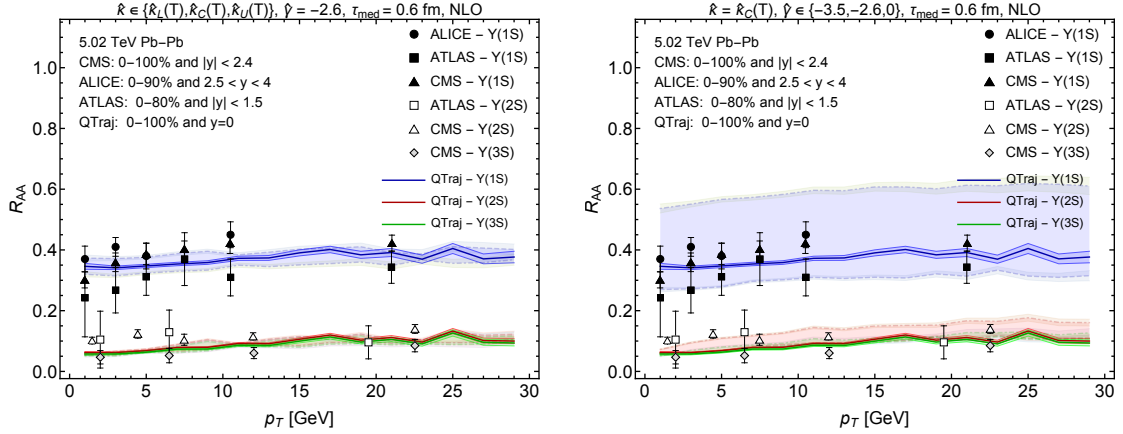
Figure 9.6: The nuclear modification factor R_{AA} of the $\Upsilon(1S)$, $\Upsilon(2S)$ and $\Upsilon(3S)$ plotted against p_T. The theoretical uncertainties are displayed as in Fig. 9.5. Our theory results are compared against experimental measurements from the ALICE [46], ATLAS [47] and CMS [48, 52] collaborations. Taken from Ref. [62].

9.3.6   Earlier medium initialization

In this subsection, we display results obtained initializing the coupling between the quarkonium and the medium at $\tau_{\mathrm{med}} = 0.25$ fm rather than $\tau_{\mathrm{med}} = 0.6$ fm as in previous works. We display $R_{AA}[\Upsilon(1S)]$, $R_{AA}[\Upsilon(2S)]$ and $R_{AA}[\Upsilon(3S)]$ as a function of N_{part} in Fig. 9.7 and as a function of p_T in Fig. 9.8. κ and γ variation are as in chapter 8, i.e., the central value of $\hat{\gamma} = -1.75$ rather than the best fit value of $\hat{\gamma} = -2.6$ is utilized. We observe that this earlier initialization of the medium coupling leads the central `QTraj` curve to match the data without tuning $\hat{\gamma}$ to a best fit value. We note that at such early times, the medium is far from isotropic thermal evolution [161,162]; the presence of large momentum anisotropies introduces uncertainties which are, at present, unquantified.

9.3.7   Width extracted κ

In this subsection, we quantify our systematic uncertainty due to use of the heavy quark momentum diffusion coefficient measured in Ref. [110]. As discussed in sec. 5.1, in Ref. [112] adjoint and fundamental versions of the transport coefficients κ and γ are identified with the adjoint coefficients related to the in-medium evolution of heavy quarkonium and the fundamental coefficients to that of heavy quarks. The explicit, perturbative calculation of Ref. [112] shows adjoint and fundamental γ to differ at order g^4 while explicit calculations show adjoint and fundamental κ to agree up to order $g^5 T^3$.

Adjoint κ is related to the in-medium width of, e.g., the $\Upsilon(1S)$ by the relation given in Eq. (5.22). In the left panel of Fig. 5.3, we display estimates of adjoint κ derived from lattice measurements of $\Gamma[\Upsilon(1S)]$ with a range given by $0.24 \lesssim \hat{\kappa} \lesssim 4.2$. In Fig. 9.9, we display $R_{AA}[\Upsilon(1S)]$, $R_{AA}[\Upsilon(2S)]$ and $R_{AA}[\Upsilon(3S)]$ as functions of N_{part} (left panel)
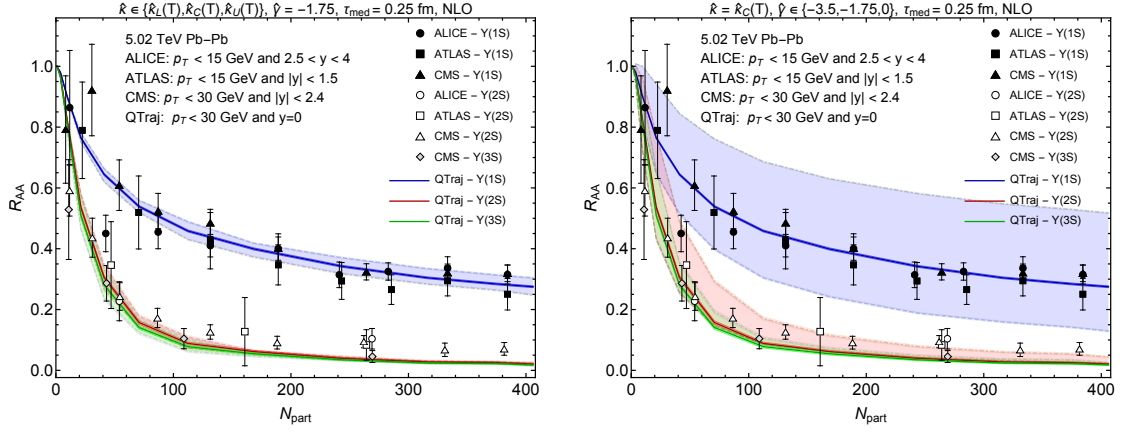
Figure 9.7: The nuclear modification factor R_{AA} of the $\Upsilon(1S)$, $\Upsilon(2S)$ and $\Upsilon(3S)$ plotted against N_{part}. In these simulations, coupling with the medium is initialized at $\tau_{\text{med}} = 0.25$ fm. The theoretical uncertainties are displayed as in Fig. 9.5. Our theory results are compared against experimental measurements from the ALICE [46], ATLAS [47] and CMS [48, 52] collaborations. Taken from Ref. [62].

and p_T (right panel). All simulations are run with $\hat{\gamma} = -2.6$; the upper, central and lower curves represent simulations run with $\hat{\kappa}(T) = 0.24$, $\hat{\kappa}(T) = \hat{\kappa}_C(T)$ and $\hat{\kappa}(T) = 4.2$, respectively. In comparison with Figs. 9.5 and 9.6, we observe the uncertainty due to κ to increase but remain smaller than that due to γ.
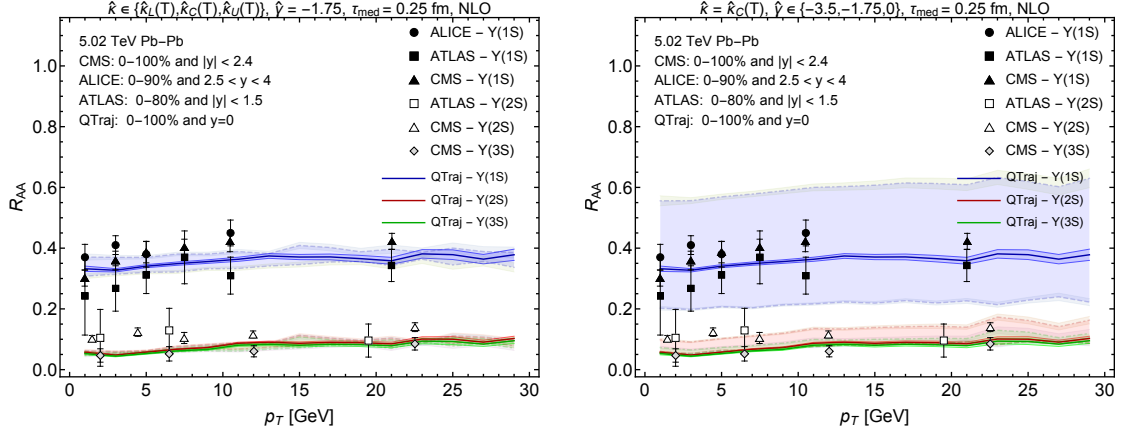
Figure 9.8: The nuclear modification factor R_{AA} of the $\Upsilon(1S)$, $\Upsilon(2S)$ and $\Upsilon(3S)$ plotted against p_T. In these simulations, coupling with the medium is initialized at $\tau_{\mathrm{med}} = 0.25$ fm. The theoretical uncertainties are displayed as in Fig. 9.5. Our theory results are compared against experimental measurements from the ALICE [46], ATLAS [47] and CMS [48, 52] collaborations. Taken from Ref. [62].
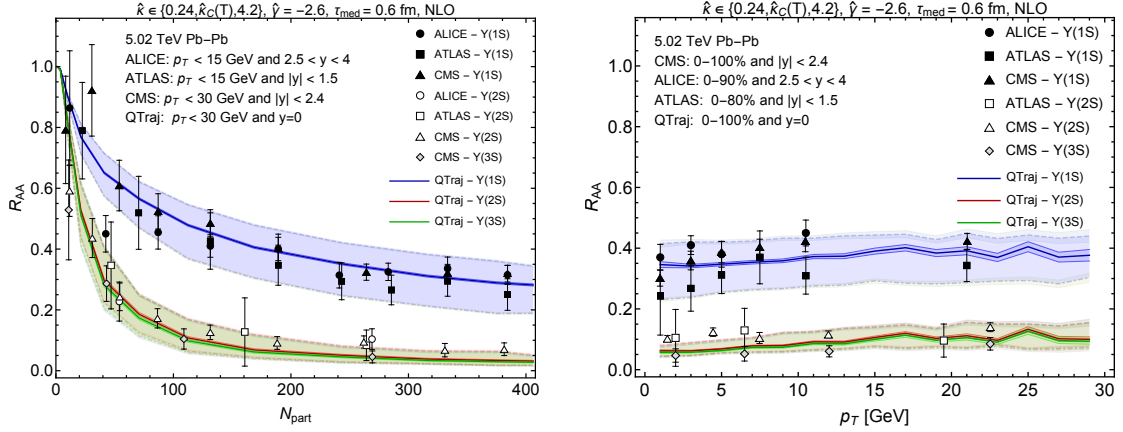
Figure 9.9: The nuclear modification factor R_{AA} of the $\Upsilon(1S)$, $\Upsilon(2S)$ and $\Upsilon(3S)$ plotted against N_{part} (left panel) and p_T (right panel). The upper, central and lower curves show results for $\hat{\gamma} = -2.6$ and $\hat{\kappa}(T) = 0.24$, $\hat{\kappa}_C(T)$ and 4.2, respectively. Our theory results are compared against experimental measurements from the ALICE [46], ATLAS [47] and CMS [48, 52] collaborations. Taken from Ref. [62].

Part IV

Conclusions

Chapter 10

Summary and Outlook

At macroscopic scales and low energies, the strong interaction confines quarks and gluons to color neutral bound states, and they are never observed as asymptotic states. Current heavy ion collision experiments create an environment of immensely high energy density within which color charged quarks and gluons may in fact propagate freely. Such a medium is denoted a quark gluon plasma and is the subject of investigate of this thesis. Our physical systems of interest in this investigation are heavy quarks and their bound states. The large mass of the bottom and charm quarks with respect to the temperatures of current HIC experiments make them ideal probes of this medium from its formation through to freeze out. The nuclear modification factor R_{AA} which quantifies the effect of the medium on yields of heavy quarkonium states is an observable of particular theoretical and experimental interest as a reduction in yield of heavy quarkonium states in HIC experiments with respect to proton-proton collisions may signal the creation of a deconfined QGP.

In part I of this thesis, we introduce QCD and nonrelativistic [18, 19] and potential nonrelativistic theories thereof [20–22], the formalism of open quantum systems and quantum field theory at finite temperature. Using pNRQCD, the OQS formalism and finite temperature QFT, we present a set of evolution equations describing the in-medium, out of equilibrium evolution of heavy Coulombic quarkonium.

In part II of this thesis, we analyze these evolution equations in dependence on the hierarchy between the temperature T of the medium and the binding energy E of the quarkonium state. In the strict $E \ll T$ limit, the evolution equations take the form of a Lindblad equation [28, 30]. Relaxing this strict assumption and including terms of order E/T, we derive a Langevin equation describing the time evolution of in-medium heavy quarkonium undergoing a random walk due to uncorrelated interactions with the medium. We perform a similar set of manipulations and field redefinitions in the single heavy quark sector using NRQCD to derive an analogous Langevin equation for the momentum evolution of a single heavy quark. The in-medium diffusion of the heavy particles described by these Langevin equations is characterized by a momentum diffusion coefficient κ. In a seminal work [104], a field theoretic definition of the heavy quark momentum diffusion coefficient κ was formulated related to the correlator of chromo-

electric fields dressed with fundamental Wilson lines. In the succeeding years, a corresponding correlator with an adjoint Wilson line describing the in-medium evolution of heavy quarkonium has become of interest. We detail the current state in the literature of the investigation of the adjoint and fundamental correlators and the difference between them and present state of the art extractions of these transport coefficients. We close part I of this thesis with a preliminary set of equations describing the in-medium evolution of heavy quarkonium valid beyond the dilute limit.

In part III of this thesis, we solve the master equation derived in part I and compute observables for comparison against experiment. At order 0 in the E/T expansion, the heavy quarkonium master equation takes the form of a Lindblad equation. We utilize the quantum trajectories algorithm to solve this Lindblad equation in a computationally efficient manner. Medium evolution is implemented via coupling to a realistic 3+1D dissipative relativistic hydrodynamics code, and the quantum trajectories algorithm realized along distinct physical trajectories through the medium. The sampling of physical trajectories allows for the calculation of the elliptic flow v_2 of the lowest lying Υ states and the presentation of v_2 and the nuclear modification factor R_{AA} of the Υ states as a function of both transverse momentum p_T and the number of participating nucleons N_{part}. These results, published in Ref. [61], show good agreement with experimental measurements by the ALICE, ATLAS and CMS collaborations. We, furthermore, investigate the effect of terms of order E/T on the in-medium evolution of heavy quarkonium. We include such terms in the pNRQCD master equation and derive a Lindblad equation accurate at order E/T thus allowing for evolution to lower temperatures closer to the pseudocritical temperature of the QGP phase transition. We utilize an NLO implementation of the quantum trajectories algorithm to solve the Lindblad equation at this order. To counterbalance the increased computational cost of solving the NLO Lindblad equation compared to its LO counterpart, we evolve the state with H_{eff} without including the effect of quantum jumps. We present $R_{AA}[\Upsilon(1S)]$, $R_{AA}[\Upsilon(2S)]$ and $R_{AA}[\Upsilon(3S)]$ as functions of N_{part} and p_T as calculated and compared against experimental measurements of the ALICE, ATLAS and CMS collaborations in Ref. [62] and observe good agreement between our theoretical results and the experimental data.

The work presented in this thesis has proven to be of interest in the experimental community. Recent measurements of the nuclear modification factor of the $\Upsilon(1S)$ and $\Upsilon(2S)$ states and their double ratio by the ATLAS collaboration [163] include comparisons against the results presented in chapter 8. Additionally, preliminary measurements by the CMS collaboration of R_{AA} of the $\Upsilon(1S)$, $\Upsilon(2S)$ and $\Upsilon(3S)$ and the double ratio $R_{AA}[\Upsilon(3S)]/R_{AA}[\Upsilon(2S)]$ include comparisons to the `QTraj` results at NLO in the E/T expansion presented in chapter 9. Finally, in Ref. [164], our results are compared against experimental measurements of $\Upsilon(1S)$ and $\Upsilon(2S)$ suppression in gold-gold collisions at $\sqrt{s_{NN}} = 200$ GeV by the STAR collaboration.

A number of theoretical and phenomenological projects remain building on the work presented in this thesis. On the theoretical side, in order to put the modified, in-medium NRQCD Lagrangian of Eq. (6.68) on more sound theoretical footing, a thorough investigation of the scale $\sqrt{MT}$ remains necessary. Furthermore, we plan a detailed

study of the nonlinear evolution equations of chapter 7 in different parameter regimes. On the phenomenological side, the diffusive E/T terms added to the Lindblad equation and analyzed in Ref. [62] present the opportunity to add to the literature studying thermalization [34, 165, 166].

Acknowledgments, Appendices and References

Acknowledgments

First and foremost, I would like to thank my doctoral advisors Nora Brambilla and Antonio Vairo for their support and direction in my research and during the writing of this thesis. Thank you for taking me into the group from a different university having worked on a significantly different topic during my master's and for always pushing for the best possible results. Thank you also to my collaborators Miguel, Mike, Johannes, Anurag and Ajaharul for all your help and our great work together on our papers. Thank you also to the postdocs who were and are here in Munich Viljami, Abhishek, Xiangpeng, Lin, Hee Sok, Wai Kin, Rafa and Yan for your help, support and company in Garching. A big thanks to the other PhDs in the group Sebastian, Gramos, Julian and Tommaso for being a great presence in the office and always being there for help with physics, forms and a great many other things that have come up over the years. Thanks as well to Petter, Kåre, Sebastian, Amy, Soobeen, Zara, Juan, Félix, Philip and Stephan for being great friends and making for a good few years in Munich. And last but not least, thank you to Mom, Dad and Anna: none of this would have been possible without your love and support.

Appendix A

QTraj code

In this appendix, we present an introduction to the `QTraj` code used in Refs. [60–62] to solve the Lindblad equation describing the in-medium evolution of Coulombic quarkonium. We aim to provide an abridged introduction to the `QTraj` code enabling the reader to download and run the code and simulate quantum trajectories converging to the solutions of the Lindblad equations given in chapters 8 and 9. We note that the full functionality of the `QTraj` code extends beyond what is presented in this appendix and direct the reader to Ref. [59] for a detailed description of the code in its entirety. The `QTraj` code is released under the GNU general public license and is available for download at Ref. [167]. The most up to date branch of the code at the time of the writing of this thesis is "NLO" which allows the user to implement the quantum trajectories algorithm at NLO and LO in the E/T expansion as in chapters 9 and 8, respectively. In sec. A.1, we give an introduction to the `QTraj` code explaining its runtime parameters. In sec. A.2, we present results showing convergence in the observables of interest (namely R_{AA} of the lowest lying Υ states) as the lattice and Monte Carlo parameters are taken to the limits in which they converge, e.g., the continuum limit and the limit of infinite quantum trajectories.

A.1 Running the `QTraj` code

In this section, we present the runtime parameters contained in the file `input/params.txt` which the user sets to run the `QTraj` code. We present an exhaustive list of these parameters in table A.1. In the text, we detail only the parameters necessary to reproduce the results shown in this thesis; the remaining parameters given in table A.1 are explained in Ref. [59].

After downloading the source code from Ref. [167], the code is compiled by running

```
$ make
```

in the top level directory producing an executable called `qtraj`. The code is executed by running

```
$ ./qtraj
```

on the executable. The physics, lattice, and simulation parameters can be set at runtime or beforehand in the file `params.txt` in the directory `input`.

Physics parameters   To implement the quantum trajectories algorithm as discussed in chapters 8 and 9, the parameter `potential` must be set to 0. For `doJumps= 1`, `QTraj` implements the full quantum trajectories algorithm including quantum jumps; for `doJumps= 0`, `QTraj` evolves the quarkonium state deterministically with H_{eff} without implementing quantum jumps. The parameter `m` sets the reduced mass of the bound state in units of GeV. The parameter `alpha` sets the value of the rescaled strong coupling $\alpha = C_f \alpha_s$ where α_s is the strong coupling in the pNRQCD potentials. The parameters `kappa` and `gam` set the values of the dimensionless quantities $\hat{\kappa}$ and $\hat{\gamma}$, respectively. `kappa`$= -1, -2$ and -3 specify the central, lower and upper fits of $\hat{\kappa}(T)$ as discussed in chapter 8; values of `kappa` ≥ 0 specify performing the simulation with a constant value of $\hat{\kappa}(T)$. Values of `gam` ≤ 0 specify performing the simulation with a fixed value of $\hat{\gamma}$.

Hydrodynamic evolution parameters   The parameter `temperatureEvolution` can be set to 0, 1, 2 or 3 to specify ideal Bjorken temperature evolution, user specified temperature evolution, temperature evolution along a specific physical trajectory or constant medium temperature, respectively. For Bjorken evolution, the initial temperature in units of GeV is set using `T0`. The final temperature in units of GeV is set using `Tf`. The initialization times of the hydrodynamic background and vacuum evolution of the bound state are set using `tmed` and `t0`, respectively.

Initial condition   The Gaussian initial condition of Eq. (8.56) is specified by setting `initType` $= 1$. The width of the Gaussian in units of a_0 and its angular momentum are set using `initWidth` and `initL`, respectively; its color state is specified using `initC` $= 0$ for singlet and `initC` $= 1$ for octet.

Simulation and lattice parameters   To output overlaps with vacuum eigenstates, `ProjType` must be set to 0. The number of quantum trajectories to simulate is specified by `nTrajectories`. The random seed for the random number generator can be set to a user defined value by specifying a positive integer value of `randomseed`; a random number based on the current system time is used by specifying `randomseed` $= 0$. The number of spatial lattice sites, lattice size in GeV^{-1} and temporal lattice spacing in units of GeV^{-1} are specified by `num`, `L` and `dt`, respectively. The implementation of the deterministic evolution of the wave function with H_{eff} is specified using `stepper`. The split-step pseudospectral method discussed in subsec. 8.2.2 is implemented at LO in the E/T expansion by setting `stepper` $= 0$; the Crank-Nicolson method discussed in subsec. 9.2 is implemented at LO and NLO in the E/T expansion by setting `stepper` $= 1$ and 2, respectively.

We note that the results of chapters 8 and 9 required on the order of hundreds of thousands of quantum trajectories. As individual quantum trajectories are independent, the quantum trajectories algorithm is embarrassingly parallelizable. To take full advantage of this, we include in the `QTraj` code repository a number of portable batch scripts (PBS) enabling many trajectories to be run in parallel on computing infrastructure supporting the PBS format. The file `manyTrajectories.pbs` in the `scripts` directory allows the user to specify the number of physical trajectories to sample, the number of quantum trajectories per physical trajectory and the number of requested nodes.

| Group	Parameter	Value/Type	Description
Potential parameter	potential	0	Munich potential (Appendix E.1)
		1	Isotropic KSU potential (Appendix E.2)
		2	Anisotropic KSU potential (Appendix E.3)
Jump parameters	doJumps	1	Perform quantum jumps; only for potential=0
		0	Do not perform quantum jumps
	maxJumps	integer ≥ 0	Maximum number of quantum jumps
Physics parameters	m	real ≥ 0	Reduced mass in units of GeV
	alpha	real ≥ 0	Coulomb coupling; $\alpha = C_F \alpha_s$
	kappa	-1	Central fit (Appendix E.1)
		-2	Lower fit (Appendix E.1)
		-3	Upper fit (Appendix E.1)
		real ≥ 0	Coefficient $\hat{\kappa}$ in Munich potential (Appendix E.1)
	gam	real ≤ 0	Coefficient $\hat{\gamma}$ in Munich potential (Appendix E.1)
Temperature parameters	temperatureEvolution	0	Ideal Bjorken evolution; $T(\tau) = T_0(\tau_{\mathrm{med}}/\tau)^{1/3}$
		1	Read from temperature evolution file (Appendix C.1)
		2	Read from "trajectory file" (Appendix C.2)
		3	constant temperature of T_0 for maxSteps
	temperatureFile	string	Specifies temperature file path
	T0	real > 0	Initial temperature in units of GeV (Bjorken)
	Tf	$0 < T0 < Tf$	Final temperature in units of GeV
	tmed	real ≥ 0	Time to turn on hydro background in units of GeV^{-1}
	t0	real ≥ 0	Time to begin vacuum evolution in units of GeV^{-1}
Initial condition parameters	initType	0	Singlet Coulomb eigenstates
		1	Gaussian delta function
		100	Computed eigenstates (Section 3.1)
		200	Loads eigenstates from file (Section 3.1)
	ProjType	0	Uses coulomb eigenstates
		1	Uses computed eigenstates
		2	Uses disk-based eigenstates (Section 3.1)
	initWidth	real ≥ 0	Initial width for Gaussian IC (initType=1)
	initN	1	Principal quantum number n; only for initType=0
	initL	0	Angular momentum quantum number l
	initC	0	Singlet color configuration
		1	Octet color configuration; only for potential=0
	basisFunctionsFile	string	Specifies basis functions file path (Section 3.1)
Simulation parameters	nTrajectories	integer ≥ 0	Number of quantum trajectories to simulate
	randomseed	0	Uses high-resolution system timer as a seed
		integer > 0	Uses specified number as a seed
		-1	Uses deterministic random numbers (for testing)
	rMax	$0 < \text{real} \leq 1$	Sets maximum initial random number (Section 4.4)
	maxJumps	integer ≥ 0	Sets maximum number of jumps (Section 4.4)
Grid parameters	num	integer ≥ 2	Number of lattice sites; 2^n for best performance
	L	real > 0	Size of simulation box in units of GeV^{-1}
	dt	real > 0	Time step in units of GeV^{-1}
	maxSteps	integer ≥ 0	Maximum number of time steps
	derivType	0	Full derivative (Section 3.2)
		1	Second-order differences (Section 3.2)
	stepper	0	Suzuki-Trotter - LO E/T
		1	Crank-Nicholson - LO E/T
		2	Crank-Nicholson - NLO E/T
Output parameters	snapFreq	integer ≥ 0	Frequency for the summary output
	snapPts	integer $\leq$ num	For best performance num/snapPts=2^n
	dirnameWithSeed	0	Output directory "output"
		1	Output directory "output-<seed>"
	saveWavefunctions	0	Turns off saving of wavefunctions
		1	Turns on saving of wavefunctions
	outputSummaryFile	0	Turns off output of the summary file summary.tsv
		1	Turns on output of the summary file summary.tsv

Table A.1: Runtime parameters of the QTraj code. Section numbers in parenthesis following descriptions denote sections of Ref. [59] in which detailed explanations are found. Taken from Ref. [59] with the parameter stepper added allowing the user to specify QTraj evolution at LO or NLO in E/T.

A.2 Parameter tests

In this section, we detail a number of scaling tests performed on the `QTraj` code to estimate systematic uncertainties associated with the lattice and Monte Carlo parameters. Our procedure is to perform $100\,000$ quantum trajectories on a lattice of 1-dimensional volume $L = 80$ GeV^{-1}, `NUM` = 4096 lattice sites, lattice spacing $a = 0.0195$ GeV^{-1} and temporal spacing $\Delta t = 0.001$ GeV^{-1}. We utilize Gaussian, singlet, s-wave initial conditions with width $c = 0.2$ and Bjorken temperature evolution with initial temperature $T_0 = 425$ MeV and medium coupling initialized at $\tau_{\mathrm{med}} = 0.6$ fm. To estimate our systematic uncertainty associated with the lattice discretization, finite size of the lattice and the finite width of the Gaussian initial condition, we vary these quantities while holding the others constant. We display these results in Fig. A.1 showing the survival probabilities of the $\Upsilon(1S)$, $\Upsilon(2S)$ and $\Upsilon(3S)$. In Fig. A.1a, we display the survival probabilities as the number of lattice points `NUM` is increased by factors of 2 from `NUM` = 512 to `NUM` = 8192; we observe good convergence at our production value of `NUM` = 4096 corresponding to a lattice spacing of $a = 0.0195$ GeV^{-1}. In Fig. A.1b, we display the survival probabilities as the lattice volume L is increased by factors of 2 from $L = 10$ GeV^{-1} to $L = 160$ GeV^{-1}; we observe good convergence at our production volume of $L = 80$ GeV^{-1}. In Fig. A.1c, we display the survival probabilities as the temporal step size Δt is decreased from $\Delta t = 0.01$ GeV^{-1} to $\Delta t = 0.0005$ GeV^{-1}; we observe good convergence at our production step size of $\Delta t = 0.001$ GeV^{-1}. In Fig. A.1d, we display the survival probabilities as the width of the Gaussian initial condition $c = \Delta/a_0$ is decreased by factors of 2 from $c = 0.8$ to $c = 0.1$; we observe good convergence at our production width of $c = 0.2$.

In Fig. A.2, we display the convergence properties of our results in dependence on the parameters of the quantum trajectories algorithm: the maximum allowed number of quantum jumps, the maximum allowed value of the initial random number and the number of quantum trajectories. Our lattice, initial condition and hydrodynamics parameters are the same as those used to produce the data shown in Fig. A.1. In Fig. A.2a, we display the survival probabilities of the Υ states as the maximum allowed number of jumps is varied between 2 and 40. In Fig. A.2b, we display the survival probabilities of the Υ states as the maximum value of the initial random number is increased by factors of 2 from `rMax` = 0.125 to `rMax` = 1. In Figs. A.2c and A.2d we display the survival probabilities of the S-, P- and D-wave bottomonium states as the number of quantum trajectories is increased from $N_{\mathrm{traj}} = 1000$ to $N_{\mathrm{traj}} = 250\,000$. Due to the structure of the Lindblad equation governing the in-medium evolution of Coulombic quarkonium, we can conceivably reduce these parameters to more efficiently arrive at a solution to the Lindblad equation. Our relevant quantum numbers are angular momentum and color; our observable of interest is the overlap with singlet, S-wave states. Considering a state of angular momentum l, we observe that the probability $p_\uparrow$ of a quantum jump to a state of angular momentum $l + 1$ is greater than the probability $p_\downarrow$ to a state of angular momentum $l - 1$. Thus, the greater the number of jumps, the lower the probability of the state having angular momentum $l = 0$ and nonzero overlap with the lowest lying S-wave

states. Furthermore, the repulsive octet potential drives the state to larger radii leading to less overlap with the lowest lying S-wave states peaked around the origin (cf. Fig. B.7 and accompanying discussion). As evident from the dedicated studies on the effect of quantum jumps (cf. subsecs. 8.3.3 and 9.3.4), the greatest contribution to the survival probability comes from states that never jumped at all, i.e., those whose evolution is described entirely by H_{eff} evolution. The results of Fig. A.2a show that the contribution to the survival probabilities of the lowest lying Υ states is relatively unaffected by excluding trajectories with a large number of jumps which are highly unlikely to be concentrated near the origin and have angular momentum $l = 0$. Setting a maximum value `rMax` < 1 of the initially generated random number excludes trajectories which jump early in their evolution and are thus unlikely to be concentrated near the origin with angular momentum $l = 0$ at the simulation end time. Excluding these trajectories allows the `QTraj` code to run faster with no strong effect on the observables of interest.
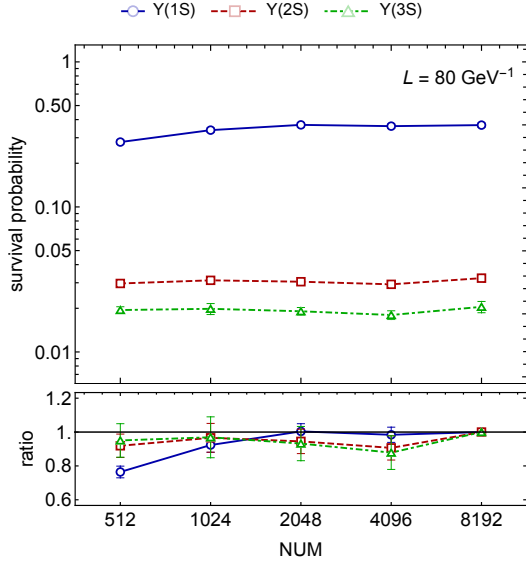
(a) Variation of number of lattice sites at constant lattice volume.
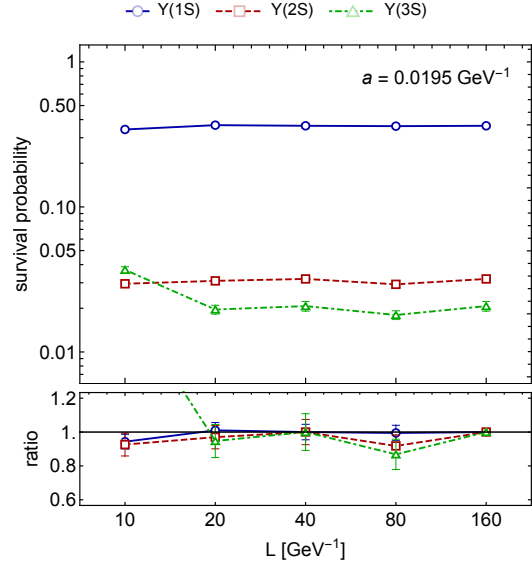
(b) Variation of lattice volume at constant lattice spacing.
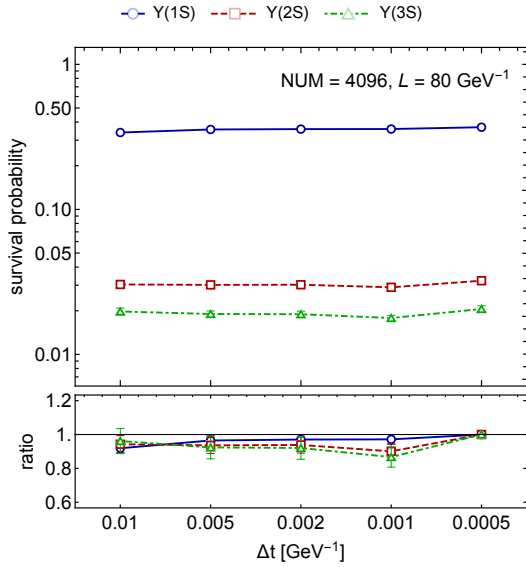
(c) Variation of temporal step size.
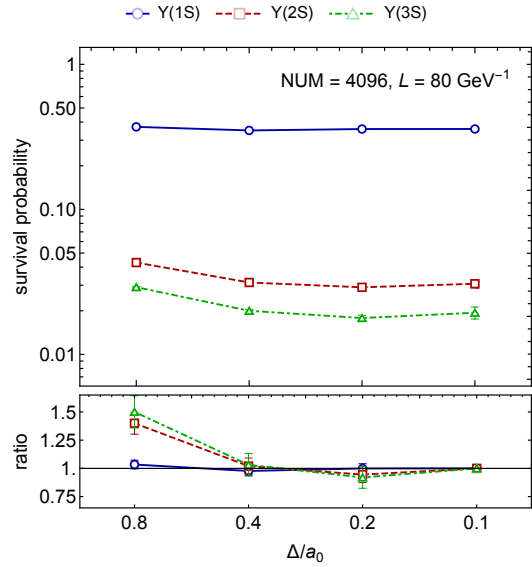
(d) Variation of width of Gaussian initial state.

Figure A.1: Scaling tests. We display the survival probabilities calculated while varying lattice and evolution parameters. In all plots, the discretization becomes more faithful to the continuum from left to right; the second to rightmost points correspond to production parameters. The error bars represent statistical uncertainty due to averaging 100 000 quantum trajectories. In all cases, we observe good convergence at the production values of the parameters. Taken from Ref. [59].
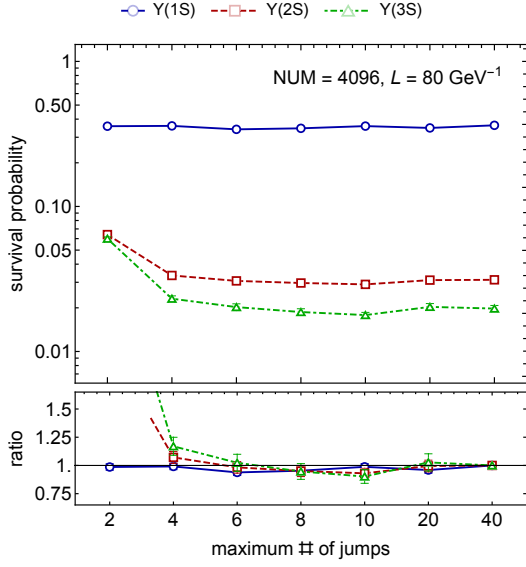
(a) Variation of the maximum allowed number of jumps.
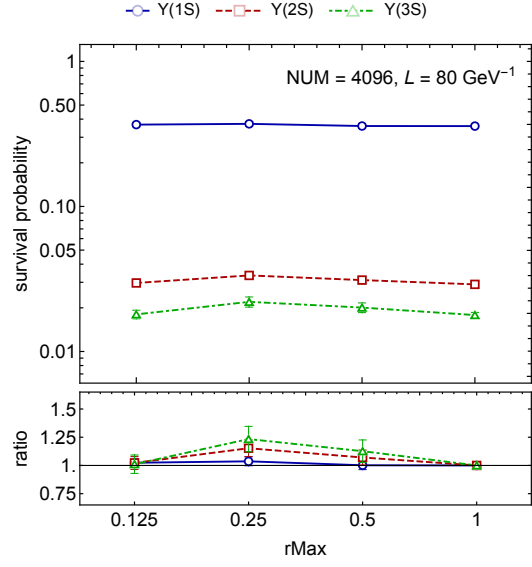
(b) Variation of the maximum allowed value of the initial random number.
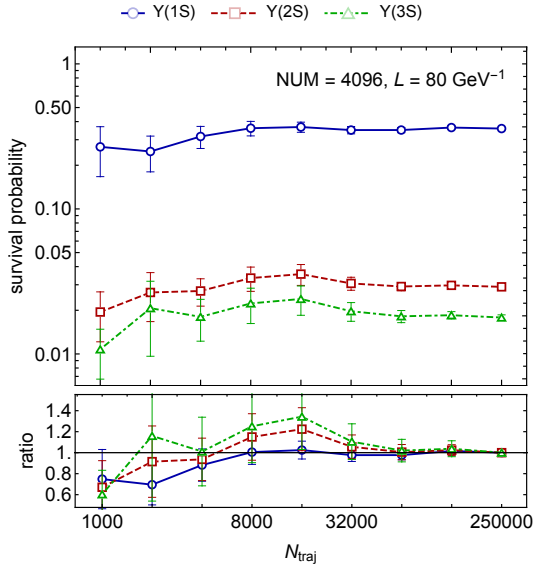
(c) Variation in the number of trajectories.
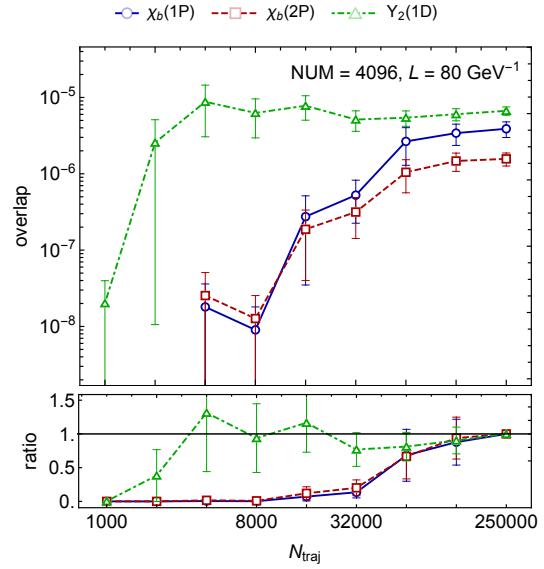
(d) Variation in the number of trajectories.

Figure A.2: Variation of simulation parameters in the `QTraj` code. In the top row, we vary the maximum allowed number of quantum jumps (left) and the maximum allowed value of the initial random number (right). In the bottom row, we estimate the necessary number of quantum trajectories for S-wave (left) and P- and D-wave (right) survival probabilities to converge. Error bars in the top row represent statistical uncertainty due to averaging 100 000 quantum trajectories. Error bars in the bottom row represent statistical uncertainty to due to averaging over the number of quantum trajectories shown on the horizontal axis. Taken from Ref. [59].

Appendix B

Trajectory averaged results

In this appendix, we present results from Ref. [60] in which the hydrodynamic evolution in the `QTraj` code is implemented as an average trajectory in each centrality bin. These results represent the solution of the Lindblad equation at LO in the E/T expansion as discussed in chapter 8. We note that these results are superseded by Ref. [61] in which the LO Lindblad equation is solved sampling distinct physical trajectories through the medium. The average physical trajectory is computed by Monte Carlo sampling approximately $132\,000$ physical trajectories per centrality bin through the plasma. The production point is sampled from the binary overlap profile of the colliding nuclei $N_{AA}^{\mathrm{bin}}(x,y)$, the transverse momentum p_T from a $p_T/\left(p_T^2 + \langle M \rangle^2\right)^2$ distribution where $\langle M \rangle$ is the average mass of the considered states and the azimuthal angle ϕ uniformly from 0 to 2π at $y = 0$. The temperature is recorded at each point along the physical trajectory and averaged in each centrality bin to arrive at a path averaged temperature evolution for each bin. We display the temperature profiles in Fig. B.1 and the corresponding number of participating nucleons in table B.1. The hydrodynamic implementation utilizes the tuning of Ref. [168].

In Fig. B.2, we plot a comparison of survival probabilities obtained using path averaged temperature evolution as in Ref. [60] and distinct physical trajectories as in chapters 8. The simulations were carried out at leading order in the E/T expansion as in chapter 8 and use the lattice and scale setting parameters given in sec. 8.2. We observe evolution along distinct physical trajectories to increase the survival probability at high N_{part} and to decrease it at low N_{part}. This effect is noticeably stronger on the excited states than the ground state most probably due to the larger dependence of the in-medium widths of the excited states on the temperature. In the remainder of this appendix, in sec. B.1, we present the results of Ref. [60], namely the nuclear modification factor R_{AA} of the $\Upsilon(1S)$, $\Upsilon(2S)$ and $\Upsilon(3S)$ states and double ratios thereof and in sec. B.2 various tests performed. We note that the phenomenological results of Ref. [60] presented below have been superseded by those presented in the chapters 8 and 9.
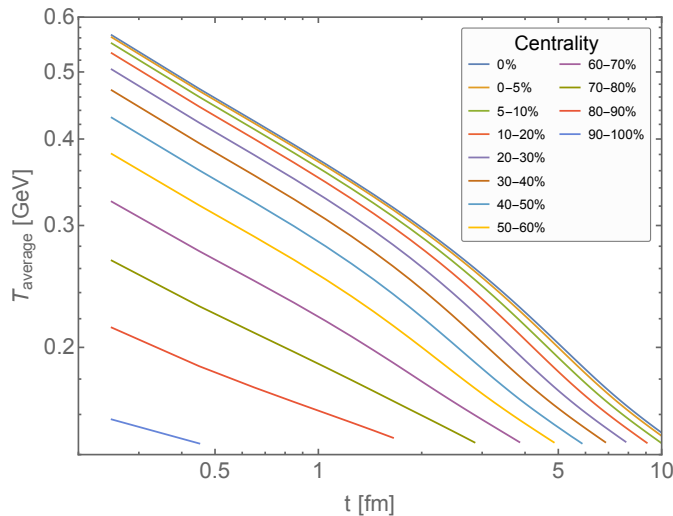
Figure B.1: The path averaged temperature as a function of time for each centrality class. Taken from Ref. [60].

B.1 Results

In this section, we present the phenomenological results Ref. [60]. As the Lindblad equation solved in Ref. [60] is LO in the E/T expansion, the split-step pseudospectral method of subsec. 8.2.2 is used for deterministic H_{eff} evolution. For consistency with values used in Refs. [28, 30], a bottom mass of $m_b = 4.881$ GeV is utilized yielding an inverse Bohr radius of $1/a_0 = 0.742$ GeV^{-1} and a strong coupling of $\alpha_s(1/a_0) = 0.414$ computed by solving Eq. (8.50). Systematic uncertainties due to κ are estimated by performing simulations with $\hat{\kappa}(T) = \hat{\kappa}_U(T), \hat{\kappa}_C(T)$ and $\hat{\kappa}_L(T)$ and uncertainties due to γ by simulating with $\hat{\gamma} = -3.5, -1.75$ and 0. The lattice parameters are identical to those given in subsec. 8.2.6, namely NUM = 4096 spatial sites, a radial volume of L = 80 GeV^{-1}, a Gaussian initial condition of width $c = 0.2$ and a spatial time step dt = 0.001 GeV^{-1}.

In Fig. B.3, we display the nuclear modification factor $R_{AA}[\Upsilon(1S)]$, $R_{AA}[\Upsilon(2S)]$ and $R_{AA}[\Upsilon(3S)]$ plotted against centrality. The bands in the left panel represent uncertainty due to κ and the bands in the right panel due to γ. We note good agreement with the experimental data from the ALICE [46], ATLAS [47] and CMS [48] collaborations. In Figs. B.4 and B.5, we plot the double ratios of $R_{AA}[\Upsilon(2S)]/R_{AA}[\Upsilon(1S)]$ and $R_{AA}[\Upsilon(3S)]/R_{AA}[\Upsilon(1S)]$, respectively, against centrality. Again, κ variation is given on the left and γ variation of the right. We note reasonable agreement with the experimental data from the ALICE [46], ATLAS [47] and CMS [49] collaborations with some tension at low N_{part}.

Centrality	$\langle b \rangle$ [fm]	$\langle N_{\text{part}} \rangle$	T_0^{central} [GeV]	T_0^{average} [GeV]
0%	0	406.1	0.630	0.565
0-5%	2.32	374.0	0.625	0.561
5-10%	4.25	315.9	0.614	0.550
10-20%	6.01	243.5	0.597	0.533
20-30%	7.78	168.5	0.571	0.504
30-40%	9.21	112.4	0.538	0.470
40-50%	10.45	70.8	0.497	0.430
50-60%	11.55	41.1	0.446	0.381
60-70%	12.56	21.3	0.386	0.325
70-80%	13.49	9.7	0.322	0.267
80-90%	14.38	3.8	0.258	0.214
90-100%	15.66	0.97	0.180	0.157

Table B.1: Relations among the centrality classes, impact parameters and number of participating nucleons with the corresponding central and average temperatures in a $\sqrt{s_{NN}} = 5.02$ TeV PbPb collision. Taken from Ref. [60].

B.2 Tests

In this section, we display the results of a number of tests of the `QTraj` code performed as part of the analysis of Ref. [60]. We note that all parameters are the same as those used in the previous section.

In Fig. B.6, we display the survival probabilities of the $\Upsilon(1S)$, $\Upsilon(2S)$ and $\Upsilon(3S)$ as functions of centrality comparing results obtained with full evolution with quantum jumps against results obtained using only H_{eff} evolution. Individual panels display the results utilizing different combinations of $\hat{\kappa}(T)$ and $\hat{\gamma}$. Apart from $\hat{\kappa}_C(T)$ and $\hat{\gamma} = 0$, we observe the effect of quantum jumps on the survival probability to be small. In Fig. B.7, we display the survival probabilities of the $\Upsilon(1S)$, $\Upsilon(2S)$ and $\Upsilon(3S)$ comparing full evolution with quantum jumps (solid curves) against evolution with only H_{eff}; we note that in the full evolution, the repulsive octet potential has been replaced by an attractive singlet potential. All simulations are performed with $\hat{\kappa}_C(T)$ and $\hat{\gamma} = -1.75$. We note the increased effect of the quantum jumps with respect to the central panel of Fig. B.6; this provides insight into the small effect of the quantum jumps. A quantum jump changes a singlet state evolved by an attractive potential to an octet state evolved by a repulsive potential; the repulsive potential evolves the wave function to larger radii and leads to low overlap with the lowest lying states concentrated at small radii. Replacing the repulsive octet potential with an attractive singlet potential increases the likelihood of overlap with the phenomenologically relevant lowest lying states after multiple jumps. In Fig. B.8, we plot the survival probabilities of the $\chi_b(1P)$ and $\chi_b(2P)$. For the central values of $\hat{\kappa}(T)$ and $\hat{\gamma}$, we observe almost total suppression in central collisions. In Figs. B.9, B.10 and B.11, we plot off diagonal overlaps, i.e., the overlap of an initial

124
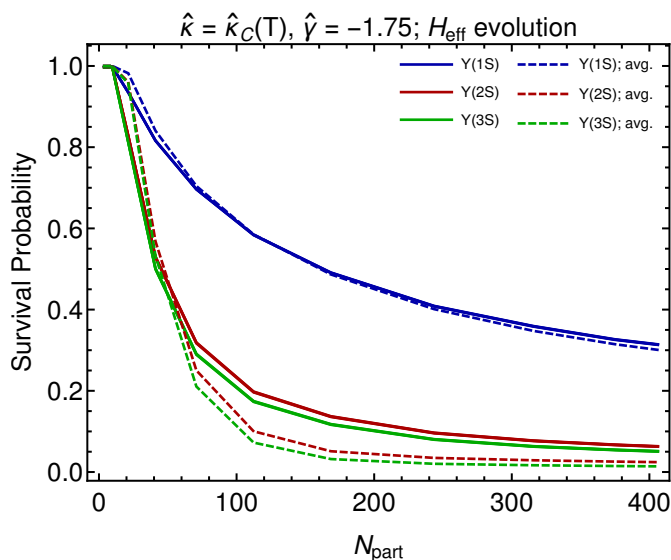
Figure B.2: Survival probability of the $\Upsilon(1S)$, $\Upsilon(2S)$ and $\Upsilon(3S)$ plotted against N_{part}. The simulations were carried out without including the effect of quantum jumps, i.e., evolving with only the effective Hamiltonian H_{eff}. Dashed lines indicate path averaged temperature evolution of the medium as in Ref. [60] while solid lines indicate sampling of distinct physical trajectories through the medium as in Refs. [61,62]. The simulations are performed using the central values of $\hat{\kappa}$ and $\hat{\gamma}$. Taken from Ref. [61].

state with a state of different quantum numbers. Fig. B.9 displays the overlaps of a P-wave, singlet initial condition with the $\Upsilon(1S)$, $\Upsilon(2S)$ and $\Upsilon(3S)$ states. Fig. B.10 displays the overlaps of an S-wave, singlet intial condition with the $\chi_b(1P)$ and $\chi_b(2P)$ states. Fig. B.11, displays the overlaps of a P-wave, octet initial condition with the $\Upsilon(1S)$, $\Upsilon(2S)$ and $\Upsilon(3S)$ states. In all cases, we observe the off diagonal overlaps to be small and note that the particularly small values of the P-wave, octet to S-wave, singlet overlap. Finally, in Fig. B.12, we display the effect on the $\Upsilon(1S)$, $\Upsilon(2S)$ and $\Upsilon(3S)$ survival probabilities of a $\pm 10\%$ variation in $T_f = 250$ MeV. The simulations utilize H_{eff} evolution. For the 1S state, we note the effect of the variation is comparable to the uncertainty due to κ and less than that due to γ.
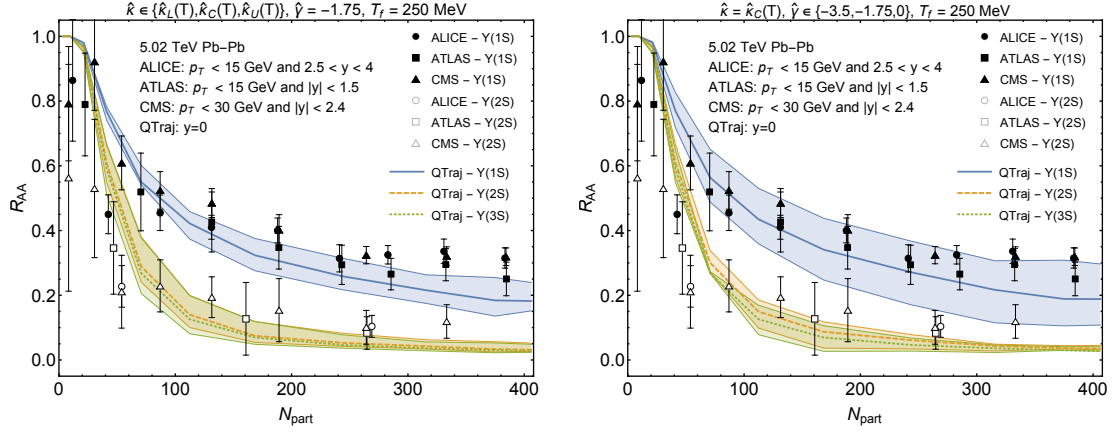
Figure B.3: The nuclear modification factor R_{AA} of the $\Upsilon(1S)$, $\Upsilon(2S)$ and $\Upsilon(3S)$ plotted against N_{part}. The left panel displays variation with respect to $\hat{\kappa}$, and the right panel variation with respect to $\hat{\gamma}$. Our theory results are compared against experimental measurements from the ALICE [46], ATLAS [47] and CMS [48] collaborations; experimental uncertainties represent statistical and systematic uncertainties combined in quadrature. Taken from Ref. [60].
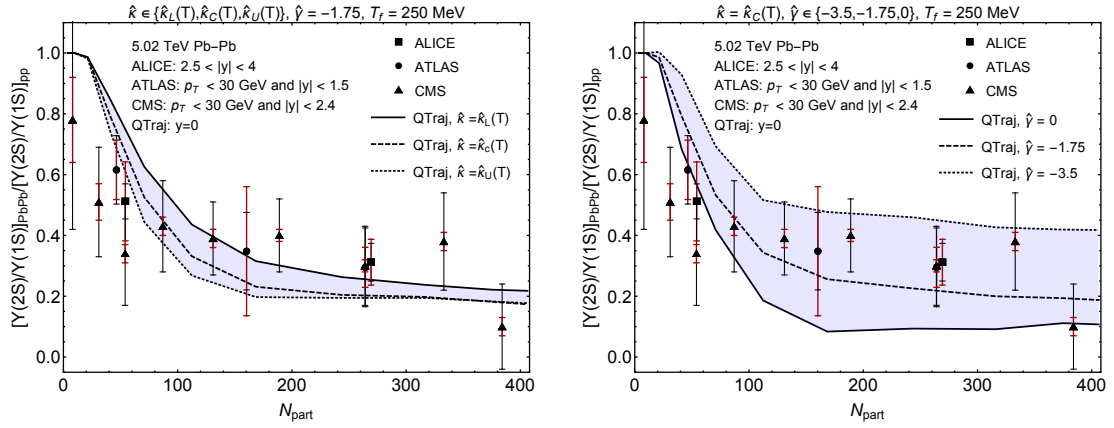
Figure B.4: The double ratio of the nuclear modification factor $R_{AA}[\Upsilon(2S)]$ to $R_{AA}[\Upsilon(1S)]$ plotted against N_{part}. The theoretical uncertainties are represented as in Fig. B.3. Our theory results are compared against experimental measurements from the ALICE [46], ATLAS [47] and CMS [49] collaborations. Red and black error bars represent experimental systematic and statistical uncertainties, respectively. Taken from Ref. [60].
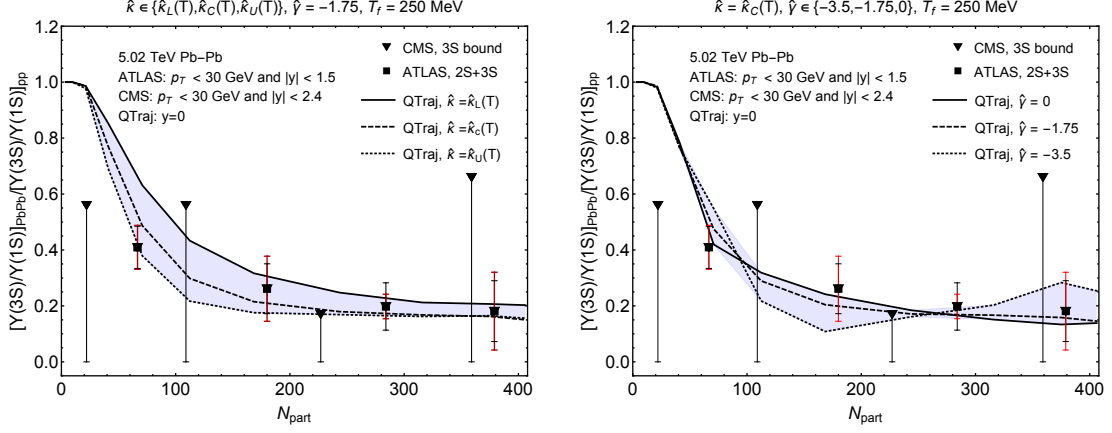
Figure B.5: The double ratio of the nuclear modification factor $R_{AA}[\Upsilon(3S)]$ to $R_{AA}[\Upsilon(1S)]$ plotted against N_{part}. Uncertainties and experimental references are as in Fig. B.4. Taken from Ref. [60].
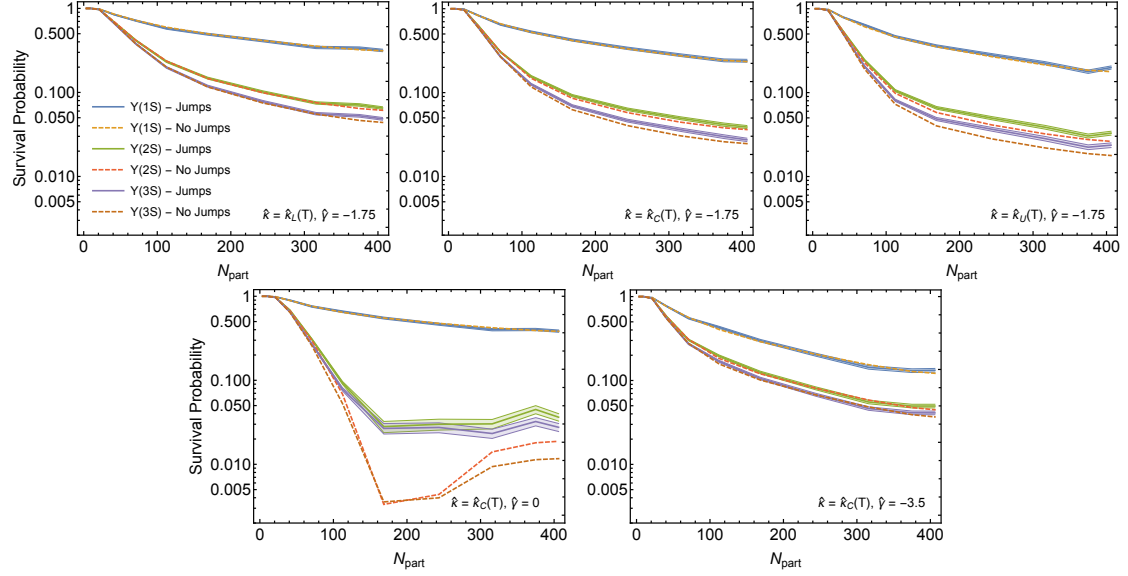

Figure B.6: The survival probabilities of the $\Upsilon(1S)$, $\Upsilon(2S)$ and $\Upsilon(3S)$ plotted against N_{part}. We compare results obtained implementing the full quantum trajectories algorithm including the effect of quantum jumps (solid curves) against results obtained evolving only with H_{eff} (dotted curves). Taken from Ref. [60].
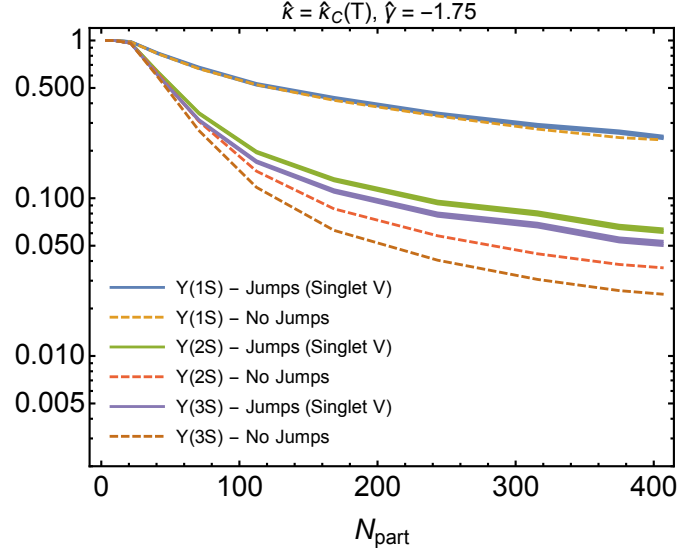
Figure B.7: The survival probabilities of the $\Upsilon(1S)$, $\Upsilon(2S)$ and $\Upsilon(3S)$ plotted against N_{part}. We compare results obtained implementing the full quantum trajectories algorithm including the effect of quantum jumps but with the repulsive octet potential replaced by an attractive singlet potential (solid curves) against results obtained evolving only with H_{eff} (dotted curves). The band around the solid curves represent statistical errors associated with the averaging over 98304 quantum trajectories per centrality point. Taken from Ref. [60].
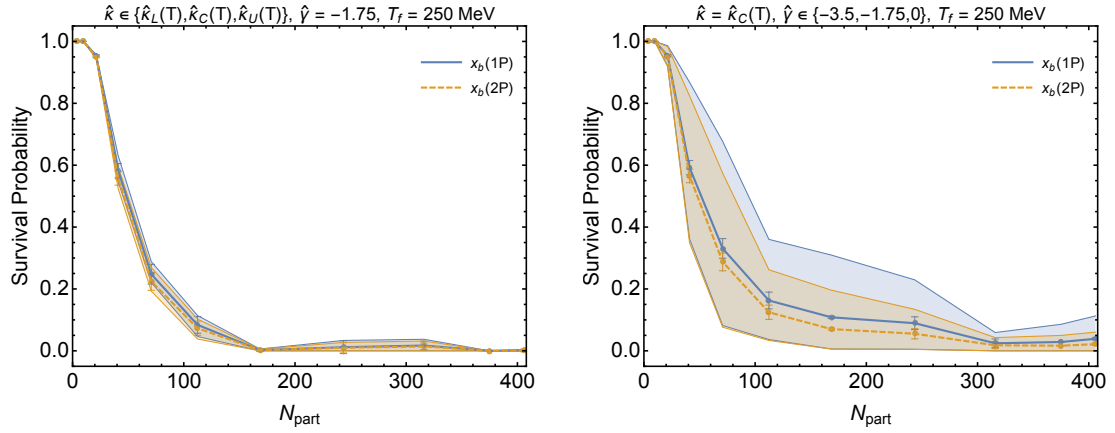

Figure B.8: The survival probabilities of the $\chi_b(1P)$ and $\chi_b(2P)$ plotted against N_{part}. The left panel displays variation with respect to $\hat{\kappa}$, and the right panel variation with respect to $\hat{\gamma}$. Error bars around the central curve represent statistical uncertainties due to the averaging over quantum trejectories. Taken from Ref. [60].

128
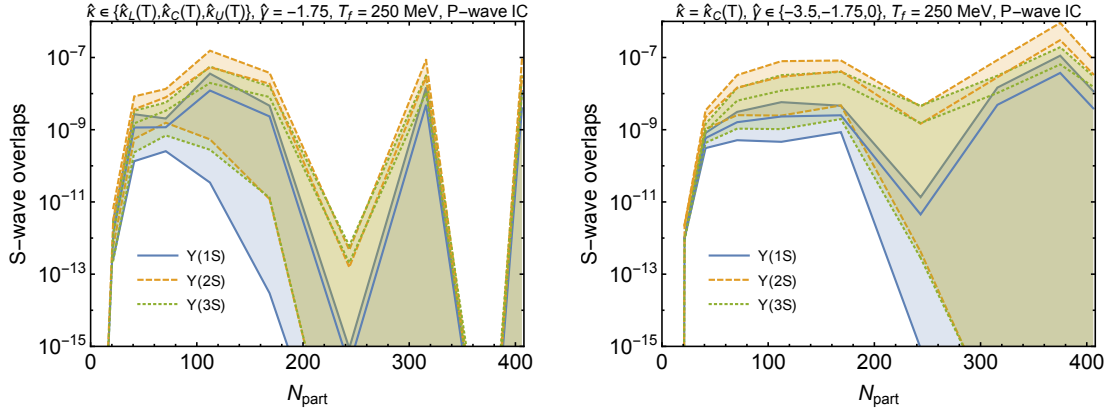
Figure B.9: The overlaps of the P-wave, singlet Gaussian initial condition with the $\Upsilon(1S)$, $\Upsilon(2S)$ and $\Upsilon(3S)$ states plotted against N_{part}. The left panel displays variation with respect to $\hat{\kappa}$, and the right panel variation with respect to $\hat{\gamma}$. Taken from Ref. [60].
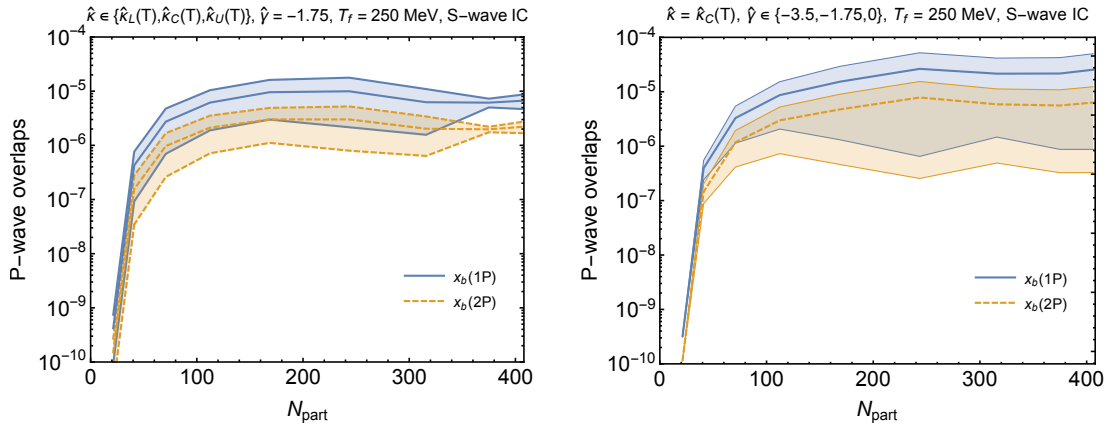

Figure B.10: The overlaps of the S-wave, singlet, Gaussian initial condition with the $\chi_b(1P)$ and $\chi_b(2P)$ states plotted against N_{part}. The left panel displays variation with respect to $\hat{\kappa}$, and the right panel variation with respect to $\hat{\gamma}$. Taken from Ref. [60].
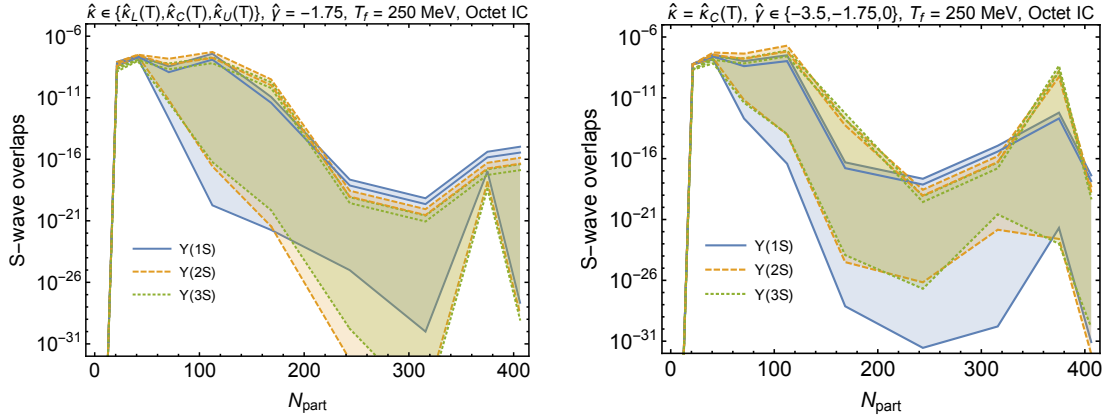
Figure B.11: The overlaps of the P-wave, octet Gaussian initial condition with the $\Upsilon(1S)$, $\Upsilon(2S)$ and $\Upsilon(3S)$ states plotted against N_{part}. The left panel displays variation with respect to $\hat{\kappa}$, and the right panel variation with respect to $\hat{\gamma}$. Taken from Ref. [60].
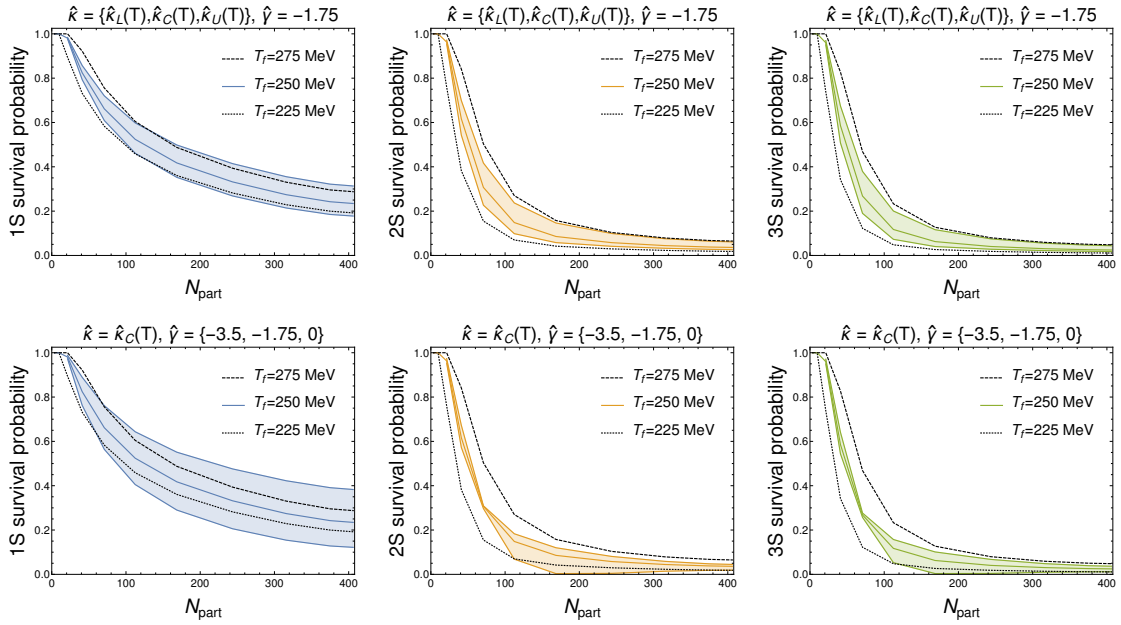

Figure B.12: $1S$, $2S$ and $3S$ survival probabilities of an initial Gaussian state evolved with H_{eff}, i.e., without jumps. The central colored line in each panel represents the evolution down to $T_{\text{f}} = 250$ MeV with $\hat{\kappa}_C(T)$ and $\hat{\gamma} = -1.75$. The colored bands represent variations in $\hat{\kappa}$ (upper row) and $\hat{\gamma}$ (lower row) with $T_f = 250$ MeV. The black dashed and dotted lines represent the evolution down to $T_{\text{f}} = 275$ MeV and 225 MeV, respectively, with $\hat{\kappa}_C(T)$ and $\hat{\gamma} = -1.75$. Taken from Ref. [60].

Appendix C

NLO Lindblad equation

In chapters 8 and 9 of this thesis, we present Lindblad equations describing the in-medium evolution of heavy Coulombic quarkonium. These equations contain 6 collapse operators corresponding to 2 color transitions and 3 spatial directions. As the heavy quarkonium system is spherically symmetric, the 6 collapse operators can be reduced to 2. In this appendix, we carry out this procedure by expanding the Lindblad equation in spherical harmonics and derive the form of the collapse operators and effective Hamiltonian.

We begin by defining the density matrix projected onto the spherical spherical harmonics

$$\rho^{l'm';lm} = \langle l'm'|\rho|lm\rangle = \int \mathrm{d}\Omega(\theta,\phi) \, Y^{l'm'*}(\theta,\phi) \, \rho \, Y^{lm}(\theta,\phi). \tag{C.1}$$

As the system is rotationally symmetric, i.e., posses no preferred direction, the density matrix is diagonal in l and m

$$\rho^{l'm';lm} = \rho^{lm;lm}\delta_{ll'}\delta_{mm'}. \tag{C.2}$$

The rotational symmetry, furthermore, implies the equal probability of all polarizations within an orbital; all information can, therefore, be encoded in

$$\rho^l = \sum_m \rho^{lm;lm}. \tag{C.3}$$

We proceed by performing this projection and summation at the level of the Lindblad equation thus deriving an evolution equation for ρ^l.

We parametrize a general collapse operator as a linear combination of the position and momentum operators in 3 dimensions

$$C_i = ar_i + bp_i, \tag{C.4}$$

where a and b are radially symmetric, complex matrix operators. We project the Lindblad equation onto eigenstates $|lm\rangle$; we, therefore, seek to calculate matrix elements of the form $\langle l'm'|C_i^{(\dagger)}|lm\rangle$. We thus make use of the Wigner-Eckart theorem

$$\langle l'm'|C_q|lm\rangle = \langle lm;1q|l'm'\rangle\langle l'||C||l\rangle, \tag{C.5}$$

where $\langle l'||C||l \rangle$ is a reduced matrix element independent of m, m' and q, and $\langle lm; 1q|l'm' \rangle$ is a Clebsch-Gordan coefficient. Here, q is an index in the basis of spherical tensors taking the values -1, 0 and 1; the components of the collapse operator C_q are defined in terms of their Cartesian counterparts C_i as

$$C_{\pm 1} = \mp \frac{1}{\sqrt{2}} (C_x \pm iC_y), \quad C_0 = C_z. \tag{C.6}$$

Inner products of the form $C_i^\dagger C_i$ are equivalent between the two bases

$$\sum_i C_i^\dagger C_i = \sum_q C_q^\dagger C_q. \tag{C.7}$$

In sec. C.1, we derive the reduced matrix element given in Eq. (C.5) with the collapse operator defined in Eq. (C.4). In sec. C.2, we use the Wigner-Eckart theorem and the reduced matrix elements to derive the form of the Lindblad equation as an expansion in spherical harmonics.

C.1   Reduced matrix elements

To evaluate the reduced matrix element $\langle l'||C||l \rangle$, we consider the case $q = m = m' = 0$; this brings Eq. (C.5) to the form

$$\langle l'||C||l \rangle = \frac{\langle l'0|C_0|l0 \rangle}{\langle l0; 10|l'0 \rangle}. \tag{C.8}$$

In spherical coordinates, we thus have

$$C_0 = a\,r_0 + ib\,p_0 = ar\cos\theta - ib \left[\cos\theta \frac{\partial}{\partial r} - \frac{\sin\theta}{r} \frac{\partial}{\partial\theta} \right]. \tag{C.9}$$

In subsecs. C.1.1, C.1.2 and C.1.3 we derive $\langle l||r||l' \rangle$, $\langle l||p||l' \rangle$ and $\langle l||C||l' \rangle$, respectively.

C.1.1 $\langle l||r||l' \rangle$

We begin by writing the angular dependent piece of $r_0 = ar\cos\theta$ in terms of spherical harmonics as

$$\cos\theta = \sqrt{(4\pi)/3}\,Y_{10}(\theta,\phi). \tag{C.10}$$

We utilize the identity

$$\int d\Omega\, Y_{l_1 m_1}(\theta,\phi)\, Y_{l_2 m_2}(\theta,\phi)\, Y_{l_3 m_3}^*(\theta,\phi) =$$
$$\sqrt{\frac{(2l_1+1)(2l_2+1)}{4\pi(2l_3+1)}} \langle l_1 m_1; l_2 m_2|l_3 m_3 \rangle \langle l_1 0; l_2 0|l_3 0 \rangle, \tag{C.11}$$

for the integral of three spherical harmonics and the Clebsch-Gordan coefficient

$$\langle l0; 10|l'0\rangle = \sqrt{\frac{l+1}{2l+1}}\delta_{l',l+1} - \sqrt{\frac{l}{2l+1}}\delta_{l',l-1}, \tag{C.12}$$

to write

$$\langle l'||r||l\rangle = \frac{\langle l'0|r\cos\theta|l0\rangle}{\langle l0; 10|l'0\rangle} \tag{C.13}$$

$$= r\sqrt{\frac{l+1}{2l+3}}\delta_{l',l+1} - r\sqrt{\frac{l}{2l-1}}\delta_{l',l-1}. \tag{C.14}$$

C.1.2 $\quad\langle l||p||l'\rangle$

The angular dependent piece of p_0 remaining to be calculated is $\sin\theta(\partial/\partial\theta)$. We thus must calculate

$$\langle l'0|\sin\theta\frac{\partial}{\partial\theta}|l0\rangle = \int d\Omega\, Y_{l'0}^*(\theta,\phi)\sin\theta\frac{\partial}{\partial\theta}Y_{l0}(\theta,\phi). \tag{C.15}$$

This integral is computed most easily by rewriting the spherical harmonics in terms of the Legendre Polynomials

$$Y_{l0}(\theta,\phi) = \sqrt{\frac{2l+1}{4\pi}}P_l(\cos\theta), \tag{C.16}$$

and performing the coordinate transformation

$$x = \cos\theta. \tag{C.17}$$

This gives

$$\int d\Omega\, Y_{l'0}^*(\theta,\phi)\sin\theta\frac{\partial}{\partial\theta}Y_{l0}(\theta,\phi) = \frac{1}{2}\sqrt{(2l'+1)(2l+1)}\int_{-1}^{-1}dx\, P_{l'}(x)(x^2-1)P_l'(x), \tag{C.18}$$

where

$$P_l'(x) = \frac{\partial}{\partial x}P_l(x). \tag{C.19}$$

Using the following orthogonality and recurrence relations of the Legendre polynomials,

$$(x^2-1)P_l' = l\left[xP_l(x) - P_{l-1}(x)\right] \tag{C.20}$$

$$= l\left[P_1(x)P_l(x) - P_{l-1}(x)\right], \tag{C.21}$$

$$\int_{-1}^{1}dx\, P_{l_1}(x)P_{l_2}(x)P_{l_3}(x) = \frac{2}{l_3+1}\langle l_10; l_20|l_30\rangle^2, \tag{C.22}$$

$$\int_{-1}^{1}dx\, P_{l_1}(x)P_{l_2}(x) = \frac{2}{l_1+1}\delta_{l_1 l_2}, \tag{C.23}$$

we rewrite Eq.(C.18) as

$$\frac{1}{2}\sqrt{(2l'+1)(2l+1)}\int_{-1}^{-1} \mathrm{d}x\, P_{l'}(x)(x^2-1)P_l'(x)$$
$$= l\sqrt{\frac{2l+1}{2l'+1}}\left(\langle l0;\, 10|l'0\rangle^2 - \delta_{l',l-1}\right).$$

(C.24)

Combing Eqs. (C.15), (C.18), and (C.24) with Eq. (C.12), we have

$$\langle l'0|\sin\theta\frac{\partial}{\partial\theta}|l0\rangle = l\frac{l+1}{\sqrt{(2l+3)(2l+1)}}\delta_{l',l+1} - l\frac{l+1}{\sqrt{(2l-1)(2l+1)}}\delta_{l',l-1}.$$

(C.25)

This gives

$$\langle l'||p||l'\rangle = \frac{\langle l'0|(-i)\left(\cos\theta\frac{\partial}{\partial r} - \frac{\sin\theta}{r}\frac{\partial}{\partial\theta}\right)|l0\rangle}{\langle l0;\, 10|l'0\rangle}$$

(C.26)

$$= -i\Bigg\{\sqrt{\frac{l+1}{2l+3}}\delta_{l',l+1}\frac{\partial}{\partial r} - \sqrt{\frac{l}{2l-1}}\delta_{l',l-1}\frac{\partial}{\partial r}$$
$$- \left(l\sqrt{\frac{l+1}{2l+3}}\delta_{l',l+1}\frac{1}{r} + (l+1)\sqrt{\frac{l}{2l-1}}\delta_{l',l-1}\frac{1}{r}\right)\Bigg\}.$$

(C.27)

C.1.3   Collapse operators

Combining Eqs. (C.8), (C.9), (C.14) and (C.27), we have

$$\langle l'||C||l\rangle = \frac{\langle l'0|\left[ar\cos\theta - bi\left(\cos\theta\frac{\partial}{\partial r} - \frac{\sin\theta}{r}\frac{\partial}{\partial\theta}\right)\right]|l0\rangle}{\langle l0;\, 10|l'0\rangle}$$

(C.28)

$$= \sqrt{\frac{l+1}{2l+3}}\left[ar - bi\left(\frac{\partial}{\partial r} - \frac{l}{r}\right)\right]\delta_{l',l+1}$$
$$- \sqrt{\frac{l}{2l-1}}\left[ar - bi\left(\frac{\partial}{\partial r} + \frac{l+1}{r}\right)\right]\delta_{l',l-1}.$$

(C.29)

To perform the appropriate projections and summations on the Lindblad equation, complex conjugate reduced matrix elements of the form $\langle l'||C||l\rangle^\dagger$ are also necessary. We note that the derivative operator transforms nontrivially under complex conjugation:

$$\langle r|\left(-i\frac{\partial}{\partial r}\right)|r\rangle^\dagger = \int_0^\infty \mathrm{d}r\, r^2\psi^*(r)\left(-i\frac{\partial}{\partial r}\right)^\dagger\psi(r) = \int_0^\infty \mathrm{d}r\, r^2\left(i\frac{\partial}{\partial r}\psi^*(r)\right)\psi(r),$$

(C.30)

implying

$$\left(-i\frac{\partial}{\partial r}\right)^\dagger \sim -i\left(\frac{\partial}{\partial r} + \frac{2}{r}\right),$$

(C.31)

after integrating by parts and solving for the Hermitian conjugate. We use this relation to calculate the four nonzero transition elements specified by Eq. (C.29) and its complex conjugate

$$\langle l+1||C||l\rangle = \sqrt{\frac{l+1}{2l+3}}\left[ar-bi\left(\frac{\partial}{\partial r}-\frac{l}{r}\right)\right],\tag{C.32}$$

$$\langle l-1||C||l\rangle = -\sqrt{\frac{l}{2l-1}}\left[ar-bi\left(\frac{\partial}{\partial r}+\frac{l+1}{r}\right)\right],\tag{C.33}$$

$$\langle l+1||C||l\rangle^\dagger = \sqrt{\frac{l+1}{2l+3}}\left[a^\dagger r-b^\dagger i\left(\frac{\partial}{\partial r}+\frac{l+2}{r}\right)\right],\tag{C.34}$$

$$\langle l-1||C||l\rangle^\dagger = -\sqrt{\frac{l}{2l-1}}\left[a^\dagger r-b^\dagger i\left(\frac{\partial}{\partial r}-\frac{l-1}{r}\right)\right].\tag{C.35}$$

In the following section, we utilize the above matrix elements to derive the form of the Lindblad equation acting on the state ρ^l.

C.2   Projected Lindblad equation

In this section, we utilize the relations derived in the previous section to write the Lindblad equation as an expansion in spherical harmonics. We work term by term and calculate the necessary matrix elements to describe the kinetic term of the Hamiltonian $\sim \vec{p}^2/M$, the LO correction to the potential $\sim r^2$, the NLO correction to the potential $\sim \{r_i, p_i\}$, the jump term $\sim C_i\rho C_i^\dagger$ and the width term $\sim \{C_i^\dagger C_i, \rho\}$.

Kinetic term

Using the Wigner-Eckart theorem of Eq. (C.5) and the reduced matrix elements of Eqs. (C.32-C.35), with $a=0$ and $b=1$, we have

$$\sum_{i,m}\langle lm|p_ip_i|lm\rangle = -\left(\frac{\partial^2}{\partial r^2}+\frac{2}{r}\frac{\partial}{\partial r}\right)+\frac{l(l+1)}{r^2}.\tag{C.36}$$

LO correction to the potential

Using the Wigner-Eckart theorem of Eq. (C.5) and the reduced matrix elements of Eqs. (C.32-C.35), with $a=1$ and $b=0$, we have

$$\sum_{i,m'}\langle lm|r_ir_i|lm\rangle = r^2.\tag{C.37}$$

135

NLO correction to the potential

Using the Wigner-Eckart theorem of Eq. (C.5) and the reduced matrix elements of Eqs. (C.32-C.35), with appropriate substitutions of a and b, we have

$$\sum_{i,m'} \langle lm|\{r_i,\, p_i\}|lm\rangle = -3i - 2ir\frac{\partial}{\partial r}. \qquad (\text{C.38})$$

Jump term

We calculate in detail the form of the jump term from the Lindblad equation; the width term can be calculated equivalently. We begin by projecting onto the eigenstate $|l'm'\rangle$

$$\sum_{i,m',l'} \langle l'm'|C_i\,\rho\,C_i^\dagger|l'm'\rangle = \sum_{q,m',l',m} \langle l'm'|C_q|lm\rangle\rho^{lm;lm}\langle lm|C_q^\dagger|l'm'\rangle \qquad (\text{C.39})$$

$$= \sum_{q,m',l',m} \langle l'm'|C_q|lm\rangle\rho^{lm;lm}\langle l'm'|C_q|lm\rangle^\dagger. \qquad (\text{C.40})$$

We rewrite this using the Wigner-Eckart theorem of Eq. (C.5)

$$\begin{aligned}
&\sum_{q,m',l',m} \langle l'm'|C_q|lm\rangle\rho^{lm;lm}\langle l'm'|C_q|lm\rangle^\dagger \\
&= \sum_{q,m',l',m} \langle lm; 1q|l'm'\rangle\langle l'||C_q||l\rangle\rho^{lm;lm}\langle lm; 1q|l'm'\rangle\langle l'||C_q||l\rangle^\dagger,
\end{aligned} \qquad (\text{C.41})$$

where we choose the Clebsch-Gordan coefficients to be real. We make use of the symmetry properties of the Clebsch-Gordan coefficients to rewrite them as

$$\langle lm; 1q|l'm'\rangle = (-1)^{1+q}\sqrt{\frac{2l'+1}{2l+1}}\langle l'(-m'); 1q|l(-m)\rangle; \qquad (\text{C.42})$$

we, furthermore, make use of the completeness relation

$$\sum_{m',q} \langle LM|l'm'; 1q\rangle\langle l'm'; 1q|L'M'\rangle = \delta_{LL'}\delta_{MM'}, \qquad (\text{C.43})$$

allowing us to perform the sums over m' and q. The only remaining m dependence is in $\rho^{lm;lm}$; we use Eq. (C.3) to perform this sum thus simplifying Eq. (C.41) to

$$\sum_{q,m',l',m} \langle l'm'|C_q|lm\rangle\rho^{lm;lm}\langle l'm'|C_q|lm\rangle^\dagger = \sum_{l'} \frac{2l'+1}{2l+1}\langle l'||C_q||l\rangle\rho^l\langle l'||C_q||l\rangle^\dagger. \qquad (\text{C.44})$$

136

Using the reduced matrix elements given in Eqs. (C.32-C.35), we find

$$
\begin{aligned}
\sum_{i,m',l'} \langle l'm'|C_i\,\rho\,C_i^\dagger|l'm'\rangle =& \left\{ \sqrt{\frac{l+1}{2l+1}} \left[ar - bi\left(\frac{\partial}{\partial r} - \frac{l}{r}\right)\right]\rho^l \right. \\
& \left. \times \sqrt{\frac{l+1}{2l+1}} \left[a^\dagger r - b^\dagger i\left(\frac{\partial}{\partial r} + \frac{l+2}{r}\right)\right] \right\} \\
& + \left\{ \sqrt{\frac{l}{2l+1}} \left[ar - bi\left(\frac{\partial}{\partial r} + \frac{l+1}{r}\right)\right]\rho^l \right. \\
& \left. \times \sqrt{\frac{l}{2l+1}} \left[a^\dagger r - b^\dagger i\left(\frac{\partial}{\partial r} - \frac{l-1}{r}\right)\right] \right\},
\end{aligned}
\tag{C.45}
$$

where the term in the first two lines of Eq. (C.45) contributes to the time evolution of ρ^{l+1} and the term in the second two lines contributions to the time evolution of ρ^{l-1}.

Width term

As mentioned above Eq. (C.39), an equivalent set of manipulations can be performed on the $\{C_i^\dagger C_i, \rho\}$ terms of the Lindblad equation. This gives

$$
\sum_{i,m} \langle lm|\{C_i^\dagger C_i, \rho\}|lm\rangle = \sum_{l'} \left\{ \frac{2l'+1}{2l+1} \langle l'||C||l\rangle^\dagger \langle l'||C||l\rangle, \rho^l \right\}
\tag{C.46}
$$

$$
\begin{aligned}
=& \left\{ \sqrt{\frac{l+1}{2l+1}} \left[a^\dagger r - b^\dagger i\left(\frac{\partial}{\partial r} + \frac{l+2}{r}\right)\right] \right. \\
& \left. \sqrt{\frac{l+1}{2l+1}} \left[ar - bi\left(\frac{\partial}{\partial r} - \frac{l}{r}\right)\right], \rho^l \right\} \\
& + \left\{ \sqrt{\frac{l}{2l+1}} \left[a^\dagger r - b^\dagger i\left(\frac{\partial}{\partial r} - \frac{l-1}{r}\right)\right] \right. \\
& \left. \sqrt{\frac{l}{2l+1}} \left[ar - bi\left(\frac{\partial}{\partial r} + \frac{l+1}{r}\right)\right], \rho^l \right\},
\end{aligned}
\tag{C.47}
$$

where the first term in Eq. (C.47) implements the reduction in norm of a state of angular momentum l due to transitions to a state of angular momentum $l+1$ and the second term in Eq. (C.47) due to transitions to a state of angular momentum $l-1$.

References

[1] T. Matsui and H. Satz, *J/ψ Suppression by Quark-Gluon Plasma Formation*, *Phys. Lett. B* **178** (1986) 416.

[2] M. Laine, O. Philipsen, P. Romatschke and M. Tassler, *Real-time static potential in hot QCD*, *JHEP* **03** (2007) 054 [`hep-ph/0611300`].

[3] N. Brambilla, J. Ghiglieri, A. Vairo and P. Petreczky, *Static quark-antiquark pairs at finite temperature*, *Phys. Rev. D* **78** (2008) 014017 [`0804.0993`].

[4] A. Beraudo, J. P. Blaizot and C. Ratti, *Real and imaginary-time Q anti-Q correlators in a thermal medium*, *Nucl. Phys. A* **806** (2008) 312 [`0712.4394`].

[5] M. A. Escobedo and J. Soto, *Non-relativistic bound states at finite temperature (I): The Hydrogen atom*, *Phys. Rev. A* **78** (2008) 032520 [`0804.0691`].

[6] N. Brambilla, M. A. Escobedo, J. Ghiglieri, J. Soto and A. Vairo, *Heavy Quarkonium in a weakly-coupled quark-gluon plasma below the melting temperature*, *JHEP* **09** (2010) 038 [`1007.4156`].

[7] N. Brambilla, M. A. Escobedo, J. Ghiglieri and A. Vairo, *Thermal width and gluo-dissociation of quarkonium in pNRQCD*, *JHEP* **12** (2011) 116 [`1109.5826`].

[8] N. Brambilla, M. A. Escobedo, J. Ghiglieri and A. Vairo, *Thermal width and quarkonium dissociation by inelastic parton scattering*, *JHEP* **05** (2013) 130 [`1303.6097`].

[9] A. Dumitru, Y. Guo and M. Strickland, *The Imaginary part of the static gluon propagator in an anisotropic (viscous) QCD plasma*, *Phys. Rev. D* **79** (2009) 114003 [`0903.4703`].

[10] ALICE collaboration, B. Abelev et al., *J/ψ suppression at forward rapidity in Pb-Pb collisions at $\sqrt{s_{NN}} = 2.76$ TeV*, *Phys. Rev. Lett.* **109** (2012) 072301 [`1202.1383`].

[11] ALICE collaboration, J. Adam et al., *Differential studies of inclusive J/ψ and ψ(2S) production at forward rapidity in Pb-Pb collisions at $\sqrt{s_{\mathrm{NN}}} = 2.76$ TeV*, *JHEP* **05** (2016) 179 [`1506.08804`].

[12] ALICE collaboration, J. Adam et al., *J/ψ suppression at forward rapidity in Pb-Pb collisions at* $\sqrt{s_{\mathrm{NN}}} = $ **5.02** *TeV*, *Phys. Lett. B* **766** (2017) 212 [`1606.08197`].

[13] ALICE collaboration, S. Acharya et al., *Studies of J/ψ production at forward rapidity in Pb-Pb collisions at* $\sqrt{s_{\mathrm{NN}}} = 5.02$ *TeV*, *JHEP* **02** (2020) 041 [`1909.03158`].

[14] P. Braun-Munzinger and J. Stachel, *(Non)thermal aspects of charmonium production and a new look at J / psi suppression*, *Phys. Lett. B* **490** (2000) 196 [`nucl-th/0007059`].

[15] R. L. Thews, M. Schroedter and J. Rafelski, *Enhanced J/ψ production in deconfined quark matter*, *Phys. Rev. C* **63** (2001) 054905 [`hep-ph/0007323`].

[16] A. Andronic, P. Braun-Munzinger, K. Redlich and J. Stachel, *Evidence for charmonium generation at the phase boundary in ultra-relativistic nuclear collisions*, *Phys. Lett. B* **652** (2007) 259 [`nucl-th/0701079`].

[17] X. Zhao and R. Rapp, *Transverse Momentum Spectra of J/ψ in Heavy-Ion Collisions*, *Phys. Lett. B* **664** (2008) 253 [`0712.2407`].

[18] W. E. Caswell and G. P. Lepage, *Effective Lagrangians for Bound State Problems in QED, QCD, and Other Field Theories*, *Phys. Lett. B* **167** (1986) 437.

[19] G. T. Bodwin, E. Braaten and G. P. Lepage, *Rigorous QCD analysis of inclusive annihilation and production of heavy quarkonium*, *Phys. Rev. D* **51** (1995) 1125 [`hep-ph/9407339`].

[20] A. Pineda and J. Soto, *Effective field theory for ultrasoft momenta in NRQCD and NRQED*, *Nucl. Phys. B Proc. Suppl.* **64** (1998) 428 [`hep-ph/9707481`].

[21] N. Brambilla, A. Pineda, J. Soto and A. Vairo, *Potential NRQCD: An Effective theory for heavy quarkonium*, *Nucl. Phys. B* **566** (2000) 275 [`hep-ph/9907240`].

[22] N. Brambilla, A. Pineda, J. Soto and A. Vairo, *Effective Field Theories for Heavy Quarkonium*, *Rev. Mod. Phys.* **77** (2005) 1423 [`hep-ph/0410047`].

[23] H. P. Breuer and F. Petruccione, *The theory of open quantum systems*. 2002.

[24] Y. Akamatsu and A. Rothkopf, *Stochastic potential and quantum decoherence of heavy quarkonium in the quark-gluon plasma*, *Phys. Rev. D* **85** (2012) 105011 [`1110.1203`].

[25] Y. Akamatsu, *Heavy quark master equations in the Lindblad form at high temperatures*, *Phys. Rev. D* **91** (2015) 056002 [`1403.5783`].

[26] J.-P. Blaizot, D. De Boni, P. Faccioli and G. Garberoglio, *Heavy quark bound states in a quark–gluon plasma: Dissociation and recombination*, *Nucl. Phys. A* **946** (2016) 49 [1503.03857].

[27] R. Katz and P. B. Gossiaux, *The Schrödinger–Langevin equation with and without thermal fluctuations*, *Annals Phys.* **368** (2016) 267 [1504.08087].

[28] N. Brambilla, M. A. Escobedo, J. Soto and A. Vairo, *Quarkonium suppression in heavy-ion collisions: an open quantum system approach*, *Phys. Rev. D* **96** (2017) 034021 [1612.07248].

[29] J.-P. Blaizot and M. A. Escobedo, *Quantum and classical dynamics of heavy quarks in a quark-gluon plasma*, *JHEP* **06** (2018) 034 [1711.10812].

[30] N. Brambilla, M. A. Escobedo, J. Soto and A. Vairo, *Heavy quarkonium suppression in a fireball*, *Phys. Rev. D* **97** (2018) 074009 [1711.04515].

[31] J.-P. Blaizot and M. A. Escobedo, *Approach to equilibrium of a quarkonium in a quark-gluon plasma*, *Phys. Rev. D* **98** (2018) 074007 [1803.07996].

[32] X. Yao and T. Mehen, *Quarkonium in-medium transport equation derived from first principles*, *Phys. Rev. D* **99** (2019) 096028 [1811.07027].

[33] N. Brambilla, M. A. Escobedo, A. Vairo and P. Vander Griend, *Transport coefficients from in medium quarkonium dynamics*, *Phys. Rev. D* **100** (2019) 054025 [1903.08063].

[34] T. Miura, Y. Akamatsu, M. Asakawa and A. Rothkopf, *Quantum Brownian motion of a heavy quark pair in the quark-gluon plasma*, *Phys. Rev. D* **101** (2020) 034011 [1908.06293].

[35] R. Sharma and A. Tiwari, *Quantum evolution of quarkonia with correlated and uncorrelated noise*, *Phys. Rev. D* **101** (2020) 074004 [1912.07036].

[36] X. Yao, W. Ke, Y. Xu, S. A. Bass and B. Müller, *Coupled Boltzmann Transport Equations of Heavy Quarks and Quarkonia in Quark-Gluon Plasma*, *JHEP* **01** (2021) 046 [2004.06746].

[37] X. Yao and T. Mehen, *Quarkonium Semiclassical Transport in Quark-Gluon Plasma: Factorization and Quantum Correction*, *JHEP* **02** (2021) 062 [2009.02408].

[38] J.-P. Blaizot and M. A. Escobedo, *Phenomenological study of quarkonium suppression and the impact of the energy gap between singlets and octets*, *Phys. Rev. D* **104** (2021) 054034 [2106.15371].

[39] Y. Akamatsu, *Quarkonium in quark–gluon plasma: Open quantum system approaches re-examined*, *Prog. Part. Nucl. Phys.* **123** (2022) 103932 [2009.10559].

[40] X. Yao, *Open quantum systems for quarkonia*, *Int. J. Mod. Phys. A* **36** (2021) 2130010 [`2102.01736`].

[41] M. L. Bellac, *Thermal Field Theory*, Cambridge Monographs on Mathematical Physics. Cambridge University Press, 3, 2011, 10.1017/CBO9780511721700.

[42] J. I. Kapusta and C. Gale, *Finite-temperature field theory: Principles and applications*, Cambridge Monographs on Mathematical Physics. Cambridge University Press, 2011, 10.1017/CBO9780511535130.

[43] A. K. Das, *Finite Temperature Field Theory*. World Scientific, New York, 1997.

[44] K.-c. Chou, Z.-b. Su, B.-l. Hao and L. Yu, *Equilibrium and Nonequilibrium Formalisms Made Unified*, *Phys. Rept.* **118** (1985) 1.

[45] J. Berges, *Introduction to nonequilibrium quantum field theory*, *AIP Conf. Proc.* **739** (2004) 3 [`hep-ph/0409233`].

[46] ALICE collaboration, S. Acharya et al., Υ *production and nuclear modification at forward rapidity in Pb-Pb collisions at* $\sqrt{s_{NN}} =$ **5.02** *TeV*, *Phys. Lett. B* **822** (2021) 136579 [`2011.05758`].

[47] Songkyo Lee (ATLAS Collaboration), "Quarkonium production in Pb+Pb collisions with ATLAS." Quark Matter 2020 `https://indico.cern.ch/event/792436/contributions/3535775/`, 2017.

[48] CMS collaboration, A. M. Sirunyan et al., *Measurement of nuclear modification factors of* $\Upsilon(1S)$, $\Upsilon(2S)$, *and* $\Upsilon(3S)$ *mesons in PbPb collisions at* $\sqrt{s_{NN}} = 5.02$ *TeV*, *Phys. Lett. B* **790** (2019) 270 [`1805.09215`].

[49] CMS collaboration, A. M. Sirunyan et al., *Suppression of Excited* Υ *States Relative to the Ground State in Pb-Pb Collisions at* $\sqrt{s_{NN}} = 5.02$ *TeV*, *Phys. Rev. Lett.* **120** (2018) 142301 [`1706.05984`].

[50] CMS collaboration, A. M. Sirunyan et al., *Measurement of the azimuthal anisotropy of Image 1 and Image 2 mesons in PbPb collisions at sNN=5.02TeV*, *Phys. Lett. B* **819** (2021) 136385 [`2006.07707`].

[51] ALICE collaboration, S. Acharya et al., *Measurement of* $\Upsilon(1S)$ *elliptic flow at forward rapidity in Pb-Pb collisions at* $\sqrt{s_{NN}} = 5.02$ *TeV*, *Phys. Rev. Lett.* **123** (2019) 192301 [`1907.03169`].

[52] Soohwan Lee (CMS Collaboration), "Observation of the $\Upsilon(3S)$ meson and sequential suppression of states in PbPb collisions at $\sqrt{s_{NN}} = 5.02$ TeV." Quark Matter 2022, Krakow, Poland, `https://indico.cern.ch/event/895086/contributions/4716202/`, 2022.

[53] STAR collaboration, L. Adamczyk et al., *Suppression of Υ production in d+Au and Au+Au collisions at $\sqrt{s_{NN}}$=200 GeV, Phys. Lett. B* **735** (2014) 127 [`1312.3675`].

[54] PHENIX collaboration, A. Adare et al., *Measurement of $\Upsilon(1S + 2S + 3S)$ production in $p + p$ and Au+Au collisions at $\sqrt{s_{NN}} = 200$ GeV, Phys. Rev. C* **91** (2015) 024913 [`1404.2246`].

[55] STAR collaboration, L. Adamczyk et al., *Υ production in $U + U$ collisions at $\sqrt{s_{NN}} = 193$ GeV measured with the STAR experiment, Phys. Rev. C* **94** (2016) 064904 [`1608.06487`].

[56] X. Du, R. Rapp and M. He, *Color Screening and Regeneration of Bottomonia in High-Energy Heavy-Ion Collisions, Phys. Rev. C* **96** (2017) 054901 [`1706.08670`].

[57] R. Katz, S. Delorme and P.-B. Gossiaux, *One-dimensional complex potentials for quarkonia in a quark-gluon plasma*, `2205.05154`.

[58] E. G. Ferreiro, *Charmonium dissociation and recombination at LHC: Revisiting comovers, Phys. Lett. B* **731** (2014) 57 [`1210.3209`].

[59] H. B. Omar, M. A. Escobedo, A. Islam, M. Strickland, S. Thapa, P. Vander Griend et al., *QTRAJ 1.0: A Lindblad equation solver for heavy-quarkonium dynamics, Comput. Phys. Commun.* **273** (2022) 108266 [`2107.06147`].

[60] N. Brambilla, M. A. Escobedo, M. Strickland, A. Vairo, P. Vander Griend and J. H. Weber, *Bottomonium suppression in an open quantum system using the quantum trajectories method, JHEP* **05** (2021) 136 [`2012.01240`].

[61] N. Brambilla, M. A. Escobedo, M. Strickland, A. Vairo, P. Vander Griend and J. H. Weber, *Bottomonium production in heavy-ion collisions using quantum trajectories: Differential observables and momentum anisotropy, Phys. Rev. D* **104** (2021) 094049 [`2107.06222`].

[62] N. Brambilla, M. A. Escobedo, A. Islam, M. Strickland, A. Tiwari, A. Vairo et al., *Heavy quarkonium dynamics at next-to-leading order in the binding energy over temperature*, `2205.10289`.

[63] Particle Data Group collaboration, R. Workman et al., *Review of Particle Physics*, .

[64] D. J. Gross and F. Wilczek, *Ultraviolet Behavior of Nonabelian Gauge Theories, Phys. Rev. Lett.* **30** (1973) 1343.

[65] H. D. Politzer, *Reliable Perturbative Results for Strong Interactions?, Phys. Rev. Lett.* **30** (1973) 1346.

[66] M. Neubert, *Heavy quark effective theory, Subnucl. Ser.* **34** (1997) 98 [`hep-ph/9610266`].

[67] A. V. Manohar, *The HQET / NRQCD Lagrangian to order alpha / m-3, Phys. Rev. D* **56** (1997) 230 [`hep-ph/9701294`].

[68] M. E. Luke and A. V. Manohar, *Reparametrization invariance constraints on heavy particle effective field theories, Phys. Lett. B* **286** (1992) 348 [`hep-ph/9205228`].

[69] A. Pineda, *Review of Heavy Quarkonium at weak coupling, Prog. Part. Nucl. Phys.* **67** (2012) 735 [`1111.0165`].

[70] N. Brambilla, D. Gromes and A. Vairo, *Poincare invariance constraints on NRQCD and potential NRQCD, Phys. Lett. B* **576** (2003) 314 [`hep-ph/0306107`].

[71] M. Berwein, N. Brambilla, S. Hwang and A. Vairo, *Poincaré invariance in NRQCD and potential NRQCD revisited, Phys. Rev. D* **99** (2019) 094008 [`1811.05184`].

[72] Quarkonium Working Group collaboration, N. Brambilla et al., *Heavy quarkonium physics*, `hep-ph/0412158`.

[73] N. Brambilla et al., *Heavy Quarkonium: Progress, Puzzles, and Opportunities, Eur. Phys. J. C* **71** (2011) 1534 [`1010.5827`].

[74] N. Brambilla, S. Eidelman, C. Hanhart, A. Nefediev, C.-P. Shen, C. E. Thomas et al., *The XYZ states: experimental and theoretical status and perspectives, Phys. Rept.* **873** (2020) 1 [`1907.07583`].

[75] P. Labelle, *Effective field theories for QED bound states: Extending nonrelativistic QED to study retardation effects, Phys. Rev. D* **58** (1998) 093013 [`hep-ph/9608491`].

[76] M. E. Luke and A. V. Manohar, *Bound states and power counting in effective field theories, Phys. Rev. D* **55** (1997) 4129 [`hep-ph/9610534`].

[77] B. Grinstein and I. Z. Rothstein, *Effective field theory and matching in nonrelativistic gauge theories, Phys. Rev. D* **57** (1998) 78 [`hep-ph/9703298`].

[78] M. E. Luke and M. J. Savage, *Power counting in dimensionally regularized NRQCD, Phys. Rev. D* **57** (1998) 413 [`hep-ph/9707313`].

[79] A. Pineda and J. Soto, *The Lamb shift in dimensional regularization, Phys. Lett. B* **420** (1998) 391 [`hep-ph/9711292`].

[80] A. Pineda and J. Soto, *Potential NRQED: The Positronium case, Phys. Rev. D* **59** (1999) 016005 [`hep-ph/9805424`].

[81] N. Brambilla, A. Pineda, J. Soto and A. Vairo, *The Heavy quarkonium spectrum at order m alpha**5(s) l n alpha(s)*, Phys. Lett. B **470** (1999) 215 [`hep-ph/9910238`].

[82] G. Lindblad, *On the Generators of Quantum Dynamical Semigroups*, Commun. Math. Phys. **48** (1976) 119.

[83] V. Gorini, A. Kossakowski and E. C. G. Sudarshan, *Completely Positive Dynamical Semigroups of N Level Systems*, J. Math. Phys. **17** (1976) 821.

[84] M. Laine and A. Vuorinen, *Basics of Thermal Field Theory*, vol. 925. Springer, 2016, 10.1007/978-3-319-31933-9, [`1701.01554`].

[85] J. Ghiglieri, A. Kurkela, M. Strickland and A. Vuorinen, *Perturbative Thermal QCD: Formalism and Applications*, Phys. Rept. **880** (2020) 1 [`2002.10188`].

[86] A. Niegawa, *Path Integral Formulation of Real Time Quantum Field Theories at Finite Temperature*, Phys. Rev. D **40** (1989) 1199.

[87] T. S. Evans, *A New time contour for equilibrium real time thermal field theories*, Phys. Rev. D **47** (1993) R4196 [`hep-ph/9209252`].

[88] T. S. Evans and A. C. Pearson, *A Reexamination of the path ordered approach to real time thermal field theory*, Phys. Rev. D **52** (1995) 4652 [`hep-ph/9412217`].

[89] F. Gelis, *The Effect of the vertical part of the path on the real time Feynman rules in finite temperature field theory*, Z. Phys. C **70** (1996) 321 [`hep-ph/9412347`].

[90] F. Gelis, *A New approach for the vertical part of the contour in thermal field theories*, Phys. Lett. B **455** (1999) 205 [`hep-ph/9901263`].

[91] J. S. Schwinger, *Brownian motion of a quantum oscillator*, J. Math. Phys. **2** (1961) 407.

[92] L. V. Keldysh, *Diagram technique for nonequilibrium processes*, Zh. Eksp. Teor. Fiz. **47** (1964) 1515.

[93] H. van Hees, M. Mannarelli, V. Greco and R. Rapp, *Nonperturbative heavy-quark diffusion in the quark-gluon plasma*, Phys. Rev. Lett. **100** (2008) 192301 [`0709.2884`].

[94] Y. Akamatsu, T. Hatsuda and T. Hirano, *Heavy Quark Diffusion with Relativistic Langevin Dynamics in the Quark-Gluon Fluid*, Phys. Rev. C **79** (2009) 054907 [`0809.1499`].

[95] W. M. Alberico, A. Beraudo, A. De Pace, A. Molinari, M. Monteno, M. Nardi et al., *Heavy-flavour spectra in high energy nucleus-nucleus collisions*, Eur. Phys. J. C **71** (2011) 1666 [`1101.6008`].

[96] M. He, R. J. Fries and R. Rapp, *Heavy-Quark Diffusion and Hadronization in Quark-Gluon Plasma*, *Phys. Rev. C* **86** (2012) 014903 [`1106.6006`].

[97] W. M. Alberico, A. Beraudo, A. De Pace, A. Molinari, M. Monteno, M. Nardi et al., *Heavy flavors in AA collisions: production, transport and final spectra*, *Eur. Phys. J. C* **73** (2013) 2481 [`1305.7421`].

[98] S. Cao, G.-Y. Qin and S. A. Bass, *Heavy-quark dynamics and hadronization in ultrarelativistic heavy-ion collisions: Collisional versus radiative energy loss*, *Phys. Rev. C* **88** (2013) 044907 [`1308.0617`].

[99] M. He, R. J. Fries and R. Rapp, *Heavy Flavor at the Large Hadron Collider in a Strong Coupling Approach*, *Phys. Lett. B* **735** (2014) 445 [`1401.3817`].

[100] S. Cao, G.-Y. Qin and S. A. Bass, *Dynamical Evolution, Hadronization and Angular De-correlation of Heavy Flavor in a Hot and Dense QCD Medium*, *Nucl. Phys. A* **932** (2014) 38 [`1404.1081`].

[101] A. Beraudo, A. De Pace, M. Monteno, M. Nardi and F. Prino, *Heavy flavors in heavy-ion collisions: quenching, flow and correlations*, *Eur. Phys. J. C* **75** (2015) 121 [`1410.6082`].

[102] S. Cao, G.-Y. Qin and S. A. Bass, *Energy loss, hadronization and hadronic interactions of heavy flavors in relativistic heavy-ion collisions*, *Phys. Rev. C* **92** (2015) 024907 [`1505.01413`].

[103] G. D. Moore and D. Teaney, *How much do heavy quarks thermalize in a heavy ion collision?*, *Phys. Rev. C* **71** (2005) 064904 [`hep-ph/0412346`].

[104] J. Casalderrey-Solana and D. Teaney, *Heavy quark diffusion in strongly coupled N=4 Yang-Mills*, *Phys. Rev. D* **74** (2006) 085012 [`hep-ph/0605199`].

[105] S. Caron-Huot and G. D. Moore, *Heavy quark diffusion in perturbative QCD at next-to-leading order*, *Phys. Rev. Lett.* **100** (2008) 052301 [`0708.4232`].

[106] S. Caron-Huot and G. D. Moore, *Heavy quark diffusion in QCD and N=4 SYM at next-to-leading order*, *JHEP* **02** (2008) 081 [`0801.2173`].

[107] S. Caron-Huot, M. Laine and G. D. Moore, *A Way to estimate the heavy quark thermalization rate from the lattice*, *JHEP* **04** (2009) 053 [`0901.1195`].

[108] Y. Burnier, M. Laine, J. Langelage and L. Mether, *Colour-electric spectral function at next-to-leading order*, *JHEP* **08** (2010) 094 [`1006.0867`].

[109] A. Francis, O. Kaczmarek, M. Laine, T. Neuhaus and H. Ohno, *Nonperturbative estimate of the heavy quark momentum diffusion coefficient*, *Phys. Rev. D* **92** (2015) 116003 [`1508.04543`].

[110] N. Brambilla, V. Leino, P. Petreczky and A. Vairo, *Lattice QCD constraints on the heavy quark diffusion coefficient*, *Phys. Rev. D* **102** (2020) 074503 [2007.10078].

[111] TUMQCD collaboration, N. Brambilla, V. Leino, J. Mayer-Steudte and P. Petreczky, *Heavy quark diffusion coefficient with gradient flow*, 2206.02861.

[112] A. M. Eller, J. Ghiglieri and G. D. Moore, *Thermal Heavy Quark Self-Energy from Euclidean Correlators*, *Phys. Rev. D* **99** (2019) 094042 [1903.08064].

[113] M. Eidemuller and M. Jamin, *QCD field strength correlator at the next-to-leading order*, *Phys. Lett. B* **416** (1998) 415 [hep-ph/9709419].

[114] S. Kim, P. Petreczky and A. Rothkopf, *Quarkonium in-medium properties from realistic lattice NRQCD*, *JHEP* **11** (2018) 088 [1808.08781].

[115] G. Aarts, C. Allton, S. Kim, M. P. Lombardo, M. B. Oktay, S. M. Ryan et al., *What happens to the Υ and η_b in the quark-gluon plasma? Bottomonium spectral functions from lattice QCD*, *JHEP* **11** (2011) 103 [1109.4496].

[116] R. Larsen, S. Meinel, S. Mukherjee and P. Petreczky, *Thermal broadening of bottomonia: Lattice nonrelativistic QCD with extended operators*, *Phys. Rev. D* **100** (2019) 074506 [1908.08437].

[117] A. Rothkopf. private communication.

[118] ALICE collaboration, S. Acharya et al., *D-meson azimuthal anisotropy in midcentral Pb-Pb collisions at $\sqrt{s_{\mathrm{NN}}} = $ **5.02** TeV*, *Phys. Rev. Lett.* **120** (2018) 102301 [1707.01005].

[119] STAR collaboration, L. Adamczyk et al., *Measurement of D^0 Azimuthal Anisotropy at Midrapidity in Au+Au Collisions at $\sqrt{s_{NN}}$=200 GeV*, *Phys. Rev. Lett.* **118** (2017) 212301 [1701.06060].

[120] J. Uphoff, O. Fochler, Z. Xu and C. Greiner, *Open Heavy Flavor in Pb+Pb Collisions at $\sqrt{s} = 2.76$ TeV within a Transport Model*, *Phys. Lett. B* **717** (2012) 430 [1205.4945].

[121] M. Monteno, W. M. Alberico, A. Beraudo, A. De Pace, A. Molinari, M. Nardi et al., *Heavy-flavor dynamics in nucleus-nucleus collisions: from RHIC to LHC*, *J. Phys. G* **38** (2011) 124144 [1107.0256].

[122] M. Djordjevic and M. Djordjevic, *Predictions of heavy-flavor suppression at 5.1 TeV Pb + Pb collisions at the CERN Large Hadron Collider*, *Phys. Rev. C* **92** (2015) 024918 [1505.04316].

[123] T. Song, H. Berrehrah, D. Cabrera, W. Cassing and E. Bratkovskaya, *Charm production in Pb + Pb collisions at energies available at the CERN Large Hadron Collider*, *Phys. Rev. C* **93** (2016) 034906 [1512.00891].

[124] M. Nahrgang, J. Aichelin, P. B. Gossiaux and K. Werner, *Influence of hadronic bound states above T_c on heavy-quark observables in Pb + Pb collisions at at the CERN Large Hadron Collider*, *Phys. Rev. C* **89** (2014) 014905 [1305.6544].

[125] J. Uphoff, O. Fochler, Z. Xu and C. Greiner, *Elastic and radiative heavy quark interactions in ultra-relativistic heavy-ion collisions*, *J. Phys. G* **42** (2015) 115106 [1408.2964].

[126] S. Cao, T. Luo, G.-Y. Qin and X.-N. Wang, *Heavy and light flavor jet quenching at RHIC and LHC energies*, *Phys. Lett. B* **777** (2018) 255 [1703.00822].

[127] H. Berrehrah, P. B. Gossiaux, J. Aichelin, W. Cassing, J. M. Torres-Rincon and E. Bratkovskaya, *Transport coefficients of heavy quarks around T_c at finite quark chemical potential*, *Phys. Rev. C* **90** (2014) 051901 [1406.5322].

[128] T. Song, H. Berrehrah, D. Cabrera, J. M. Torres-Rincon, L. Tolos, W. Cassing et al., *Tomography of the Quark-Gluon-Plasma by Charm Quarks*, *Phys. Rev. C* **92** (2015) 014910 [1503.03039].

[129] V. Ozvenchuk, J. M. Torres-Rincon, P. B. Gossiaux, L. Tolos and J. Aichelin, *D-meson propagation in hadronic matter and consequences for heavy-flavor observables in ultrarelativistic heavy-ion collisions*, *Phys. Rev. C* **90** (2014) 054909 [1408.4938].

[130] M. Nahrgang, J. Aichelin, S. Bass, P. B. Gossiaux and K. Werner, *Elliptic and triangular flow of heavy flavor in heavy-ion collisions*, *Phys. Rev. C* **91** (2015) 014904 [1410.5396].

[131] M. He, R. J. Fries and R. Rapp, **D_s**-*Meson as Quantitative Probe of Diffusion and Hadronization in Nuclear Collisions*, *Phys. Rev. Lett.* **110** (2013) 112301 [1204.4442].

[132] S. Cao, T. Luo, G.-Y. Qin and X.-N. Wang, *Linearized Boltzmann transport model for jet propagation in the quark-gluon plasma: Heavy quark evolution*, *Phys. Rev. C* **94** (2016) 014909 [1605.06447].

[133] L.-G. Pang, Y. Hatta, X.-N. Wang and B.-W. Xiao, *Analytical and numerical Gubser solutions of the second-order hydrodynamics*, *Phys. Rev. D* **91** (2015) 074027 [1411.7767].

[134] L. Pang, Q. Wang and X.-N. Wang, *Effects of initial flow velocity fluctuation in event-by-event (3+1)D hydrodynamics*, *Phys. Rev. C* **86** (2012) 024911 [1205.5019].

[135] X. Dong, Y.-J. Lee and R. Rapp, *Open Heavy-Flavor Production in Heavy-Ion Collisions*, *Ann. Rev. Nucl. Part. Sci.* **69** (2019) 417 [1903.07709].

[136] L. Altenkort, A. M. Eller, O. Kaczmarek, L. Mazur, G. D. Moore and H.-T. Shu, *Heavy quark momentum diffusion from the lattice using gradient flow*, Phys. Rev. D **103** (2021) 014511 [`2009.13553`].

[137] D. Banerjee, R. Gavai, S. Datta and P. Majumdar, *Temperature dependence of the static quark diffusion coefficient*, `2206.15471`.

[138] M. Luscher, *Topology, the Wilson flow and the HMC algorithm*, PoS **LATTICE2010** (2010) 015 [`1009.5877`].

[139] M. Luscher and P. Weisz, *Perturbative analysis of the gradient flow in non-abelian gauge theories*, JHEP **02** (2011) 051 [`1101.0963`].

[140] A. Bouttefeux and M. Laine, *Mass-suppressed effects in heavy quark diffusion*, JHEP **12** (2020) 150 [`2010.07316`].

[141] D. Banerjee, S. Datta and M. Laine, *Lattice study of a magnetic contribution to heavy quark momentum diffusion*, `2204.14075`.

[142] B. Scheihing-Hitschfeld and X. Yao, *Gauge Invariance of Non-Abelian Field Strength Correlators: the Axial Gauge Puzzle*, `2205.04477`.

[143] PARTICLE DATA GROUP collaboration, M. Tanabashi et al., *Review of Particle Physics*, Phys. Rev. **D98** (2018) 030001.

[144] J. Johansson, P. Nation and F. Nori, *QuTiP: An open-source Python framework for the dynamics of open quantum systems*, Computer Physics Communications **183** (2012) 1760 .

[145] J. Johansson, P. Nation and F. Nori, *QuTiP 2: A Python framework for the dynamics of open quantum systems*, Computer Physics Communications **184** (2013) 1234 .

[146] A. J. Daley, *Quantum trajectories and open many-body quantum systems*, Adv. Phys. **63** (2014) 77 [`1405.6694`].

[147] B. Fornberg and G. Whitham, *A numerical and theoretical study of certain nonlinear wave phenomena*, Phil. Trans. Roy. Soc. **289** (1978) 373.

[148] T. Taha and M. Ablowitz, *Analytical and numerical aspects of certain nonlinear evolution equations. II. Numerical, nonlinear Schrödinger equation*, Journal of Computational Physics **55** (1984) 203 .

[149] J. Boyd, T. Cook, A. Islam and M. Strickland, *Heavy quarkonium suppression beyond the adiabatic limit*, Phys. Rev. D **100** (2019) 076019 [`1905.05676`].

[150] NVIDIA Corporation, "NVIDIA CUDA Fast Fourier Transform (FFT)." `https://developer.nvidia.com/cufft`, 2020.

[151] LHCʙ collaboration, R. Aaij et al., *Study of χ_b meson production in p p collisions at $\sqrt{s} = 7$ and 8 TeV and observation of the decay $\chi_b(3P) \to \Upsilon(3S)\gamma$*, *Eur. Phys. J. C* **74** (2014) 3092 [1407.7734].

[152] H. S. Chung, private communication.

[153] CMS collaboration, V. Khachatryan et al., *Measurement of the production cross section ratio $\sigma(Xb2(1P)) / \sigma(Xb1(1P)$ in pp collisions at $\sqrt{s} = 8$ TeV*, *Phys. Lett. B* **743** (2015) 383 [1409.5761].

[154] Particle Data Group collaboration, P. A. Zyla et al., *Review of Particle Physics*, *PTEP* **2020** (2020) 083C01.

[155] M. Laine, *A Resummed perturbative estimate for the quarkonium spectral function in hot QCD*, *JHEP* **05** (2007) 028 [0704.1720].

[156] R. Snellings, *Elliptic Flow: A Brief Review*, *New J. Phys.* **13** (2011) 055008 [1102.3010].

[157] HotQCD collaboration, A. Bazavov et al., *Chiral crossover in QCD at zero and non-zero chemical potentials*, *Phys. Lett. B* **795** (2019) 15 [1812.08235].

[158] S. Borsanyi, Z. Fodor, J. N. Guenther, R. Kara, S. D. Katz, P. Parotto et al., *QCD Crossover at Finite Chemical Potential from Lattice Simulations*, *Phys. Rev. Lett.* **125** (2020) 052001 [2002.02821].

[159] Y. Akamatsu, *Real-time quantum dynamics of heavy quark systems at high temperature*, *Phys. Rev. D* **87** (2013) 045016 [1209.5068].

[160] Armadillo contributors, "Armadillo: C++ library for linear algebra and scientific computing." http://arma.sourceforge.net/download.html, 2022.

[161] M. Strickland, *Thermalization and isotropization in heavy-ion collisions*, *Pramana* **84** (2015) 671 [1312.2285].

[162] D. Almaalol, A. Kurkela and M. Strickland, *Nonequilibrium Attractor in High-Temperature QCD Plasmas*, *Phys. Rev. Lett.* **125** (2020) 122302 [2004.05195].

[163] ATLAS collaboration, *Production of $\Upsilon(nS)$ mesons in Pb+Pb and pp collisions at 5.02 TeV*, 2205.03042.

[164] STAR collaboration, *Observation of sequential Υ suppression in Au+Au collisions at $\sqrt{s_{NN}} = 200$ GeV with the STAR experiment*, 2207.06568.

[165] Y. Akamatsu, M. Asakawa, S. Kajimoto and A. Rothkopf, *Quantum dissipation of a heavy quark from a nonlinear stochastic Schrödinger equation*, *JHEP* **07** (2018) 029 [1805.00167].

[166] T. Miura, Y. Akamatsu, M. Asakawa and Y. Kaida, *Simulation of Lindblad equations for quarkonium in the quark-gluon plasma*, `2205.15551`.

[167] Strickland et al, "QTraj 1.0 - Public Repository." `https://bitbucket.org/kentphysics/qtraj-fftw`, 2021.

[168] M. Alqahtani and M. Strickland, *Bulk observables at 5.02 TeV using quasiparticle anisotropic hydrodynamics*, *Eur. Phys. J. C* **81** (2021) 1022 [`2008.07657`].